Exploring Galaxy Evolution with Luminosity Functions across Cosmic Time

Holly Elbert

Oriel College

University of Oxford

A thesis submitted for the degree of

Doctor of Philosophy

August 2016

Abstract

In this thesis I investigate galaxy evolution by measuring the luminosity functions of galaxies across a wide range in redshift. I measure the abundances of high redshift galaxies in deep *HST* imaging of the GOODS-North field from the CANDELS survey. I follow this evolution to lower redshift by measuring the luminosity functions of galaxies in ground-based imaging of the XMM-LSS field from the VIDEO survey with optical data from the CFHTLS.

First, at high-redshift, I identify 22 candidate $z \approx 7$ and 6 candidate $z \approx 8-9$ galaxies. By comparing the number of candidate galaxies with those found in the GOODS-South field, I determine that cosmic variance is not the dominant source of uncertainty on the number counts. I constrain the Schechter parameters for the UV luminosity function at $z \approx 7$ and $z \approx 8-9$, finding evidence for evolution in the number density of high redshift galaxies.

Next, I present the K_s-band luminosity functions in the 1 degree^2 and 4.5 degree^2 overlaps between the VIDEO-XMM field and the CFHTLS-D1 and CFHTLS-W1 fields. I measure the luminosity functions with the $1/V_{max}$ method over the range $0.2 < z < 3$ in VIDEO-CFHTLS-D1, and over the range $0.2 < z < 1.5$ in the shallower VIDEO-CFHTLS-W1 field. I find the evolution of these luminosity functions is best described by luminosity dependent density evolution, where the characteristic magnitude has dimmed at a constant rate since $z = 3$, while the density has increased since $z = 3$, first rapidly from $z = 3$ to $z \approx 1.5$ and then more slowly from $z \approx 1.5$ to $z = 0.2$. I measure a significant upturn at the faint end of the luminosity function at low redshift.

Finally, I compare the VIDEO-CFHTLS-D1 and VIDEO-CFHTLS-W1 luminosity functions with predicted K-band luminosity functions from the Horizon-AGN simulation. I find both an over-prediction in the numbers of faint galaxies and an under-prediction in the numbers of bright galaxies, implying that the feedback from supernovae is insufficient while the feedback from AGN is over-sufficient.

Acknowledgements

Firstly and most importantly, I thank my supervisors, Andy Bunker, Matt Jarvis and Aprajita Verma. Thank you to Andy for all of your advice and help throughout my DPhil, and particularly with my first project. Thank you to Matt for your guidance, and for having confidence in me when I didn't. Aprajita, thank you for being such a fantastic mentor, and for giving me not only academic advice, but also offering your friendship and support however I needed it. Both of you have done far more than I could have asked.

Thank you also to all of the other people who've supported me in Oxford. In particular, thank you to Danielle and Jamie for being such wonderful housemates and for making my time here so special. Thank you to the other group members, Peter, Sarah, Boris and Sam, who have made working here so enjoyable, and to Rebecca and Catherine for all your help and friendship. Thank you to my officemates, Adam, Silvio, Phil, Rupert, Simon, Ben and Marisa, who have been a source of great conversation and companionship. Thank you also to Ashling, who has provided kind and expert support from my first day.

Thank you to Tim, for listening to me talk about space for four years, encouraging me whenever I needed it, and reminding me of what really matters. Thank you to Bryony, who has been a source of inspiration and support my whole life, and to my Mum and Dad, whom I cannot thank enough, for all of your help and love throughout my life.

Declaration

No part of this thesis has been accepted, or is currently submitted, for any other degree or qualification in this University or elsewhere. The work presented in this thesis is my own, with clarification that the measurement of the UV luminosity function in GOODS-North presented in Chapter 3 was computed in collaboration with Andrew Bunker, but the analysis and text were written by me.

Contents

List of Figures

List of Tables

Chapter 1

Introduction

In 1924, Edwin Hubble proved that the 'Great Andromeda Nebula' was another galaxy separate from our own through observations of variable stars (Hubble, 1925). Combined with earlier observations of other variable stars in M33, this ended the debate about whether there was a universe outside of the Milky Way. Hubble followed up his discovery in 1929 by measuring the recession velocities of galaxies and discovering they were proportional to their distances (Hubble, 1929), a fact now known as Hubble's law, providing evidence that the Universe was expanding. From this point onwards, the study of the nature of galaxies has been an active area of astronomy. Much of the scientific interest in galaxy evolution originally stemmed from its use as a probe of the cosmological nature of the Universe. It has since become an important field in its own right, as well as continuing to act as an observational test of cosmology.

Studying populations of galaxies grants us the ability to follow the changes in their bulk properties with time, environment, galaxy type and more in a way that helps us to understand how they form and evolve. One such property is the luminosity function, which describes the number distribution of galaxies with brightness. It is one of the most direct and fundamental means of tracing the evolution of galaxies and underpins the bulk of the work presented in this thesis.

In this Chapter, I first give a brief overview of the cosmological framework within which galaxy evolution operates and define some useful quantities which will be used throughout this thesis. I describe our current understanding of galaxy evolution theory, before detailing some of the observations and simulations that have helped form it. I then discuss the characteristics of galaxies at high redshift, as well as explaining techniques for selecting them used later in the thesis. Finally, I give an introduction to the galaxy luminosity function, describing how it can be measured and how it evolves before discussing measurements of the luminosity function from the local universe to high redshift.

1.1 Brief History of the Universe

Our current best description of how the Universe has evolved from the Big Bang to show the structure and complexity we see today is underpinned by the Standard Model of cosmology and ΛCDM. Under this formalism, the current Universe is flat and dark energy dominated. Dark energy in the form of a 'cosmological constant' Λ constitutes $\sim$ 70 per cent of the total mass-energy density of the Universe, collisionless cold dark matter (CDM) contributes $\sim$ 25 per cent and $\sim$ 4 per cent is made up of baryonic matter, namely the particles that form the elements and make up all of the stars and visible matter in the Universe (it should be noted that not all baryonic matter is visible, as not all baryonic matter will emit light). Despite having very little knowledge about what either dark matter or dark energy are, ΛCDM is extremely well supported by key observations of the Universe such as the Cosmic Microwave Background (CMB), shown in Figure 1.2 (Hinshaw et al., 2013; Planck Collaboration, 2015), the expansion of the Universe as measured with Type Ia supernovae (Perlmutter et al., 1999; Riess et al., 1998) and the clustering scales of galaxies (i.e. Baryon Acoustic Oscillations; Alam et al., 2016).

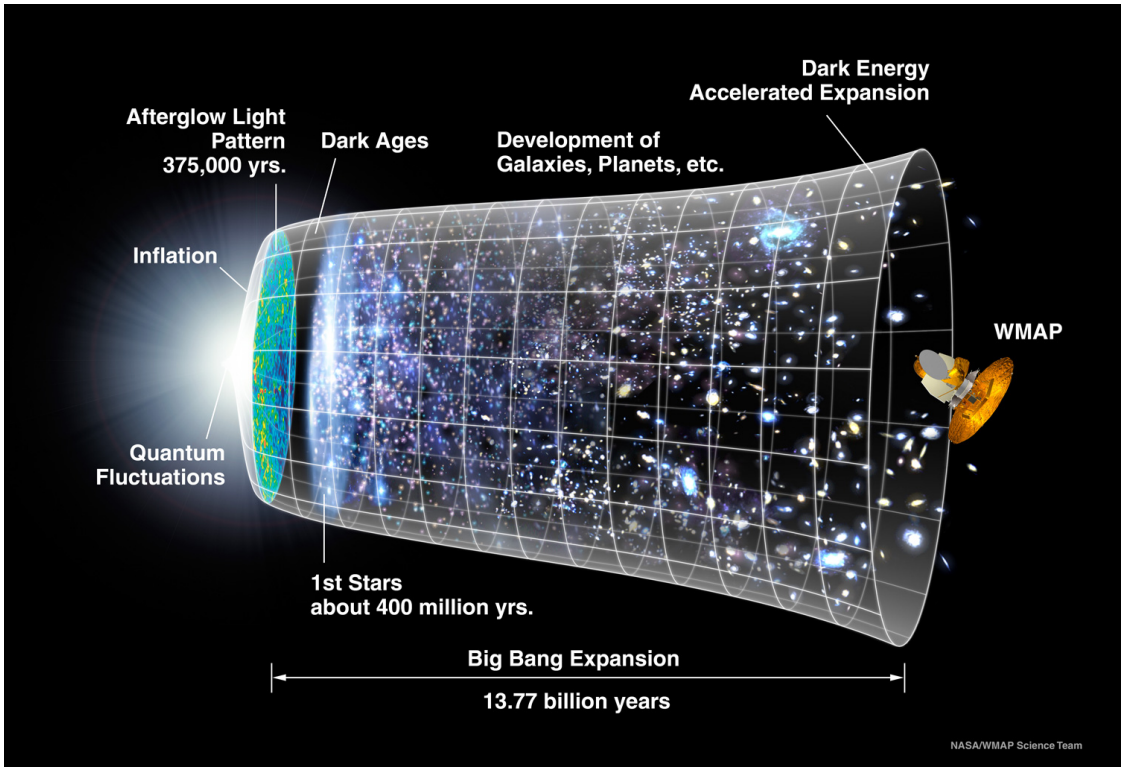

Figure 1.1: A schematic of the evolution of the Universe. Initial perturbations in the matter density seed density peaks visible in the CMB which eventually grow large enough to host galaxies and clusters. *Source: NASA*

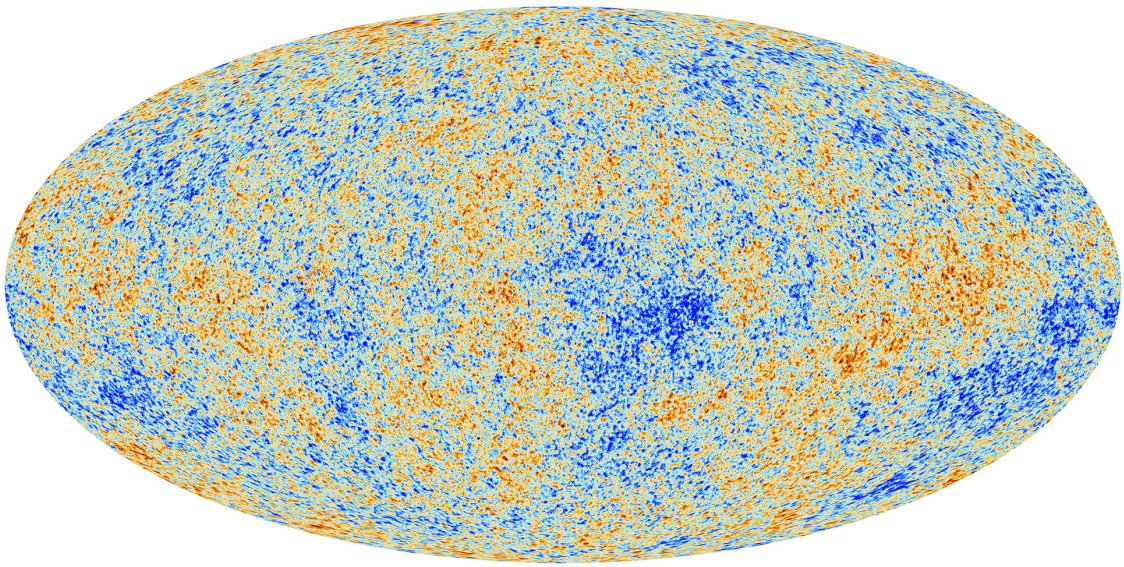

Figure 1.2: All-sky temperature map of the CMB as measured by Planck (Planck Collaboration, 2015), where red is hot and blue is cold. The temperature fluctuations map the future sites of structure formation. The smallest structures visible on the figure will correspond to structures much larger than individual galaxies, and will go on to host clusters of galaxies. *Source: ESA*

In the Standard Model of cosmology, the Universe starts off as hot and dense, with approximately homogenous contents; this is known as the Hot Big Bang (Peebles, 1980). Quantum fluctuations in the initial matter density field are expanded during the inflationary epoch into small inhomogeneities in density. 380,000 years later (at $z \approx 1100$), the Universe has expanded and cooled enough to allow atoms of hydrogen to form, changing from ionised and optically thick to neutral and transparent in a process called recombination. The inhomogeneities in density are imprinted onto the subsequently released photons which we now see as the CMB, causing anisotropies in temperature and polarisation. Figure 1.2 shows the temperature map of the CMB as measured in astonishing detail by the Planck mission (Planck Collaboration, 2014).

After recombination, the peaks in the matter density continue to grow via the gravitational collapse of dark matter while the background density decreases due to the expansion of the Universe. Once a peak has a high enough overdensity relative

to the background, it becomes gravitationally self-bound and collapses until the dark matter is thermalized, supporting itself through the random motion of particles, and forms a dark matter halo. These dark matter haloes continue to grow via accretion and mergers with other dark matter haloes.

Gas, which is initially distributed homogeneously, follows the dark matter and collapses towards the dark matter haloes, where it becomes gravitationally bound within them. It continues to collapse as mediated by the depth of the gravitational potential wells and the pressure of the gas until there are regions dense enough to form stars, making the dark matter haloes the sites of galaxy formation. As the first light sources in the Universe since the CMB switch on, the universal dark ages come to an end. The stars start to produce the first elements heavier than those formed soon after the Big Bang, and the ultraviolet (UV) light from the first stars, galaxies and black holes ionises the still-neutral intergalactic medium (IGM) in a process called reionisation (Arons & Wingert, 1972; Gunn & Peterson, 1965; Robertson et al., 2010).

1.1.1 Cosmological Redshift and Distance Measures

As light travels to us from across our expanding Universe, the change in wavelength introduced by the recession velocity of the source can be written as

$$\lambda_{observed} = (1 + z)\lambda_{emitted} \tag{1.1}$$

where z is defined as the redshift of the source. The scale factor, $a(t)$, is the ratio of some scale at an earlier time in the history of the Universe to the same scale now, and is related to redshift by

$$a(t) = \frac{a(t_e)}{a(t_0)} = \frac{1}{1 + z} \tag{1.2}$$

where $a(t_e)$ is the scale factor of the Universe when a photon is emitted and $a(t_0)$ is the scale factor of the Universe now, when the photon is observed. For the rest of this section, subscript 0 will denote the value of that quantity at the current time.

The proportionality constant at the current time between distance and recession velocity is defined as the Hubble constant, H_0:

$$v = H_0 d, \text{ where } H_0 = 100\ h \text{ km s}^{-1} \text{ Mpc}^{-1}, \tag{1.3}$$

and h is a dimensionless number used to parameterise the effect of different possible cosmologies. Equation 1.3 is only valid in the limit of small redshift and H_0 is only constant at low redshift; therefore it is more generally defined in terms of the scale factor, a, and its time derivative, $\dot{a}$:

$$H^2 \equiv \left(\frac{\dot{a}}{a}\right)^2 = \frac{8\pi G}{3}\rho - \frac{kc^2}{a^2} + \frac{\Lambda c^2}{3}. \tag{1.4}$$

where G is the gravitational constant, ρ is the matter-energy density in the Universe, k describes the curvature of the Universe ($k > 0$ for closed, 0 for flat and < 0 for open) and Λ is the cosmological constant used to modify Einstein's equations of motion so that they describe an accelerating universe. Equation 1.4 is known as the Friedmann equation (Friedmann, 1922, 1924), and it describes the expansion of a homogenous, isotropic universe with a particular ρ, k and Λ. The fractional contributions of matter, vacuum energy, and curvature to the total energy density of the universe, Ω_{total}, when Ω_{total} is equal to the critical density can be written as

$$\Omega_{total} = \Omega_M + \Omega_\Lambda + \Omega_K = 1, \tag{1.5}$$

where the dimensionless density parameters are defined as

$$\Omega_M = \frac{8\pi G\rho_0}{3H_0^2},\ \Omega_K = -kc^2 \text{ and } \Omega_\Lambda = \frac{\Lambda c^2}{3H_0^2}. \tag{1.6}$$

We can define the following function

$$E(z) \equiv \sqrt{\Omega_M(1+z)^3 + \Omega_K(1+z)^2 + \Omega_\Lambda} \tag{1.7}$$

which is proportional to $(\dot{a}/a)$, as can be seen by substituting the definitions given in Equation 1.6 along with Equation 1.2 into Equation 1.4. The comoving distance, defined as the proper distance to an object at redshift z divided by the scale factor, is then

$$D_C = \frac{c}{H_0}\int_0^z \frac{dz'}{E(z')}, \tag{1.8}$$

where $E(z)$ gives us the dependence of D_C on redshift and cosmology. The ratio of an object's physical size to its observed angular diameter on the sky is defined as the angular diameter distance, D_A. In a flat universe, it is related to the comoving distance by

$$D_A = \frac{D_C}{1+z}. \tag{1.9}$$

Together, these give us the formula for the comoving volume element in terms of the angular diameter distance as

$$dV_C = \frac{c}{H_0}\frac{(1+z)^2 D_A^2}{E(z)} d\Omega dz. \tag{1.10}$$

The last cosmological distance I will describe is the luminosity distance, D_L. The observed bolometric flux of an object S is related to the intrinsic luminosity of the

object L via the inverse-square law:

$$= \frac{L}{4\pi D_L^2}. \tag{1.11}$$

There are two further effects that act to reduce the amount of flux measured; the energy of each photon is reduced by a factor of $1+z$ and the arrival rate of the photons is reduced by another of $1+z$, giving

$$S = \frac{L}{4\pi D_C^2 (1+z)^2}, \text{ and so } D_L = D_C(1+z). \tag{1.12}$$

If, as is most common, one is dealing with differential flux S_ν and luminosity L_ν, then the flux must be corrected for the fact that the observed wavelength range will access both a different spectral width and a different part of the spectrum of the object. This adds a factor of $1+z$ for the stretching of the bandwidth and the ratio of the luminosities of the source at both the emitted and the observed wavelengths, $L_\nu(1+z)$ and L_ν:

$$S_\nu = (1+z)\frac{L_{\nu(1+z)}}{L_\nu}\frac{L_\nu}{4\pi D_C^2(1+z)^2}. \tag{1.13}$$

When this is applied to magnitudes, this extra term forms the K-correction

$$K = -2.5\log\left[(1+z)\frac{L_{\nu(1+z)}}{L_\nu}\right], \tag{1.14}$$

so that

$$m_\nu = M_\nu + 5\log\left(\frac{D_L}{10\text{ pc}}\right) + K. \tag{1.15}$$

These equations will be used throughout this thesis, and I use standard ΛCDM cosmology with $\Omega_\Lambda = 0.7$, $\Omega_M = 0.3$ and $H_0 = 70\text{ km s}^{-1}\text{ Mpc}^{-1}$, consistent with Cira-

suolo et al. (2010); Johnston et al. (2015); Lorenzoni et al. (2013).

1.2 Overview of Galaxy Formation

In this section I discuss the theory behind the formation of galaxies, as well as giving a summary of the observations and models that have influenced this theory.

1.2.1 Galaxy Formation Theory

The current theoretical picture of galaxy evolution is one of hierarchical merging. The smallest overdensities collapse first to form dark matter haloes, which merge with other nearby haloes. This is equivalent to the collapse of the larger overdensity which contains all of these merging haloes.

Gas in the Universe, initially uniformly distributed, will follow the dark matter haloes, concentrated in on them by gravity in a similar way to the dark matter itself. How the gas actually accretes into a dark matter halo, which will set many of the properties of the potential resultant galaxy, is dependent on the size of the halo and how the gas cools. Infalling gas will undergo a virial shock (Binney, 1977), heating the gas until it is thermally supported. Lower gas masses can cool efficiently enough that they collapse on dynamical timescales, whereas higher masses are limited by their cooling timescales (Rees & Ostriker, 1977; White & Frenk, 1991). Both the gas and the dark matter haloes will have some angular momentum, arising from the tidal torques from the surrounding large scale structure (Hoyle, 1949; Peebles, 1969). This angular momentum will eventually lead the gas to form a rotating disk.

If the gas is ionised or metal rich, it can cool atomically via the collisions of ionised particles, releasing energy via recombination, excitation and decay, and Bremsstrahlung (Mo et al., 2010). However, early in the Universe when the gas is still colder and neutral, it cannot cool this way, and mostly relies on cooling via the small fraction of molecular

hydrogen (Abel et al., 1997). The gas is also being heated, both by the presence of a photoionising background in the shape of the CMB and the light from other stars and galaxies, as well as thermal output from star formation and Active Galactic Nuclei (AGN) if a galaxy has already formed.

Once the gas has cooled and collapsed onto a dark matter halo, forming a proto-galaxy, the gravitational and thermal instabilities inherent in cooling lead it to fragment, forming dense clouds (Balbus, 1986; Field, 1965; Maller & Bullock, 2004). These clouds continue to collapse, becoming the first sites of star formation. The first stars, called population III stars, form from pristine gas (e.g. Larson, 2000; Ostriker & Gnedin, 1996). This means that they can only cool inefficiently via molecular hydrogen, rather than much more efficient line emission of heavier elements. This leads them to have very high masses (potentially as high as $\sim 10^3 M_\odot$), and as such they live very short lives before dying spectacularly in supernovae expected to trigger more fragmentation of the gas and further star formation, and forming black holes (Larson, 2000).

Interactions

When dark matter haloes merge, they carry along any embedded galaxies with them. It previously appeared that no trace of the earlier haloes would survive the merging process (Katz & White, 1993; Summers & Davis, 1995), but N-body simulations have since shown that a smaller dark matter halo continues to exist as a sub-halo inside a larger halo with which it has merged (Springel et al., 2008; Tormen et al., 1998), potentially carrying a galaxy, which forms a satellite to the presumably larger galaxy at the centre of the larger halo. As these sub-haloes travel through their host halo, dynamical friction causes their orbits to decay, leading the satellite galaxies towards the larger central galaxy (Chandrasekhar, 1943). If the orbital decay happens on a fast enough timescale, the two galaxies will merge (see Binney & Tremaine, 1987).

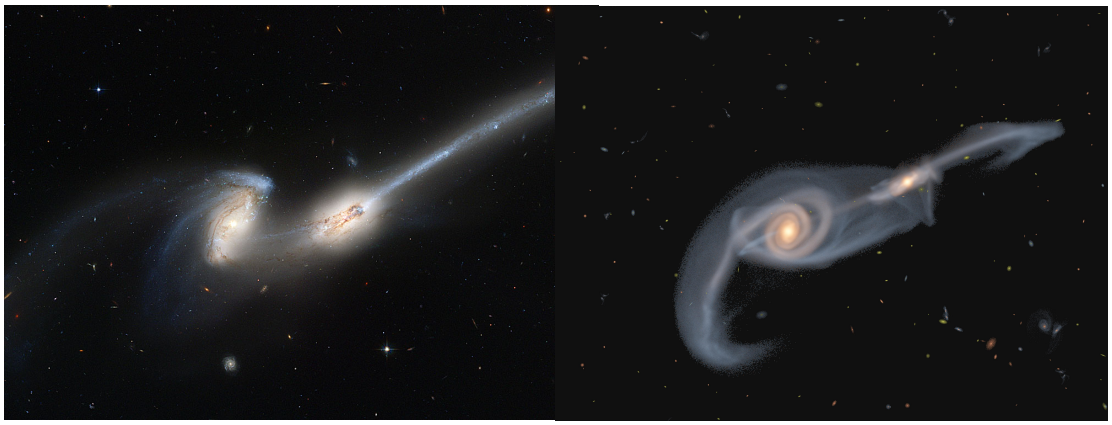

Figure 1.3: Left: The Mice Galaxies, a *Hubble Space Telescope* image showing two merging galaxies in the Coma cluster which have already collided once, leaving streams of gas and stars behind them, and will keep colliding as they merge. *Source: NASA*. Right: a simulation of a merger event similar to the Mice galaxies. Both galaxies were originally disk-like spirals before merging to form a spheroid. The simulation and image were made by John Dubinski. *Source: Canadian Institute for Theoretical Astrophysics*.

On its orbit, a satellite galaxy will interact with the environment around it. Tidal forces can strip away the outer regions of the galaxy or potentially completely disrupt it, leaving behind a stellar stream. If less strong, the tidal forces can cause a process known as harassment, whereby the stars gain energy in the form of random motion, effectively heating up the galaxy, leading to its expansion and destroying ordered structures such as disks (Mastropietro et al., 2005; Moore et al., 1996; Smith et al., 2013). Ram pressure from the IGM can lead to a galaxy being stripped of its atmosphere and losing its interstellar medium (ISM) in processes called strangulation and starvation, thought to have an important role in the conversion of blue, star-forming galaxies into red, passive galaxies in clusters (Font et al., 2008).

If a merger occurs, the outcome will depend on the properties of the progenitor galaxies as well as their mass ratios. If a small galaxy merges with one much larger than itself, it will be destroyed and absorbed into the larger galaxy in a process called a minor merger. If the large galaxy is disk-like, such as a late-type spiral galaxy, the disk

may survive, although it could be thickened. This is thought to be the main process by which large spiral galaxies grow, accreting their satellites over time. If the two galaxies have comparable masses, as in the case shown in Figure 1.3, this is known as a major merger. In this case, the galaxies will be significantly disrupted, and eventually violent relaxation (Lynden-Bell & Ostriker, 1967; where orbits undergo large scale velocity and energy changes due to time-varying fluctuations in the gravitational potential) will lead to the formation of a spheroid, with the stars following randomised orbits equivalent to a thermal gas, where the temperature is proportional to the stellar mass. This is a possible formation mechanism for elliptical, or early-type galaxies, which tend to be very large, with red stellar populations and low star formation rates. If the merger is 'wet', i.e. involving a significant gas fraction, the merger can trigger intense bursts of star formation (Somerville et al., 2001).

Star Formation and AGN feedback

The galaxy luminosity function (LF), the distribution of the number density of galaxies as a function of luminosity, does not follow the distribution of dark matter halo sizes, as one might assume it should (see Figure 1.4; Silk & Mamon, 2012). In particular, the ratio of faint galaxies to bright galaxies is very much lower than the ratio of small haloes to large haloes (see e.g. Cole et al., 2001; Reed et al., 2007; Springel et al., 2008), implying some feedback mechanism inhibiting galaxy formation in small haloes. In the largest haloes, even though cooling is inefficient, galaxies are predicted to form that are far more luminous than those observed (e.g. Benson et al., 2003). The suggested solutions to these mismatches are quenching effects from star formation in low mass galaxies and AGN in high mass galaxies (e.g. Benson, 2010; Silk & Mamon, 2012).

Star formation feedback is mostly thought to come from energy injected into the ISM by supernovae and star-formation induced winds. The physical mechanisms by

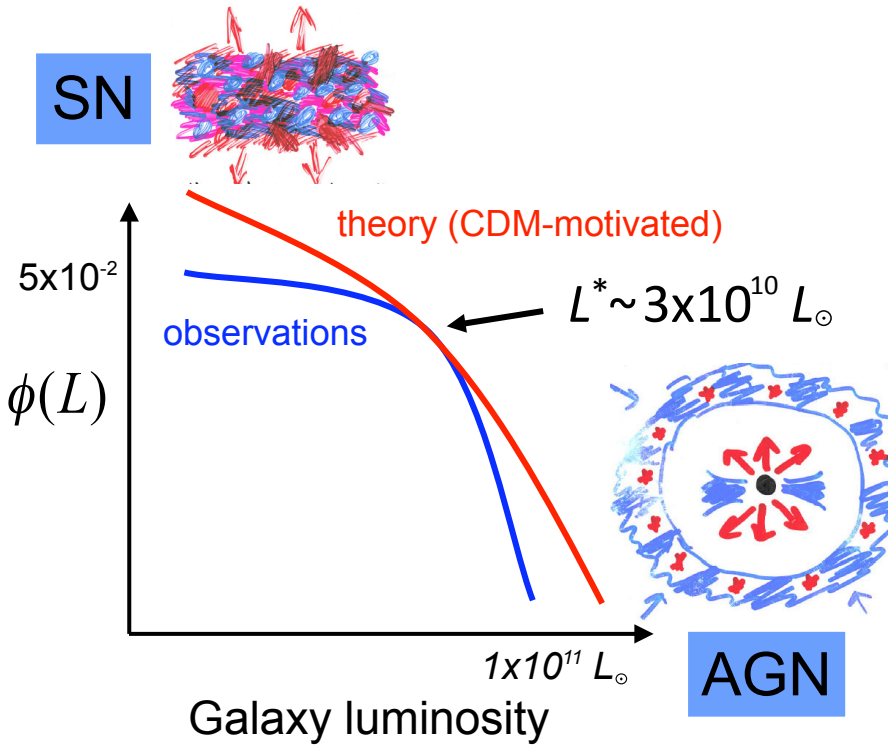

Figure 1.4: The effect of feedback on the galaxy LF. Both axes have a logarithmic scale. The red line shows the predicted LF given the underlying power law shape of the halo mass functions, while the blue line shows the observed LF which has both fewer faint and fewer bright galaxies. The $\phi(L)$ value is in units of $h^3\mathrm{Mpc}^3 d\log L$. Figure taken from Silk & Mamon (2012), with values estimated from Yang et al. (2009).

which supernova feedback operates are unclear. Consider an ISM consisting of cold, dense clouds containing most of the mass that are set within hot, diffuse gas which fills most of the volume. Outflows from supernovae and star formation will evaporate the dense clouds, and, if the temperature is hot enough, they can also eject the gas from the galaxy. This will act to both reduce the amount of gas available to form new stars and to destroy the sites of star formation. However, there will also be some increase in star formation triggered by compression from supernova winds. The small scale of this form of feedback compared to the size of a galaxy makes it ineffective on galaxies of higher mass, where supernovae fail to stop cold flows of accreting gas from streaming into the centre of the halo and continuing to form stars (e.g. Powell et al., 2011).

Larger galaxies require something more drastic to stop them from growing overluminous. This is a problem both at early times when they initially form, and later on, when the gas ejected from supernova feedback could accrete onto large haloes, forming over-massive galaxies. As all galaxies appear to have a supermassive black hole at their centre with a mass roughly in proportion to the mass of the galaxy (Magorrian et al., 1998; McLure & Dunlop, 2002), and the correlation between black hole mass and galaxy properties implies some sort of feedback or co-evolution, this is generally thought to be provided by AGN feedback from supermassive black holes. The nature of the feedback can be split into two main modes: the radio and the quasar mode, using the terminology of Croton et al. (2006). The quasar, or radiative, mode is a high accretion scenario where large amounts of gas are pushed inward to the circumnuclear disk from much larger scales by, for example, a merger, instabilities in the spiral arms, or the formation of a bar, causing the growth of the black hole and releasing amounts of energy exceeding the binding energy of the galaxy. It results in both radiative heating of the cool gas in the galaxy stopping star formation and extreme radiatively driven winds removing gas from the galaxy and heating the surrounding IGM. This

mode is expected to be dominant at high redshift when the AGN is a young quasar that is highly luminous, dying away as the fuel supply diminishes.

At later epochs, the radio, or kinetic, mode is thought to be the dominant effect. Here, the black hole is accreting at a much slower rate, producing little optical radiation but large amounts of radio output. The low accretion rate is due to the high temperature of the halo, as cold clouds may have to form via thermal instability and drift into the sphere of influence of the black hole to accrete, or the hot gas must accrete via Bondi accretion, which is slow (Bondi, 1952; Bondi & Hoyle, 1944; Mo et al., 2010). The accretion drives jets which heat bubbles of relativistic plasma next to the AGN (e.g. Churazov et al., 2000; McNamara et al., 2000). These bubbles then rise up through the IGM, causing weak shocks that will heat the surrounding gas, and stopping it from accreting onto the galaxy (this will also affect satellite galaxies). This mode of feedback is seen in radio galaxies at the centre of clusters, with most objects at low redshift (Best et al., 2014), and seems to be a sustainable maintenance mode as the energy output from the black hole varies with the amount of matter accreting onto it.

1.2.2 Observations of Galaxy Formation

The galaxy LF has been measured across a range of wavelengths and redshifts. At low and intermediate redshifts, it has been well measured in optical and infrared, which can reveal information both about the star formation rates and the stellar mass of a galaxy. At higher redshift, it has predominantly been measured in the UV, as the observatories that are able to image faint, high redshift galaxies are rarely able to access longer wavelengths than rest-frame UV. A more complete introduction to the galaxy LF can be found in Section 1.4 and so I will not go into detail here, but will briefly outline the major trends.

Galaxies have steadily increasing comoving densities from $z > 8$ to $z = 3$ as the

number counts are raised by new galaxies forming, until at $z \sim 1-3$ this evolution begins to slow as mergers take effect (Cirasuolo et al., 2010; Finkelstein et al., 2015; Loveday et al., 2012). They appear to be equally bright on average at $z = 8$ as $z = 4$ (Bouwens et al., 2015), but since $z = 4$ they have dimmed, indicating passive evolution at later times (Cirasuolo et al., 2010; Loveday et al., 2012; Marchesini et al., 2007). At $z > 4$, there are relatively more faint galaxies than at lower redshift (Bouwens et al., 2015), while at $z > 6$ there also are relatively more bright galaxies than expected, implying that the mechanisms that stop the largest galaxies from becoming very luminous, such as mass quenching (Peng et al., 2010) and AGN feedback, may not have started long before this point (Bowler et al., 2014).

The measurement of the LFs of galaxies across a wide redshift range has also allowed the determination of the star formation rate density (SFRD) from luminosity density (the integral of the LF). The SFRD can be converted from measurements in the far-UV, which access the light produced by very blue stars with short lifetimes. It has been measured via the far-UV locally (Robotham & Driver, 2011; Wyder et al., 2005), at intermediate redshifts between $1 < z < 4$ (Cucciati et al., 2012; Reddy & Steidel, 2009) and high redshift between $4 < z < 8$ (Bouwens et al., 2012; Schenker et al., 2013). However, an important and non-trivial step in measuring the SFRD from the far-UV is accounting for dust extinction. Much of the UV light emitted by star formation is absorbed by dust and reradiated at longer wavelengths, with only a small fraction escaping the galaxy as UV, particularly at $0 < z2$ (Madau & Dickinson, 2014). The attenuation due to dust can be estimated by measuring the UV spectral slopes of star-forming galaxies and converting to dust attenuation using the attenuation-reddening relations from Calzetti et al. (2000); Meurer et al. (1999). However, particularly at higher redshift, there is an observed trend that less luminous galaxies have bluer UV slopes, which would lead to a smaller inferred dust attenuation and so a luminosity dependent dust correction (Bouwens et al., 2014).

This is particularly problematic when measuring the SFRD at high redshift, as the relatively higher numbers of faint galaxies means they contain a significant amount of the SFRD, leading it to be very sensitive to the integration limits used (Madau & Dickinson, 2014). Other techniques include fitting stellar population models to the UV-optical SEDs (e.g. Cucciati et al., 2012), and energy-balanced SEDs, based on the conservation of energy between the light absorbed and the light reemitted (e.g. Da Cunha et al., 2008; Smith & Hayward, 2015). Alternatively, one can compare the far infrared (IR) and the uncorrected far UV luminosity densities, as the absorbed light should be reradiated by the dust in the far IR, allowing for the measurement of the full SFRD as well as the amount of light attenuated (Burgarella et al., 2013).

The SFRD can also be measured using IR data, as much of the UV light produced by star formation is absorbed by dust and then re-radiated in the IR. This has led to measurements of the SFRD locally (Sanders et al., 2003; Takeuchi et al., 2003) as well as out to $z > 2$ (Gruppioni et al., 2013; Magnelli et al., 2009, 2013). At this point the rest-frame IR becomes hard to access as it is redshifted to lower wavelengths which can only be seen from above the atmosphere, as well as the difficulty in building detectors with high sensitivities in this range. A combination of these results is shown in Figure 1.5 from an analysis in Madau & Dickinson (2014). It shows the SFRD rising consistently from $z = 8$ to $z = 3$ before peaking at $z \approx 2 - 1.5$ and then gradually declining to the present day.

Galaxy Colours

There is a significant bimodality in the relationship between the colour of galaxies and their magnitudes (Baldry et al., 2004; Balogh et al., 2004; Strateva et al., 2001). Red galaxies are on average brighter than blue galaxies, and the two populations appear to have different characteristics in LFs, mass functions and their evolution (e.g. Loveday et al., 2012) as well as age (Thomas et al., 2010), while the relative fraction of each

is highly dependent on environment (Baldry et al., 2006). There is also a difference in morphology; red galaxies are generally large spheroids, whereas blue galaxies tend to be disks with spiral arms, or small and irregular. The two populations have been termed the blue cloud and the red sequence (e.g. Bell et al., 2004; Schawinski et al., 2014) due to the shape of the colour-size distributions. Galaxies are thought to be in the blue cloud when they form before, at some point, star formation is mostly switched off and they move to the red sequence, continuing to grow by accreting satellite galaxies and become redder as their stellar populations age (e.g. Bell et al., 2004; Faber et al., 2007; Wyder et al., 2007).

The way in which galaxies move from the blue cloud to the red sequence, through the so-called green valley, is still uncertain. Major mergers are thought to be part of the solution, given the link to the formation of elliptical galaxies (e.g. Barro et al., 2013; Darg et al., 2010a,b). The prevalence of AGN in galaxies in the green valley initially led to the suggestion that AGN feedback was responsible for the change, driving the gas out of the galaxy and quenching star formation (e.g. Bower et al., 2006; Croton et al., 2006; Di Matteo et al., 2005; Schawinski et al., 2007). However, more recently this has become less popular. In particular, Schawinski et al. (2014) find evidence for two possible pathways from the blue cloud to the red sequence that produce red galaxies with either spiral (late-type) or spheroidal (early-type) morphology. They suggest that late-type galaxies have their gas supply cut-off, inducing a slow decline in star formation rate over Gyr timescales as the gas in the galaxy is gradually used up. The mechanisms associated with this may be the same as those which cause AGN activity, such as bars, and the decreasing star formation rate may also lead to less stellar feedback which increases accretion onto the black hole. In this scenario, AGN are either a co-evolution or a consequence of the decline in star formation, not the cause. For late-type galaxies, the star formation rates are seen to decline over much faster timescales ($\sim 200 - 300$ Myr) consistent with a merger,

which may also trigger AGN feedback which, along with the merger, drive the gas out of the galaxy and shut off star formation swiftly. A similar, if more gradated, picture is also found by Smethurst et al. (2015), who find that most transitions appear to be a combination of mergers removing the gas in the galaxy and the gas supply of the galaxy being shut off, producing red galaxies with more or less remaining structure depending on which pathway played a larger role.

One of the most interesting developments over the last 15-20 years has been the growing evidence for the effect known as downsizing (Cowie et al., 1996). Unlike what might be assumed from hierarchical structure formation where the smallest dark matter haloes form first, the evidence is mounting that more massive galaxies assembled the bulk of their stellar mass very early, before smaller galaxies. Measurements of the stellar mass of galaxies out to $z \approx 4$ have shown that the largest galaxies assemble the bulk of their stars very quickly and early, while lower mass galaxies assemble their stars increasingly slowly and at later times (Pérez-González et al., 2008; Thomas et al., 2010). The right-hand plot of Figure 1.5 illustrates this by showing when late-type galaxies of different masses formed their stars, with the largest galaxies forming stars quickest and at highest redshift. This has been observed with the metallicity ratio [α/Fe], which provides an estimated star formation timescale by comparing metallicities produced in short-scale core collapse supernovae with long-scale Type Ia supernovae.

1.2.3 Modelling Galaxy Formation

The lack of an observer's ability to frame an experiment has led to astronomers developing other methods by which to test the theories behind galaxy formation, namely, simulations. The nonlinear nature of the processes governing galaxy evolution make it impossible to follow with analytical methods, and so any models must find a way to manage this. The two main techniques are to either directly solve the equations

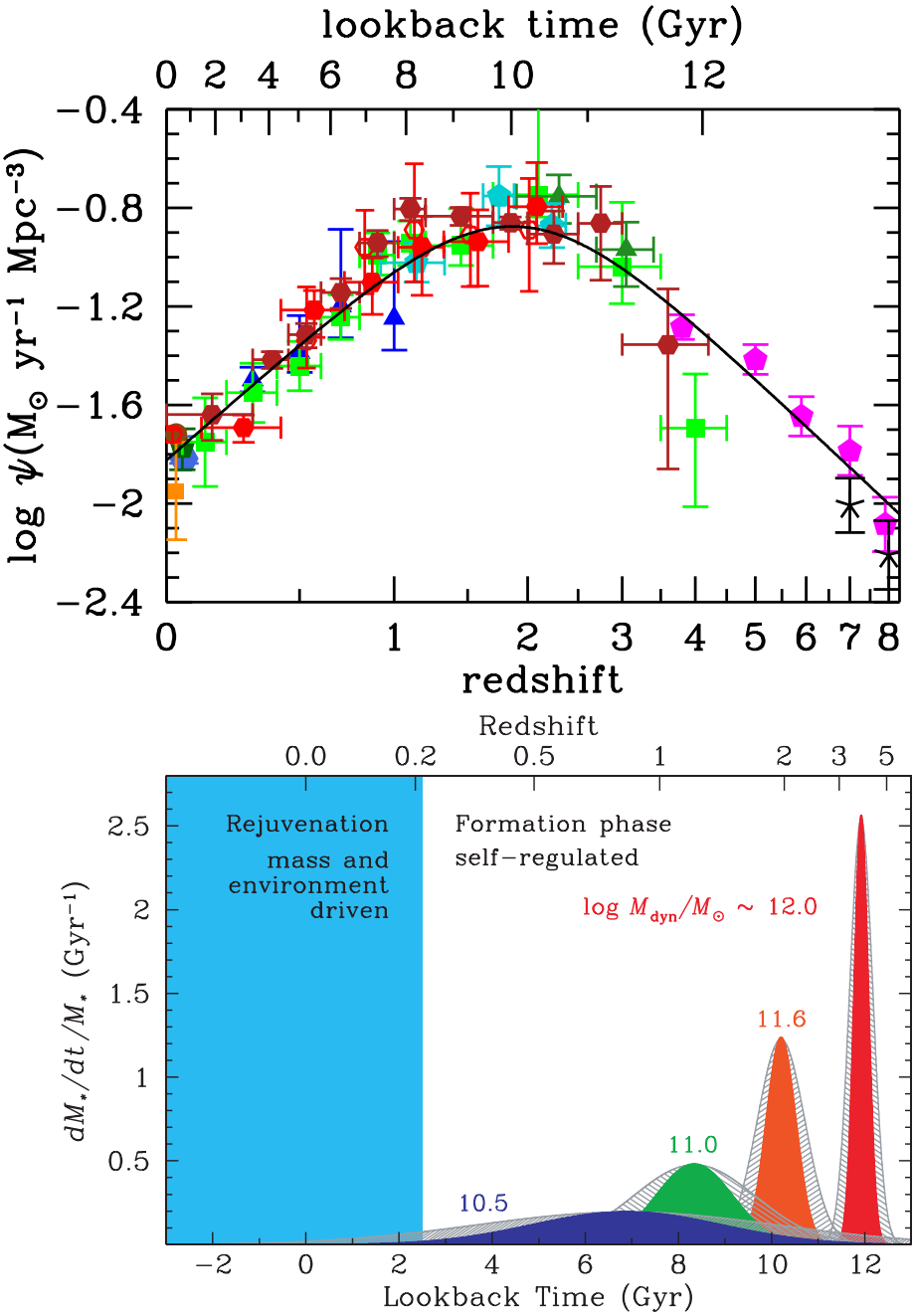

Figure 1.5: Top: the history of cosmic star formation from $z = 8$ to $z = 0$ as measured in the Far-UV (green, blue and pink points) and IR (red and orange points), taken from Madau & Dickinson (2014). Bottom: Specific star formation rate as a function of look-back time for early-type galaxies of various masses as indicated by the labels. High mass galaxies form their stars in an extreme, fast burst at high redshift (the red peak), intermediate mass galaxies form their stars over a slightly longer timescale and at lower redshift (the orange and green peaks) and lower mass galaxies form their stars over the longest timescales, peaking at the lowest redshift (the blue peak). Figure taken from Thomas et al. (2010).

of gravity, hydrodynamics and radiative transfer in large, N-body hydrodynamical simulations, or to attempt to approximate many of the processes that cannot be explicitly modelled and solve a simplified set of equations in semi-analytic models (SAMs).

Hydrodynamical and N-body simulations

Hydrodynamical simulations attempt to directly solve the equations that govern galaxy evolution. They are either cell-based, such as adaptive mesh refinement (AMR; Kravtsov et al., 1997; Teyssier, 2002), which uses the formation of smaller and smaller cells based on a condition such as density to produce both a large simulation size and high resolution in the places where it is required, or particle-based, such as Smooth Particle Hydrodynamics (SPH; Gingold & Monaghan, 1977; Springel, 2010), where gas and dark matter are treated as particles, but properties such as temperature or metal content are smoothed over multiple particles. Initially, much progress was driven by SPH, which allowed a much better resolution over the wide range of scales needed than initial cell-based methods, but was seen to struggle to produce sharp phenomena such as shocks (Scannapieco et al., 2012), which led to increased focus on cell-based methods, where AMR offers a way for cell-based simulations to manage the range of scales necessary.

Hydrodynamical simulations include direct modelling of gravity, by modelling the gravitational force on each matter particle from every other matter particle according to Newtonian gravity, as the correction compared to General Relativity is small. This is set within a comoving box expanding according to the Friedmann equation (Equation 1.4; Friedmann, 1922, 1924), obtained from General Relativity. As the mass is dominated by dark matter, which only feels gravity, dark matter only N-body simulations have produced excellent insight into the merger histories and substructures of dark matter haloes which can be fed into SAMs (e.g. Reed et al., 2009; Springel

et al., 2008).

Gas physics is normally modelled using the Euler equations, which are a form of the Navier-Stokes equations assuming no viscosity or conduction, for mass, momentum and energy conservation (see e.g. Batchelor, 2000; Landau & Lifshitz, 1987). This can either be done via the Lagrangian method, where the particles carry information about the fluid, or the Eulerian method, where the fluid is split into discrete cells and properties are computed across the cell boundaries. SPH is a Lagrangian method, which tend to be better at producing dynamic range, while AMR is an Eulerian method, which is better at handling boundary-based situations such as shocks and surface instabilities (Somerville & Davé, 2015), however AMR can offer the ability to resolve extremely large dynamic range if necessary, such as to study mergers in zoom simulations (e.g. Kim et al., 2009).

Radiative processes also have a huge effect on the behaviour of galaxies, and as such radiative cooling and photo-ionization heating are commonly included, as well as cooling by metal line emission, and radiation transport, which is necessary for the study of reionisation. The cooling effect of metals also means that tracking the chemical evolution of a galaxy is important. This can by done by tracking the Type II supernovae to reproduce oxygen abundance, asymptotic giant branch stars to follow carbon production and Type Ia supernovae to trace iron production.

Computational constraints make it unfeasible to resolve both the scales on which haloes form as well as on which star formation occurs and so hydrodynamical simulations must include sub-grid physics to describe this. Star formation is normally implemented following Katz (1992), where star-cluster particles form at a rate based on the gas density and tuned to the observed Kennicutt relation between gas density and star formation rate (Kennicutt, 1998) once the gas has reached some critical density (e.g. Springel & Hernquist, 2003). Black holes are seeded in haloes above some critical mass, and then accrete following Bondi accretion (Bondi, 1952). The

number of core collapse supernovae are predicted using an initial mass function, and then the energy output is deposited into the gas both thermally and kinetically. AGN feedback is similarly added in, with output energy from the AGN coupling thermally and kinetically to the gas in a method dependent on the accretion rate of the AGN, i.e., whether it is in the 'quasar' or 'radio' mode (Croton et al., 2006).

Hydrodynamical simulations are useful as they offer the opportunity to study things which are observationally inaccessible, such as the density and velocity (or temperature) of dark matter, gas and stars as well as the metallicity of the gas over cosmic time. This provides the full formation history of the simulated galaxies, gives us information on their structure and kinematics and their relative distributions with any number of characteristics such as mass, luminosity, or position. Crucially, they also allow us to study the imperfections in observational techniques by comparing measurements of the properties of the simulation made using observational methods with the true value, helping to improve the future analysis of observations.

These simulations are limited, however, by computational ability, producing resolution-based effects that can be difficult to tell from physics-based effects (such as whether a halo would show any trace of its progenitors, Katz & White, 1993; Tormen et al., 1998), and necessitating the use of sub-grid physics to describe phenomena below the resolution of the simulation. These sub-grid recipes can be hard to test sensibly due to the amount of time a simulation takes to run, leading to somewhat arbitrary choices, although SAMs can help by testing a range of sub-grid physics much faster.

Semi-Analytical Models

As it is not currently possible to resolve both the sub-parsec scales necessary to model star formation or black hole accretion disks as well as the super-megaparsec scales on which the largest haloes form, SAMs provide a necessary middle-ground

that allows astronomers to make predictions over very large volumes and numbers of galaxies using a combination of N-body techniques with added in approximations to describe sub-grid physics. Because they are so much faster to run, they also allow for comprehensive testing of sub-grid recipes, whereas hydrodynamical simulations have a much more limited ability to do this.

The effects of gravity can be included via the merger trees and halo structures taken from N-body simulations. Halo finders are used to identify dark matter haloes and sub-haloes (see Knebe et al., 2011), which are then traced through the simulation, producing a record of their masses and the times at which they merge, represented by a merger tree. Merger trees can also be produced semi-analytically using Press-Schechter theory (Press & Schechter, 1974), extended and modified to better match numerical merger trees (Bower, 1991; Lacey & Cole, 1993). This produces a population of dark matter haloes, each with a mass assembly history.

Once the mass assembly history of a halo is known, the evolution of the galaxies within can be modelled. Galaxies are formed following analytical descriptions of how gas cools and condenses inside haloes (White & Frenk, 1991). Stars are formed in a very similar way to hydrodynamical simulations, based on the gas density as determined by the cooling model and the size of the disk, which is estimated using the initial angular momentum. Black holes are formed and evolved either following results from hydrodynamical simulations, or by, for instance, growing black holes after mergers.

When haloes merge, the fate of the sub-halo and its satellite galaxy are modelled by estimating the timescale of the decay of the orbit due to dynamical friction (Chandrasekhar, 1943), sometimes with corrections from N-body simulations (e.g. Boylan-Kolchin et al., 2008; Jiang et al., 2008b). If the sub-haloes are not destroyed en route, they are assumed to merge with the central galaxy, at which point a set of recipes will cause effects like bursts of enhanced star formation and morphological change

such as the formation of spheroids from disks.

SAMs require a much reduced computational cost compared to hydrodynamical simulations. This allows for the simulation of large populations of galaxies over a wide mass range for comparison with observations. They are not affected by some of the numerical issues that can cause difficulties in hydrodynamic simulations (such as discreteness effects, Romeo et al., 2008). They also offer an ideal way to test different recipes to describe sub-grid physics, and recent work has used a Bayesian inference approach to better explore values of model parameters or different families of models (e.g. Henriques et al., 2009; Lu et al., 2011).

The fact that much of the physics input into SAMs is chosen by simulator rather than measured is a significant limitation. While there has been good agreement with some observations (e.g. Guo et al., 2011), this agreement is often forced at the detriment of other observations, such as the stellar mass function both at low and high redshift (Fontanot et al., 2009). An obvious problem with the input sub-grid physics (in both SAMs and hydrodynamical simulations) is highlighted by downsizing, which is the opposite of what would be expected if galaxy and star formation simply follow the hierarchical formation of dark matter haloes; this has led to the modification of the recipes for star formation and the feedback from supernovae by, for example, modifying outflow efficiencies and accretion timescales (Henriques et al., 2013; White et al., 2014).

1.3 Galaxies at High Redshift

When the first galaxies form, the gas around them is cold and still neutral following recombination. UV photons emitted by the first stars are absorbed by the neutral hydrogen, forming a small bubble of ionised gas around each galaxy. As more galaxies form, the bubbles grow and merge until eventually, almost all of the hydrogen is hot

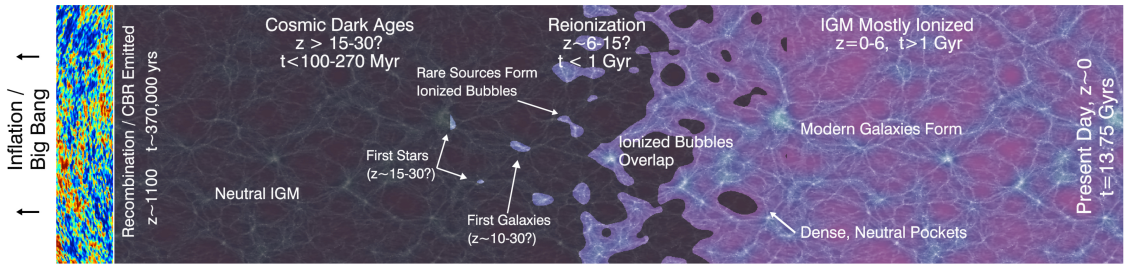

Figure 1.6: Schematic of the transition from neutral to ionised IGM. On the left, after recombination, dark matter haloes collapse until the first stars and galaxies form. These ionise small bubbles of the IGM, which slowly overlap until the IGM is predominantly ionised on the right. Figure taken from Robertson et al. (2010).

and ionised. This process is called reionisation and constitutes the last phase change of the Universe. When and how it occurred are still largely unknown, with spectra of high-redshift quasars showing evidence for complete reionisation by $z \sim 6$ (Fan et al., 2006; see Figure 1.8), while the measurements of the CMB give a redshift of 8.8 ± 0.9 as the point when half of the universe is reionised (Planck Collaboration, 2016). Quite how the ionised bubbles percolated throughout the Universe, and the properties of the galaxies that ionised the hydrogen are topics of current research. Figure 1.6 shows a schematic demonstrating how it is thought to have happened, with galaxies initially forming at $z \sim 15 - 30$ and causing a gradual reionisation starting from $z \sim 20$ and ending at $z \sim 6$ (Robertson et al., 2010), although this does require the presence of star-forming galaxies at $z > 10$ (Robertson et al., 2015).

Following the installation of Wide Field Camera 3 (WFC 3) on the *Hubble Space Telescope* (*HST*) in 2009, samples of large numbers of galaxies at $z > 6$ have allowed us to study the Epoch of Reionisation. The LFs of these galaxies have been seen to have extremely steep shapes at the faint end (e.g. Schenker et al., 2013), showing a population of mostly faint star-forming galaxies that appear to produce a high enough density of UV photons to reionise the Universe, if only just (Robertson et al., 2013, 2015). The detections of several extremely bright galaxies at $z > 10$ (Bouwens et al.,

2015; Coe et al., 2013; Infante et al., 2015; Oesch et al., 2016) also suggest that the required presence of star-forming galaxies at $z > 10$ is reasonably likely.

More than a thousand galaxies have been detected at $z > 6$, with possible detections up to $z \gtrsim 10$ (Bouwens et al., 2015; Oesch et al., 2016). The galaxies in this redshift range have been found to be small and compact, with half-light radii of $r_{1/2} < 0.5$ kpc (Oesch et al., 2010; Ono et al., 2013), and the faintest galaxies potentially having only $r_{1/2} \sim 100 - 200$ pc (Bouwens et al., 2016). There is some evidence of size evolution with redshift (Bouwens et al., 2004a; Oesch et al., 2010; Ono et al., 2013), this cannot ruled out as merely an observational effect (Curtis-Lake et al., 2016). The morphology of the brightest galaxies is very clumpy, potentially showing evidence of merging systems (Ouchi et al., 2013) although it is possible these may be star-forming clumps with an underlying substructure that is not visible in the UV (see Bowler et al., 2016). There is not noticeable morphology evolution and galaxies appear approximately as disturbed at $z \sim 8$ as they are at $z \sim 4$ (Curtis-Lake et al., 2016).

High redshift galaxies are extremely blue. The steepness of the UV-continuum slope can be quantified by assuming a power law slope, where $F_\lambda \propto \lambda^\beta$, and measuring the exponent, β, via the photometry. On average, galaxies at $z \sim 6$ have UV slopes with $\beta \lesssim -2$, as would be expected from star forming galaxies with a lower dust content than is seen at later times. β has been seen to steepen both with redshift, suggesting a trend of decreasing dust fraction at earlier times, and at low luminosity, suggesting that the smaller galaxies have less dust than larger galaxies at the same redshift (Bouwens et al., 2014; Willott et al., 2013).

The process of reionisation can also be probed by studying Lyman-α emission at high redshift. Lyman-α emission from very high redshift galaxies is expected to be damped by the neutral IGM. Studying the fraction of galaxies with Lyman-α emission, Lyman-α emitters (LAEs), allows us to study the formation of ionised bubbles, as

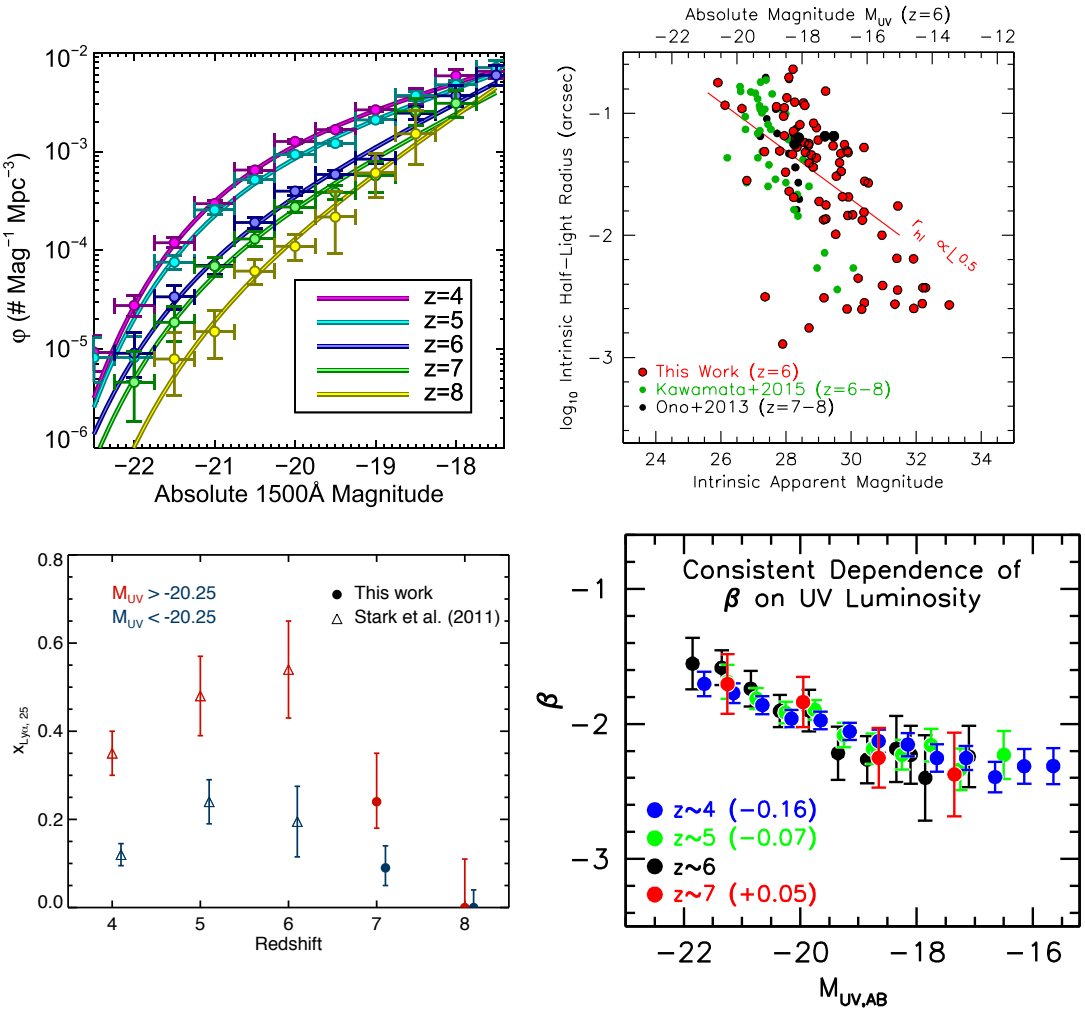

Figure 1.7: A summary of the characteristics of high redshift galaxies. Top left: the evolution of the UV LF from $z \sim 4$ to $z \sim 8$, taken from Finkelstein et al. (2015). Top right: the size-magnitude relation of galaxies at $z \sim 6$, taken from Bouwens et al. (2016). Bottom left: evolving fraction of LAEs, taken from Schenker et al. (2014). Bottom right: the β-magnitude relationship, also showing the steepening of β with redshift, taken from Bouwens et al. (2014).

Lyman-α will only be visible from a galaxy if it is within a bubble large enough for redshift to have an appreciable affect on the wavelength of the line emission across the width of the bubble. After initially increasing from $z \sim 3-6$ due to the changing amount of dust in galaxies, the fraction of LAEs decreases at $z > 6$ as the IGM becomes increasingly neutral (Caruana et al., 2014; Pentericci et al., 2014; Schenker et al., 2012; Schmidt et al., 2016). The clustering of LAE can reveal the presence of large or overlapping bubbles (Castellano et al., 2016), and faint galaxies have been seen to have a higher fraction of LAEs, supporting the idea that reionisation is caused by faint galaxies rather than bright ones (Oyarzún et al., 2016; Stark et al., 2010, 2011).

1.3.1 Selection of high-redshift galaxies

The faint apparent magnitudes of high redshift galaxies make it very hard to obtain reliable spectroscopic redshifts, and the low surface densities of high redshift galaxies make them extremely impractical to find with a spectroscopic survey, as the very low number counts of high redshift galaxies compared to low redshift sources seriously lowers the chances of finding them in a particular sample. Narrow band searches for high redshift LAEs do not sample very much redshift space at any one time, making them reasonably inefficient ways of building up samples (e.g. Cowie & Hu, 1998).

More powerful techniques to find large samples of potential high redshift objects rely on photometric selection. In some ways, it is easier to select high redshift galaxies using only photometry than low redshift galaxies; they are characterised by a sharp spectral feature that lends itself very well to both photometric redshift fitting and colour selection and can provide a reasonably precise redshift. The situation is also simpler at higher redshift, with galaxies having had less time to evolve and change, producing a slightly more uniform population. The two main methods are photometric redshift fitting, and the Lyman break technique.

Lyman Break Technique

The Lyman break technique is a powerful selection method based on the ability to isolate high redshift galaxies in colour-space due to their sharp spectral features (e.g. Steidel et al., 1996). Neutral hydrogen around stars absorbs UV light short-wards of the Lyman-limit at 912 Å, truncating the SED (or spectral energy distribution) at wavelengths shorter than this and producing a sharp spectral break. For a galaxy at high redshift, as the light travels through the intergalactic medium, intervening clouds of neutral hydrogen will each leave a Lyman-α absorption feature at the rest-frame wavelength of the cloud, creating what is known as the Lyman-α forest blue-wards of the galaxy's rest-frame Lyman-α at 1216 Å. For galaxies with $z > 4$ the cumulative effect of these lines extends the spectral break to the wavelength of rest-frame Lyman-α, forming the Lyman break. A demonstration of this can be seen in Figure 1.8, which shows the spectra of a sample of high redshift quasars. With increasing redshift, the emission left of Lyman-α (8147 Å at $z = 5.71$ and 9022 Å at $z = 6.42$) is damped as the Lyman-α forest turns into a Gunn-Peterson trough (Gunn & Peterson, 1965). Lyman-α is a resonant transition line; therefore, it takes very little neutral hydrogen in the line of sight to produce a large damping effect. The presence of emission blue-wards of Lyman-α in quasar spectra at $z < 6$ tell us that the concentration of neutral hydrogen is so low that the Universe must be completely reionised by $z \sim 6$ (Fan et al., 2006).

The Lyman break will produce an extremely red colour in two filters either side of the break, which can be photometrically selected for. If only one colour is used, the Lyman break can be hard to distinguish from the Balmer break at 4000 Å, leading to contamination by lower redshift galaxies. For this reason, a second colour cut is used to select on the intrinsic properties of the high redshift galaxies themselves. Lyman break galaxies are star-forming, blue galaxies, and so will have very blue colours in bands above the break to reflect this, separating them from the lower redshift, in-

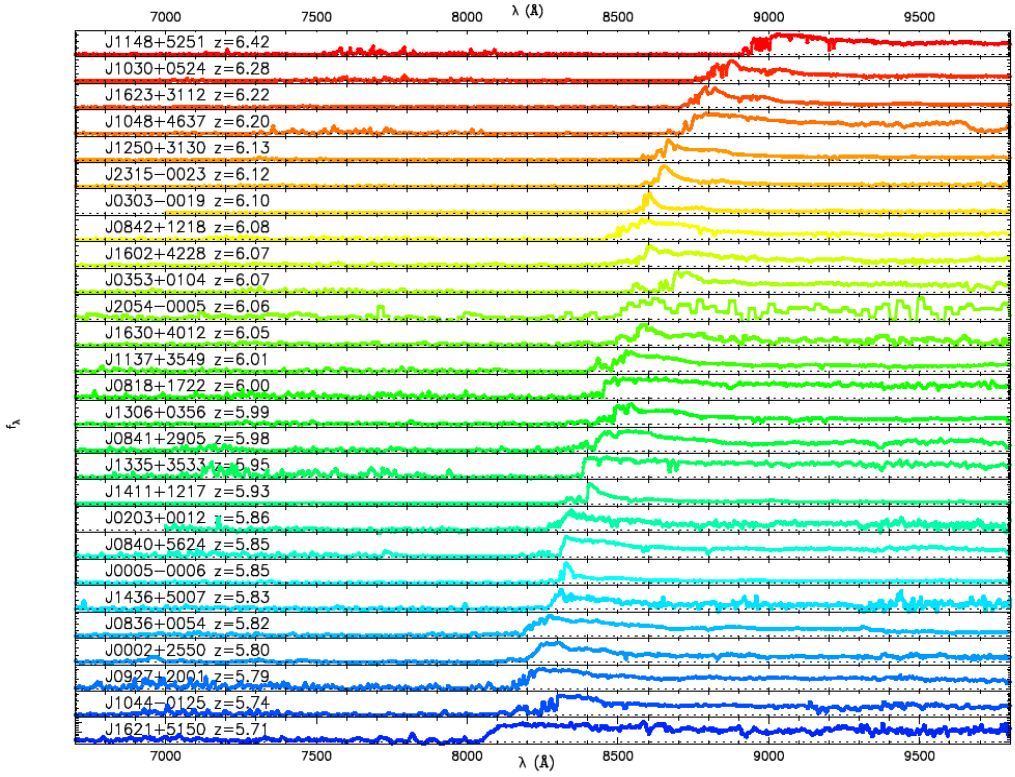

Figure 1.8: Spectra of 27 high redshift quasars plotted against observed wavelength, adapted from Fan et al. (2006) and Jiang et al. (2008a, 2009). The flux blue-wards of Lyman-α is increasingly suppressed at high redshift, showing the development of a Gunn-Peterson trough.

trinsically red galaxies. Finally, because of the extreme spectral damping particularly above rest-frame 912 Å, non-detection limits can be used to further weed out contaminants. Dwarf stars also have a sharply reddening spectral shape in contaminating wavelength ranges, but they can be removed by ignoring any unresolved sources as well as with the extra colour cut, and imaging in further infrared bands (Stanway et al., 2008; Wilkins et al., 2014). This can be seen in Figure 1.9, where the region in colour space inhabited by Lyman break galaxies is shown. By selecting specific filters above and below the Lyman break, a narrow redshift range can be isolated and galaxies within this range can be efficiently selected.

The Lyman break technique has its advantages; it is a simple, reproducible method that can powerfully select high redshift candidates down to faint magnitudes without requiring too much data. Three photometric bands (one blue-wards of the break and two red-wards) are needed to isolate the right area in colour space, as well as a further lower wavelength band to ensure non-detection at wavelengths blue-wards of the rest-frame Lyman limit. Additional observations at longer wavelengths are required to cleanly remove stars and other contaminants, but it is relatively straightforward to model the selection function, contamination and completeness of a particular survey, allowing the observer to derive intrinsic properties of a galaxy population despite the uncertainty on the redshift of any individual object.

It also has it downsides, however; as it only selects a particular type of galaxy, which one cannot safely assume is the only type of high redshift galaxy, it produces an incomplete sample. It does not give individual redshift information, only confirmation that an object is probably within a redshift range. It also provides no information about how reliable any one candidate is, only group contamination rates. The fact that it uses a blue intrinsic colour as a selection criterion biases any samples to bluer galaxies, which can give misleading measurements of the UV slope (Dunlop et al., 2012; McLure et al., 2011). Finally, as we move further into the era of surveys with

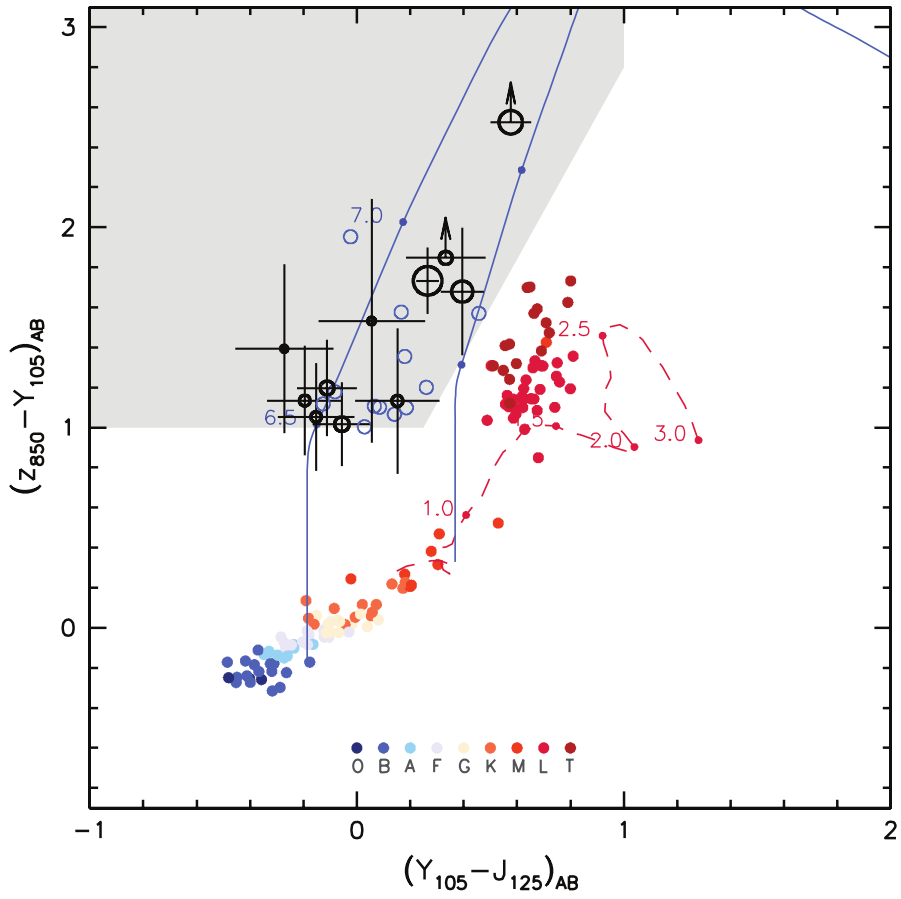

Figure 1.9: Colour-colour plot showing the selection of $z \approx 7$ candidates in the HUDF. The y-axis shows the colour across the break, in which only red colours must be selected, and the x-axis shows the colour red-wards of the break, in which only blue colours must be selected, leaving the grey area as the region with possible high redshift galaxies. The predicted redshift tracks taken by high redshift galaxies are shown by the blue lines. The plot also shows the colours of Galactic stars (coloured filled circles; a key to stellar type is at the bottom of the plot) and a passively evolving instantaneous burst of star formation that occurred at z = 10 (red dashed line). The high redshift candidates are shown by black circles, with candidates that failed the optical non-detection criterion in small blue circles. Figure taken from Wilkins et al. (2011a).

high numbers of photometric bands, the fact that this technique does not use all of the available wavelength data will make it less attractive.

Photometric redshift selection

As the number of surveys with deep multi-wavelength information builds, photometric redshift selection has become an increasingly robust and popular technique. With good optical data and spectroscopic training sets it is possible to get reliable redshift information for large numbers of galaxies at once (e.g McLure et al., 2009, 2011). The current most common method relies on fitting photometry to modelled SEDs of different galaxy types, with different amounts of reddening and absolute luminosities over a range of redshifts (see e.g. Arnouts et al., 2007; McLure et al., 2011). The sharpness of the Lyman break, which produces the extreme colours necessary for the Lyman break technique, also provides a very strong requirement when it comes to fitting photometry (McLure et al., 2013). In principle, photometric redshift fitting to templates works on a similar basis to the Lyman break technique, but it offers a far more tailorable approach which can take into account many different galaxy types, is not limited to a particular redshift range and makes the best use of all of the available data (e.g. Dunlop et al., 2012; Finkelstein et al., 2010; McLure et al., 2009, 2010, 2013). Other methods than template fitting are becoming more common; improvements in computational techniques have lead to the use of machine learning with, for instance, neural networks and genetic algorithms (Firth et al., 2003; Hogan et al., 2015).

It has, however, both advantages and drawbacks; on the plus side, one automatically has information derived from the best-fit SED such as galaxy type, stellar mass, age, and star formation history. However, this is all based on the models used in the first place and so must be interpreted very carefully. Photometric redshift samples have very good agreement with their spectroscopic training sets, but these are obser-

vationally biased to bright galaxies at low redshift and there is no way of knowing if the agreement covers all of the redshifts measured. Still, the statistical nature of the technique makes it possible to deal with the uncertainties in redshift, either by only looking at the most robust fits or by using the fitting information at different redshift ranges.

At very high redshift, it is difficult to access the bulk of the optical and infrared parts of the SED, making the redshifts more uncertain and the derived properties (especially those which come from unconstrained parts of the SED) more of an extrapolation, but this lack of information can be dealt with in a statistically rigorous way (e.g. McLure et al., 2009, 2011); furthermore, data sets with a variety of photometric information can be handled in a consistent manner, with detections in some bands but not others causing no issues (e.g. McLure et al., 2009).

It is very challenging to obtain samples of spectroscopically confirmed high redshift galaxies to use as training sets, but recent progress has been made in building up samples of galaxies with spectroscopic redshifts with several hundred confirmations at $z > 4$ (e.g. Curtis-Lake et al., 2013; Schenker et al., 2012; Stark et al., 2009, 2010, 2011).

At lower redshift, the Lyman break technique starts to become limited by what filters are available. At $z \sim 3$, galaxies can be selected by looking at the optical u-B colour, but at $z \sim 1$, photometry in the far and near UV is necessary (Burgarella et al., 2006), which is more difficult to obtain than optical imaging. For this reason, photometric redshift fitting is far more popular at lower redshift, where it is much more common to have good photometric data on sources, as well as huge spectroscopic redshift samples by surveys such as the Sloan Digital Sky Survey (SDSS), the Galaxy And Mass Assembly (GAMA) survey and the Vimos-VLT Deep Survey (VVDS) providing very good spectroscopic training sets. The continual accumulation of spectroscopic samples both at high and low redshift means that photometric red-

shifts are improving, as well as advancing computational techniques such as machine learning (e.g. Almosallam et al., 2016; Ball et al., 2008; Firth et al., 2003; Hogan et al., 2015) leading to very promising results.

1.4 Galaxy Luminosity Functions

The galaxy luminosity function (LF) offers one of the most basic tools to study galaxy evolution over cosmic time. It characterises the relative distribution of galaxies at different luminosities or magnitudes by counting the number of galaxies in a volume per unit luminosity, such that

$$dN = \phi(L)dLdV. \tag{1.16}$$

The volume here is comoving, such that an unchanging sample of galaxies at different redshifts will have the same volume density. This makes the LF a way of directly comparing galaxies at different redshift, with changes produced by differences in the populations themselves rather than cosmic expansion, allowing us to concentrate on the effects of evolutionary stage, galaxy type and environment.

The galaxy LF is one of the more direct population characteristics that can be measured, more so than, for example, mass functions or star formation histories which rely on fitted model galaxy SEDs. It furnishes us with a reliable metric with which to evaluate different populations of galaxies, different stages in the history of the Universe and different theories of galaxy evolution. The way it is shaped by the underlying distribution of dark matter haloes and the processes that cause it to differ from this, such as feedback from star formation and AGN, makes it an ideal testbed to learn about these different evolutionary pressures.

1.4.1 Measuring the LF

The galaxy LF is normally parameterised using a Schechter function, which has historically been very successful in describing the galaxy LF. This was first proposed by Schechter (1976) following Press-Schechter theory for describing the mass function of galaxies (Press & Schechter, 1974). It is a three-parameter combination of a power law with an exponential cut-off:

$$\phi(L)dL = \phi^* \left(\frac{L}{L^*}\right)^{\alpha} \exp\left(\frac{-L}{L^*}\right) \frac{dL}{L^*}. \tag{1.17}$$

L^* is the characteristic luminosity of the sample, and describes the 'knee' of the function as it changes most rapidly from a power law (fainter than L^*) to an exponential cut-off (brighter than L^*). ϕ^* is a normalisation factor describing the volume density of galaxies, normally quoted in either $\mathrm{Mpc}^{-3}/\Delta\mathrm{L}$ or $\mathrm{h}^3\mathrm{Mpc}^{-3}/\Delta\mathrm{L}$, and α defines the slope of the power law at the faint end of the LF. The Schechter function diverges for $\alpha = -2$ but can be integrated to give the total luminosity density, which can be expressed in the form of the incomplete gamma function:

$$J_L = \int_{L_{lim}}^{\infty} L\phi(L)dL = \phi^* L^* \Gamma(\alpha + 2, L/L^*). \tag{1.18}$$

It is also common to convert from luminosity to magnitudes via

$$\phi(M)dM = \phi(L)d(-L)M - M^* = -2.5 \log\left(\frac{L}{L^*}\right) \tag{1.19}$$

to give

$$\phi(M) = 0.4 \ln(10) \phi_1^* 10^{-0.4(M-M_1^*)(\alpha+1)} \exp\left(-10^{-0.4(M-M_1^*)}\right), \tag{1.20}$$

where the double exponential leads to an extremely sharp cut-off at bright magni-

tudes. While a Schechter function (shown in the top left panel of Figure 1.7) is the most popular functional form assumed, there are other variations such as a double power law, which is frequently used to fit populations of quasars and can be used to fit high redshift galaxies (e.g. Bowler et al., 2015).

The LF can be estimated both parametrically and non-parametrically, and both methods have their advantages and disadvantages. Sandage et al. (1979) developed a very popular approach to estimating the LF parametrically based on Maximum Likelihood Estimation. This is very useful in situations where one is reasonably sure of a parameterisation, and in many cases where the use of a parameterisation like the Schechter function naturally lends itself to analytically calculating properties such as the overall luminosity or number density, or tracking the changes in parameters with for instance, redshift, environment or galaxy type to quantify how populations of galaxies differ.

Non-parametric estimations, such as the $1/V_{max}$ estimator, offer a way of measuring the LF without assuming an underlying functional form. This allows a direct measurement that does not restrict the shape of the LF, but can be more subject to observational bias which must be taken into account.

1.4.2 Evolution

Measuring the evolution of the LF allows us to see changes in the statistical properties of galaxy populations in a way that we cannot measure for a single galaxy. This can be done most simply by measuring a LF separately in different redshift slices, as is shown in the top left plot of Figure 1.7 where the UV LFs of galaxies at high redshift are compared to one another and the change in Schechter parameters studied. A second method involves fitting a parameterised form of evolution to the Schechter parameters themselves. In this method, parameterisations can be split into pure luminosity evolution and pure density evolution, or combined to give luminosity

dependent density evolution.

Pure luminosity parameterisation assumes that the evolution is dominated by galaxies that have undergone secular evolution with no mergers, leading them to brighten and fade but not change in number density. This normally takes the form of

$$L^*(z) = L^*_{(z=0)}(1+z)^k \tag{1.21}$$

in terms of luminosity, or

$$M^*(z) = M^*_{(z=0)} + 2.5k \log_{10}(1+z) \tag{1.22}$$

in magnitude. The speed and direction of the evolution since $z = 0$ is governed by the luminosity evolution parameter, k.

Pure density evolution, on the other hand, assumes that galaxies have evolved in numbers, either via the formation of new galaxies at higher redshift, which would increase the number density, or more recently by merging, which acts to decrease the number density. This parameterisation normally takes the form

$$\phi^*(z) = \phi^*_{(z=0)}(1+z)^k \tag{1.23}$$

where k this time is the density evolution parameter.

Although frequently fit globally, both luminosity and density evolution will be highly dependent on galaxy characteristics such as type, mass and environment. For this reason, it can be very useful to split LFs by different characteristics and measure the different evolutions, such as separately examining the evolution of red early-type

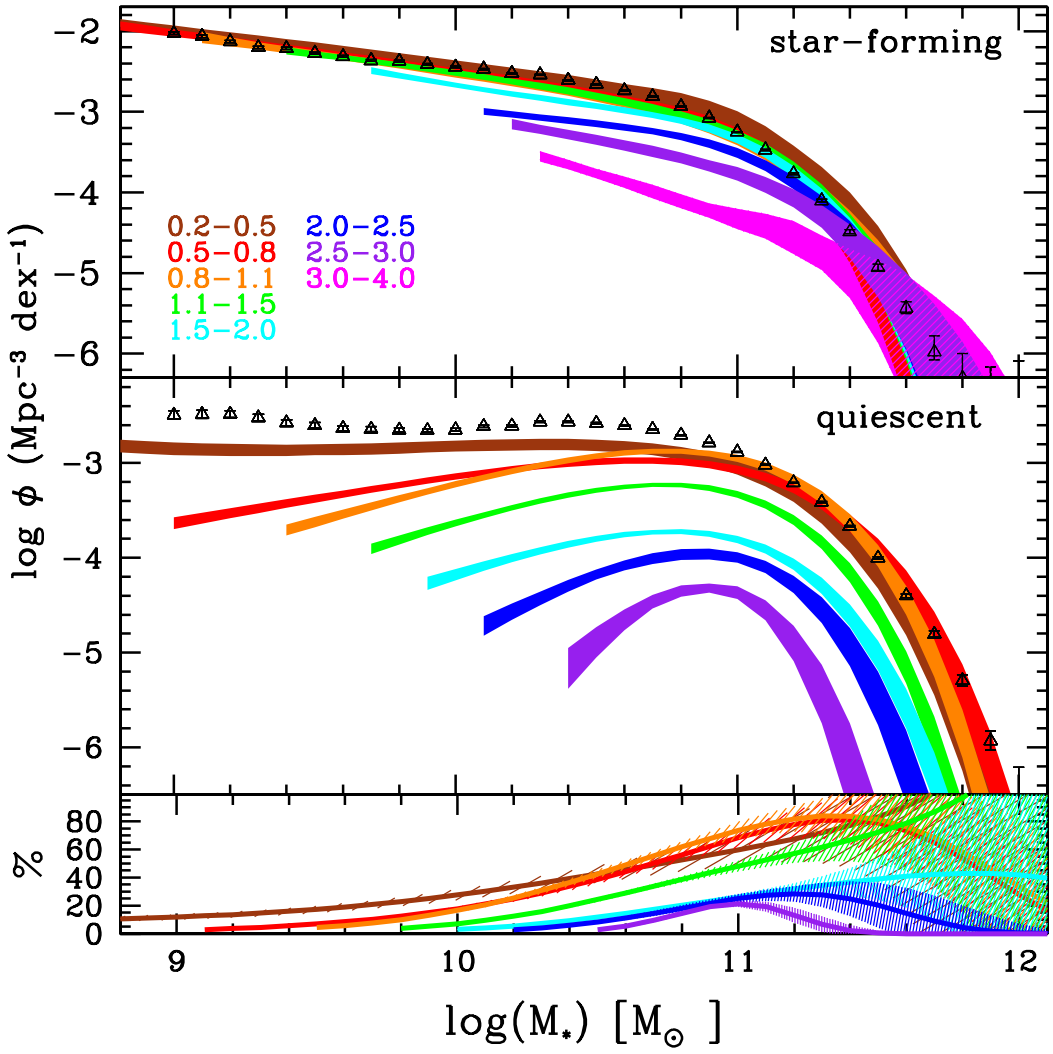

Figure 1.10: Galaxy stellar mass function up to $z = 4$ for the star-forming population (*top panel*), and for the quiescent population (*middle panel*). Filled regions correspond to the 1σ confidence level, and the black triangles and squares correspond to the local estimates by Moustakas et al. (2013) and Baldry et al. (2012). The *bottom panel* shows the percentage of quiescent galaxies as a function of stellar mass in the same redshift bins. Figure and caption from Ilbert et al. (2013).

galaxies that are expected to be passively dimming in luminosity with little density change versus the evolution of blue late-type galaxies, which are expected to have significant density evolution as they form and undergo mergers. The usefulness of this can be seen in Figure 1.10, which shows the mass functions of galaxies up to $z = 4$ in UltraVISTA from Ilbert et al. (2013), which have been split into star-forming and quiescent, showing the different shape of the mass functions, and the difference in their evolution.

1.4.3 Measurements of the Galaxy LF

The galaxy LF has been extensively studied with measurements across a wide range of wavelengths and redshifts, from the UV LFs of Lyman break galaxies at $z > 7$ (Finkelstein et al., 2015) to the radio luminosity functions of AGN and star-forming galaxies at low redshift (Prescott et al., 2016).

At low redshift, surveys such as the Two Degree Field Galaxy Redshift Survey (2dFGRS; Colless et al., 2001) ushered in the current era of large scale mapping of the local universe with their use of multi-fibre technology, allowing them to measure multiple spectroscopic redshifts at once and producing a final catalogue of $\sim 220,000$ spectroscopically confirmed galaxies out to $z_{max} \sim 0.3$. Norberg et al. (2002) used their data to measure the b_J-band LF at $z = 0$, measuring $M^*_{b_J} - 5\log h = -19.66 \pm 0.07$, $\alpha = 1.21 \pm 0.03$ and $\phi^* = (1.61 \pm 0.17) \times 10^{-2} h^3 \mathrm{Mpc}^{-3}$.

This was followed in fantastic style by the SDSS (York et al., 2000). This was the first survey to image the sky in five filters (u', g', r', i', z') at once and eventually supplied spectroscopic redshifts of $\sim 1,000,000$ galaxies. The commissioning data yielded a first LF determination from 11,275 galaxies presented in Blanton et al. (2001), before a follow-up in Blanton et al. (2003) presented the rest-frame r'-band LF from 147,986 galaxies at $z = 0.1$ in the second data release, SDSS-DR2, finding $M^* - 5\log h = -20.44 \pm 0.01$, $\alpha = -1.05 \pm 0.02$ and $\phi^* = (1.49 \pm 0.04) \times 10^{-2} h^3 \mathrm{Mpc}^{-3}$.

The final update in SDSS-DR6 (Adelman-McCarthy et al., 2008) measured $M^* - 5\log h = -20.71 \pm 0.04$, $\alpha = -1.26 \pm 0.02$ and $\phi^* = (0.93 \pm 0.07) \times 10^{-2} h^3 \mathrm{Mpc}^{-3}$ using 516,891 galaxies.

More recently, large scale spectroscopic redshift surveys have been pushing away from $z < 0.1$. The GAMA survey allowed the measurement of the *ugriz* galaxy LFs out to $z = 0.5$ as well as their evolution since then (Loveday et al., 2012). Both GAMA and SDSS could also provide LFs split by galaxy colour, allowing the investigation of how the bimodal nature of the colour-magnitude distribution of galaxies (Baldry et al., 2004, 2006) affects the evolution of the different LFs. Loveday et al. (2012) found that red galaxies have shown passive evolution since $z = 0.5$, while blue galaxies have shown evidence of mergers. Cool et al. (2012), using the AGN and Galaxy Evolution Survey (AGES; Kochanek et al., 2012), found that both blue and red galaxies brighten in a similar fashion from $z = 0$ to $z = 0.75$, and while both populations show evidence of density evolution, with higher density now than at $z = 0.75$, the change is much more extreme for red galaxies than blue galaxies.

With the rise of surveys with large amounts of photometric data, it has become possible to find photometric redshifts for large samples of galaxies out to higher redshift. The COMBO-17 survey made a breakthrough in this area, providing photometric redshifts for $\sim 25,000$ galaxies in an area of 0.78 degree^2 using 17 bands in the redshift range $0.2 < z < 1.2$ (Wolf et al., 2003). Because of the SED fitting necessary to find photometric redshifts, they could split up their sample by galaxy type, and trace separate evolution of the LFs. They found red, early-type galaxies are far more abundant at low redshift than high redshift, while bluer, late-type galaxies do not show much change in either luminosity or density. VVDS (e.g. Ilbert et al., 2005) followed on from this, probing evolution out to $z \sim 1.5$. Zucca et al. (2006) performed a similar analysis to that of COMBO-17 with VVDS and found that, unlike COMBO-17, they did not measure a strong density evolution in early-type galaxies,

instead measuring strong density evolution of late-type galaxies, with lower density at high redshift. The redshift survey zCOSMOS (Lilly et al., 2007; Zucca et al., 2009) presented LFs from 10,644 objects in the range $0.01 < z < 1.3$, both divided up by spectrophotometric and morphological type, with Zucca et al. (2009) finding the same evolution as seen in VVDS.

Stepping up in redshift, Marchesini et al. (2007) measured the K-band LF of 1000 galaxies in 378 arcmin^2 over the redshift range $2 < z < 3.5$. They found that galaxies at $z > 2$ had characteristic magnitudes that were ~ 1.2 magnitudes brighter in the R-band, and were ~ 5 times less dense than current values. Cirasuolo et al. (2010) presented the evolution of the K-band LF out to $z \simeq 4$ from the UKIDSS Ultra Deep Survey (UDS; Lawrence et al., 2007), which contributed $\sim 50,000$ galaxies over 0.7 degrees^2 in the redshift range $0.2 < z < 4$, representing the most accurate measurement at the time of the evolution of the near-infrared galaxy LF from high to low redshift. They found that the evolution was different for galaxies of different luminosity, with bright galaxies assembling at high redshift and passively evolving since $z < 1$ and fainter galaxies forming at lower redshift, in line with downsizing.

These observations give a picture of the Universe where galaxies form with blue colours initially, and some evolve into early type galaxies, possibly via mergers. Large galaxies form their stellar mass at high redshift, and then dominate the luminosity evolution as they passively age while small galaxies continue to form until later times.

Some of the first LFs measured for high redshift galaxies were from rest-frame UV observations of Lyman break galaxies at $z \sim 3$ and $z \sim 4$ (Steidel et al., 1996, 1999). Since then, the numbers of galaxies detected at high redshift have grown, with detections of Lyman break galaxies now numbering over 1000 at $z > 6$ (Bouwens et al., 2015; Finkelstein et al., 2015), with some candidates possibly at redshifts as high as 10 (e.g. Bouwens et al., 2011, 2015; Ellis et al., 2013; Oesch et al., 2013). Surveys undertaken with Wide Field Camera 3 (WFC 3) on the *HST* such as the Hubble Ultra

Deep Field (HUDF; Beckwith et al., 2006; Ellis et al., 2013; Illingworth et al., 2013) and the Cosmic Assembly Near-Infrared Deep Extragalactic Legacy Survey (CANDELS; Grogin et al., 2011; Koekemoer et al., 2011) have provided the extremely deep imaging needed to find very high redshift galaxies. While these have led to multiple measurements of the UV LF for fainter galaxies out to $z \leq 8$ (Finkelstein et al., 2015; Lorenzoni et al., 2013; McLure et al., 2009; Wilkins et al., 2011a), the small survey sizes (CANDELS covers a total area of ~ 790 arcmin^2 while the UDF is a miniscule ~ 5 arcmin^2) makes it difficult to measure the bright end of the LF, leading to the need to for larger area coverage which has been provided by ground-based surveys such as the UDS (Lawrence et al., 2007) and the UltraVISTA survey (McCracken et al., 2012).

With this wedding cake of surveys, the UV LF has been found to decrease in characteristic magnitude by ~ 1 mag between $z = 3$ and $z = 8$, with the faint-end slope steepening to $\alpha \sim -2$ by $z \geq 7$ (Bouwens et al., 2007; Finkelstein et al., 2015; Lorenzoni et al., 2013; McLure et al., 2013; Schenker et al., 2013). Measurements of the bright end slope have also found it to be potentially less steep at very high redshift, steepening from $z = 7$ to $z = 5$ (Bowler et al., 2014, 2015), which may be caused by evolution in the dust properties of high redshift galaxies or the onset of mass quenching (as described in Peng et al., 2010).

1.5 Thesis Overview

In this thesis I present luminosity functions of galaxies from the nearby universe to high redshift galaxies at $z \gtrsim 7$. In Chapter 2, I present an analysis of imaging of the GOODS-North field by the *HST* as part of the CANDELS survey. I describe a method for selecting Lyman break galaxies at high redshift, and then present candidate galaxies at $z \approx 7$ and $z \approx 8 - 9$. In Chapter 3 I compare high redshift

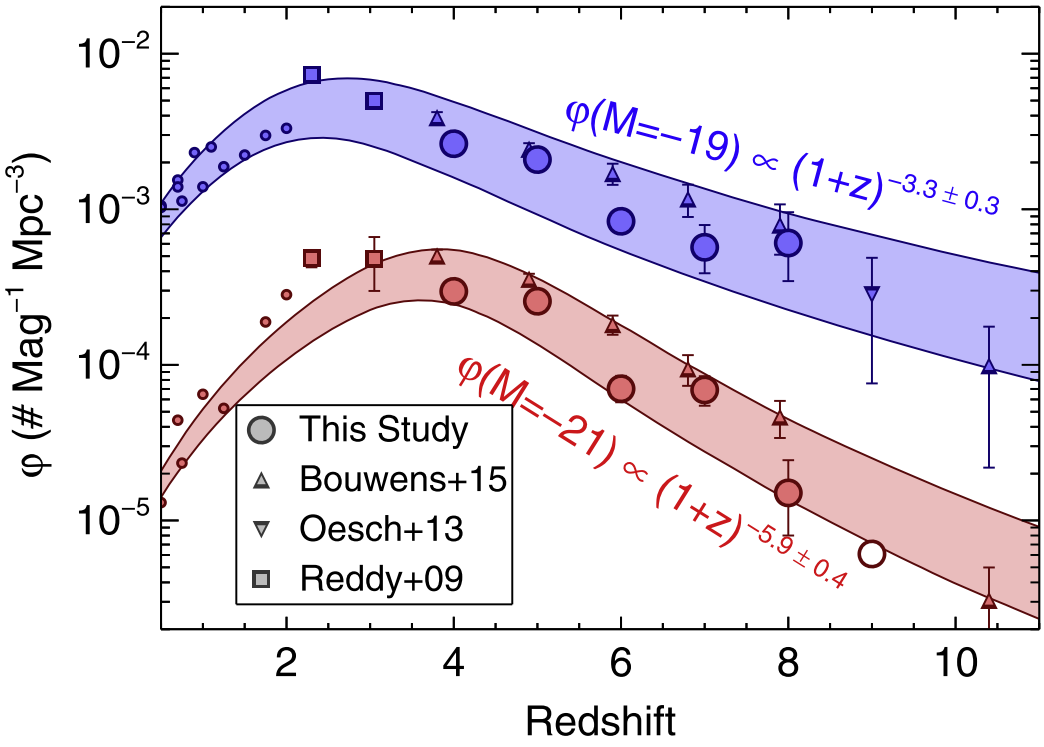

Figure 1.11: The number densities of bright ($M_UV = -21$) and faint ($M_UV = -19$)galaxies at a variety of redshifts. Bright galaxies become more numerous from $z = 8$ to $z = 4$ faster than faint galaxies, after which they become less common. Bright galaxies also peak earlier than faint galaxies, at $z = 3.1 - 3.2$ compared to $z = 2.4 - 2.7$. Figure taken from Finkelstein et al. (2015)

candidates from the GOODS-North and GOODS-South fields, commenting on the cosmic variance between the two fields before measuring the combined UV LF for both GOODS-North and GOODS-South at $z \approx 7$ and $z \approx 8 - 9$. In Chapter 4, I present near-IR luminosity function analysis of a catalogue of sources from the 1 degree^2 overlap in the Vista Infrared Deep Extragalactic Observations (VIDEO) survey imaging of part of the XMM3-LSS field and the Canada France Hawaii Legacy Survey (CFHTLS) Deep 1 (D1) field. I investigate the evolution of the K_s-band luminosity function from $z \approx 0.2$ to $z \approx 3$, testing the amount of evolution in both number density and characteristic magnitude. In Chapter 5, I extend this analysis to the 4.5 degree^2 overlap between the VIDEO imaging of the XMM3-LSS field and the CFHTLS Wide 1 field, presenting K_s-band LFs and their evolution from $z \approx 2$ to $z \approx 1.5$. I finish by describing my conclusions and suggesting ideas for future work.

Throughout this thesis, all magnitudes quoted will be in the AB magnitude system.

Chapter 2

Lyman break galaxies at $z \approx 7 - 9$ from GOODS-North/CANDELS

2.1 Introduction

Over the last fifteen years we have been able to identify star-forming galaxies within a billion years of the Big Bang at redshifts beyond 6 (Bouwens et al., 2003; Stanway et al., 2003) through the Lyman break technique (e.g., Steidel et al., 1996). This technique rests on the fact that as light leaves a galaxy and passes through the intervening intergalactic medium along the line of sight, Lyman-α absorption occurs at wavelengths shorter than that of the rest-frame Lyman-α. For distant galaxies, much of the flux below the wavelength of the rest-frame Lyman-α is damped, resulting in a very sharp spectral break which can be photometrically selected for. By $z \sim 6$ and beyond, the Lyman-α break has been redshifted out through the red end of the visible spectrum and into the infrared. Since the Wide Field Camera 3 (WFC 3) was added to the Hubble Space Telescope (*HST*) in 2009, which extended its capabilities out to wavelengths of 1600nm, it has been possible to search for populations of galaxies at still earlier times than $z \sim 6$ using data from deep photometric surveys such as the

HUDF (e.g. Bouwens et al., 2004b). This has led to the build up of large catalogues of candidate primordial star forming galaxies (Bouwens et al., 2015; Bowler et al., 2014; Bradley et al., 2012; Bunker et al., 2010; McLeod et al., 2016; McLure et al., 2010, 2013; Oesch et al., 2013; Schenker et al., 2013) out to very high redshift, with one probable galaxy at $z \approx 11$ (Oesch et al., 2013). This has allowed us to probe the evolution of these early galaxies through their individual star formation rates and overall rest-ultraviolet (UV) luminosity function, shedding light on the reionisation of the Universe and the sources responsible for it.

In this chapter, I examine the northern part of the Great Observatories Origins Deep Survey (GOODS) field (Dickinson et al., 2003), which was imaged as part of the Cosmic Assembly Near-Infrared Deep Extragalactic Legacy Survey, or CANDELS (Grogin et al., 2011; Koekemoer et al., 2011). The original GOODS imaging combined Spitzer, *HST*, Chandra, Herschel and XMM-Newton observations as well as data from several ground-based facilities, including ESO's Very Large Telescope (the VLT). The original GOODS *HST* imaging was performed with the Advanced Camera for Surveys' (ACS) optical filters. The CANDELS survey is a multi-cycle treasury program undertaken with *HST*, consisting of a 'Wide' program which observes to depths of ~ 27 AB mag (5σ) and a 'Deep' program, which observes to ~ 28 mag (5σ), and covers a total area of $790\,\mathrm{arcmin}^2$. As well as the GOODS fields, it includes observations of the Extended Groth Strip, or EGS, the UKIDSS Ultra-Deep Survey, or UDS, and the Cosmological Evolution Survey, or COSMOS. All of the fields were chosen to minimise any overall cosmic variance through their separation. The EGS, UDS and COSMOS fields are also purposefully elongated, which also reduces the effect of cosmic variance (Grogin et al., 2011). The CANDELS observations of GOODS-North and -South provided imaging taken with the YJH filters on WFC 3. Most important of these for us is the F105W, or Y, filter, which is crucial for the clean photometric selection of $z \approx 7 - 9$ objects as the Lyman break moves through

it over this redshift range. Of the other CANDELS fields, none of which were imaged to as great a depth as the GOODS fields (most are ~ 1 mag shallower in the J-band, the EGS and COSMOS were not imaged in the Y-band at all, and although the UDS does have Y-band coverage from HAWK-I (the High Acuity Wide Field K-band Imager, an instrument on the VLT), the resolution and depth are not nearly as good as was obtained with WFC 3 in GOODS (Galametz et al., 2013; Hickey et al., 2010). This makes them much less suitable for the search for galaxies at very high redshift.

The CANDELS fields form a data set ranging from the very large shallow fields, such as the EGS, UDS and COSMOS, which comprise $\approx 670\,\mathrm{arcmin}^2$ to smaller, deeper fields such as GOODS, which are $\approx 120\,\mathrm{arcmin}^2$. The GOODS fields also contain the deepest images taken of the sky, the HUDF in the south and to a lesser extent, the Hubble Deep Field in the North. These two fields are imaged to $\approx$ 29.5-30 (5σ in F105W, F125W, F140W and F160W) and ≈ 28 (5σ in F300W, F450W, F606W and F814W) magnitudes respectively, but only cover ~ 4 arcmin^2 each. Together, these fields, along with others, provide a huge dynamic range from bright, rare objects which can be found in the larger, shallower fields to the fainter objects which have only been seen in the HUDF.

In this Chapter I will first describe the data in Section 2.2 and my method for selecting high-redshift galaxies in Section 2.3.1 before presenting candidate lists of galaxies at $z \approx 7$ and $z \approx 8-9$ in the GOODS-North field in Section 2.4. The selection method is identical to that used in Lorenzoni et al. (2013) to select $z \approx 7$ and $z \approx 8-9$ in the GOODS-South field, the candidate list from which will be discussed more in Chapter 3.

2.2 Data

2.2.1 Observations

I used the new WFC 3 near-infrared observations of the GOODS-North field taken as part of the CANDELS programme (P.I.: S. Faber, *HST* program ID: 12442–5). CANDELS consists of 902 orbits spread over three large area fields, the UDS, EGS and COSMOS, as well as the two GOODS fields, which are slightly smaller. The CANDELS/GOODS observations add (among others) the F105W, F125W and F160W filters (corresponding approximately to the Y-, J- and H-bands) to the four ACS images through the F435W, F606W, F775W & F850LP filters (the b-, v-, i'- and z'-bands) already taken as part of the original GOODS survey (Giavalisco et al., 2004). The CANDELS observational plan for GOODS-North is largely identical to that of GOODS-South in exposure time and tiling strategy, and is detailed in Grogin et al. (2011). The GOODS-North field surrounds the Hubble Deep Field (HDF, Williams et al., 1996), with central co-ordinates 12:36:54.87 and +62:14:18.86 (J2000). The ACS images cover $10 \times 16\,\mathrm{arcmin}^2$, and the WFC 3 imaging comprises a deep region of $10 \times 6.8\,\mathrm{arcmin}^2$ in the centre (from 5×3 WFC 3 pointings), and two $8 \times 4\,\mathrm{arcmin}^2$ shallow but wide regions north-east and south-west of this (with 2×4 WFC 3 pointings in each). More information on how the observations were carried out can be found in Koekemoer et al. (2011) and Grogin et al. (2011).

I used the interim data products that the CANDELS team have made available from the completed *HST* visits[1]. Koekemoer et al. (2011) describes the data reduction process. The images were reduced using `Multidrizzle` Koekemoer et al. (2002) with an output pixel scale of $0\farcs06$ (twice that of the ACS drizzled data products from the GOODS team), from an original scale of $0\farcs13$ for the IR arm of WFC 3. A `pixfrac` of 0.8 was used. In the Y-band, the interim products cover the whole

[1]The data products from the CANDELS team are on candels.ucolick.org/data_access/GOODS-N.html

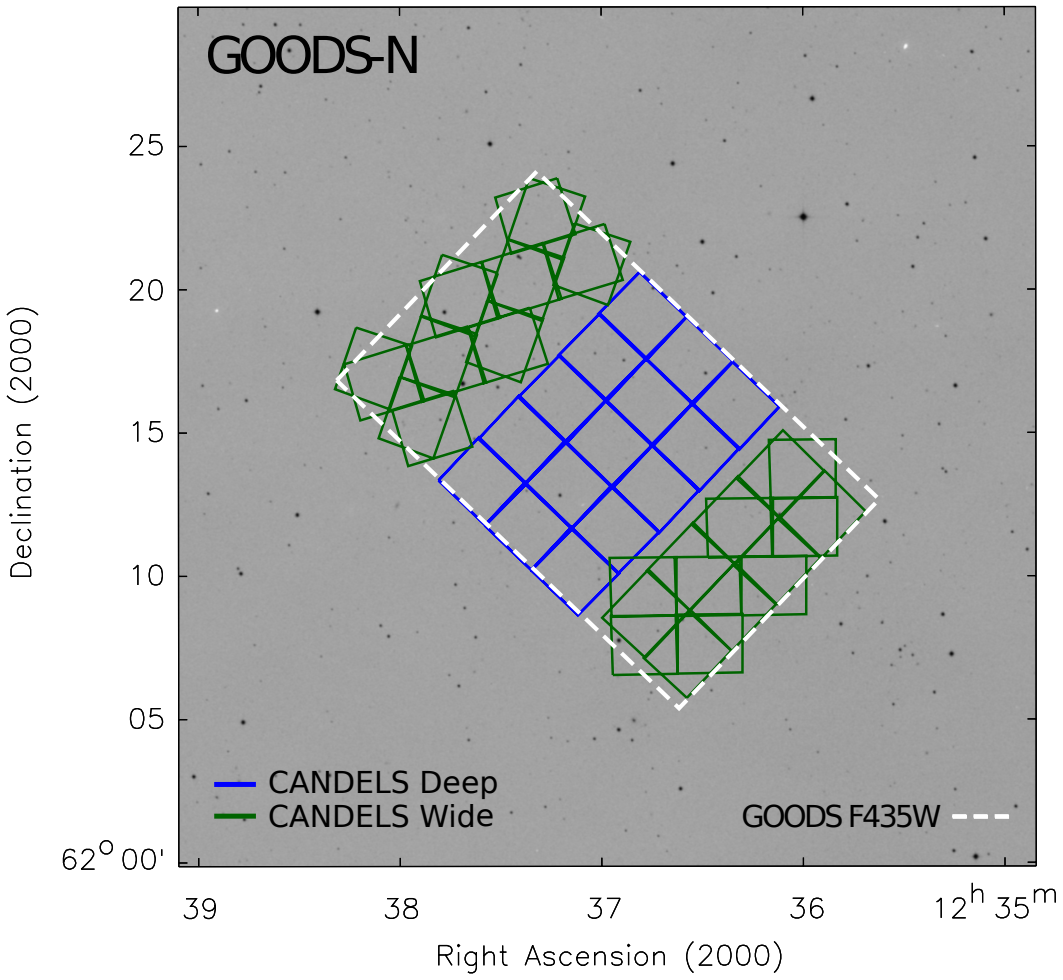

Figure 2.1: Simplified layout of the observations GOODS-North field. The WFC 3 imaging of the 'Wide' and 'Deep' sections of the field are shown in green and blue respectively, while the white dashed outline shows the footprint of the ACS imaging. Figure taken from Grogin et al. (2011).

Table 2.1: The total exposure time (in ksec) is listed for each WFC 3 filter used in this study for both the South and North GOODS 'Wide' and 'Deep' fields, along with the ACS b-band, v-band, i'-band and z'-band. In parenthesis, the average depth for each filter over the area listed is shown. These are 5σ limits calculated in apertures of $0\farcs6$ diameter, corrected as described in the text for aperture loss and reddening.

	ACS/WFC3 exposure times in ksec (5σ Depth in AB mag)			
Field ID	GOODS-N DEEP	GOODS-S DEEP	GOODS-N WIDE	GOODS-S WIDE
b-band	7.2 (27.5)	7.2 (27.6)	7.2 (27.5)	7.2 (27.6)
v-band	5.7 (27.7)	5.5 (27.8)	5.7 (27.7)	5.5 (27.8)
i'-band	8.5 (27.1)	7.0 (27.3)	8.5 (27.1)	7.0 (27.3)
z'-band	24.7 (26.9)	18.2 (27.3)	24.7 (26.9)	18.2 (27.3)
Y-band	8.9 (27.1)	8.1 (27.8)	2.7 (26.6)	2.7 (26.8)
J-band	10.6 (27.4)	7.4 (27.3)	1.9 (26.7)	2.1 (26.9)
H-band	11.2 (27.2)	7.7 (27.2)	2.8 (26.6)	2.1 (26.6)
Area (arcmin^2)	63	63	32	33

field, and were observed over four epochs - two in the 'Wide' region and two in the 'Deep'. Both regions were split into two sections to be observed to full depth in one go in one epoch each. In the J- and H-band, the interim images cover all of the field with observations built up over 8 epochs. I combined the multiple epochs using `IRAF imcombine`, weighting by the exposure time at each spatial location to produce an output mosaic in each band with pixel rejection using the `ccdclip` algorithm. I then block-averaged the original GOODS ACS images in the b-, v-, i'- and z'-bands on a 2×2 scale to give them the same output pixel scale as the WFC 3 images (converting from $0\farcs03$ per pixel to $0\farcs06$), with checks to ensure astrometric accuracy.

2.2.2 Construction of Catalogues

I use the Lyman break technique to identify candidate distant galaxies on the basis of a large flux decrement at wavelengths shorter than the rest-frame Lyman-α (1216Å),

caused by the large optical depth of the intervening Lyman-α forest absorption. At $z \approx 7$, the Y-band filter lies just above this break, and the z'-band straddles the break, so the $z' - Y$ colour for these galaxies will be large (very red). The other ACS filters lie below, and in particular the b- and v-bands are short-wards of the rest-frame Lyman limit at 912 Å, and so no flux should be detected from $z > 7$ objects in these filters. At $z \approx 8 - 9$, the J-band filter lies at a longer wavelength than Lyman-α, and the Y-band lies below, so a red $Y - J$ colour is a signature of galaxies at these redshifts. Figure 2.3 shows an example SED of a $z \approx 8$ galaxy with a spectral break lying between the Y- and J-bands.

The source catalogues were constructed using version 2.5.0 of the SExtractor photometry package (Bertin & Arnouts, 1996). I ran SExtractor in dual-image mode using the appropriate weight maps (derived from the maps of exposure time), so that it identified sources and laid down apertures in a filter uncontaminated by the Lyman-α break and then applied those apertures to measure the flux in the other filters. I set the threshold for object identification to be five connected pixels which were more than twice the pixel-to-pixel rms. For candidate $z \approx 7$ galaxies I selected in the J-band image while for $z \approx 8 - 9$ candidates I selected in the H-band (both corresponding to about 1500 Å in the rest-frame and uncontaminated by the Lyman-α break).

I measured the fluxes of objects in a range of apertures (0.″3, 0.″39, 0.″48, 0.″6 and 0.″84), and based the near-infrared WFC 3 photometry on the flux within a 0.″6-diameter aperture, corrected for flux falling outside using an aperture correction. This aperture correction was 0.2 mag in the Y-band and 0.25 mag for the J- and H-band, and this was determined through aperture photometry of bright but unsaturated stars in the field. High-redshift galaxies seem typically compact (Bunker et al., 2004; Oesch et al., 2010; Ono et al., 2013)), and so should have similar aperture corrections to point sources. To further quantify this, I measure the full-width half maximum

(FWHM) of each dropout candidate from SExtractor, and deconvolve this with the point spread function, or PSF, (subtracting in quadrature the FWHM determined for point sources, which was 3.2 resampled pixels in J-band, or $0\farcs02$). For the drop-outs, the typical deconvolved half-light radius was about 0.5 kpc (see Table 2.2), consistent with the work of Ono et al. (2013) and Curtis-Lake et al. (2016) at an absolute magnitude of about $M_{UV} = -20$ appropriate for the GOODS-North survey. If I were to adopt an aperture correction for a marginally extended source of this size then the corrected near-infrared magnitudes would be 0.1 mag brighter than if these were point sources. However, I use the point source corrections to the aperture magnitudes since the individual sizes and total fluxes of these faint galaxies are uncertain. The colours are essentially unaffected at the 0.01 mag level adopting the point-source or extended-source aperture correction.

For the ACS z'-band I used an identically-sized $0\farcs6$-diameter aperture, with an aperture correction of 0.1 mag, while the b-, v- and i'-band photometry was done in $0\farcs3$-diameter apertures. The smaller aperture was used to enhance the point-source sensitivity at shorter wavelengths where the resolution is better. I have also corrected for the foreground Galactic extinction using the *COBE*/DIRBE & *IRAS*/ISSA dust maps of Schlegel et al. (1998). The optical reddening is $E(B-V) = 0.01$, equivalent to extinctions of $A_{F850LP} = 0.015$, $A_{F105W} = 0.010$, $A_{F125W} = 0.008$ & $A_{F160W} = 0.005$.

As the pixel-to-pixel noise in drizzled images is highly correlated, the noise values measured by SExtractor are reduced compared to the true noise. I determined the true noise by placing a large number of $0\farcs6$-diameter apertures on the reduced images, avoiding regions occupied by sources with the use of the SExtractor segmentation maps. The standard deviation in the counts measured per aperture gives us the noise in the aperture photometry, including the correlations introduced by drizzling. The corresponding $5\,\sigma$ detection limits (corrected for aperture losses) are listed in Table 2.1, along with the exposure times for each filter.

2.3 Candidate Selection

As described in Section 2.2.2, I use the Lyman break technique to colour-select high-redshift galaxies. A flux decrement, defined as $1-f_z/f_Y$ (or $1-f_Y/f_J$), of 0.6 between the z'- and Y-bands gives us a redshift window of $6.5 < z < 8.0$ as the spectral break moves red-wards through the bands, while a decrement of 0.56 between the Y- and J-bands gives a range of $7.6 < z < 9.8$. This can be seen in Figure 2.2. The selection efficiency is much reduced near the edges of the ranges. At the low redshift end, this is due to photometric scatter as well as the non-uniform transmission of the filters. At the high redshift end, this is due to the fact that fewer candidates are bright enough to be above the sensitivity limits. As the spectral break moves through the Y- (for $z \approx 7$) or J-band (for $z \approx 8-9$), a galaxy with fixed luminosity will appear increasingly faint as the break nears the edge of the filter, making it less likely that a galaxy of fixed luminosity at the higher redshift end of the selection function will appear brighter than my detection limit.

Although I do use a photometric redshift fitting code to simulate intermediate redshift contaminants in Section 2.3.2, I use the Lyman break colour selection technique to select the sample of high redshift galaxies following the method of Lorenzoni et al. (2013) to enable us to compare the candidates presented here with the GOODS-South candidates presented in Lorenzoni et al. (2013) to study the cosmic variance between the two fields, as well as combining the samples to produce luminosity functions in Chapter 3.

2.3.1 Selection Criteria

I have used the same sets of selection criteria as Lorenzoni et al. (2013) to ensure the same selection volume. These are shown in Figure 2.4. This consists of two sets of cuts; one set from Wilkins et al. (2011a) and Lorenzoni et al. (2011) for z'-drops and

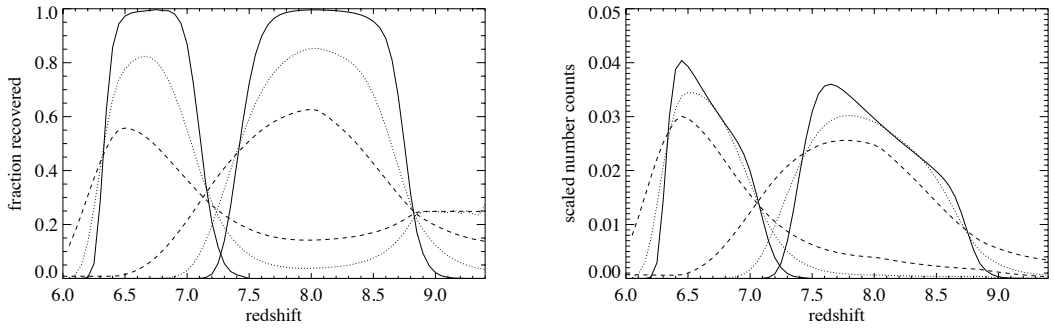

(a) (b)

Figure 2.2: (a): Fractional recoverability of z'-drops (peaking on the left between 6.5 and 7) and Y-drops (peaking on the right between 7.5 and 8.5) above the detection limit due to the imposition of the colour cuts at depths of $J_{AB} = 25.5$, 26.5 and 27.5 for the z'-drops and $H_{AB} = 25.5$, 26.5 and 27.5 for the Y-drops (solid, dotted and dashed lines respectively). The fainter the apparent magnitude, the more the photometric scatter smears the edges of the function.

(b) Scaled differential number counts of z'-drops (peaking on the left between 6.5 and 7) and Y-drops (peaking on the right between 7.5 and 8.5) plotted for $J_{AB} = 25.5$, 26.5 and 27.5 for the z'-drops and $H_{AB} = 25.5$, 26.5 and 27.5 for the Y-drops (solid, dotted and dashed lines respectively) and scaled by 1, 20 and 100 respectively for comparison of the shape. The fainter the apparent magnitude, the more the shape of the selection function is spread out.

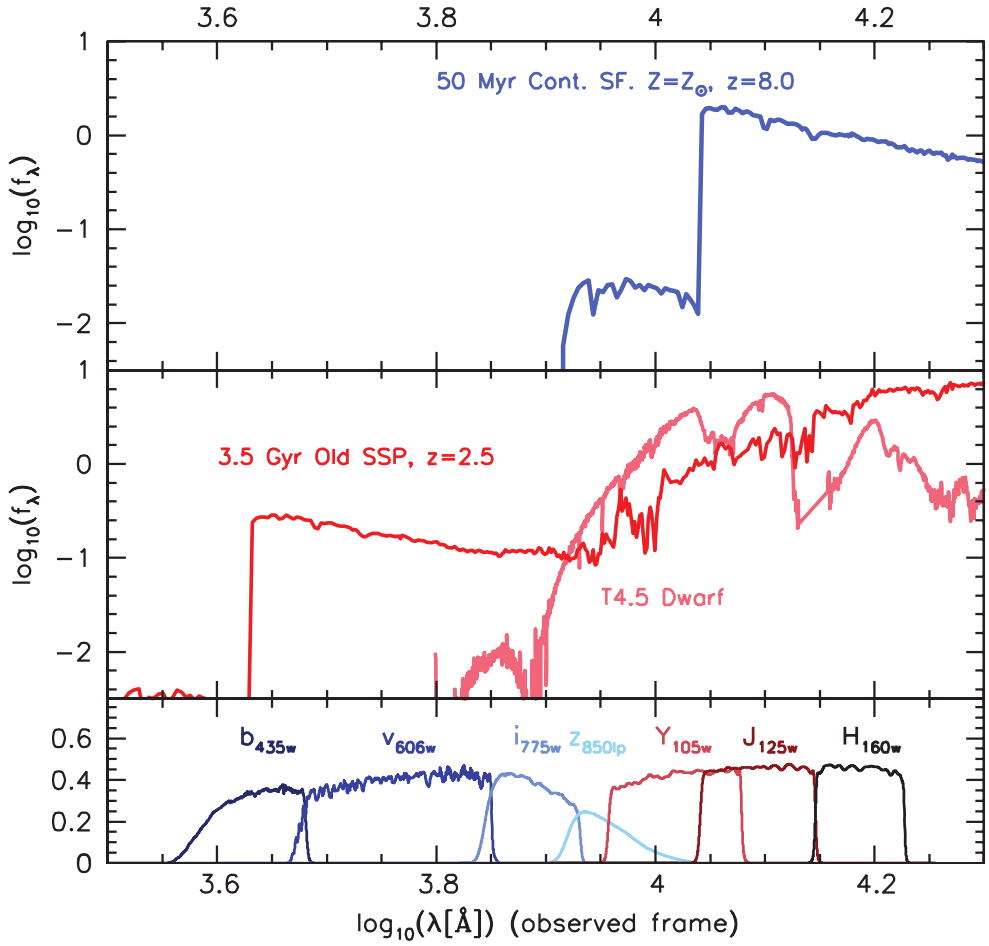

Figure 2.3: Top panel: model (from the STARBURST99; Leitherer et al., 1999) SED of redshifted z = 7 star-forming galaxy. Middle panel: potential contaminants; observed SED of a low-mass dwarf star (class: T4.5, Knapp et al., 2004) together with the model (STARBURST99) SED of a 3.5-Gyr single-aged stellar population at z = 1.8. The bottom two panels show the transmission functions of the ACS and WFC 3 filters available. Figure and caption adapted from Wilkins et al. (2011a).

Y-drops respectively, which are the blue selection areas (candidates are marked with a circle) and one set laid out in Bouwens et al. (2011), which are shown in pink (the candidates are marked with a point). The Bouwens et al. (2011) cuts are slightly less conservative than the Wilkins et al. (2011a) and Lorenzoni et al. (2011) cuts and so they give higher number counts and consequently better statistics, though the candidate list may be less robust.

There are potentially other objects besides high-redshift galaxies which could give colours that comply with cuts in $z' - Y$ or $Y - J$, as can be seen in Figure 2.3. Most of the contaminants are either very red intermediate redshift galaxies or LTY dwarf stars. To identify them I use filters above the Lyman break to impose a second colour cut, which will select objects that have blue colours above the break. This returns objects which are consistent with high redshift star-forming galaxies rather than intrinsically red foreground objects.

As well as being illustrated in Figure 2.4, the colour-cuts are outlined below. The cuts used for the z'-drops at $z \approx 7$ (Wilkins et al., 2011a, W11 hereafter) are:

$$\begin{aligned}
(z_{850LP} - Y_{105W}) &> 1.0 \\
(z_{850LP} - Y_{105W}) &> 2.4 \times (Y_{105W} - J_{125W}) + 0.9 \\
(Y_{105W} - J_{125W}) &< 1.0
\end{aligned}$$

and for the Y-drops at $z \approx 8 - 9$ (Lorenzoni et al., 2011, L11 hereafter) are:

$$\begin{aligned}
(Y_{105W} - J_{125W}) &> 0.9 \\
(Y_{105W} - J_{125W}) &> 0.73 \times (J_{125W} - H_{160W}) + 0.9 \\
(J_{125W} - H_{160W}) &< 1.5
\end{aligned}$$

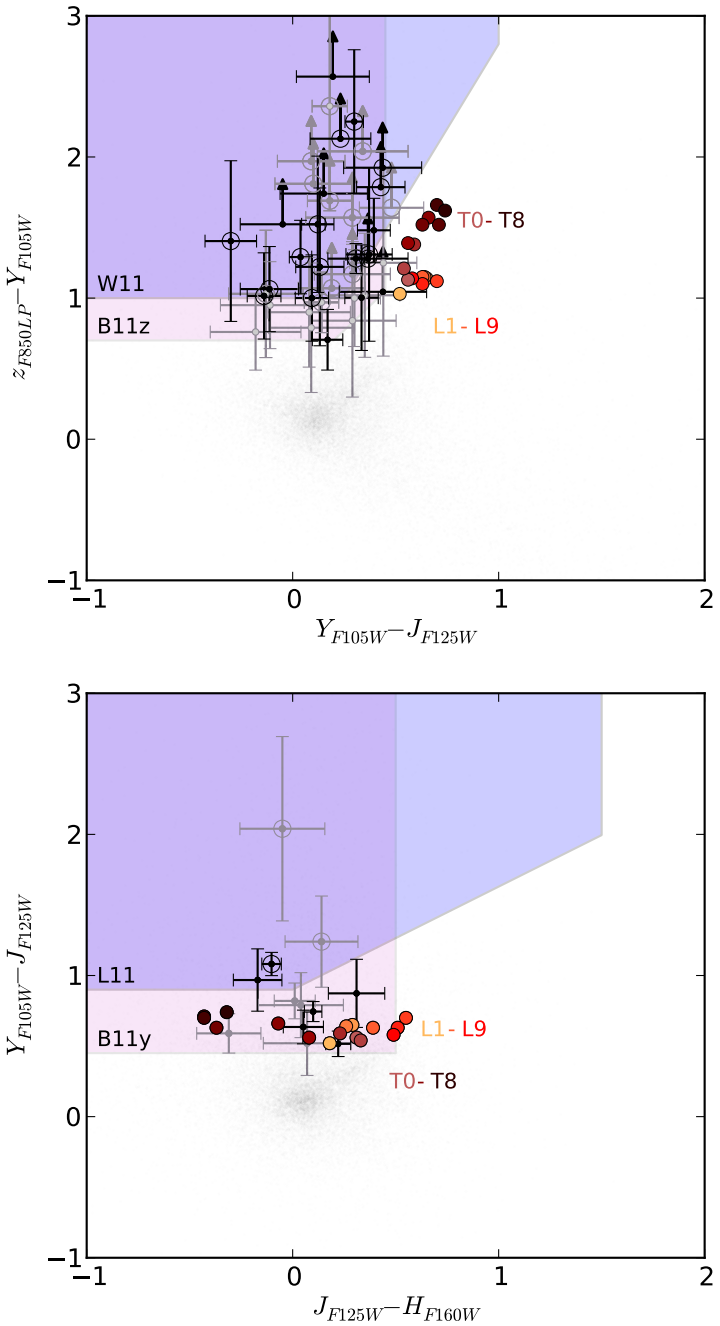

Figure 2.4: Top: the $Y_{F105W}-J_{F125W}$ and $z_{F850LP}-Y_{F105W}$ colour-colour plane. The black points are the $z \approx 7$ z-drop candidates from GOODS-North field while the grey points are the equivalent candidates from GOODS-South presented in Lorenzoni et al. (2011). Those in the W11 cut are circled in black or grey. The two coloured areas represent the colour-colour selections, with the B11z cut in pink and the W11 cut in pink.

Bottom: the $J_{F125W}-H_{F160W}$ and $Y_{F105W}-J_{F125W}$ colour-colour plane. The colour schemes are the same as above, with L11 instead of W11.

In both plots, stellar contaminants in the form of simulated colours for L/T dwarfs (taken from Wilkins et al. (2014)) are shown as yellow, red and brown circles and the grey cloud shows the SExtractor catalogue objects which do not obey my colour cuts (i.e., lower redshift objects).

The Bouwens et al. (2011) cuts for $z \approx 7$ z'-drops (B11z hereafter) are:

$$\begin{aligned}(z_{850LP} - Y_{105W}) &> 0.7 \\ (z_{850LP} - Y_{105W}) &> 1.4 \times (Y_{105W} - J_{125W}) + 0.42 \\ (Y_{105W} - J_{125W}) &< 0.45\end{aligned}$$

and $z \approx 8 - 9$ Y-drops (B11y hereafter) are

$$\begin{aligned}(Y_{105W} - J_{125W}) &> 0.45 \\ (J_{125W} - H_{160W}) &< 0.5\end{aligned}$$

The candidates that I present in Table 2.2 and Table 2.3 have been selected to obey either of the above colour cuts, as can be seen in Figure 2.4. I have added the condition that they have at least a 5σ detection in a band above the break. For the $z \approx 7$ z'-drops, this is in the J-band, in which the catalogues are selected, and for the $z \approx 8 - 9$ Y-drops this is in the H-band. Additionally, the z'-drops are required to have at least a 4σ detection in the H-band. To minimize possible contamination from intrinsically red objects at lower redshift, I applied a non-detection criterion in each of the optical wavebands (b-, v- and i'-band) at the $2\,\sigma$ level within the $0\farcs3$ aperture. This helps to rule out lower redshift objects, as objects at $z > 6$ have lost too much of their flux below the spectral break to be seen in these bands due to absorption by the intervening intergalactic medium. The candidate list was also visually inspected to remove objects with artefacts such as diffraction spikes.

2.3.2 Contamination

I attempt to quantify the level of contamination in the GOODS-North candidate list by looking at a very much deeper set of images, namely the XDF (Hubble eXtreme Deep Field, Illingworth et al., 2013), which goes down to $\approx$ 30 mag at 5σ across all filters. First, 10 sets of images were created that had been artificially degraded to the depth of the GOODS-North field. Pure 2D noise frames were created using IRAF.artdata with 10 different random seeds and then added to the XDF images to mimic the GOODS-North data. I created 10 catalogues and subsequent candidate lists according to my GOODS-North selection criteria from these noisier data sets (this was done for the B11z/B11y and the W11/L11 criteria). This included a step where the candidates were visually checked so that artefacts could be removed, as was done for the GOODS-North candidates, which limited the number of catalogues that could be simulated. These were compared to two candidate lists with photometry measured from the deeper XDF frames; the first was built from catalogues which were trained in the deeper XDF images, while the second was from catalogues which were trained in the degraded images. Both candidate lists also obeyed my GOODS-North selection criteria and were truncated to objects brighter than the same limiting magnitudes of $J_{AB} = 27.4$ (for the z-drops) or $H_{AB} = 27.2$ (for the Y-drops), corresponding to $5\,\sigma$ in the 'Deep' section of GOODS-North. By comparing the shallower candidates with their deep counterparts, I could estimate how many of them were genuine high redshift galaxies and how many were contaminants. I found a contamination rate of $\sim$ 22 per cent for a data set at the depth of GOODS-North across the four candidate lists (this does not count i'-drops at $z \approx 6$ as contaminants as they are candidate high redshift galaxies picked up due to the spreading of the redshift selection function at lower sensitivities (see Figure 2.2), and are well accounted for in later calculations). This translates to surface density of 0.06 arcmin^{-2} down to a magnitude of $J_{AB} = 27.4$, or a total of four contaminants in the GOODS-North B11z z'-drop candidate list,

and surface density of 0.02 arcmin^{-2} down to a magnitude of $H_{AB} = 27.2$, or one contaminant in the B11y Y-drop list.

As well as measuring the contamination of my sample by looking at real candidate galaxies in the XDF, I have also investigated a simulated mix of $z \approx 6-9$ star forming galaxies and $z \approx 1-3$ red interlopers. The colours of the galaxies at these redshifts were produced using the photometric redshift code LePhare[2] (Arnouts et al., 1999; Ilbert et al., 2006). This is done using galaxy templates from Arnouts et al. (2007), which are based on the four observed spectra in Coleman et al. (1980) of an elliptical, two spirals and an irregular galaxy along with two observed starburst templates from Kinney et al. (1996). Each of these has been extrapolated to IR and UV wavelengths using the GISSEL synthetic models (Bruzual & Charlot, 2003). With the addition of the *HST* filter information and the Madau (1995) method of accounting for intergalactic neutral hydrogen, LePhare outputs theoretical observed magnitudes for these templates over a range of redshifts. I then inserted a population of simulated galaxies into the GOODS-North images. These galaxies were gaussian light profiles with a range of widths representing the range of widths in my candidate lists, with the theoretical colours predicted from LePhare, and were placed according to luminosity functions at $z \approx 2$ from Ilbert et al. (2005) and at $z \approx 7$ from McLure et al. (2013), who use a photometric method to select high redshift candidates. Finally, I ran these simulated galaxies through the catalogue construction and candidate selection procedures, leaving us with a theoretical candidate list of ≈ 20 objects with a contamination rate of ~ 20 per cent. This method supports the previous technique, leading us to apply a ~ 22 per cent correction to account for contaminants. It should be noted that this contamination rate does not account for interlopers that are outside, but near the selection region, and so could be photometrically scattered inside. While scattering of 2 or 3σ may be rare, the relatively small population size of high

[2]The LePhare code is publicly available at http://www.cfht.hawaii.edu/~arnouts/LEPHARE/lephare.html

redshift galaxies when compared with lower redshift red galaxies makes this a source of contamination that is potentially non-negligible (see Mortlock et al. 2012 for a discussion of this problem when searching for high redshift quasars).

The stellar contamination is expected to be low, due to the low surface densities of cool dwarf stars on the sky at such high Galactic latitudes. I have estimated a lower limit on the surface density following Wilkins et al. (2014), as follows. Using Kirkpatrick et al. (2012), who find 33 LTY dwarfs within 8 pc of the Sun, we can assume a space density of $\gtrsim 0.015$ pc^3. As T-dwarfs have absolute H-band magnitudes $M_H \approx 15-20$ and Y-dwarfs have $M_H > 20$, we can estimate a surface density of 5.2 deg^{-2}, from 2×10^5 sources out to a radius of 0.15 kpc that are brighter than $H_{AB} = 27.2$. For the area of the GOODS-North survey, this translates to 0.09 stellar contaminants in total. While the catalogue of local dwarfs may not be representative of all sightlines, the high Galactic latitude of the GOOD-North field does mean that it should be freer of Galactic contamination than most sightlines. Although this is a lower limit due to the incompleteness of the sample of local LTY dwarfs used, the actual number is not expected to be much increased beyond this, partially due to the high Galactic latitude of the field, and so the real number of contaminants is likely to be close to 0.09. Therefore, stellar contamination has a negligible effect on the sample.

2.4 Lyman break Galaxies at $z \approx 7-9$

I have employed the Lyman break technique to identify 22 z'-drops (Table 2.2) and 6 Y-drops (Table 2.3). I present these candidate galaxies here, and defer discussion of their number statistics and luminosity functions at $z \approx 7$ and $z \approx 8-9$ until Chapter 3.

z'-band drop-outs at $z \approx 7$

Thumbnails of the 22 z'-drops that I selected using the B11z colour cut are shown in Figure 2.5 as well as their photometry in Table 2.2. Table 2.2 also lists the half-light radius of each candidate as calculated by SExtractor and deconvolved with the instrument point-spread function, as described in Section 2.2.2. Of the 22 candidates, 14 candidates were also found by the W11 cut. These are marked with a superscript in Table 2.2.

Firstly, there is a 60 per cent overlap between the candidate list in the 'Deep' section of the field presented here and that analysed in Bouwens et al. (2014). Other than this, four of the candidates have previously been identified as potential high redshift sources. GN.D-zD2 was previously noted in Thompson (2003) in F160W (H-band) *HST*/NICMOS imaging (#1596 in the Thompson 2003 catalogue, who ascribes a photometric redshift of $z_{phot} = 6.16$). Given the $z' - Y$ colour, the redshift from the WFC 3 imaging is more likely to be $z \approx 6.8$. GN.D-zD3 appears in the catalogue of Bouwens et al. (2006) from the original ACS imaging of the HDF, detected in the z'-band but undetected in i' with $i' - z' > 1.6$. GN.W-zD1 is also in the catalogue of Bouwens et al. (2006), where it was also detected in the z'-band but undetected in i' with $i' - z' > 1.6$, as well as in the i'-drop catalogue of Dickinson et al. (2004) as NiD050. It was observed to have a narrow-band excess emission (Hu et al., 2010) through the NB912 filter with SuprimeCam on Subaru, consistent with Lyman-α emission at $z = 6.5$, and has since been spectroscopically confirmed with both *HST* grism spectrocopy from PEARS (Probing Evolution And Reionization Spectroscopically Pirzkal et al. 2013; Straughn et al. 2009) and Keck/DEIMOS spectroscopy, confirming it has a redshift of $z = 6.573$ (Rhoads et al., 2013). Finally, another of the candidates in the 'Wide' section of the field, GN.W-zD2, has been spectroscopically confirmed by Ono et al. (2012) as having z=7.213, and Stark et al. (2015) find a tentative detection of $C_{III]}$ emission with Keck/MOSFIRE spectroscopy.

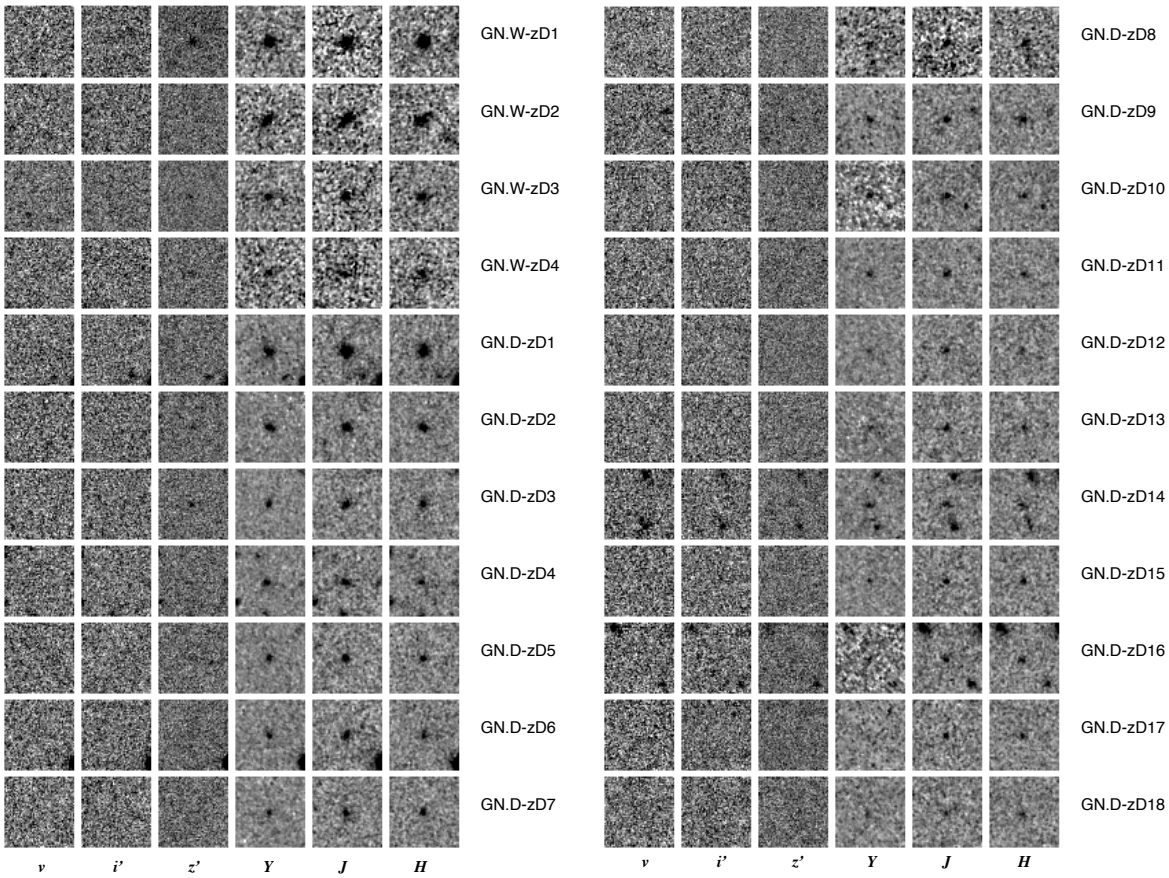

Figure 2.5: 3×3 **arcsec**^{2} **thumbnails of the candidate** $z \approx 7$ **star-forming galaxies from the** $vi'z'YJH$**-band images. These candidates were selected because they obeyed the B11z colour cuts (they should be easily visible in the** YJH**-bands, but drop out of detection in the** z'**-band and below) along with the other criteria set out in Section 2.3.1. The first four are in the 'Wide' section of the field, while the remainder are in the 'Deep' section. The greyscale is inverted, with a stretch of** -2σ **white to** $+2\sigma$ **black per** $0\farcs06$ **pixel.**

It is also worth noting that GN.D-zD9 is listed in the catalogue of Conselice et al. (2011) (as GNS 2022), who search for massive galaxies between $1.7 < z < 3$. However, they only have a single-band detection in the NICMOS H-band along with optical non-detections and find an extremely uncertain photometric redshift of $z \approx 6.5$, and do not list it as a potential high mass galaxy at intermediate redshift. Due to this, and the fact that it is well within my colour cuts, I regard it as no less reliable than any of my other candidates and include it in further analysis.

There were two very luminous objects presented by Hathi et al. (2012) as candidate galaxies at $z \gtrsim 6.5$. While these objects do appear in my catalogue (they are located in the southern 'Wide' flanking area), they do not fulfil my selection criteria and so do not appear in this candidate list. The brighter object is just outside my colour cuts (it appears to the right of the W11 selection area in Figure 2.4, with $z' - Y = 2.38 \pm 0.02$ and $Y - J = 0.89 \pm 0.14$), and the dimmer object has optical detections. Given that both of the objects are well detected in the z-band (and in one case, the i'-band), these are likely to be just below the lower end of my redshift selection function.

In Table 2.2 I have quoted values for the UV slope parameter β, which has been calculated according to the method in Wilkins et al. (2011b). This technique probes the rest-frame UV continuum of the candidate galaxies using the $J - H$ colour, which combines the only two bands unpolluted by the Lyman-α break at $z \approx 7$. If one assumes that the UV slope can be described by a perfect power law ($f_\lambda \propto \lambda^\beta$), then β, the UV slope parameter, can be found using an unpolluted colour above the break, such as $J - H$. Following Wilkins et al. (2011b), $\beta = 4.28 \times (J - H) - 2.0$ and the errors on each value of β are found by adding the J- and H-band errors in quadrature. I find an average $\beta = -1.70 \pm 1.15$, which is consistent with other determinations in the literature and representative of the spread of values measured (e.g. Bouwens et al., 2009, 2012, 2014; Castellano et al., 2012; Dunlop et al., 2013; Finkelstein et al., 2012; Stanway et al., 2005; Wilkins et al., 2011a). It is also consistent with the value

of $\beta = -2$ which is used for the UV luminosity function calculations in Chapter 3.

Table 2.2: z'-band drop out candidates at $z \approx 7$ meeting either of the selection criteria described in Section 2.3.1 (all of the objects in the W11 cut satisfy the B11 as well). Objects are ordered by apparent $J_{\rm AB}$ magnitude. Where quoted, limits are 1σ. I also list the UV slope parameter β for each candidate, calculated according to Wilkins et al. (2011b) as well as the SExtractor half-light radius.

ID	RA (J2000)	Dec (J2000)	$z_{\rm AB}$	$Y_{\rm AB}$	$J_{\rm AB}$	$H_{\rm AB}$	$(z-Y)_{AB}$	$(Y-J)_{AB}$	β	r_e (kpc)
GN.W-zD1	12:37:25.653	+62:17:43.13	26.55 ± 0.14	25.27 ± 0.06	24.97 ± 0.04	25.03 ± 0.05	1.28 ± 0.16	0.31 ± 0.07	-2.27 ± 0.28	0.90
GN.W-zD2	12:36:22.683	+62:08:07.94	> 28.43	25.97 ± 0.11	25.53 ± 0.07	25.66 ± 0.09	> 2.46	0.44 ± 0.13	-2.54 ± 0.47	2.45
GN.W-zD3	12:36:07.797	+62:12:59.12	27.65 ± 0.36	26.17 ± 0.13	25.78 ± 0.09	25.81 ± 0.10	1.48 ± 0.38	0.39 ± 0.16	-2.14 ± 0.56	0.67
GN.W-zD4	12:36:13.975	+62:08:41.26	27.64 ± 0.35	26.57 ± 0.19	26.69 ± 0.19	26.19 ± 0.14	1.06 ± 0.40	-0.11 ± 0.27	0.14 ± 1.00	1.32
GN.D-zD1[1]	12:36:19.841	+62:15:08.91	28.37 ± 0.61	26.12 ± 0.08	25.82 ± 0.05	25.88 ± 0.07	2.25 ± 0.61	0.30 ± 0.10	-2.25 ± 0.35	1.64
GN.D-zD2[1]	12:36:54.928	+62:12:14.44	27.64 ± 0.35	26.35 ± 0.10	26.31 ± 0.08	26.21 ± 0.09	1.29 ± 0.37	0.04 ± 0.13	-1.58 ± 0.50	0.93
GN.D-zD3	12:37:01.699	+62:10:02.48	27.44 ± 0.29	26.75 ± 0.14	26.58 ± 0.10	26.45 ± 0.11	0.70 ± 0.32	0.17 ± 0.17	-1.45 ± 0.62	0.78
GN.D-zD4[1]	12:36:37.266	+62:17:11.26	28.31 ± 0.58	26.79 ± 0.15	26.67 ± 0.10	26.86 ± 0.16	1.52 ± 0.60	0.12 ± 0.18	-2.83 ± 0.80	1.74
GN.D-zD5[1]	12:37:20.940	+62:12:05.72	27.76 ± 0.39	26.77 ± 0.15	26.67 ± 0.10	26.63 ± 0.13	1.00 ± 0.41	0.10 ± 0.18	-1.83 ± 0.71	0.75
GN.D-zD6	12:36:56.455	+62:17:44.14	28.04 ± 0.48	27.04 ± 0.18	26.70 ± 0.10	26.84 ± 0.15	1.00 ± 0.51	0.33 ± 0.21	-2.59 ± 0.80	1.18
GN.D-zD7[1]	12:37:13.074	+62:12:06.06	28.53 ± 0.68	27.22 ± 0.21	26.85 ± 0.12	26.81 ± 0.15	1.31 ± 0.71	0.37 ± 0.25	-1.82 ± 0.82	0.95
GN.D-zD8	12:37:45.527	+62:18:08.61	> 28.37	27.02 ± 0.18	26.87 ± 0.12	26.65 ± 0.13	> 1.34	0.15 ± 0.22	-1.06 ± 0.77	1.22
GN.D-zD9[1]	12:37:07.445	+62:14:50.33	27.80 ± 0.40	26.78 ± 0.15	26.92 ± 0.13	26.50 ± 0.11	1.02 ± 0.42	-0.14 ± 0.20	-0.20 ± 0.74	0.68
GN.D-zD10[1]	12:36:48.629	+62:16:31.83	> 28.66	27.39 ± 0.25	26.96 ± 0.13	27.24 ± 0.21	> 1.27	0.43 ± 0.28	-3.17 ± 1.08	1.58
GN.D-zD11[1]	12:36:37.108	+62:17:34.51	28.46 ± 0.64	27.24 ± 0.21	27.10 ± 0.15	27.28 ± 0.22	1.22 ± 0.68	0.13 ± 0.26	-2.77 ± 1.15	1.30
GN.D-zD12[1]	12:37:05.453	+62:10:02.71	> 28.96	27.49 ± 0.27	27.26 ± 0.17	27.28 ± 0.22	> 1.47	0.23 ± 0.32	-2.13 ± 1.20	–
GN.D-zD13[1]	12:37:26.327	+62:12:21.51	> 28.73	27.69 ± 0.31	27.30 ± 0.18	27.15 ± 0.20	> 1.04	0.38 ± 0.36	-1.34 ± 1.15	1.25
GN.D-zD14[1]	12:37:13.565	+62:11:14.84	28.47 ± 0.65	27.06 ± 0.19	27.36 ± 0.19	27.11 ± 0.19	1.40 ± 0.68	-0.26 ± 0.26	-0.90 ± 1.15	–
GN.D-zD15[1]	12:37:26.558	+62:14:44.04	> 29.04	27.81 ± 0.35	27.38 ± 0.19	27.03 ± 0.18	> 1.22	0.44 ± 0.39	-0.51 ± 1.12	0.68
GN.D-zD16	12:37:32.457	+62:14:11.26	> 28.59	27.83 ± 0.35	27.39 ± 0.19	27.22 ± 0.21	> 0.76	0.44 ± 0.40	-1.27 ± 1.23	1.28
GN.D-zD17	12:37:12.026	+62:16:49.27	> 29.38	27.73 ± 0.32	27.54 ± 0.22	27.17 ± 0.20	> 1.65	0.20 ± 0.39	-0.43 ± 1.28	0.67
GN.D-zD18	12:36:10.803	+62:15:14.15	> 28.69	27.70 ± 0.31	27.55 ± 0.22	27.29 ± 0.22	> 1.00	0.15 ± 0.38	$-0.04 \pm 1.47*$	–

[1] also in W11 selection. * outside the colour-colour selection window used in Wilkins et al. (2011b) for a reliable β determination.

Table 2.3: Y'-band drop out candidates at $z \approx 8-9$ meeting either of the selection criteria described in Section 3.1 (similarly to Table 2.2, all of the objects in the L11 cut also satisfy the B11 cut). Objects are ordered by apparent $H_{\rm AB}$ magnitude. Where quoted, limits are 1σ. I also quote the SExtractor half-light radius.

ID	RA (J2000)	Dec (J2000)	$Y_{\rm AB}$	$J_{\rm AB}$	$H_{\rm AB}$	$(Y-J)_{AB}$	$(J-H)_{AB}$	r_e (kpc)
GN.D-YD1	12:37:19.933	+62:15:26.065	26.80 ± 0.15	26.05 ± 0.06	25.96 ± 0.07	0.74 ± 0.16	0.01 ± 0.09	0.70
GN.D-YD2[1]	12:36:38.189	+62:12:20.726	27.10 ± 0.19	26.02 ± 0.06	26.13 ± 0.08	1.08 ± 0.20	-0.10 ± 0.10	1.13
GN.D-YD3	12:37:29.132	+62:15:07.732	26.98 ± 0.17	26.46 ± 0.09	26.24 ± 0.09	0.52 ± 0.19	0.22 ± 0.12	0.75
GN.D-YD4	12:37:02.501	+62:17:21.875	27.55 ± 0.28	26.91 ± 0.13	26.86 ± 0.16	0.64 ± 0.31	0.05 ± 0.20	0.47
GN.D-YD5	12:36:47.926	+62:14:59.300	28.30 ± 0.50	27.42 ± 0.20	27.11 ± 0.19	0.87 ± 0.54	0.31 ± 0.28	–
GN.D-YD6	12:37:27.418	+62:12:44.388	27.95 ± 0.39	26.99 ± 0.14	27.16 ± 0.20	0.97 ± 0.41	-0.17 ± 0.24	–

[1] also in L11 selection.

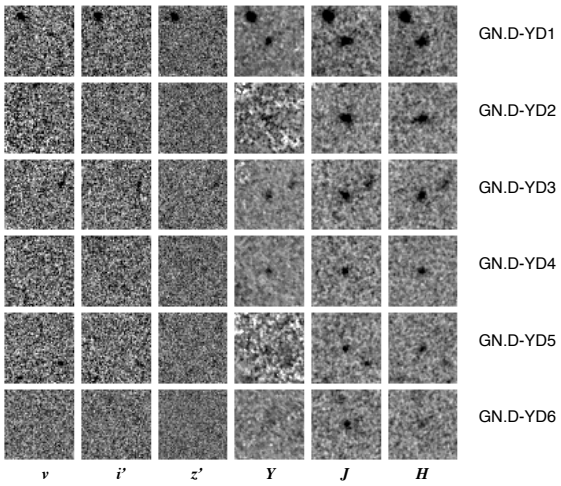

Figure 2.6: 3×3 arcsec^2 thumbnails of the candidate $z \approx 8-9$ star-forming galaxies from the $vi'z'YJH$-band images. These candidates were selected because they obeyed the B11y colour cuts (as with Figure 2.5, but dropping out of detection in the Y-band) along with the other criteria set out in Section 2.3.1. The greyscale is the same as Figure 2.5.

Y-band drop-outs at $z \approx 8-9$

As well as finding 22 z'-drops, I found 6 Y-drops using the B11y colour cut. Thumbnails of these 6 objects are shown in Figure 2.6, along with their photometry in Table 2.3. Only one of these possible galaxies also satisfies the L11 cut. All of these candidates appeared in the 'Deep' sections of the field. Similarly to the z-drops, there is a 67 per cent overlap with Bouwens et al. (2014).

I also quote the half-light radius of each candidate for the Y-drops, again as calculated by SExtractor and deconvolved with the instrument point-spread function. I do not quote the β parameter, as there are not enough bands unpolluted by the Lyman-α to reliably calculate it.

2.5 Conclusions

I have analysed *HST*/WFC 3 and ACS imaging of the CANDELS/GOODS-North field, producing a catalogue of objects from which I could select candidate high

redshift galaxies. I have done this using the Lyman break technique, relying on colour-cuts which isolate relatively uncontaminated regions of colour space to build a reasonably robust list of potential galaxies. I have estimated both the contamination of this candidate list using a combination of putting simulated low redshift galaxies through my selection process and simulating the survey using deeper images to test the fraction of expected interlopers, as well as estimating the stellar contamination fraction from the expected surface density of dwarf stars in the GOODS-North field.

I have presented a list of candidate Lyman break galaxies at $z \approx 7$ and $z \approx 8-9$ revealed by *HST*/WFC 3 imaging of the CANDELS/GOODS-North field. I identify 22 z'-drops (at $z \approx 7$) and 6 Y-drops (at $z \approx 8-9$) with magnitudes brighter than an AB magnitude of ≈ 27.5 – this new sample comprises relatively bright sources amenable to follow-up spectroscopy from the Northern Hemisphere.

Chapter 3

Constraining Cosmic Variance and the UV Luminosity Function at $z \approx 7-9$ in GOODS/CANDELS

3.1 Introduction

Using the candidate list of high redshift galaxies obtained in Chapter 2, it is possible to start building diagnostics of the state of the Universe at $z \approx 7-9$. In particular, here I discuss the Schechter parameterisation (Schechter, 1976) of the rest-frame UV LF, which allows us to quantify the balance in the volume densities of bright galaxies with faint galaxies, giving insight into the processes which shape this distribution. By investigating the changes to the LF with redshift,we can also draw conclusions about the evolutionary processes shaping the development of high redshift galaxies.

An important aspect of the CANDELS/GOODS data is the similarity between the North and South fields. The fields were selected to have approximately the same Galactic extinction and lie at similar Galactic latitudes, so should have reasonably comparable foregrounds. They have equivalent areas and were observed to similar

depths, making them ideal for comparison. I shall use the fact that these two fields provide two separate, but equivalent, lines of sight to discuss the variation in number counts which is predicted due to the large-scale structure of the Universe (i.e., the clustering of galaxies), otherwise known as cosmic variance. The GOODS-South field for $z \approx 7-9$ has already been analysed in Lorenzoni et al. (2013) and in this chapter I carry out a similar analysis on the GOODS-North field and compare the two.

In this Chapter I discuss the cosmic variance between the GOODS-North candidate list presented in Chapter 2 and the one presented for GOODS-South by Lorenzoni et al. (2013) (Section 3.2) and then derive the UV luminosity function at $z \approx 7$ and $z \approx 8-9$ from this sample in Section 3.3. I present my conclusions in Section 3.4.

3.2 Cosmic variance between GOODS-North and GOODS-South

The similarities in observing strategy, field layout and Galactic foreground make the CANDELS/GOODS fields ideal for exploring the effect of cosmic variance on deep, small-field surveys. I now compare the number counts of high-redshift Lyman break galaxies in the two GOODS fields (North and South) to assess the level of cosmic variance. I re-iterate that the selection used here in GOODS-North uses the same criteria over the same depth and area as the analysis of GOODS-South (Lorenzoni et al., 2013). I have compared only the 'Deep' sections of the fields, as the number counts in both the North and South 'Wide' sections are too low to make any meaningful comments.

First, I show the histograms of number counts in bins of apparent magnitudes for the z'-drops (Figure 3.1) and Y-drops (Figure 3.2). As can be seen, the number counts in the two fields agree within the Poisson errors in each 0.5 mag bin. A K-S test gives a >99 per cent confidence that both z'-drop samples are drawn from the

same parent population (i.e. the same luminosity function). For the Y-drops, the small number statistics render the K-S test less meaningful, but the two fields are consistent with both having 6 candidates in each. Looking at the B11z selection window (which includes all of the candidates), I have 18 z'-drops in the North and 17 in the South - a difference of five per cent, which is within the Poisson noise of 33 per cent on the ratio (i.e. combining the fractional errors on the number counts in the two fields in quadrature). Splitting these in brightness into two bins, I have a field-to-field variation of 12 percent at $J < 26.9$ and 22 per cent at $J > 26.9$. Again, these are within the Poisson noise expectations of 47 per cent for these two bins. Hence, the variation on the number counts in the fields appear entirely consistent with the small number count statistics, and any cosmic variance must be small in comparison. Similarly, for the W11z selection window I find 12 z'-drops in the North and 10 in the South. This gives a field-to-field variation of 17 per cent, which is again within the Poisson noise of 39 per cent.

I compare my findings with theoretical predictions of cosmic variance. From Muñoz et al. (2010), the expected cosmic variance at $z = 6 - 8$ and $J_{AB} < 27$ (a good approximation to my z'-drop sample) should be 20 per cent, for the 'Deep' survey area of 63 arcmin^2 per field (i.e. using $\theta = 8$ arcmin on a side in figure 1 of Muñoz et al., 2010). A similar number of 18 per cent is obtained from Somerville et al. (2004) for the cosmic variance at $z \approx 6$ (the highest redshift addressed in their paper), using the z'-drop comoving survey volume of $\approx 10^5\,\mathrm{Mpc}^3$ and $\phi^* \approx 10^{-3}\,\mathrm{Mpc}^{-3}$ (see Section 3.3). Further to this, the prescription laid out in Moster et al. (2011) predicts a cosmic variance of 18 per cent at most, depending on the redshift bin width used. I have also used the online Cosmic Variance Calculator from Trenti [1] based on Trenti & Stiavelli (2008). Using a typical incompleteness factor of three to account for all of the photometric scatter and sensitivity effects (see Figure 3.7(a)), a redshift bin

[1]The Cosmic Variance Calculator can be found at http://casa.colorado.edu/~trenti/CosmicVariance.html

width of $\Delta z \approx 1$ and adding in my galaxy sample and the correct survey geometry ($6\farcm8 \times 10'$) with a Sheth-Tormen bias (Sheth & Tormen, 1999), I obtain a slightly higher value for the cosmic variance of 26 per cent.

Hence, it seems that the predicted cosmic variance of 26 per cent or less is entirely consistent with my observations, and is less than or comparable to the Poisson noise on the number counts. However, from figure 1 of Muñoz et al. (2010) it can be seen that they would expect cosmic variance to be the dominant effect. To obtain their predicted Poisson noise for my survey statistics I would need a sample of 200 galaxies, which is ten times the size of the GOODS-North candidate list. This disparity in number counts may be due to a combination of the broader redshift range that they employ and the fact that they use a top hat selection function in redshift, producing an unrealistically complete sample. This can be seen by looking at Figure 2.2, which shows my redshift selection functions.

It is also worth mentioning survey geometry here. Long, thin fields can reduce the effects of cosmic variance as any two galaxies are further apart on average, reducing the chance of any correlation (Newman & Davis, 2002). This effect was taken into account when designing the CANDELS survey (Grogin et al., 2011) and had a large effect on the layout of the shallower fields, such as the EGS. However, for the GOODS 'Deep' fields the axial ratio is 0.8, which will not have much of an effect on the cosmic variance, but which has been taken into account for the calculations using Somerville et al. (2004), Moster et al. (2011) and the online Cosmic Variance Calculator (Trenti & Stiavelli, 2008).

To better distinguish between the two effects of variance on number counts and intrinsic structural variance, higher number counts of galaxies are needed. As larger survey areas will average out the effects of cosmic variance and small surveys will be dominated by Poisson noise, it is extra depth which will provide a clearer view by maximising the difference between the predicted effects of Poisson noise and cosmic

variance. More sightlines are also needed to improve the measurement itself. To this end, the *HST* Frontier Fields may be useful as they provide multiple sightlines of similar depth to the HUDF. The extra depth over CANDELS (ACS and WFC 3 imaging of the Frontier Fields is reaching depths of ≈ 29 AB magnitudes at 5σ; Koekemoer et al. 2014; Lotz et al. 2014) would help to further constrain the effect of cosmic variance on sample populations of galaxies at these early times. Each of these 6 fields should yield approximately 25 z'-drops, and according to Muñoz et al. (2010) an HUDF-sized field should have cosmic variance of 20 per cent for z'-drops down to 29 magnitude. Therefore with 6 independent sightlines, the difference between a 20 per cent total deviation due to purely Poisson shot noise and a 30 per cent deviation from a combination of Poisson noise and cosmic variance should just be measurable and so enable a test of the theoretical predictions of the amount of structure. Bouwens et al. (2014) discuss this, and they find that while the field-to-field variation in the *HST* Frontier Fields is $\lesssim 20$ per cent at $z \sim 4$, $z \sim 5$ and $z \sim 6$, it is nearly 50 per cent at $z \sim 7$.

3.3 UV Luminosity Function at $z \approx 7$ and $z \approx 8-9$

I use the surface densities of the drop-outs to constrain the rest-frame UV luminosity function at high redshift, as in Lorenzoni et al. (2011, 2013) and Wilkins et al. (2011a). I focus on $z \approx 7$ due to the higher number counts of candidates in this range, but I also present a determination of the $z \approx 8-9$ luminosity function. Because I have shown that the Poisson noise on the small number statistics dominates over any observed cosmic variance between the two CANDELS/GOODS fields (Section 3.2), I combine and bin in apparent magnitude the samples from both fields to constrain the bright end of the luminosity function. For extra dynamic range, I have added in the candidates from the XDF (Hubble eXtreme Deep Field, Illingworth et al., 2013)

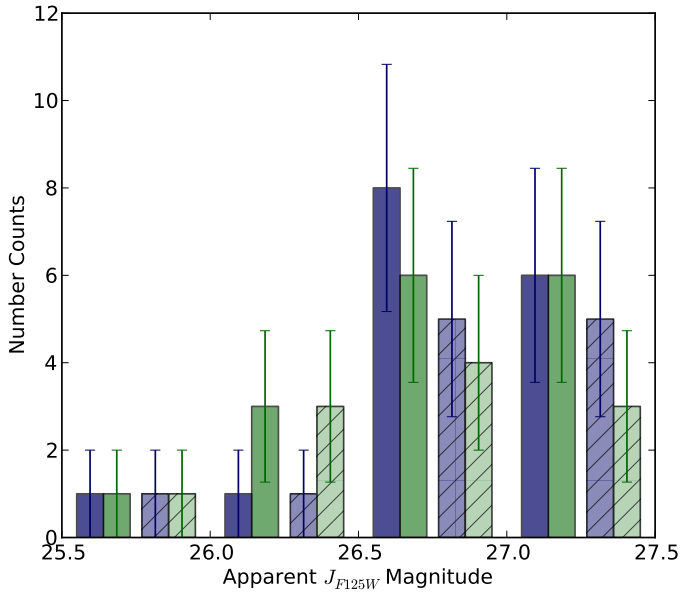

Figure 3.1: Number counts of $z \approx 7$ candidates in half-magnitude bins, with $1\,\sigma$ error bars. The blue bars (left) are from GOODS-North, and the green bars (right) are from GOODS-South, while the lighter, hatched bars show the W11z candidates and the darker, unhatched bars show the B11z candidates. The number counts agree to within one error bar.

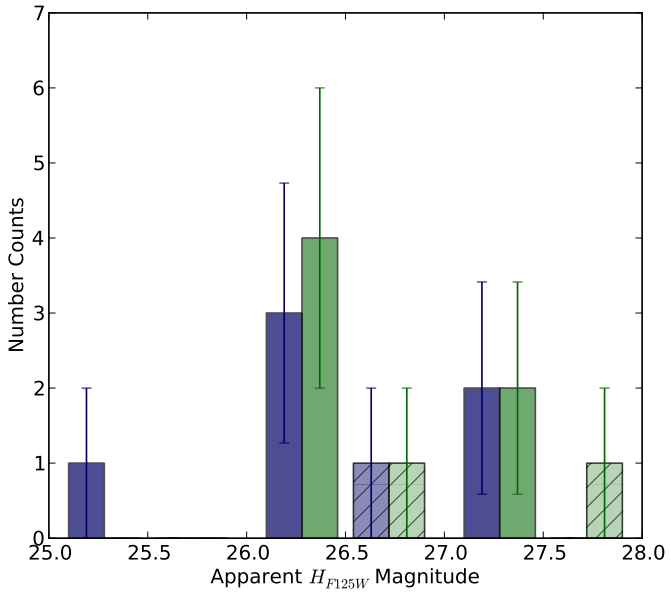

Figure 3.2: As for Figure 3.1, but using Y-drop candidates at $z \approx 8 - 9$, and with the lighter hatched bars showing the L11y candidates and the darker unhatched bars showing the B11y candidates.

which will be reported in Lorenzoni et al. (in prep) for the z'-drops with $J_{AB} > 27.5$ and for the Y-drops with $H_{AB} > 27.5$. They use identical colour cuts to those I apply in this work. I expect galaxies at these faint magnitudes to be less susceptible to cosmic variance, as they are not strong tracers of structure.

3.3.1 The Maximum Likelihood method

I use a Maximum Likelihood method based on that of Sandage et al. (1979) to determine the luminosity functions of $z \approx 7 - 9$ Lyman break galaxies. This is done by creating a family of luminosity functions parameterized by the Schechter function (Schechter, 1976), with a range of $-22.1 < M^*_{1600} < -18.4$ and $-1 < \alpha < -3$, where M^*_{1600} is the characteristic UV magnitude at 1600Å (corresponding to the J-band for z'-drops and the H-band for Y-drops). After constructing a population of simulated galaxies for each trial luminosity function, the effects of the GOODS-North survey are simulated to produce theoretical surface densities as a function of apparent magnitude. The Maximum Likelihood method is used to estimate which of the grid of models fits the data best, and so determine the most likely values of the Schechter parameters (ϕ^*, the characteristic volume density of galaxies and the normalisation of the Schechter function, M^*_{1600}, the absolute magnitude at 1600Å of a galaxy at the normalisation point, and α, the exponent of the faint-end slope of the Schechter function). This method works by maximising the logarithm of the likelihood function $\mathcal{L}$.

If a model luminosity function predicts an expected number of galaxies λ in the i^{th} magnitude bin, the probability p_i of observing n galaxies is given by:

$$p_i = \frac{\lambda^n e^{-\lambda}}{n!}. \tag{3.1}$$

The likelihood function is then the product of the probabilities for each of the i

magnitude bins:

$$\mathcal{L} = \prod_i p_i. \tag{3.2}$$

3.3.2 Model luminosity functions

As in Lorenzoni et al. (2013), a model galaxy spectrum is used, with a power-law UV slope and a large Lyman-α forest decrement of $D_A = 0.999$, appropriate for the Gunn-Peterson era. The model spectrum has a spectral slope of $\beta = -2$, where $f_\lambda \propto \lambda^\beta$, which is flat in f_ν and agrees with the average measured slope for the high-redshift populations (e.g. Dunlop et al., 2012, 2013; Stanway et al., 2005; Wilkins et al., 2011b). No intrinsic scatter in β is added, as the size of the intrinsic scatter is sufficiently small that it is not the dominant source of error.

I consider small redshift slices ($\Delta z = 0.05$) spanning the range of redshifts covered by the Lyman break technique. For each of these, the volume of the slice and the absolute magnitude in the rest-frame UV corresponding to my limiting apparent magnitude in the filter above the break is computed. I then consider whether my colour-colour selections (Section 2.3.1) would pick out galaxies at this redshift by folding the redshifted model galaxy spectrum through the *HST* filter response curves. I consider apparent magnitude intervals of $\Delta m = 0.05$ down to my limiting magnitude, and, by integrating the Schechter UV luminosity function within the corresponding absolute magnitude range, get the number of Lyman break galaxies within the redshift slice and within that apparent magnitude interval. Summing up the galaxies with the appropriate colours across the redshift slices gives the total expected number of galaxies as both a function of apparent magnitude in bins of $\Delta m = 0.5$ (the observable quantity) and of redshift for the input luminosity function (as can be seen

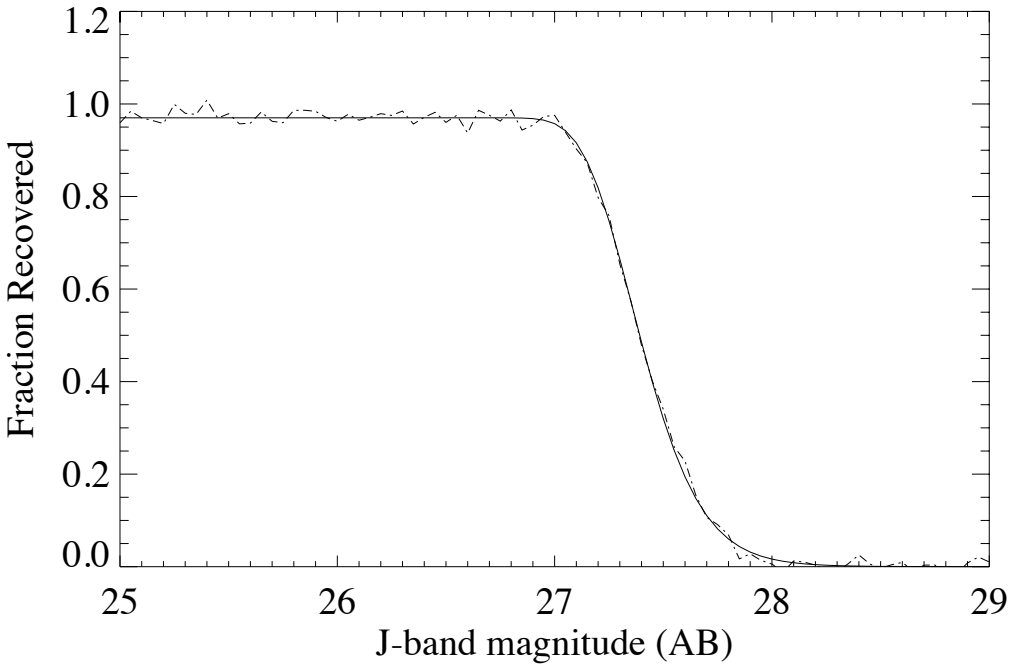

Figure 3.3: The completeness of the 'Deep' region of the J-band image as a function of magnitude. The dot-dashed line is the fraction of sources recovered as a function of aperture-corrected point source magnitude in the J-band image of GOODS-North, while the solid line is the expected completeness given the noise from the image, as modelled by a Gaussian, and a three per cent correction for source confusion.

in Figure 2.2). It should be noted that it is possible to take the limit of small bins and avoid binning either the observed number counts or the modelled number counts, provided that all empty bins with no galaxies are included in the total likelihood. A grid of predicted numbers for different values of M^*_{1600} (the characteristic magnitude) and α (the faint-end slope) is built to compare with the observed number counts (as a function of apparent magnitude) where the normalization, ϕ^* (the volume density), is treated as a parameter to be fit.

3.3.3 Effect of photometric scatter

Each magnitude bin is corrected for photometric scatter. One aspect of this is the

probability that a galaxy with a particular apparent magnitude will be identified by SExtractor and will fall either above or below my signal-to-noise cut. This acts in both directions; the sample will be incomplete at fainter magnitudes as galaxies close to the signal-to-noise cut have a larger chance of scattering below the limit, but there will also be a number of galaxies that are intrinsically fainter than the cut which get scattered above it and into my selection. First, the incompleteness is determined by repeatedly adding in a 50 by 50 grid of spatially-compact artificial sources (a scaled unsaturated star) to the GOODS-North images (see Figure 3.3), and assessing the fraction which are recovered as a function of brightness. This also accounts for confusion with foreground sources, which reduces the maximum completeness by three per cent. Figure 3.3 shows the fraction of sources recovered at a S/N>5 as a function of input magnitude, along with a modelled completeness simulated by a Gaussian with a width from the J-band $1\,\sigma$ noise, scaled by 0.97 to account for confusion. As the fraction of recovered sources is well described by the simulated incompleteness, the predicted number of galaxies from the Schechter functions is then convolved with a Gaussian to account for scatter both out of and into the selection. This was done by converting the model apparent magnitudes from the luminosity functions into S/N slices using the survey properties, then applying a Gaussian smoothing to this S/N distribution using a width of 1σ. This perturbed the magnitudes both up and down according to Gaussian random errors.

Another aspect I consider is what fraction of genuine high-redshift drop-out galaxies are detected above my S/N cut, but which do not obey my colour criteria due to photometric scatter out of the colour-colour selection window. This fraction was simulated assuming a Gaussian distribution of errors using the S/N in each band. Finally, as I have imposed a strict $2\,\sigma$ non-detection criterion in the three optical bands (b, v & i') I correct for the 14.3 per cent possibility (5 per cent in each band) that a genuine Lyman break galaxy with zero intrinsic flux at these wavelengths will have a

noise spike in one or more spectral bands and thus be excluded from the sample.

3.3.4 Schechter parameter fits

Using the corrections described above, which depend on the limiting depths of the survey field (the completeness calculations were carried out identically in both the GOODS fields and the XDF), predicted surface densities are produced as a function of apparent magnitude. The Maximum Likelihood method described above is then used to find the best combination of M^*_{1600} and α to fit the observed surface densities, with errors derived from the counting statistics of the number of observed galaxies in each bin ($\Delta m = 0.5$), before obtaining the best fit normalisation for each model luminosity function to find ϕ^*.

As well as using the Maximum Likelihood method to determine what values of the Schechter parameters are most likely, it can also be used to find the associated confidence intervals (Figures 3.5 to 3.6). The confidence intervals can be calculated following Equation 3.3, where $\frac{1}{2}\Delta\chi^2$ is the change in χ^2 appropriate for the confidence level and number of free parameters:

$$\ln \mathcal{L} = \ln \mathcal{L}_{max} - \frac{1}{2}\Delta\chi^2. \tag{3.3}$$

Starting with a 3-dimensional Likelihood cube in M^*_{1600}, ϕ^* and α, I produce marginalised 2-dimensional contours in, for example, M^*_{1600} and ϕ^* by summing the e^{-p_i} values over α at every value of M^*_{1600} and ϕ^*. To marginalise further for 1-dimensional errors on M^*_{1600}, I can sum again at every value of ϕ^*. This process is identical to summing over the probabilities.

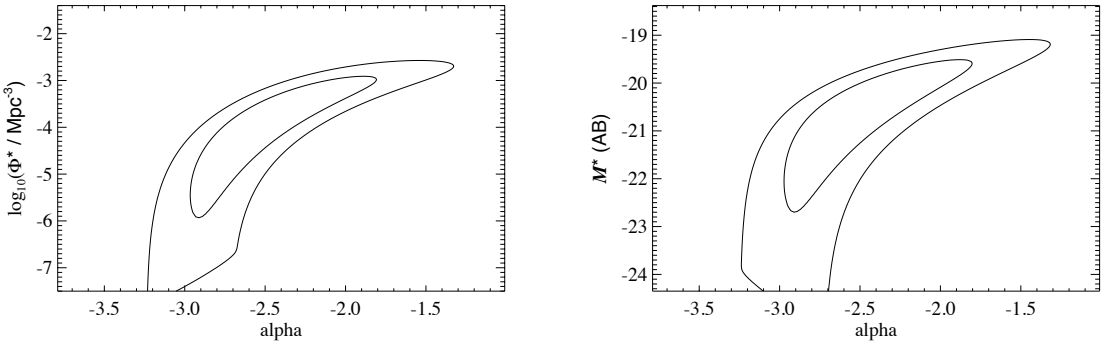

(a) ϕ^* and α, with M^*_{1600} marginalised.

(b) M^*_{1600} and α, with ϕ^* marginalised.

Figure 3.4: Marginalised likelihood contours for M^*_{1600}, ϕ^* and α at $z \approx 7$. This was obtained with a maximum likelihood fit between the model-predicted surface densities and the observed values shown by the diamonds in Figure 3.7(a). The contours are plotted at the 95 per cent and 68 per cent confidence levels.

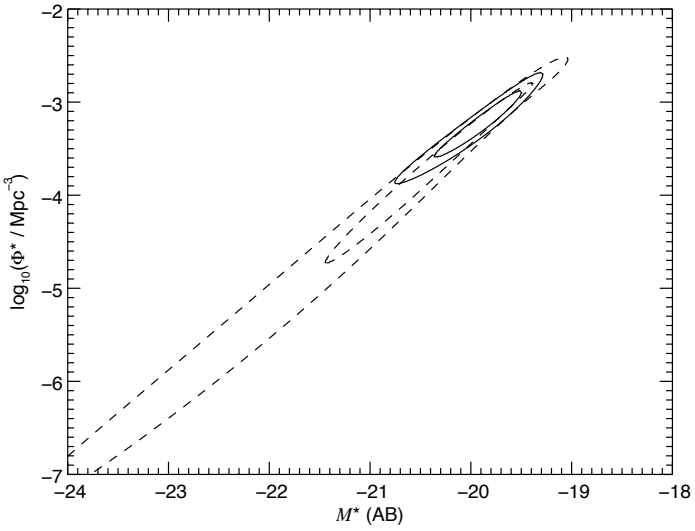

Figure 3.5: Likelihood contours for M^*_{1600} and ϕ^* marginalised over α at $z \approx 7$. The larger, dashed contours have been marginalised over the whole range of α, whereas the smaller, solid contours have been constrained to $\alpha = -2.06 \pm 0.13$ (Bouwens et al., 2015). These were obtained with a maximum likelihood fit between the model-predicted surface densities and the observed values shown by the diamonds in Figure 3.7(a). The contours are plotted at the 95 % and 68 % confidence levels.

Table 3.1: Best fit values for the Schechter parameters at $z \approx 7$ and $z \approx 8-9$.

	$z \approx 7$			$z \approx 8-9$		
Reference [Area/arcmin^2]*	α	M^*_{1600}	$\log_{10}(\phi^*/\mathrm{Mpc}^{-3})$	α	M^*_{1600}	$\log_{10}(\phi^*/\mathrm{Mpc}^{-3})$
This work [191]	-2.54 ± 0.36	-21.28 ± 1.28	-4.55 ± 1.2	–	–	–
constrained α	-2.06 ± 0.13	-20.01 ± 0.34	-3.32 ± 0.28	-2.02 ± 0.23	20.33 ± 0.53	-3.89 ± 0.51
Lorenzoni et al. (2013) [96]	-1.9 (fixed)	-20.14	-3.09	-1.9 (fixed)	-19.66	-3.22
Schenker et al. (2013) [78.7]	$-1.87^{+0.18}_{-0.17}$	$-20.14^{+0.36}_{-0.48}$	$-3.19^{+0.27}_{-0.24}$	$-1.94^{+0.21}_{-0.24}$	$-20.44^{+0.47}_{-0.35}$	$-3.50^{+0.35}_{-0.32}$
McLure et al. (2013) [476.2]	$-1.90^{+0.14}_{-0.15}$	$-19.90^{+0.23}_{-0.28}$	$-2.96^{+0.18}_{-0.23}$	$-2.02^{+0.22}_{-0.23}$	$-20.12^{+0.37}_{-0.48}$	$-3.35^{+0.28}_{-0.47}$
Oesch et al. (2012) [94.5]	–	–	–	$-2.06^{+0.35}_{-0.28}$	$-20.04^{+0.44}_{-0.48}$	$-3.30^{+0.38}_{-0.46}$
Bouwens et al. (2011) [53.3]	-2.01 ± 0.21	-20.14 ± 0.26	-3.07 ± 0.26	-1.91 ± 0.32	-20.10 ± 0.52	-3.23 ± 0.43
Bouwens et al. (2015) [730.9]	-2.06 ± 0.13	-20.87 ± 0.26	-3.54 ± 0.23	-2.02 ± 0.23	-20.63 ± 0.36	-3.68 ± 0.32
Bradley et al. (2012) [135]	–	–	–	$-1.98^{+0.23}_{-0.22}$	$-20.26^{+0.29}_{-0.34}$	$-3.37^{+0.26}_{-0.29}$
Finkelstein et al. (2015) [301.2]	$-2.03^{+0.21}_{-0.20}$	$-21.03^{+0.37}_{-0.50}$	$-3.80^{+0.29}_{-0.19}$	$-2.36^{+0.54}_{-0.40}$	$-20.89^{+0.74}_{-1.08}$	$-4.14^{+0.65}_{-1.01}$

* The areas quoted are the totals for all of the fields combined in each study, but the area available to searches for candidate $z \approx 7$ and $z \approx 8-9$ galaxies will be less than this due to the range of depths and filters available in each field.

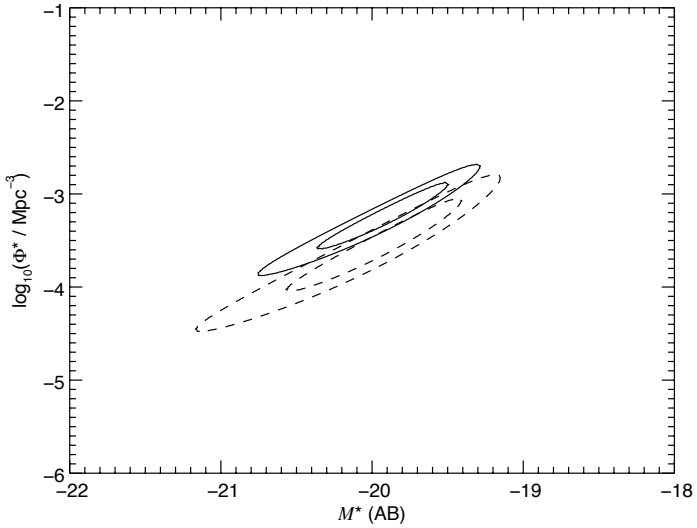

Figure 3.6: As for Figure 3.5, with likelihood contours for M^*_{1600} and ϕ^* at $z \approx 7$ (solid lines) and $z \approx 8-9$ (dashed lines), marginalised with a prior of $\alpha = -2.06 \pm 0.13$ for the z'-drops and $\alpha = -2.02 \pm 0.23$ for the Y-drops.

For the z'-drops, ϕ^*, M^*_{1600} and α were allowed to vary, creating a three-dimensional likelihood cube in intervals of $\Delta M^*_{1600} = 0.03$ between $-24.35 < M^*_{1600} < -18.38$, $\Delta \log_{10}(\phi^*/\mathrm{Mpc}^{-3}) = 0.025$ between $-7.5 < \log_{10}(\phi^*/\mathrm{Mpc}^{-3}) < -1.4$ (a range in ϕ^* from 3.2×10^{-8} Mpc^{-3} to 0.04 Mpc^{-3}) and $\Delta\alpha = 0.02$ between $-3.79 < \alpha < -1.01$.

As can be seen from Figure 3.4, with the limited data I am using I am unable to constrain α well. Because of this, a prior of $\alpha = -2.06 \pm 0.13$ found by Bouwens et al. (2015) (see Table 3.1) was applied so as to more strongly constrain M^*_{1600} and ϕ^*. To do this, a Gaussian prior was applied based around their 1σ limits on α and then marginalised over to both constrain the possible values of α and account for the uncertainty in their value. Figure 3.5 shows contours for both the full fit marginalised over all α (larger, dashed contours) and the constrained fit (smaller, solid contours), where both are plotted at the 68 per cent and 95 per cent, corresponding to a $\Delta\chi^2$ of 2.3 and 6.17 (1 and 2 σ equivalent confidence levels for 2 degrees of freedom). I quote both of these sets of values in Table 3.1. As the Schechter parameters are highly

correlated, the 1-dimensional errors quoted in Table 3.1 are very conservative, and so the error contours shown in Figures 3.4, 3.5 and 3.6 give a more accurate picture of the constraints.

Given the increased difficulty in fitting α for the Y-drops rather than the z'-drops due to the smaller number of candidates and the weaker constraints this gives, I similarly adopted a Gaussian prior of $\alpha = -2.02 \pm 0.23$ (Bouwens et al., 2015) and marginalised over the α range, with ϕ^* and M^*_{1600} varying over the same grid of values as the z'-drops. Figure 3.6 shows the 68 per cent and 95 per cent contours (at the same chi-squared levels as the z'-drops) for the constrained α. Figure 3.7 shows the surface densities predicted by the best-fit luminosity functions at both redshift ranges and the best-fit values are quoted in Table 3.1. This Table also shows a range of values in the literature.

It is instructive to compare my values with those of other groups, as well as to compare the two redshift ranges. At $z \approx 7$, my unconstrained fit of $\alpha = -2.39 \pm 0.34$ lies within $1 - 2\sigma$ of all of the literature values in Table 3.1, as can be seen from Figure 3.8(a), which shows my best-fit luminosity function along with two other determinations. The M^*_{1600} and ϕ^* values are more useful to look at, as the fact that I have shown the variance between these two fields to be Poisson-dominated makes them robust in the face of structural variation (cosmic variance), to which they are more sensitive than the faint end slope is. Both parameters agree well with previous results in Lorenzoni et al. (2013) as well as with the other literature values. The value of ϕ^* with a constrained α matches the Bouwens et al. (2015) value very well.

As described above, at $z \approx 8 - 9$ the range of allowed α was constrained in the same way as for the z'-drops around a value of $\alpha = -2.02 \pm 0.23$, also from Bouwens et al. (2015). My values for M^*_{1600} and ϕ^* broadly agree with others reported, but the uncertainties are too large to draw strong conclusions from them. It is interesting to note that unlike the z'-drops, the $z \approx 8 - 9$ best-fit for ϕ^* is not particularly close to

the value from Bouwens et al. (2015). There is very good consistency with Finkelstein et al. (2015) for M^*_{1600} and ϕ^* in both redshift ranges. The luminosity function does appear to continue declining from $z \approx 7$ to $z \approx 8-9$, with the most likely M^*_{1600} potentially fainter at higher redshift, though the values presented here are within 1σ of each other, in broad agreement with the evolution found in Bouwens et al. (2007, 2011, 2015). Slightly more convincing, however, is a potentially lower value of ϕ^* at higher redshift, as seen in McLure et al. (2013), Schenker et al. (2013) and Finkelstein et al. (2015), as my values at $z \approx 7$ and $z \approx 8.9$ are separated from each other by more than 1σ.

3.4 Conclusions

I have studied drop-out samples from the GOODS-North and GOODS-South fields of CANDELS. The candidate selection has been done using the colour-cuts from Lorenzoni et al. (2013) to ensure comparability, and so enable the direct comparison of the candidate lists. I have therefore been able to investigate the effect of cosmic variance on the two GOODS fields, as well as to derive the UV luminosity function parameters at $z \approx 7$ and $z \approx 8-9$. The observations indicate that the cosmic variance between the GOODS-North and -South fields is less than the Poisson noise, which is consistent with theoretical predictions (Moster et al., 2011; Muñoz et al., 2010; Somerville et al., 2004). Therefore, larger samples from deeper surveys will be needed to more effectively constrain the effect that cosmic variance has on the number counts of galaxies, as well as additional lines of sight to more accurately determine what that variance is.

The above conclusion has allowed me to use both the candidates from GOODS-North presented in Chapter 2 and those from GOODS-South in Lorenzoni et al. (2013) to constrain the bright end of the UV luminosity function, while using identically

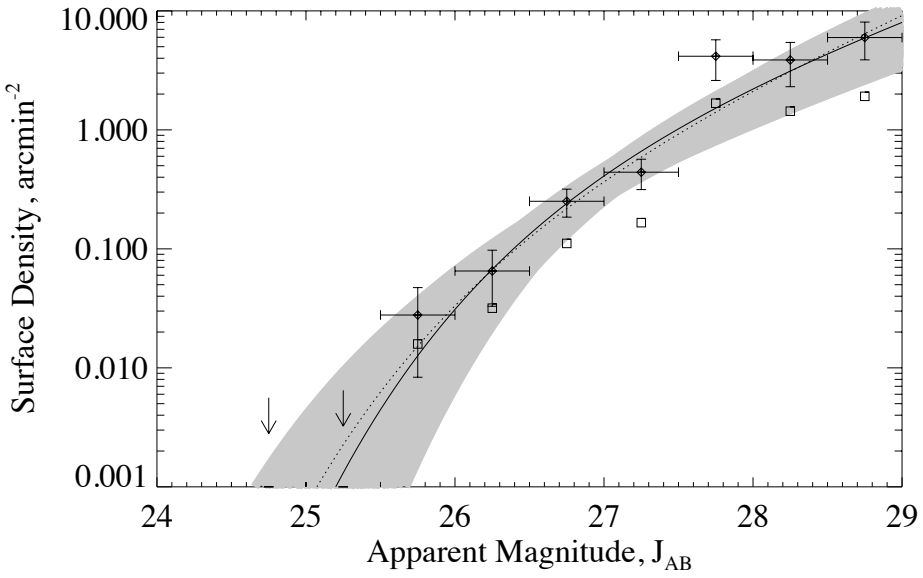

(a) $z \approx 7$

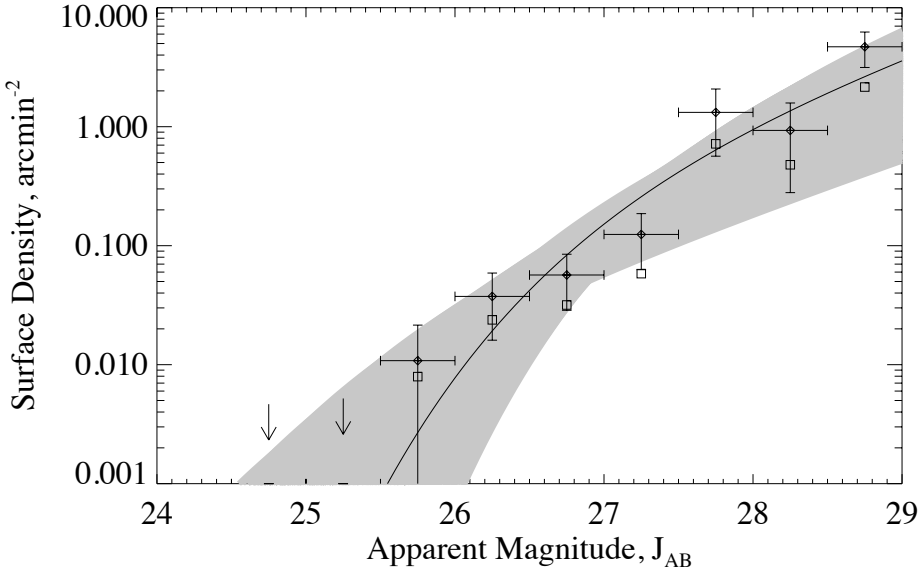

(b) $z \approx 8 - 9$

Figure 3.7: (a): Observed surface density of Lyman break galaxies with apparent J-band magnitude at $z \approx 7$. The diamonds are the completeness-corrected observed surface densities and the squares are the raw observed surface densities. The error bars are purely Poisson number statistics. The solid line is predicted by my best-fit luminosity function using a constraint that $\alpha = -2.06 \pm 0.13$, which gives best-fit parameters of $\log_{10}(\phi^*/\mathrm{Mpc}^{-3}) = -3.57$ and $M^*_{1600} = -20.05$. The dotted line is predicted when α is allowed to vary, giving best-fit parameters of $\alpha = -2.39$, $\log_{10}(\phi^*/\mathrm{Mpc}^{-3}) = -4.20$ and $M^*_{1600} = -20.65$. The light-grey area is the 1σ tolerance using a constrained α.

(b): As (a), but in apparent H-band magnitude at $z \approx 8{-}9$. The solid line uses $\alpha = -2.02 \pm 0.23$, giving best-fit parameters of $\log_{10}(\phi^*/\mathrm{Mpc}^{-3}) = -4.07$ and $M^*_{1600} = -20.33$.

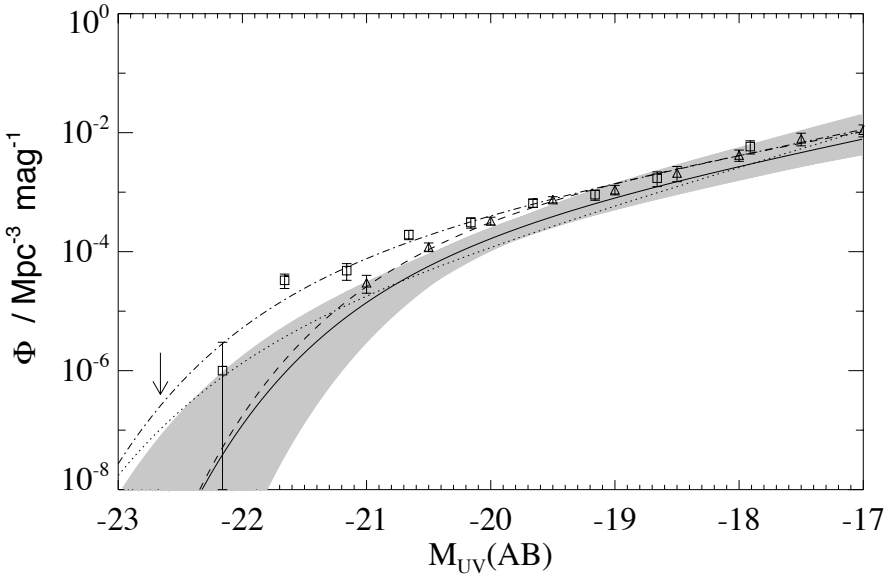

(a) $z \approx 7$

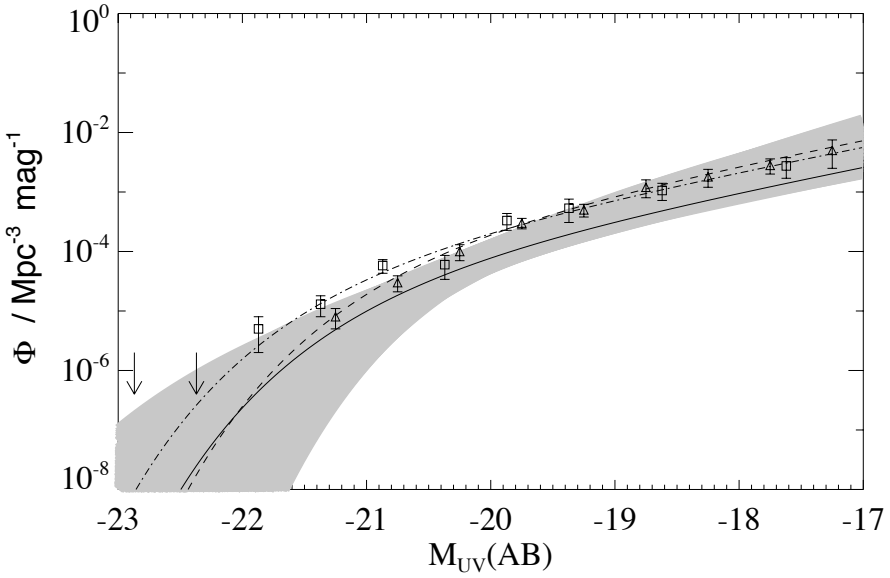

(b) $z \approx 8 - 9$

Figure 3.8: (a): The luminosity function at $z \approx 7$. The solid line is my best-fit luminosity function and the light-grey area is the 1σ confidence interval for a constrained α, and the dotted line is my best-fit luminosity function when α is allowed to vary. Also shown are data points from the stepwise maximum likelihood fits and resulting best-fit luminosity functions from McLure et al. (2013) and Bouwens et al. (2015). The triangle symbols and the dashed line are from McLure et al. (2013) and the square symbols and dot-dashed line are from Bouwens et al. (2015).

(b): As (a), but at $z \approx 8 - 9$. Only the best-fit luminosity function for a constrained α is shown, with the associated 1σ confidence interval.

selected candidates from the XDF (Lorenzoni et al., in prep) to somewhat constrain the faint end. This was done at both $z \approx 7$ and $z \approx 8-9$, finding Schechter parameters which agree with those determined by other groups. The $z \approx 8-9$ luminosity function is based on too few galaxies to be reliable, but is also broadly in agreement with other values determined for this redshift range, as well as the evolution in the UV luminosity function with redshift. I broadly see more of an evolution in ϕ^* than M^*_{1600}, possibly implying the formation of new galaxies is more dominant than the growth of individual galaxies.

The *HST* Frontier Fields campaign should shed more light onto the effects of cosmic variance by providing multiple sight lines with deep *HST* imaging. Ultimately the *James Webb Space Telescope* will better constrain the faint-end slope α by reaching to fainter fluxes, as well as identifying Lyman break galaxies out to much higher redshift to further explore the evolution of the UV luminosity function.

Chapter 4

Luminosity Functions in the VIDEO-CFHTLS-D1 Field

4.1 Introduction

The recent availability of surveys producing large samples of galaxies out to increasingly high redshifts has allowed for the build up of a statistical view of what the Universe looked like at different times in its history. We have been able to start discerning a picture of how galaxy populations have been changing out to $z \gtrsim 9$, covering the bulk of the age of the Universe. The more local Universe has been astonishingly well catalogued by surveys such as the Two Degree Field Galaxy Redshift survey, which contains $\sim 220,000$ spectroscopic galaxy redshifts out to a $z_{max} \sim 0.3$, the Sloan Digital Sky Survey, which provides $\sim 1,000,000$ galaxies with spectroscopic redshifts out to $z \lesssim 0.3$, and the Galaxy And Mass Assembly survey, which measured 230,000 spectroscopic redshifts over an area of 283 degree^2 out to $z \lesssim 0.9$, but the situation is not so clear past $z \sim 1$. This is a key stage in galaxy evolution; star formation rates and AGN activity both peak between $1 < z < 3$. The evolution of galaxies since this point is best described by passive evolution, with star formation

rates plummeting and galaxies dimming as they stop forming so many new stars, instead become increasingly dominated by older stellar populations (Caputi et al., 2006; Cirasuolo et al., 2007; Giallongo et al., 2005; Hopkins & Beacom, 2006; Lilly et al., 1995, 1996). Before this is another story; galaxies were building their stellar mass quickly, with increasing star formation rates. In order to better understand this crucial time in the history of our Universe, deep multi-wavelength large-area data sets are needed, providing large samples of galaxies for which we can measure redshifts, group and individual characteristics, allowing us to glean knowledge about the processes which govern galaxy evolution.

One of the ways to capture the characteristics of a galaxy population is to measure a luminosity function. By comparing the volume densities of galaxies at different luminosities, we can learn about the processes that determine the distribution of bright versus small galaxies, and those that cause it to differ from the underlying distribution of dark matter, namely AGN activity and star-formation. To understand these processes, a combination of the following is needed: a significant area to capture enough of the rare objects that make up the bright end of the luminosity function, enough depth to reach the faint end of the luminosity function, as well as a way of reliably determining redshifts. Realistically, it is much more feasible to obtain a large sample of photometric redshifts than spectroscopic redshifts, and so good data across multiple wavebands are necessary.

The VISTA Deep Extragalactic Observations Survey (VIDEO) does a very good job of addressing these requirements. In total, it covers an area of ~ 12 degree^2 in five near-IR filters (the VISTA telescope's $ZYJHK_s$) down to a 5σ depth of $K_s = 23.8$ (see Table 4.1 for the 5σ depths). The data are spread out over three of the most widely observed fields at high Galactic latitude, allowing for the combination of the VIDEO near-IR data with observations from the radio to X-rays. In particular, there is a 1 degree^2 overlap with one of the Canada-France-Hawaii Telescope Legacy

Survey (CFHTLS; Gwyn, 2012) Deep fields (CFHTLS-D1) and a 4.5 degree^2 with CFHTLS-Wide (CFHTLS-W1), which provide deep optical data that is invaluable for estimating photometric redshifts.

In this chapter I analyse catalogues produced from the 1 degree^2 VIDEO and CFHTLS-D1 overlap, VIDEO-CFHTLS-D1, aiming to present luminosity functions out to $z = 3$ and down to an absolute magnitude of $M_{K_s} \sim -20$ at $z = 1$. These can be used to constrain the influence of AGN activity and star-formation through the stage when they are most energetic and into the present day, casting some light on their effects on galaxy evolution.

The structure of this chapter is as follows: first, I describe the VIDEO survey and the creation of the catalogues in Section 4.2.1, and the method used to extract photometric redshifts in Section 4.2.2. Then I describe the method of measuring luminosity functions using the $1/V_{max}$ procedure, first by laying out the procedure itself in Section 4.3.1 before describing in depth my recipe in Section 4.3.2. I present K_s-band luminosity functions for the VIDEO-CFHTLS-D1 field in Section 4.4, fitting them with a variety of evolving Schechter functions in Section 4.4.1 before discussing these results in Section 4.5 and presenting my conclusions in Section 4.6.

4.2 Data

4.2.1 The VIDEO survey

The VIDEO survey covers three high Galactic latitude fields with some of the widest range of observations available. These are the ELAIS-S1 field, covered with two 1.5 degree^2 VISTA tiles, the XMM-Newton Large Scale Structure field (XMM-LSS), covered with three VISTA tiles, and the extended Chandra Deep Field South, covered with a further three VISTA tiles. This is a total of $\approx$ 12 degree^2 with $\approx$ 3 degree^2 in ELAIS-S1 and $\approx$ 4.5 degree^2 in the Chandra Deep Field South and $\approx$ 4.5

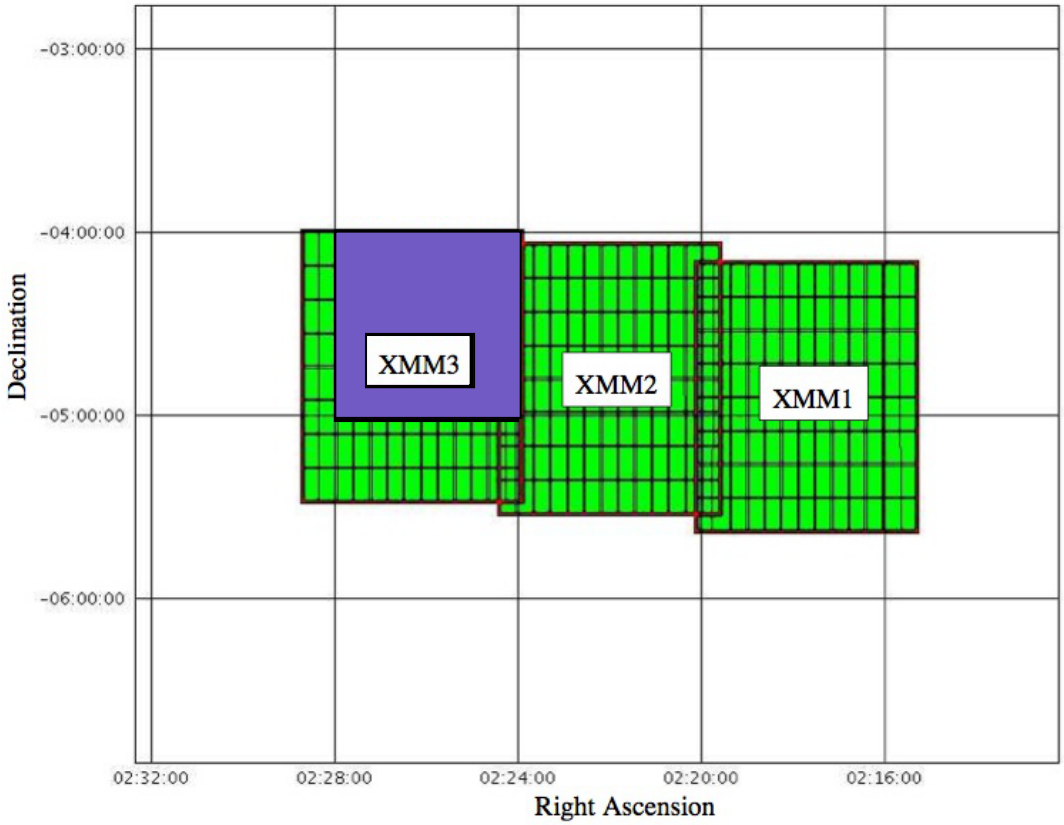

Figure 4.1: Diagram showing the layout of the VIDEO and CFHTLS fields. The green rectangles show the VIDEO data over the three XMM-LSS fields, and the purple square shows the CFHTLS-D1 data in XMM3. The CFHTLS-W1 data covers the whole of the area shown, and extends beyond for several degrees in each direction. Figure adapted from Jarvis et al. (2013).

degree^2 in XMM-LSS. The catalogues used here are from the XMM-LSS field, with VISTA providing near-infrared $ZYJHK_s$ photometry along with optical $ugriz$ coverage from CFHTLS combining to give very deep imaging (see Table 4.1, which shows the depths for the different bands) in 10 bands. 1 degree^2 of the XMM3 tile is covered by the CFHTLS-D1 field, while the whole of the XMM-LSS fields are covered by the CFHTLS-W1 field to shallower depth. The layout of these fields is shown in Figure 4.1, and the $ugriz$ and $ZYJHK_s$ filter curves are shown in Figure 4.2.

The data reduction and catalogue production for the VIDEO survey are fully

Table 4.1: Depths for the VIDEO and CFHTLS-D1/W1 data. The VIDEO depths are for a point source in a 2″ aperture, taken from Jarvis et al. (2013), and the CFHTLS depths are the 80% completeness limit for point sources (taken from the T0007 Technical Documentation http://www.cfht.hawaii.edu/Science/CFHTLS/T0007/CFHTLS_T0007-TechnicalDocumentation.pdf).

VIDEO		CFHTLS-D1		CFHTLS-W1
Filter	5σ depth	Filter	5σ depth	5σ depth
Z	25.66	u	26.3	25.2
Y	24.51	g	26.0	25.5
J	24.44	r	25.6	25.0
H	24.14	i	25.4	24.8
K	23.77	z	25.0	23.9

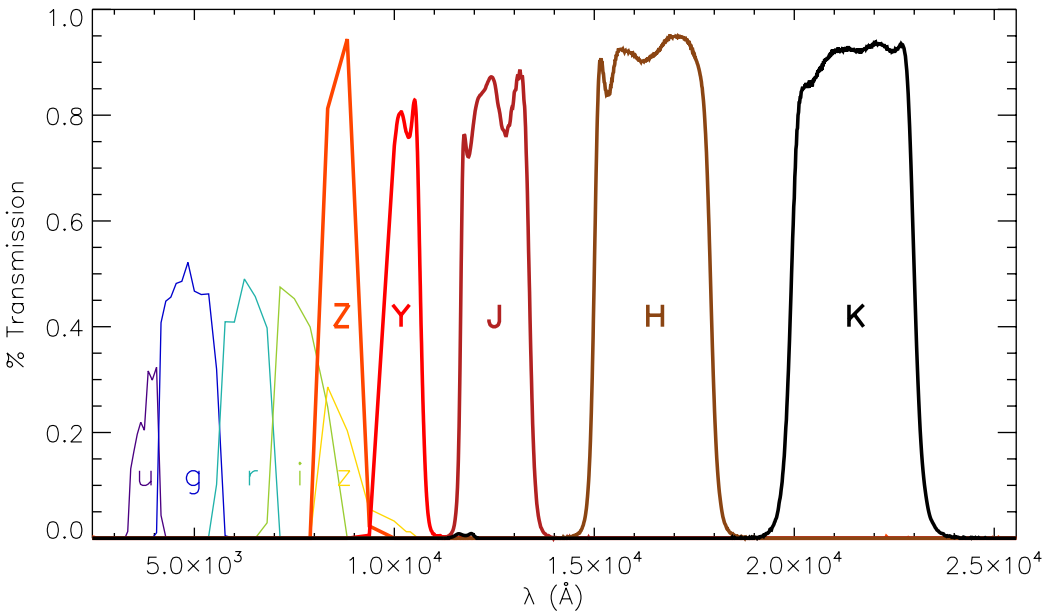

Figure 4.2: Transmission curves for the CFHTLS and VIDEO filters. The CFHTLS optical $ugriz$ filters are on the left-hand side in thin lines, while the VIDEO $ZYJHK_s$ filters are on the right in bold.

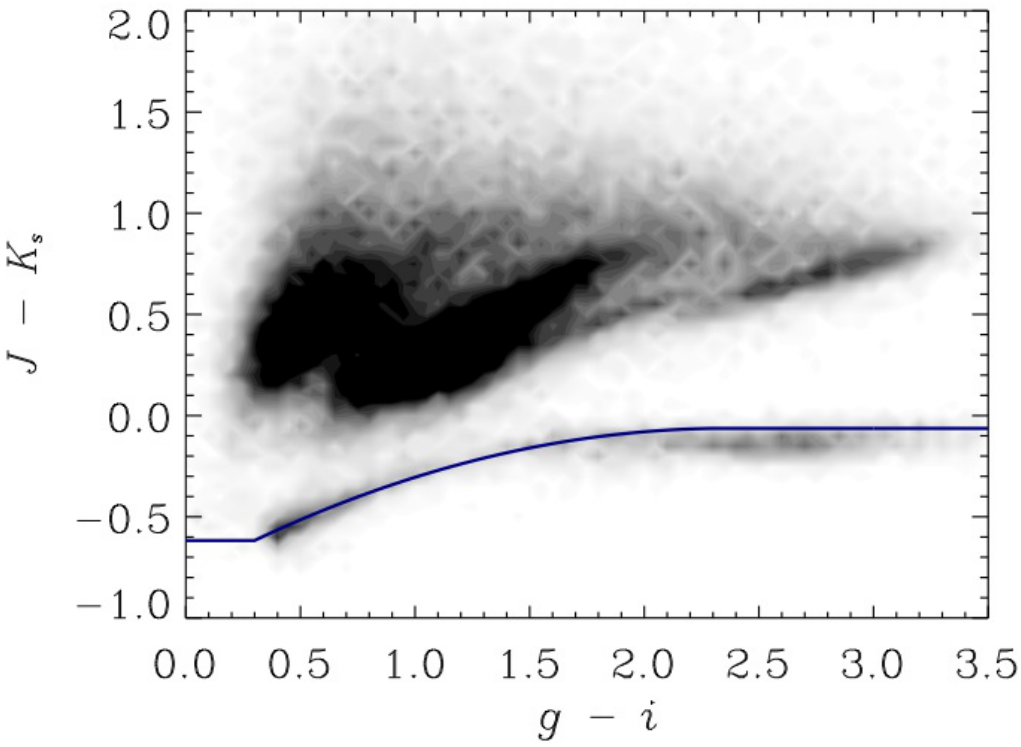

Figure 4.3: $g-i$ versus $J-K_s$ colour-colour diagram showing objects in the CFHTLS-D1 field with $K_s < 23.5$ in VIDEO. The stellar locus fit described in Equation 4.1 is shown with a sold blue line. (Figure from Jarvis et al., 2013.)

described in Jarvis et al. (2013). The final catalogue used for the VIDEO-CFHTLS-D1 field was produced using SExtractor (Bertin & Arnouts, 1996), and has 481,685 objects in total, all detected in at least one of the ten VIDEO or CFHTLS bands. Bright foreground objects were removed using a mask. Quasars have been removed with the help of table E1 from White et al. (2015), which lists the positions of the 74 Quasars in the VIDEO-CFHTLS-D1 tile. Stars were removed from the catalogue using the method described in Baldry et al. (2010), which is estimated to leave less than 5% stellar contamination (McAlpine et al., 2012). The $g-i$ and $J-K_s$ colours allow for clear separation between the stars and galaxies, as can be seen in Figure 4.3 (taken from Jarvis et al., 2013).

The stellar locus can be described with a quadratic function:

$$f_{locus}(x) = \begin{cases} -0.6127 & x \leqslant 0.3 \\ -0.79 + 0.615x - 0.13x^2 & 0.3 < x \leqslant 2.3 \\ -0.0632 & 2.3 < x, \end{cases} \tag{4.1}$$

and then sources with the following criterion are removed:

$$J - K_s < f_{locus}(g - i) + 0.1. \tag{4.2}$$

For the current work, only the objects detected in the K_s-band at $K_s < 23.5$ were used, with photometry measured in all other bands at the K_s detected positions, leaving a catalogue of 90,519 galaxies. The photometry was extracted in apertures with 1, 2, 3 and 4 arcsec diameters, as well as Kron fluxes (using SExtractor's MAG_AUTO). The photometric redshifts were produced using the 2 arcsec aperture fluxes (which have a higher signal-to-noise ratio), and Kron fluxes were used to calculate the absolute magnitudes used in the luminosity functions. The number counts are shown in Figure 4.4, also from Jarvis et al. (2013), along with those in several other fields for comparison.

4.2.2 Photometric Redshifts

The large number of bands and depth of the photometry in the VIDEO-CFHTLS-D1 data makes photometric redshift fitting a reliable method to produce reasonably accurate redshifts for a large number of objects, without the need to spectroscopically confirm them. This is crucial for deriving science from the survey, as this redshift information, along with extra information extracted at the same time such as object

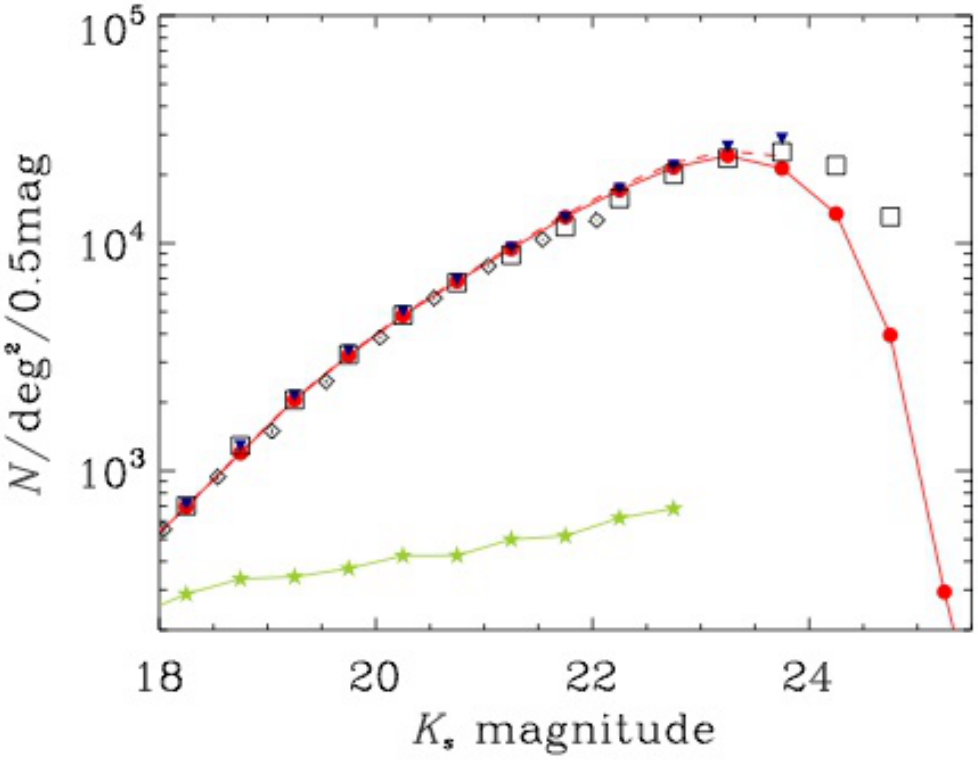

Figure 4.4: Total magnitude differential number counts for galaxies detected in the K_s-band in the VIDEO-CFHTLS-D1 field. Filled red circles and the solid red line show the number counts uncorrected for completeness and the red dashed line shows the completeness corrected source counts. The Poisson uncertainties are smaller than the symbol size. The stellar number counts, separated as discussed in Section 4.2.1 are shown as green stars. Also shown are the number counts from other studies in the filters available, these are; CFHT-WIRDS (inverted filled blue triangles; Bielby et al., 2011), the UKIDSS-DXS (black diamonds; Kim et al., 2011) and the UltraVISTA (open black squares; McCracken et al., 2012), showing excellent agreement. (Figure and caption from Jarvis et al., 2013.)

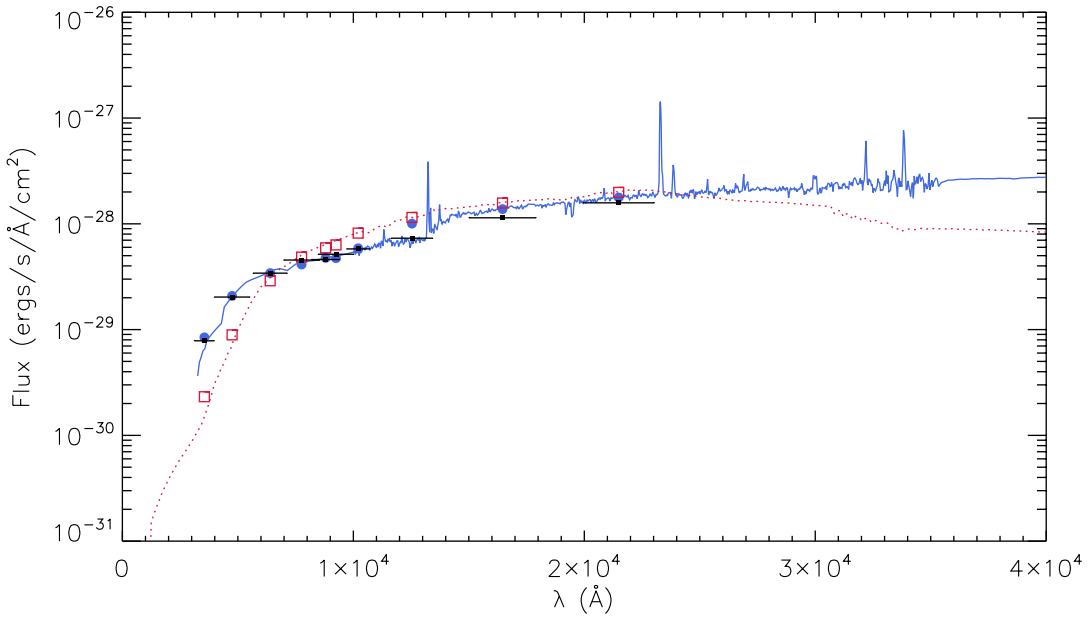

Figure 4.5: Comparison of two potential galaxy SED templates for a particular object in the VIDEO catalogue. The solid blue line, a Starburst galaxy at $z = 2.5$, is the best fit template to the object, whereas the red dotted line, an Elliptical galaxy at $z = 0.3$ is a much worse fit.

classification into stellar, quasar and galaxy, the galaxy type and the stellar mass, allows us to probe the physical processes with diagnostics such as luminosity functions, mass functions or galaxy clustering.

Photometric redshift fitting using templates generally works by making a χ^2 comparison between fluxes measured in photometric bands and a range of galaxy SED templates at different redshifts which have had dust attenuation applied to them, and have been scaled to account for different absolute magnitudes. Figure 4.5 shows photometry for one object compared to two potential SEDs. The blue line is the best fit SED, a Starburst galaxy at $z = 2.5$, while the red line shows the SED for an Elliptical galaxy at $z \approx 0.3$, which is a much worse match for the photometry. By comparing the goodness-of-fit for each template, the best combination of redshift, galaxy type, reddening and absolute brightness can be found.

The photometric redshifts used in this Chapter were calculated using

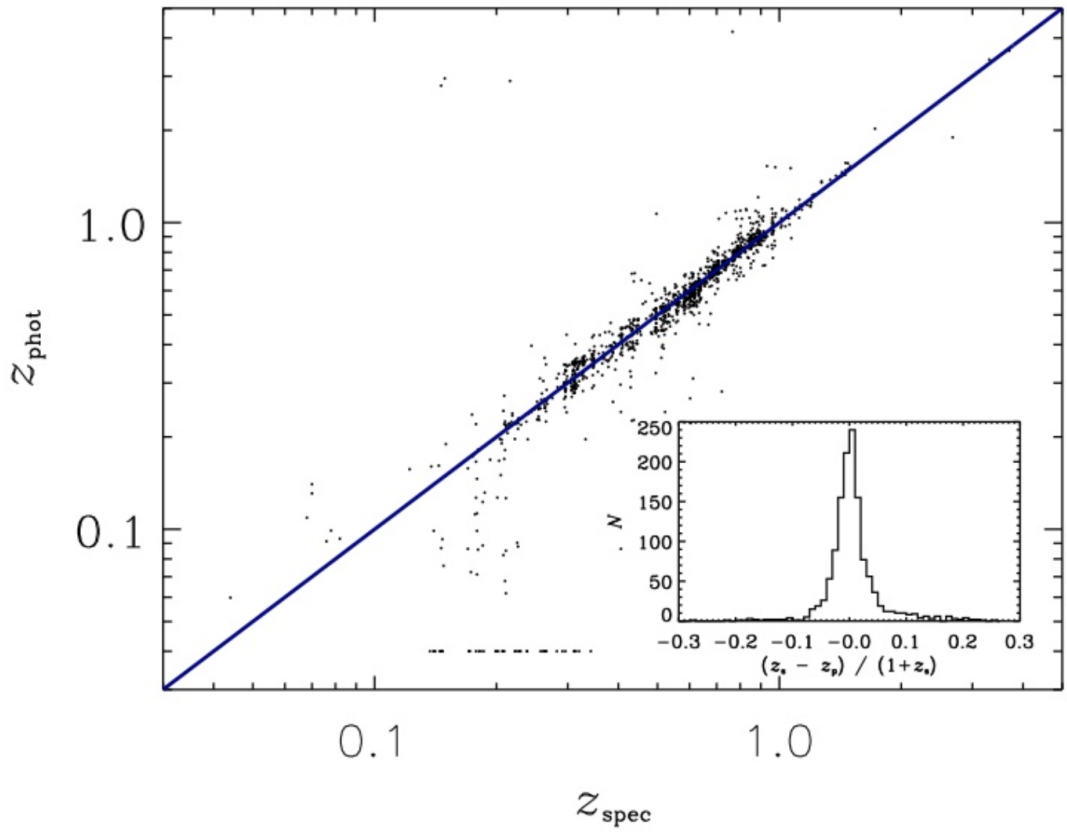

Figure 4.6: Photometric redshifts versus high-reliability spectroscopic redshifts from the VVDS spectroscopic survey (Le Fèvre et al., 2005) with photometric redshifts estimated without any luminosity function prior. The main panel shows a comparison with the photometric redshift determined using the combined CFHTLS and $ZYJHK_s$ VIDEO filters. The stripe of objects along the horizontal at z = 0.04 is due to the photometric redshifts fitting to their lowest allowed value. The inset shows the histogram of $\Delta z/(1+z)$. Figure from Jarvis et al. (2013).

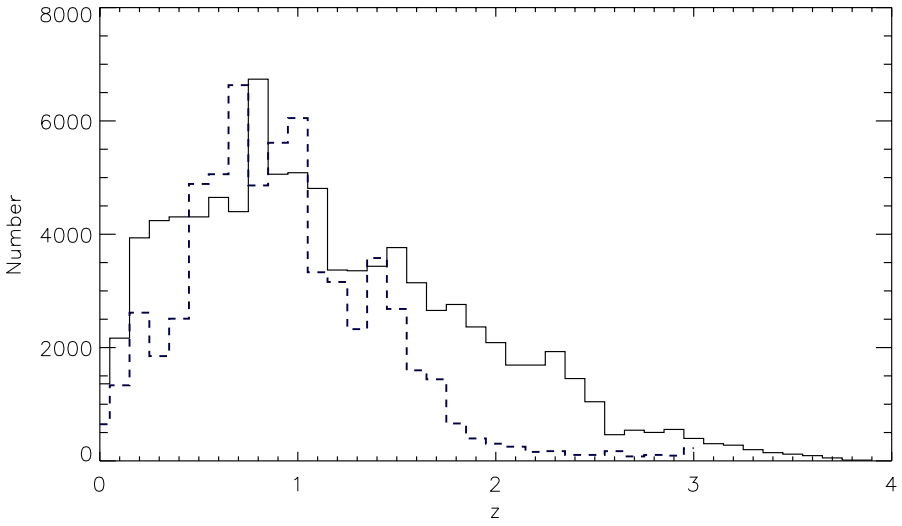

Figure 4.7: Redshift distribution of sources in the catalogue (black solid histogram), trimmed according to the criteria layed out in Section 4.2.1. The blue dotted line shows the redshift distribution of sources in the UDS sample used in Cirasuolo et al. (2010) scaled to the size of the VIDEO-CFHTLS-D1 catalogue. The UDS catalogue has 25,564 sources compared to 90,519 in the VIDEO-CFHTLS-D1 catalogue.

Le Phare (Arnouts et al., 1999; Ilbert et al., 2006), a freely available photometric redshift fitting code. The process is fully described in Jarvis et al. (2013), but I will summarise here. The SED templates were produced by Arnouts et al. (2007) and consist of 64 templates based on an interpolation of the observed spectra of an elliptical, an irregular and two spiral galaxies in Coleman et al. (1980) and two observed starburst templates from Kinney et al. (1996). The construction of these templates is described in Ilbert et al. (2006). The Scd and later types were modified by dust attenuation modelled with the interstellar extinction law measured in the Small Magellanic Cloud by Prevot et al. (1984), producing templates with reddening excess $E(B-V)$ of 0.0, 0.05, 0.1, 0.15, 0.2 and 0.3 mag. The effect of the intergalactic medium was also included using the prescription of Madau (1995). A sample of 3000 objects with spectroscopic redshifts from the Vimos VLT Deep Survey (VVDS; Le Fèvre et al., 2005) were also used to determine any offsets caused by possible bias in the template

set, as in Ilbert et al. (2006). Figure 4.6 shows a comparison of the final VIDEO photometric redshifts with the VVDS spectroscopic redshifts and Figure 4.7 shows the redshift distribution of the sources with redshift distribution of the UKIDSS Ultra Deep Survey (UDS) catalogue used in Cirasuolo et al. (2010) for comparison. There is a discrepancy in the number of sources at high redshift between the VIDEO and the UDS catalogue, with less sources at high redshift in the UDS than in VIDEO. This may simply be caused by the different photometric codes used (they use HYPERZ; Bolzonella et al. 2000), the difference in photometric bands between the two fields or the fact that they also consider sources that were selected in z'-band images, rather than just a K_s-selected catalogue.

4.3 Luminosity Functions

4.3.1 The $1/V_{max}$ Method

The $1/V_{max}$ method is the classic non-parametric way of estimating the LF of a sample, first proposed by Rowan-Robinson & McCrea (1968) and Schmidt (1968). It relies on calculating the maximum possible volume, $V_{max,i}$ within which a given galaxy with absolute magnitude M_i could be detected, and using this as a weighting to give the number density of galaxies in a magnitude bin. The $1/V_{max,i}$ are summed over the N galaxies in a particular absolute magnitude bin of width ΔM according to Equation 4.3:

$$\phi(M) = \frac{1}{\Delta M} \sum_{i=1}^{N} \frac{1}{V_{max,i}}. \tag{4.3}$$

This accounts for the Malmquist bias, whereby we are biased to observe an intrinsically brighter population at higher redshift while observing fainter objects nearby

where the volumes are smaller, and produces an unbiased estimate of the number density.

The error on $\phi(M)$ is given by

$$\sigma_{\phi(M)} = \frac{1}{\Delta M}\sqrt{\sum_{i=1}^{N}\left(\frac{1}{V_{max,i}}\right)^2}. \tag{4.4}$$

The $V_{max,i}$ for each galaxy is found by first calculating the apparent magnitude track with redshift for a galaxy with absolute magnitude M_i and a given SED and finding the redshift where it drops below the detection limit of the survey, $z_{max,i}$. This is dependent on both the actual redshift of the galaxy, which allows the calculation of the absolute magnitude, and the SED of the galaxy, as for each different redshift the observed frame K_s-band would access a different part of the rest-frame SED. For a LF in a particular redshift bin, $z_{max,i}$ must be corrected for the fact that a galaxy could not be found outside of its own redshift bin. This is done by limiting $z_{max,i}$ to within the top edge of the bin.

Using $z_{max,i}$, it is possible to calculate the maximum possible volume, $V_{max,i}$, in which this galaxy might be found by using Equation 4.5, where A is the area of the survey in degree^2, $z_{min,i}$ is the lower edge of the redshift bin and $D_C(z)$ is the comoving distance defined in Equation 1.8. This formula can be found by integrating Equation 1.10,

$$V_{max,i} = \frac{A}{3}\left(\frac{\pi}{180}\right)^2\left(D_C(z_{max,i})^3 - D_C(z_{min,i})^3\right). \tag{4.5}$$

This method has its advantages and drawbacks. Having a non-parametric way to estimate a LF is very useful as it makes no assumptions about the shape of the underlying distribution. However, as it gives an average density of sources within a

redshift slice, it is biased in surveys with strong large-scale clustering. It can also lead to a biased shape if there is significant evolution within a redshift slice, boosting the numbers of faint objects and suppressing the numbers of bright ones (an increase in $\log \phi^*$ of 0.3 over a redshift slice of $\Delta z = 0.5$ causes an increase in $\log \phi$ of ~ 0.1 at the faint-end and a decrease of $\lesssim 0.1$ at the bright end).

4.3.2 Measuring the VIDEO-CFHTLS-D1 LF

Using the method described above along with the best-fit redshift and the best-fit SED for each galaxy output from LePhare, I determine the LF for the VIDEO-CFHTLS-D1 field in 10 redshift bins between $0.2 < z < 3.0$, shown in Figure 4.9. I do not analyse objects with redshifts of $z < 0.2$ as the photometric fits are tailored to higher redshifts than this and so will be less reliable.

First, I redshift each galaxy's SED through $0 < z < 9$ in steps of $\Delta z = 0.04$, convolving with the K_s filter curve to evaluate the integrated flux, adding in the effects of band-stretching with redshift and distance dimming to find the apparent magnitude that would be measured in the VIDEO survey at each redshift step. The apparent magnitude track is compared with the K_s-band limit of 23.5, thus measuring z_{max}. Example magnitude tracks are shown in Figure 4.8; the $z_{max,i}$ cut-off (vertical lines) can be seen when a detectable object (black line) crosses $K_s = 23.5$ (horizontal line) and becomes undetectable (grey line).

I limit each $z_{max,i}$ to make sure that it is not higher than the upper bound of the redshift bin, before calculating the volume of the shell from the lower bound of the redshift bin out to $z_{max,i}$, $V_{max,i}$ for each galaxy. I also calculate the absolute magnitude M_i of each galaxy by applying the K_s filter to the rest-frame SED with no dimming. This absolute magnitude is aperture corrected using the difference between the aperture fluxes (used by LePhare) and Kron fluxes.

I use magnitude bins of $\Delta M = 0.5$, and sum the $1/V_{max,i}$ in each magnitude bin to

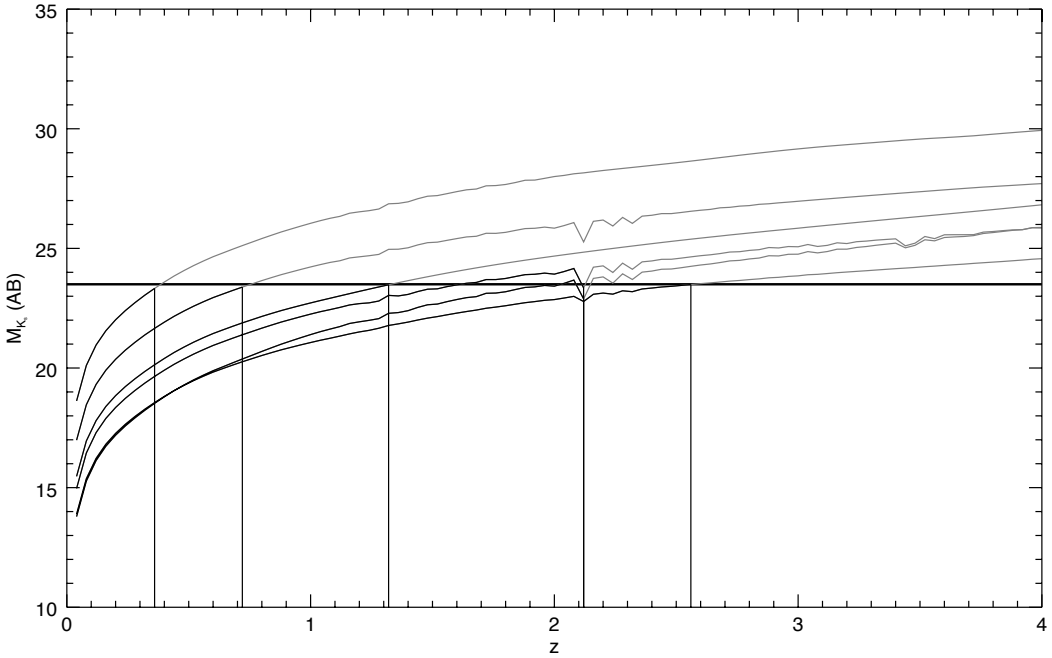

Figure 4.8: Magnitude tracks in redshifts for a subset of the catalogue, showing the apparent K_s band magnitude for each object evaluated as it is shifted through the redshift range. The $K_s < 23.5$ cut is shown, with black lines brighter (detectable) and grey lines fainter (undetectable). The thick, horizontal black line shows the $K_s < 23.5$ magnitude cut-off, and the vertical lines pick out the maximum possible redshift for each object.

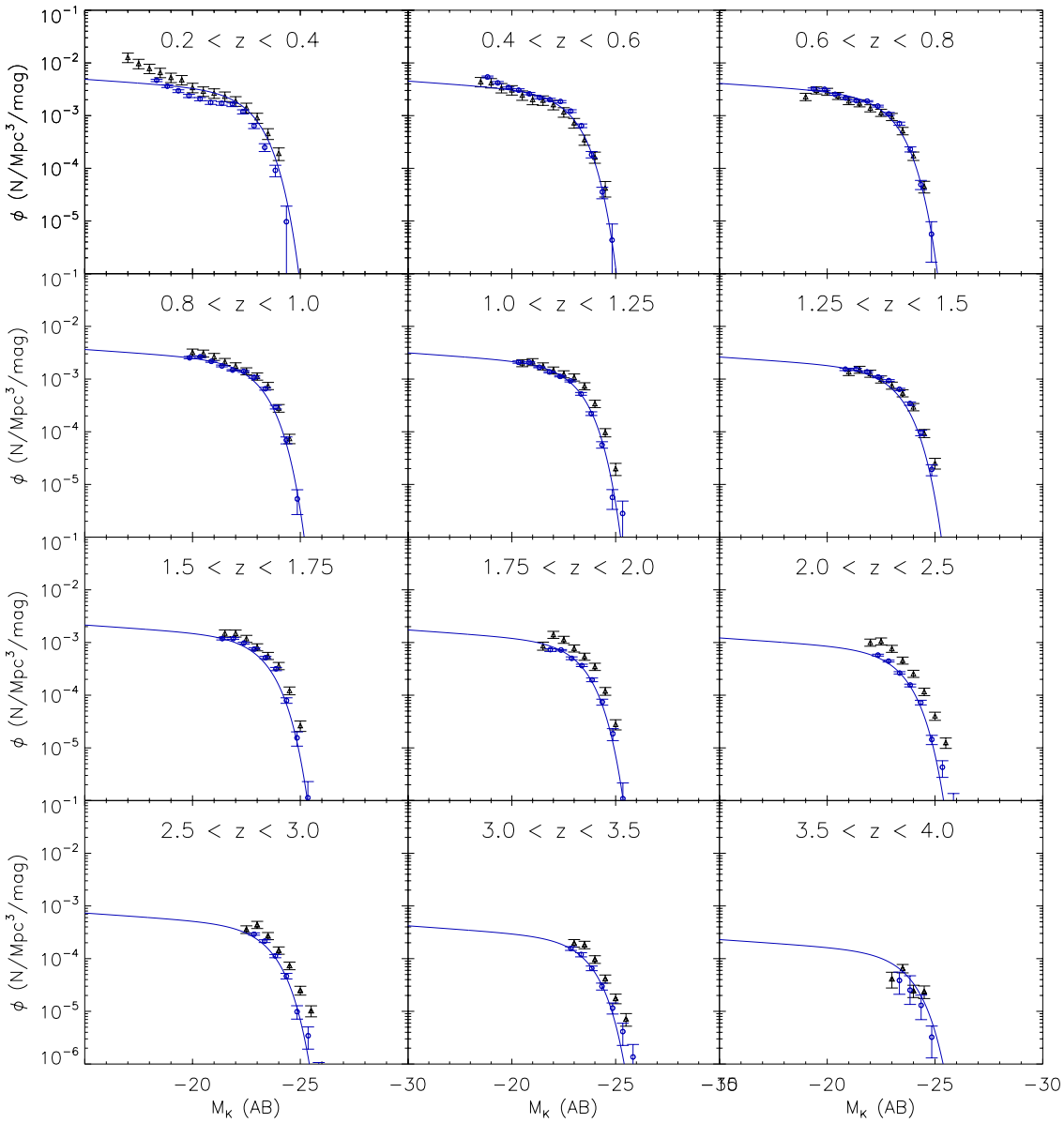

Figure 4.9: $1/V_{max}$ **LF in the VIDEO-CFHTLS-D1 field. The black triangles represent the** $1/V_{max}$ **LF from the VIDEO-CFHTLS-D1 catalogue presented here. The blue open circles and the solid blue line are the** $1/V_{max}$ **LF and the best-fit evolving Schechter function obtained by maximum likelihood analysis from the UKIDSS Ultra Deep Survey from Cirasuolo et al. (2010).**

produce LFs for each redshift bin. The final errors are a combination of the statistical error in Equation 4.4 and the error due to cosmic variance taken from Johnston et al. (2015) figure 7, who calculate the effects of cosmic variance in the same 1 degree^2 of the VIDEO survey using the publicly available `GETCV` code from Moster et al. (2011). There is a slight downturn visible in the faintest bin of some of the redshift slices; this is an artefact of the binning process, and not a real trend.

As well as the VIDEO-CFHTLS-D1 LF shown in Figure 4.9, I also show a LF determination using the UKIDSS Ultra Deep Survey (UDS) from Cirasuolo et al. (2010). The data used in Cirasuolo et al. (2010) is over a smaller area (0.7 degree^2) and shallower depth ($K_s = 23.1$) compared to the VIDEO-CFHTLS-D1 field. The $1/V_{max}$ points compare well between VIDEO and the UDS, mostly agreeing to within $1-2\sigma$. The uncertainties on the UDS points do not take into account cosmic variance, so will be underestimated. There is a higher density in the VIDEO-CFHTLS-D1 field compared to the UDS at around $z \approx 2$, and as can be seen from Figure 4.7 the UDS is under dense compared to the VIDEO-CFHTLS-D1 field at these redshifts. In the lowest redshift bin the start of the upturn at faint magnitudes that is visible in the UDS is also seen to extend down to $M_K = -17$ in the VIDEO-CFHTLS-D1 field.

4.4 Fitted Schechter Functions in the VIDEO-CFHTLS-D1 Field with CFHTLS-Deep

Fitting a parametric form of the LF can provide useful information about how the underlying distribution has evolved over the course of time, both by examining how the parameters describing one equation change and by looking for evidence of different forms at different redshifts. I use the Schechter parameterisation, described by the characteristic brightness of a galaxy population, the volume density at that characteristic density and a faint-end slope governing the number of fainter galaxies.

Tracing the evolution of these parameters is very useful, as they can show how the processes shaping galaxies have changed.

Given the observed upturn in the LF at low luminosity, I fit a double Schechter parameterisation to the LF determined using the $1/V_{max}$ method in Section 4.3.1. This is given by

$$\begin{aligned}\phi(M) = 0.4\ln(10)\phi_1^* 10^{-0.4(M-M_1^*)(\alpha+1)} \exp\left(-10^{-0.4(M-M_1^*)}\right) \\ +0.4\ln(10)\phi_2^* 10^{-0.4(M-M_2^*)(\beta+1)} \exp\left(-10^{-0.4(M-M_2^*)}\right). \end{aligned} \tag{4.6}$$

A comparison between a single and a double Schechter parameterisation fitted in the lowest redshift slice is shown in Figure 4.10. While the steep faint-end slope of the single Schechter function describes the faint upturn well, it is not able to also describe the knee of the Schechter function simultaneously, leading to the choice of a double Schechter parameterisation. This comparison shows only the lowest redshift slice which has the most pronounced upturn; the other redshift slices are much closer to a single Schechter function than this.

I allow ϕ_1^* and M_1^*, the characteristic volume density and the absolute magnitude of the knee in the brighter Schechter function, to evolve separately with redshift using

$$\phi_1^*(z) = \phi_{1_c}^* \left(\frac{1+z}{1+z_c}\right)^{k_{\phi 1,2}} \tag{4.7}$$

$$M_1^*(z) = M_{1_c}^* + 2.5k_{M1,2}\log_{10}\left(\frac{1+z}{1+z_c}\right), \tag{4.8}$$

i.e. with pure luminosity or pure density evolution, or luminosity dependent density evolution. The parameters k_ϕ and k_M set the strength of the evolution for ϕ_1^* and M_1^* respectively. These are fit separately above and below z_c to allow for different behaviour across different redshift ranges, with the change in evolution occurring at

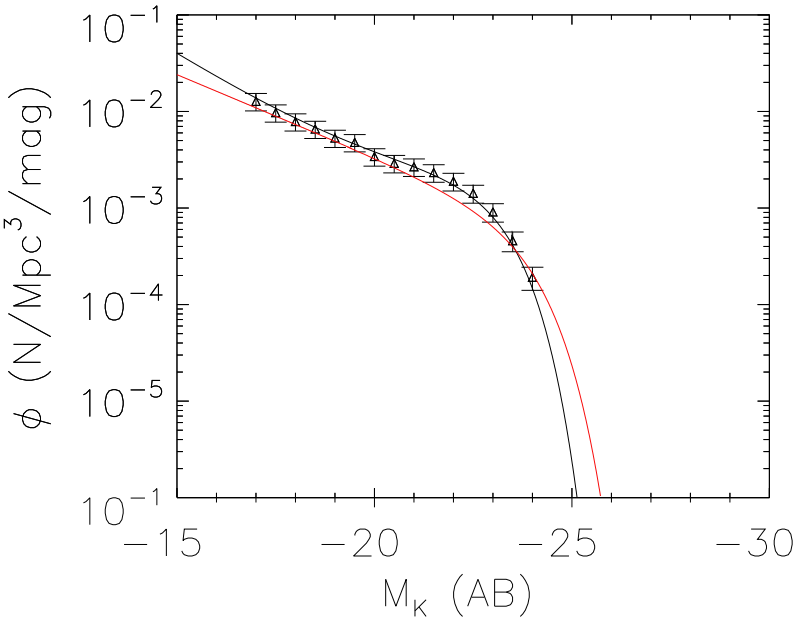

Figure 4.10: The comparison between the use of a single (red) or a double (black) Schechter function to parameterise the lowest redshift VIDEO-CFHTLS-D1 LF.

z_c (also where $\phi_1^* = \phi_{1_c}^*$ and $M_1^* = M_{1_c}^*$), i.e.,

$$k_\phi(k_M) = \begin{cases} k_{\phi 1}(k_{M1}) & z < z_c \\ k_{\phi 2}(k_{M2}) & z_c < z, \end{cases} \tag{4.9}$$

so that z_c is the redshift at which the evolutionary behaviour switches from one regime to the other. I do not evolve either α, the faint-end slope, or the fainter of the two Schechter functions as there is not enough information out to high enough redshift at the faint end of the luminosity function to reliably constrain any evolution.

I also allow ϕ_1^* and M_1^* to evolve using the parametric form described in Cirasuolo et al. (2010). It is important to note that they use a single Schechter function, instead of the double Schechter function used here. Their evolution is described in equations 4.10 and 4.11 from equations 2 and 3 of Cirasuolo et al. (2010):

$$\phi_1^*(z) = \phi_{z=0}^* \times \exp\left[-\left(\frac{z}{z_\phi}\right)\right]^{k_\phi} \tag{4.10}$$

$$M^*(z) = M_{z=0}^* - \left(\frac{z}{z_M}\right)^{k_M}. \tag{4.11}$$

The Schechter functions were fit using Metropolis-Hastings Markhov-Chain Monte Carlo (MCMC). This involves using a number of walkers to explore the parameter space for the models. The walkers are initialised in different positions in the parameter space, chosen by producing a Gaussian cluster of walkers around several starting positions chosen by trial and error. For each walker, the χ^2 value at the initial position is evaluated and the position recorded before moving a distance drawn from another Gaussian distribution characterised by a tuned step-size. The χ^2 value at this new position is compared to the old position, and if the ratio of new to old is higher than 1, or than a random number drawn uniformly from between 0 and 1, then the walker moves to the new position and records the step, before the process repeats. Step by step, this builds up a chain of χ^2 and explores the parameter space, preferentially spending time in areas with lower χ^2 values and eventually converging to oscillate around the best-fit value. Using multiple walkers makes the process less sensitive to starting position, while using long chains makes it more likely that each walker will have converged. As well as finding the best-fit values of the parameters, the propensity for walkers to spend more time in areas of lower χ^2 leads to an estimate of the posterior probability distribution function (PDF).

4.4.1 Results

Here I present the best-fit solutions for the evolving Schechter functions. In order to better separate out the different effects of luminosity and density evolution, Schechter functions with pure luminosity evolution, pure density evolution and luminosity de-

pendent density evolution are all presented. MCMC samples the posterior PDF of a parameterisation in line with a maximum likelihood approach, but I quote reduced χ^2 values when discussing the goodness of fit for the different Schechter functions as it is a useful diagnostic. All best-fits discussed are global solutions, and both the fit with the lowest χ^2 value (referred to as best fit) and the fit with the median likelihood (referred to as median) are presented and discussed.

Figure 4.11 shows the median and best-fit pure luminosity evolution, and Figure 4.12 shows the associated posterior PDF for all parameters, with 95 and 68 per cent confidence contours plotted. The median parameters are listed in the first column of Table 4.2 along with the best reduced χ^2 sampled. While this evolutionary form fits the bright end of the LF reasonably well across all redshifts, it struggles to fit the knee and/or the faint-end of the LF in most cases; as such the fainter, second Schechter function compensates and becomes more important and ϕ_2^* has a higher value due to this. Interestingly, a single evolutionary term seems sufficient; k_{m1} and k_{m2} are within 1σ of each other, and z_c is at the very upper end of the redshift range, meaning that the luminosity evolution is almost entirely described by k_{m1}. The evolution is also very gentle, producing a dimming of only 0.3 mag from $z = 3$ to $z = 0.5$. The obvious discrepancies at the faint end of the LF as well as the high reduced χ^2 make this evolution difficult to believe, although it does look more promising in the higher redshift bins.

Figure 4.13 shows the median and best-fit Schechter functions with pure density evolution and Figure 4.14 shows the associated plots of the posterior PDF, and the median parameters are listed in the second column of Table 4.2, along with the best reduced χ^2 sampled. Overall, the reduced χ^2 is lower than pure luminosity evolution, but conversely, it struggles to fit the bright-end of the LF which is less strongly effected by density evolution than the faint end. This does show a clear two part evolution, with k_ϕ changing from $k_{\phi 1} = -1.01$ below $z_c = 1.71$ to $k_{\phi 2} = -2.02$ above it. k_ϕ has

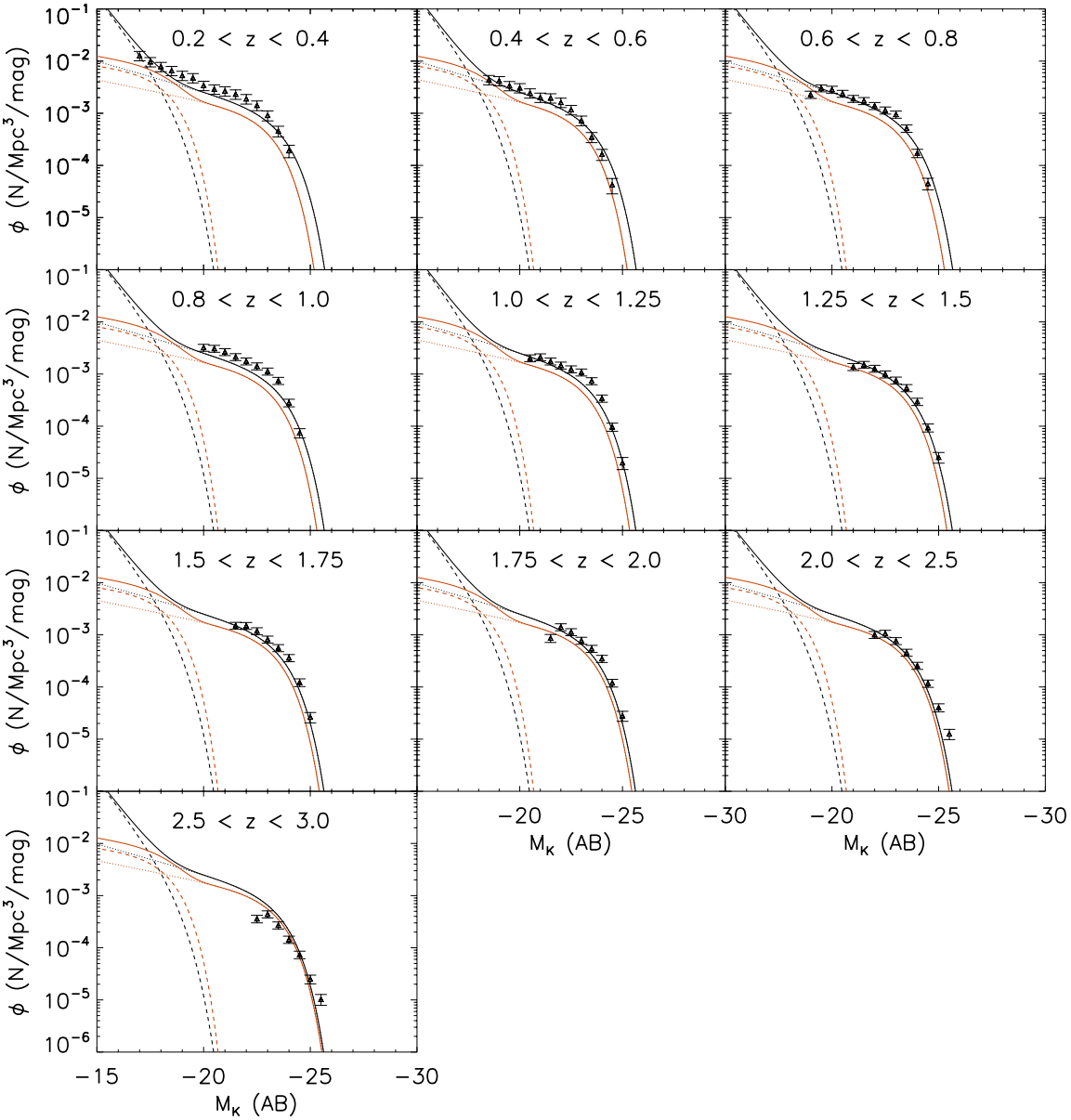

Figure 4.11: Median and best-fit double Schechter functions between $0.2 < z < 3$ in VIDEO-CFHTLS-D1 with pure luminosity dependent evolution. The fit parameters are listed in the first column of Table 4.2. Black triangles are the VIDEO-CFHTLS-D1 $1/V_{max}$ points, the solid lines are the double Schechter functions and the dotted and dashed lines show the bright and faint parts of the double Schechter function respectively. The best-fit is shown in black and the median in red.

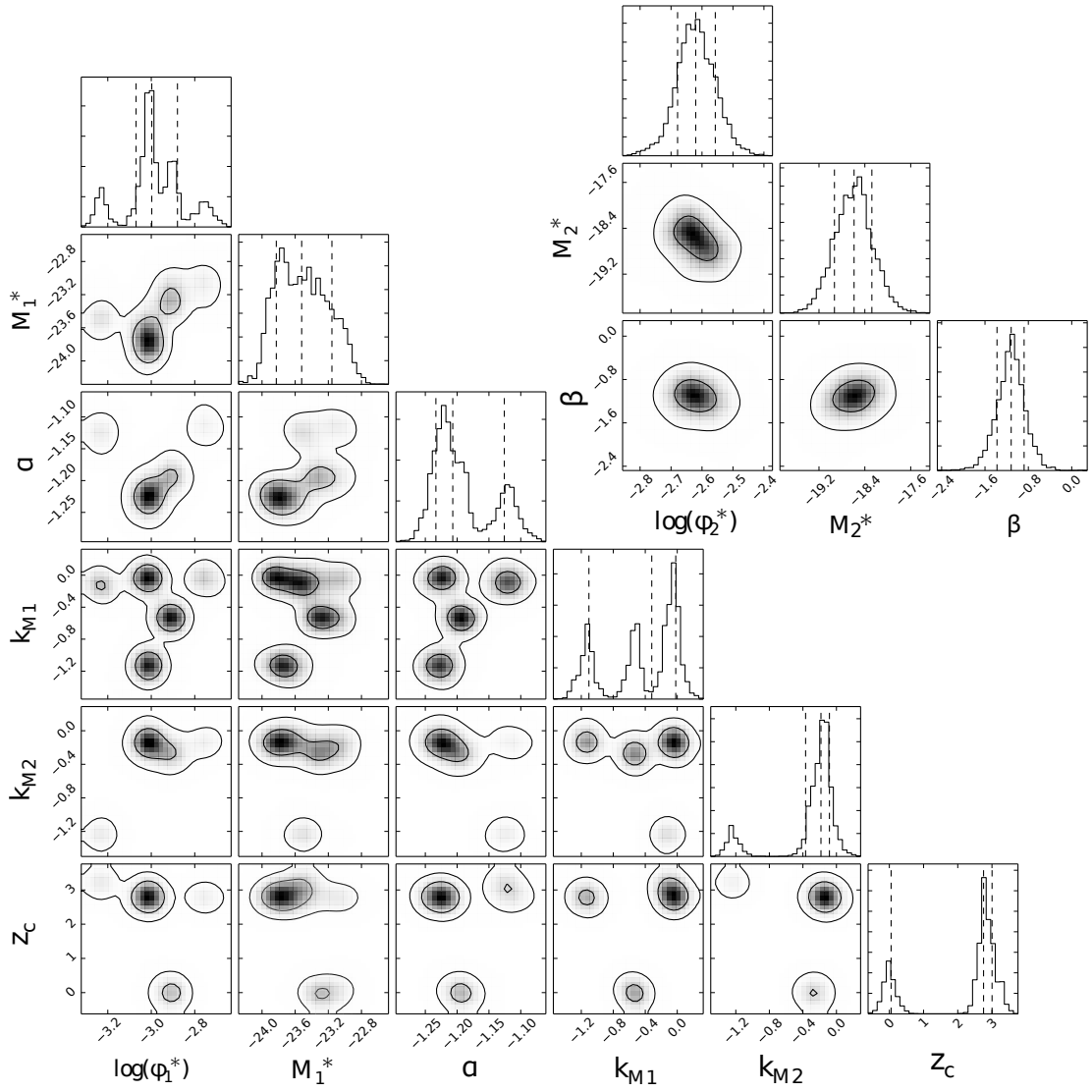

Figure 4.12: Estimation of the posterior PDF for a double Schechter function with pure luminosity dependent evolution. The 2-D plots show the marginalised PDF for each two parameters with contours plotted at the 95 and 68 per cent confidence levels, while the 1-D histograms show the marginalised PDF for each parameter individually, with dotted lines showing the 16th, 50th and 84th percentiles.

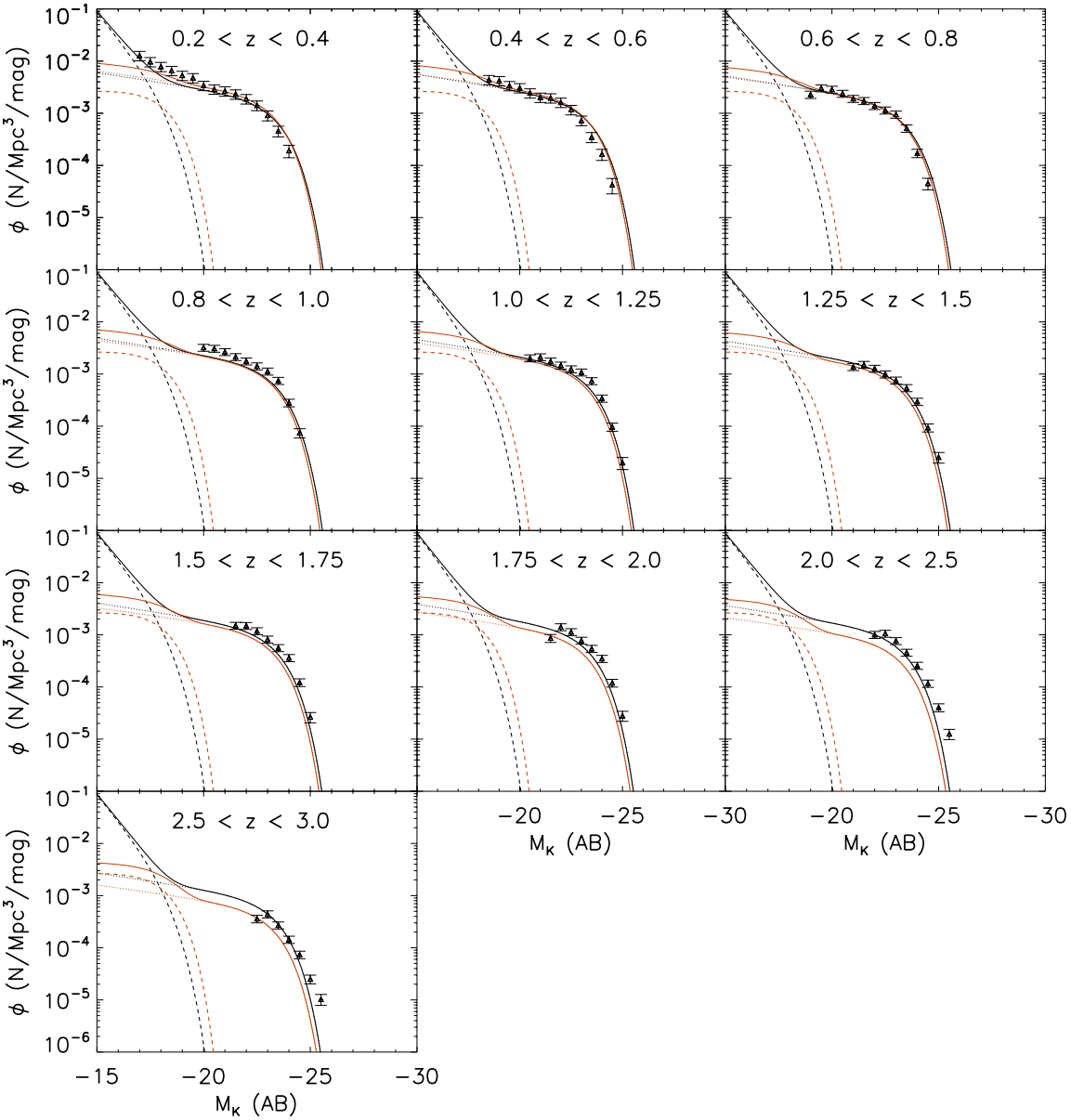

Figure 4.13: Median and best-fit double Schechter functions between $0.2 < z < 3$ in VIDEO-CFHTLS-D1 with pure density dependent evolution. The fit parameters are listed in the middle column of Table 4.2. Black triangles are the VIDEO-CFHTLS-D1 $1/V_{max}$ points, the solid lines are the double Schechter functions and the dotted and dashed lines show the bright and faint parts of the double Schechter function respectively. The best-fit is shown in black and the median in red.

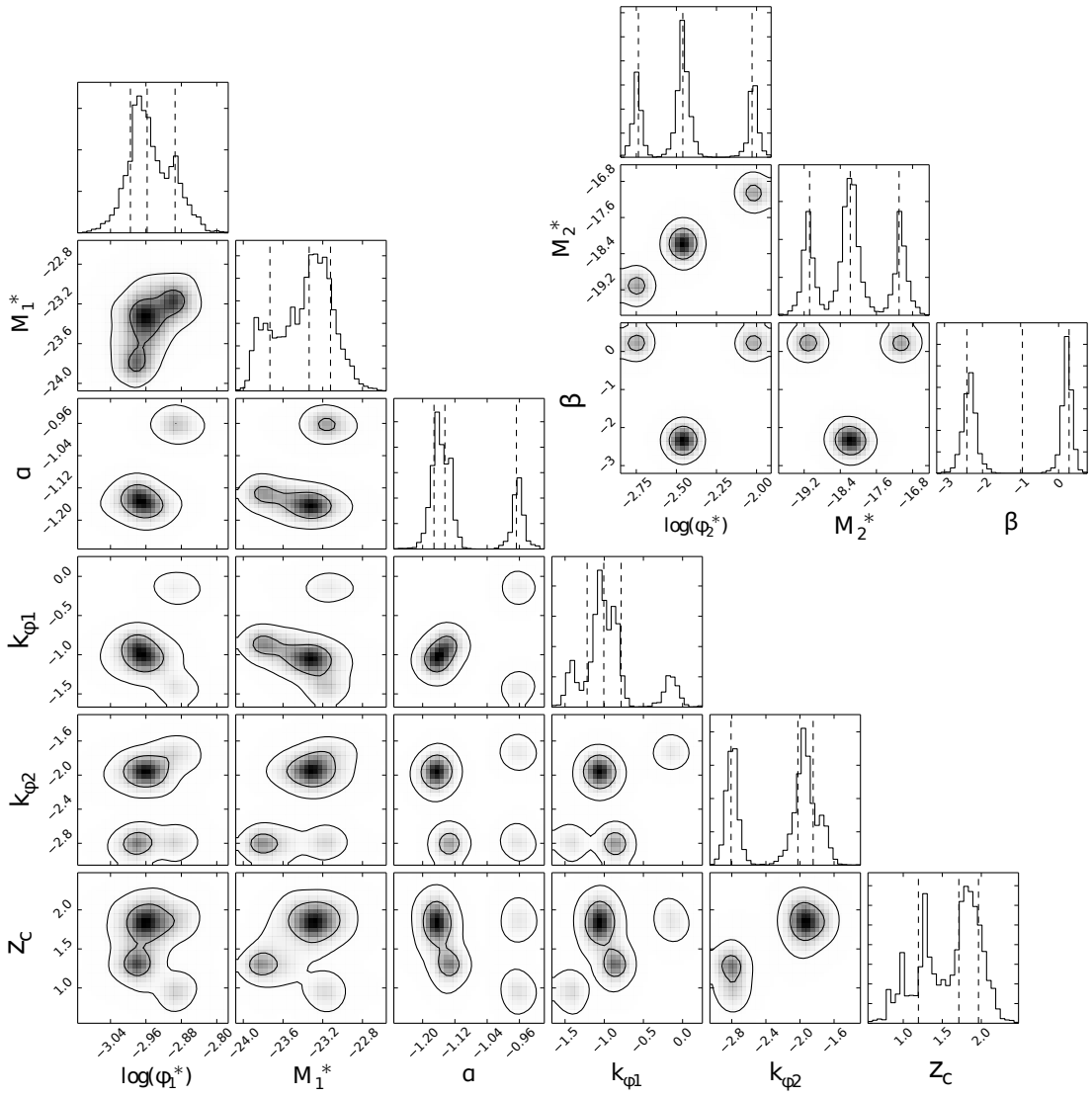

Figure 4.14: Estimation of the posterior PDF for a double Schechter function with pure density dependent evolution. The 2-D plots show the marginalised PDF for each two parameters with contours plotted at the 95 and 68 per cent confidence levels, while the 1-D histograms show the marginalised PDF for each parameter individually, with dotted lines showing the 16th, 50th and 84th percentiles.

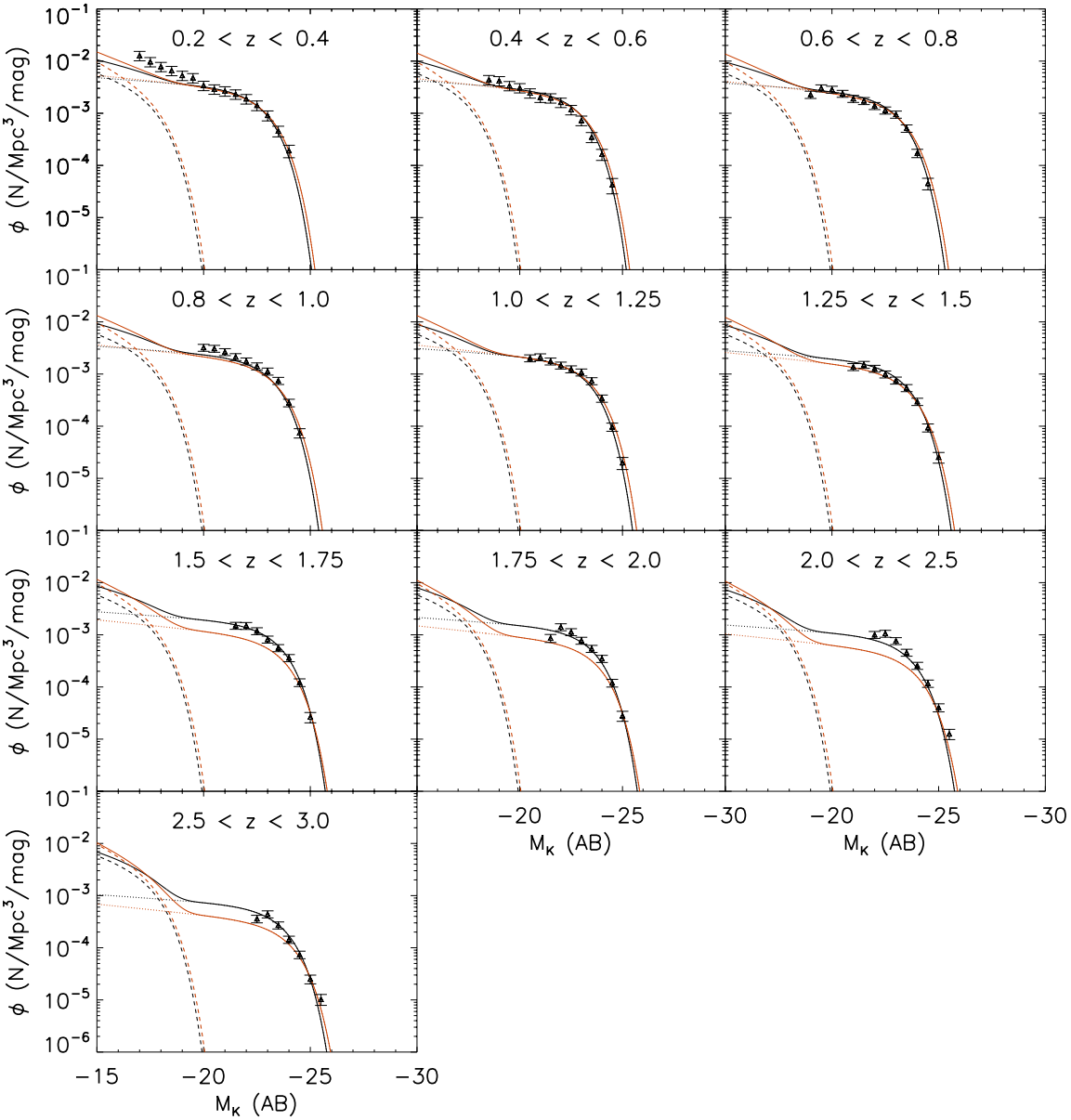

Figure 4.15: Median and best-fit double Schechter functions between $0.2 < z < 3$ in VIDEO-CFHTLS-D1 with luminosity dependent density evolution. The fit parameters are listed in the last column Table 4.2. Black triangles are the VIDEO-CFHTLS-D1 $1/V_{max}$ points, the solid lines are the double Schechter functions and the dotted and dashed lines show the bright and faint parts of the double Schechter function respectively. The best-fit is shown in black and the median in red.

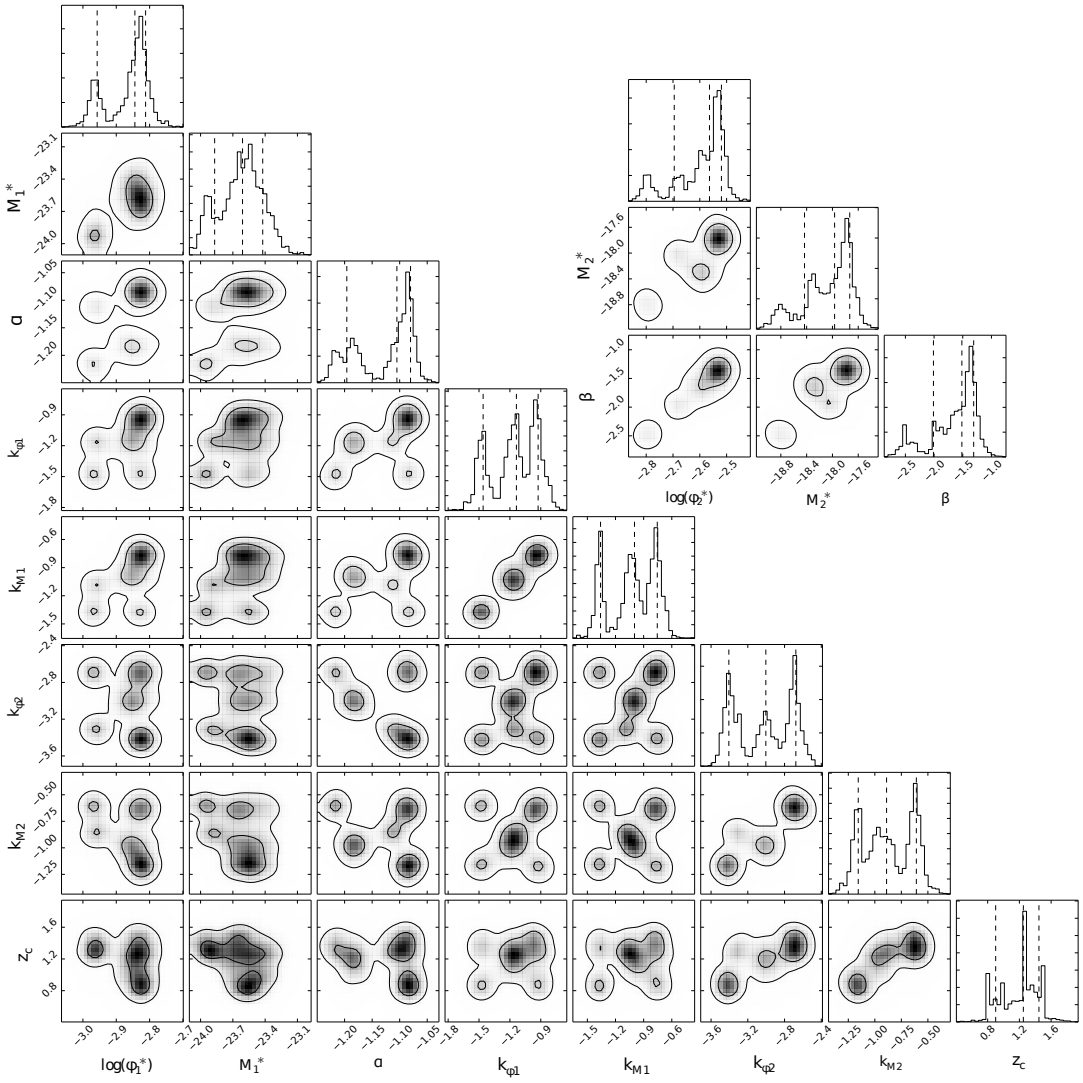

Figure 4.16: Estimation of the posterior PDF for a double Schechter function with luminosity dependent density evolution. The 2-D plots show the marginalised PDF for each two parameters with contours plotted at the 95 and 68 per cent confidence levels, while the 1-D histograms show the marginalised PDF for each parameter individually, with dotted lines showing the 16th, 50th and 84th percentiles.

a stronger evolution here than k_M in Figure 4.11, increasing approximately fourfold between $z = 3$ and $z = 0.5$. This stronger evolution is why pure density evolution gives a better fit than pure luminosity evolution, though the fainter magnitude bins where the number counts are high, which pure luminosity evolution fails to describe well, will have more of a penalising effect than the bright bins. This evolutionary form does struggle in some of the high redshift bins, particularly around $z \approx 2$, which is also where there is the greatest discrepancy between the volume densities measured in the VIDEO-CFHTLS-D1 field here and in the UDS from Cirasuolo et al. (2010).

Figure 4.15 shows the median and best-fit luminosity dependent density evolution, which gives the best fit. The associated plots of the posterior PDF are shown in Figure 4.12 and the median parameters along with the best-fit reduced χ^2 are listed in the third column of Table 4.2. Both the luminosity and the density evolution are steeper, which is to be expected as they compensate for each other (the correlation between $\phi^*_{1_z}$ and $M^*_{1_z}$ and between the $k_{\phi 1,2}$ and $k_{M1,2}$ is visible in Figure 4.12). As in the pure luminosity evolution case, k_{M1} and k_{M2} are similar, agreeing to within 1σ, whereas $k_{\phi 1}$ and $k_{\phi 2}$ are still significantly different from each other. $k_{\phi 2}$ still gives a very steep evolution above $z_c = 1.25$. Overall, the density evolution is still stronger than the luminosity evolution, with a dimming of 1.1 mags compared to an approximately tenfold increase in volume density from $z = 3$ to $z = 0.5$. The combined evolution produces Schechter functions which fit the changes in both the bright-end and the knee of the LF well. The high number density of sources at faint magnitudes, clearly visible in the low redshift bins, is also well fitted by the fainter of the two Schechter functions, which has a high ϕ^*_2 and a steep faint-end slope.

Together, these three sets of luminosity functions give evidence for a very strong increase in the number density of galaxies from $z \approx 3$ to $z \approx 1.25$ followed by a slightly weaker increase since then, and a gentle decrease in luminosity that is constant over the whole redshift range.

Table 4.2: The median and best-fit double Schechter parameters and best-fit reduced χ^2 from Equation 4.6 with either luminosity evolution, density evolution or luminosity dependent density evolution, according to either Equation 4.8 or Equation 4.7, or both.

	Evolution type		
	M_1^* only	ϕ_1^* only	M_1^* & ϕ_1^* both
	Median values		
$\log_{10}(\phi^*_{1_z}/\mathrm{Mpc}^{-3})$	$-3.00^{+0.12}_{-0.07}$	$-2.96^{+0.06}_{-0.04}$	$-2.84^{+0.03}_{-0.11}$
$M^*_{1_z}$	$-23.52^{+0.36}_{-0.31}$	$-23.34^{+0.22}_{-0.39}$	$-23.61^{+0.19}_{-0.26}$
α	$-1.21^{+0.08}_{-0.03}$	$-1.14^{+0.18}_{-0.03}$	$-1.11^{+0.02}_{-0.09}$
$k_{\phi 1}$	0 (fixed)	$-1.01^{+0.22}_{-0.21}$	$-1.14^{+0.21}_{-0.32}$
$k_{\phi 2}$	0 (fixed)	$-2.02^{+0.18}_{-0.78}$	$-3.00^{+0.33}_{-0.40}$
k_{m1}	$-0.32^{+0.30}_{-0.79}$	0 (fixed)	$-1.00^{+0.24}_{-0.36}$
k_{m2}	$-0.18^{+0.10}_{-0.18}$	0 (fixed)	$-0.89^{+0.28}_{-0.27}$
z_c	$2.75^{+0.25}_{-2.70}$	$1.71^{+0.25}_{-0.52}$	$1.25^{+0.18}_{-0.35}$
$\log_{10}(\phi^*_2/\mathrm{Mpc}^{-3})$	$-2.20^{+0.04}_{-0.43}$	$-2.46^{+0.43}_{-0.28}$	$-2.56^{+0.04}_{-0.13}$
M^*_2	$-18.37^{+0.58}_{-0.44}$	$-18.18^{+1.08}_{-0.90}$	$-17.97^{+0.23}_{-0.47}$
β	$-1.12^{+0.30}_{-1.15}$	$-0.95^{+1.23}_{-1.46}$	$-1.52^{+0.21}_{-0.50}$
	Best-fit values		
$\log_{10}(\phi^*_{1_z}/\mathrm{Mpc}^{-3})$	$-2.98^{+0.22}_{-0.06}$	$-2.95^{+0.07}_{-0.04}$	$-2.82^{+0.10}_{-0.03}$
$M^*_{1_z}$	$-23.61^{+0.10}_{-0.22}$	$-23.46^{+0.05}_{-0.07}$	$-23.58^{+0.03}_{-0.11}$
α	$-1.29^{+0.30}_{-0.03}$	$-1.16^{+0.05}_{-0.10}$	$-1.07^{+0.08}_{-0.04}$
$k_{\phi 1}$	0 (fixed)	$-0.56^{+0.10}_{-0.07}$	$-0.96^{+0.10}_{-0.03}$
$k_{\phi 2}$	0 (fixed)	$-2.00^{+0.07}_{-0.04}$	$-2.77^{+0.11}_{-0.04}$
k_{m1}	$-0.04^{+0.09}_{-0.22}$	0 (fixed)	$-0.93^{+0.04}_{-0.09}$
k_{m2}	$-0.00^{+0.09}_{-0.23}$	0 (fixed)	$-0.57^{+0.08}_{-0.04}$
z_c	$3.11^{+0.15}_{-0.18}$	$2.27^{+0.04}_{-0.11}$	$1.74^{+0.05}_{-0.08}$
$\log_{10}(\phi^*_2/\mathrm{Mpc}^{-3})$	$-2.63^{+0.06}_{-0.27}$	$-2.54^{+0.04}_{-0.13}$	$-2.54^{+0.05}_{-0.06}$
M^*_2	$-18.63^{+0.10}_{-0.23}$	$-18.16^{+0.06}_{-0.04}$	$-17.78^{+0.10}_{-0.03}$
β	$-2.31^{+0.10}_{-0.22}$	$-2.21^{+0.05}_{-0.06}$	$-1.34^{+0.10}_{-0.03}$
χ^2 (reduced)	4.79	3.94	1.64

4.4.2 Comparison with UDS

In this section I determine Schechter functions with ϕ_1^* and M_1^* evolving according to Equations 4.10 and 4.11, taken from Cirasuolo et al. (2010). Similarly, these are presented with pure luminosity evolution, pure density evolution, and luminosity dependent density evolution.

As before, Figure 4.17 shows the median fit with pure luminosity evolution and Figure 4.12 shows the associated plots of the posterior PDF, Figure 4.19 shows the median Schechter functions with pure density evoltuion and Figure 4.20 shows the associated plots of the posterior PDF, and Figure 4.21 shows the median fit with luminosity dependent density evolution and Figure 4.22 the plots of the posterior PDF. The median parameters for each evolution are listed in Table 4.3, as are the best reduced χ^2 values. Similarly to before, pure luminosity evolution provides the highest reduced χ^2, and is again described by a very weak evolution. It also struggles to reproduce the faint end at lower redshifts, producing an evolution that is not entirely believable. Pure density evolution gives a slightly lower reduced χ^2, with again, a stronger evolution than that seen in the pure luminosity case, but is also not a very believable fit. The best-fit is provided by combined evolution, as expected, with evolution in both luminosity and density that agrees with when they evolve separately. The best-fit parameters for the VIDEO-CFHTLS-D1 field and the UDS in Cirasuolo et al. (2010) mostly agree to within $1-2\sigma$, but there is some disagreement between the measurements of $\phi_{1_0}^*$ and k_ϕ. The difference in $\phi_{1_0}^*$ may be due to the upturn at the faint end of the LF in the lowest redshift bin, as the $\phi_{1_0}^*$ parameter describes the value of ϕ_1^* at $z = 0$. Also, as can be seen in Figure 4.9 the volume densities measured in the UDS (either by the $1/V_{max}$ method or the maximum likelihood method) are slightly lower than those measured in VIDEO in the key redshift bins around z_ϕ, which may be causing this effect (given the similarity in the VIDEO-CFHTLS-D1 and the UDS fields, I would expect the UDS to have an equivalent cosmic variance of

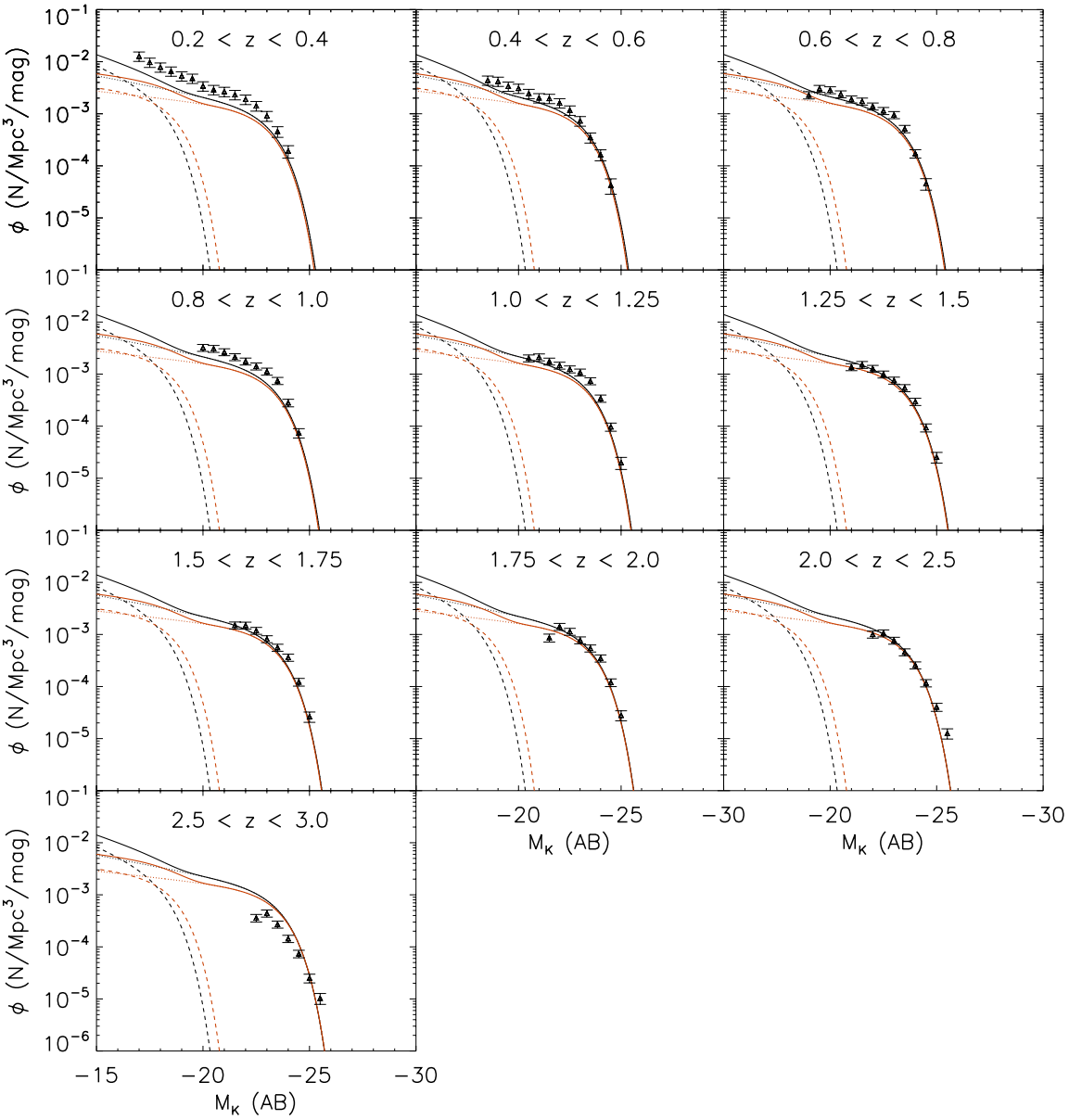

Figure 4.17: Median and best-fit double Schechter functions between $0.2 < z < 3$ in VIDEO-CFHTLS-D1 with pure luminosity dependent evolution following the Cirasuolo et al. (2010) parameterisation. The fit parameters are listed in the first column Table 4.3. Black triangles are the VIDEO-CFHTLS-D1 $1/V_{max}$ points, the solid lines are the double Schechter functions and the dotted and dashed lines show the bright and faint parts of the double Schechter function respectively. The best-fit is shown in black and the median in red.

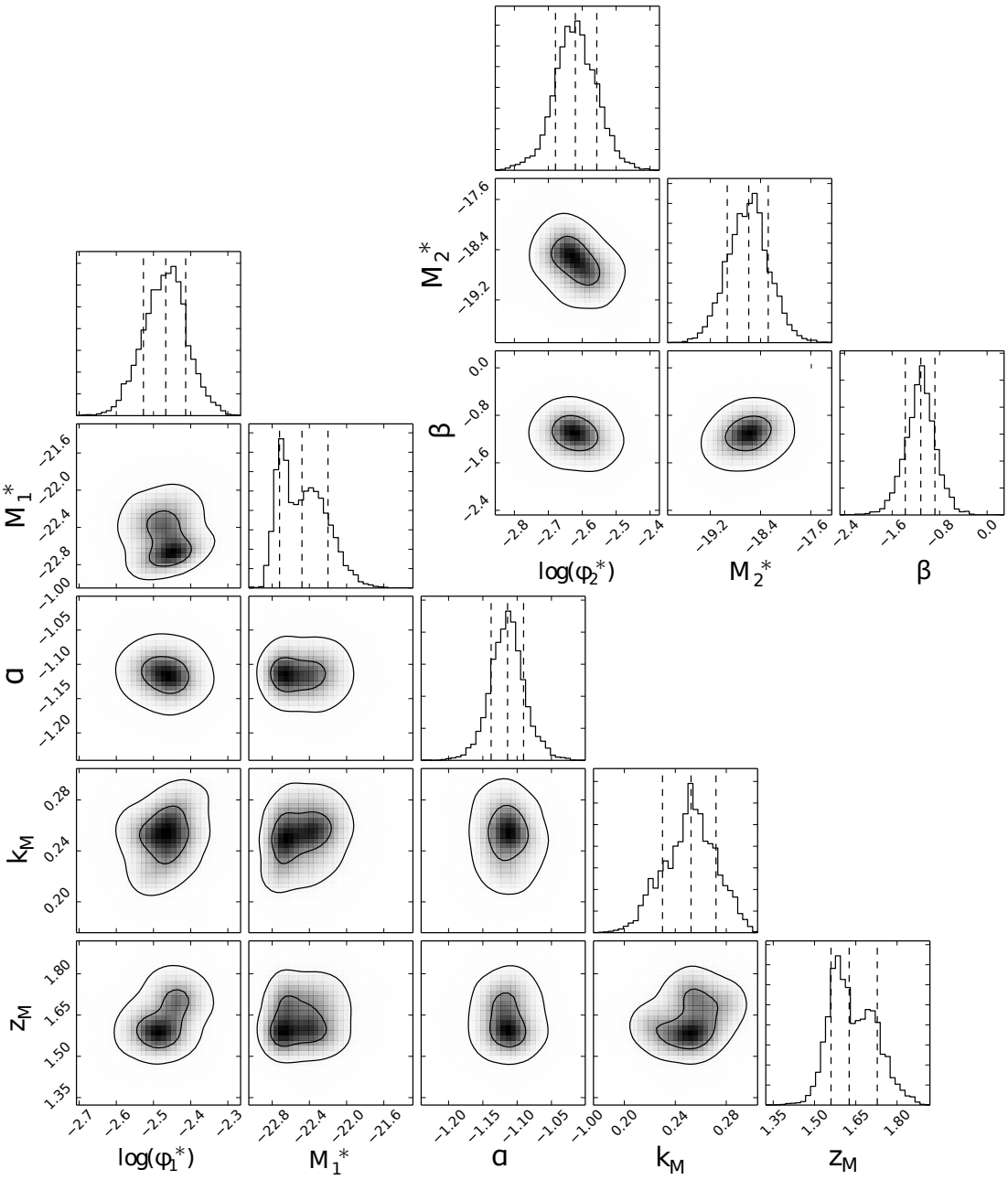

Figure 4.18: Estimation of the posterior PDF for a double Schechter function with pure luminosity dependent evolution following the Cirasuolo et al. (2010) parameterisation. The 2-D plots show the marginalised PDF for each two parameters with contours plotted at the 95 and 68 per cent confidence levels, while the 1-D histograms show the marginalised PDF for each parameter individually.

$\sim$ 15 per cent). As this is the higher end of the redshift range, it may also be causing the discrepancy in k_ϕ, as a higher value would be needed to describe the lower volume densities at high redshift seen in the UDS.

The best-fit LF with luminosity dependent density evolution from Section 4.4.1 has a lower reduced χ^2 than the best-fit LF from Section 4.4.2. As can be seen from the red line in Figure 4.23, Equations 4.7 & 4.8 are better at describing the brightening of the bright end of the LF out to $z \approx 3$, although both types of evolution struggle to reproduce the faint-end volume densities at high redshift. The upturn in the faint-end visible at the lowest redshifts is well described by the blue line, as the fainter schechter function has a very steep slope. The two forms of evolution combine to give a picture of stronger density evolution than luminosity evolution, though the evolutions take slightly different shapes. The best-fit parameters describing the two M_1^* evolutions lead to qualitatively similar forms, where as the significant differences in the two values $k_{\phi 1}$ and $k_{\phi 2}$ produce a qualitatively different form of density evolution, with Equation 4.10 giving a flatly increasing density as opposed to the clear split in regimes displayed in Equation 4.7.

Many of the contours associated with the fits presented here show a very multi-modal nature. This may be because the posterior is multi-modal, but it may also be a sign that the fits have struggled to converge. The fitting process was tuned so that the MCMC chains had an acceptance rate of between 20 and 50 per cent, ensuring that they would travel well through the parameter space (see e.g. Dunkley et al., 2005; Gelman et al., 1996, but the high number of parameters makes the various posteriors difficult to sample and the success very sensitive on the initial guess. The fits may be improved by using a peak-finding algorithm to identify the best-fit parameters before sampling the posterior and using this to inform the starting points of the walkers, guiding them to sample the most important section of the parameter space. Convergence tests such as the Gelman-Rubin test (Gelman & Rubin, 1992) could be

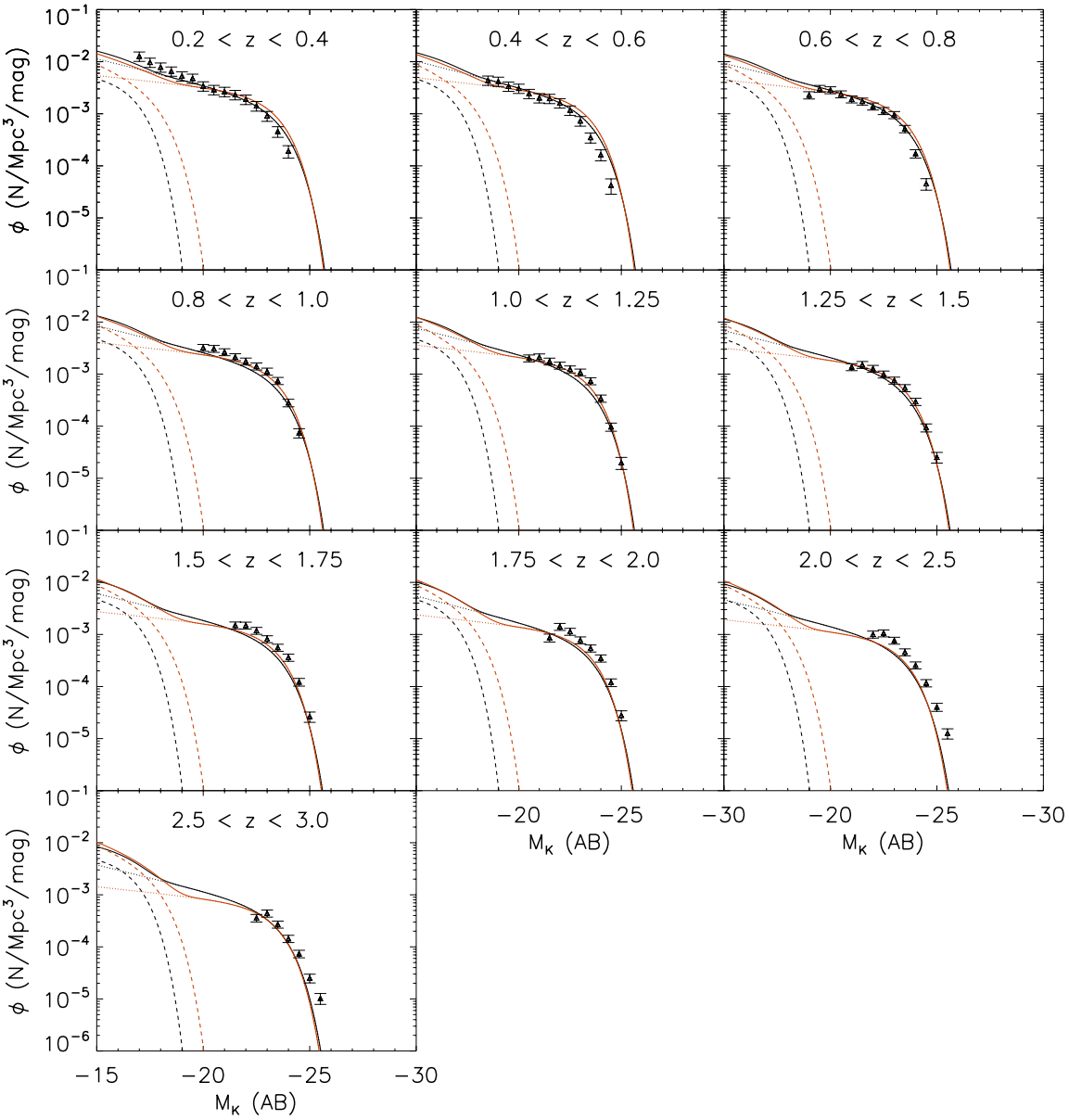

Figure 4.19: Median and best-fit double Schechter functions between $0.2 < z < 3$ in VIDEO-CFHTLS-D1 with pure density dependent evolution following the Cirasuolo et al. (2010) parameterisation. The fit parameters are listed in the second column of Table 4.3. Black triangles are the VIDEO-CFHTLS-D1 $1/V_{max}$ points, the solid lines are the double Schechter functions and the dotted and dashed lines show the bright and faint parts of the double Schechter function respectively. The best-fit is shown in black and the median in red.

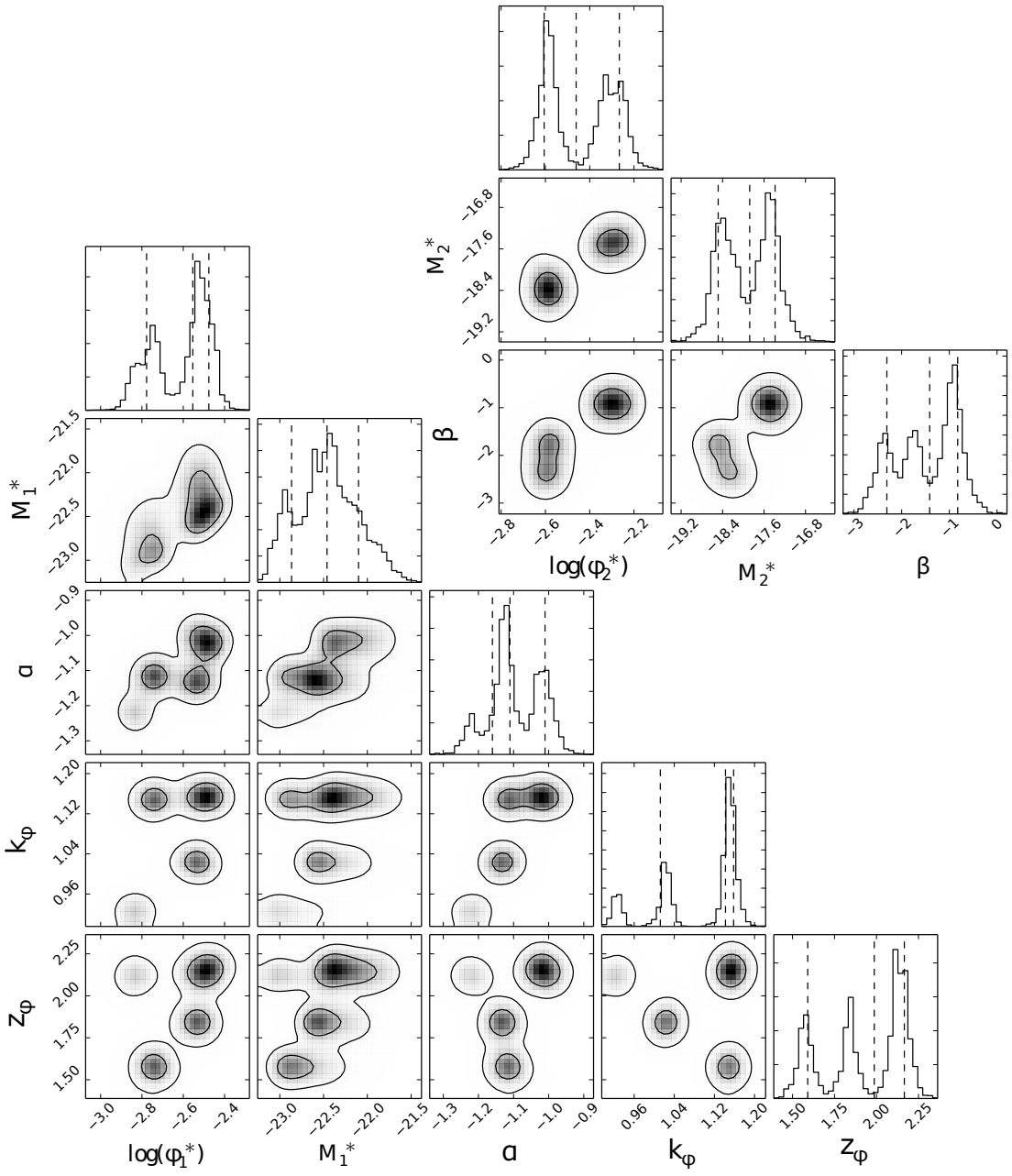

Figure 4.20: Estimation of the posterior PDF for a double Schechter function with pure density dependent evolution following the Cirasuolo et al. (2010) parameterisation. The 2-D plots show the marginalised PDF for each two parameters with contours plotted at the 95 and 68 per cent confidence levels, while the 1-D histograms show the marginalised PDF for each parameter individually.

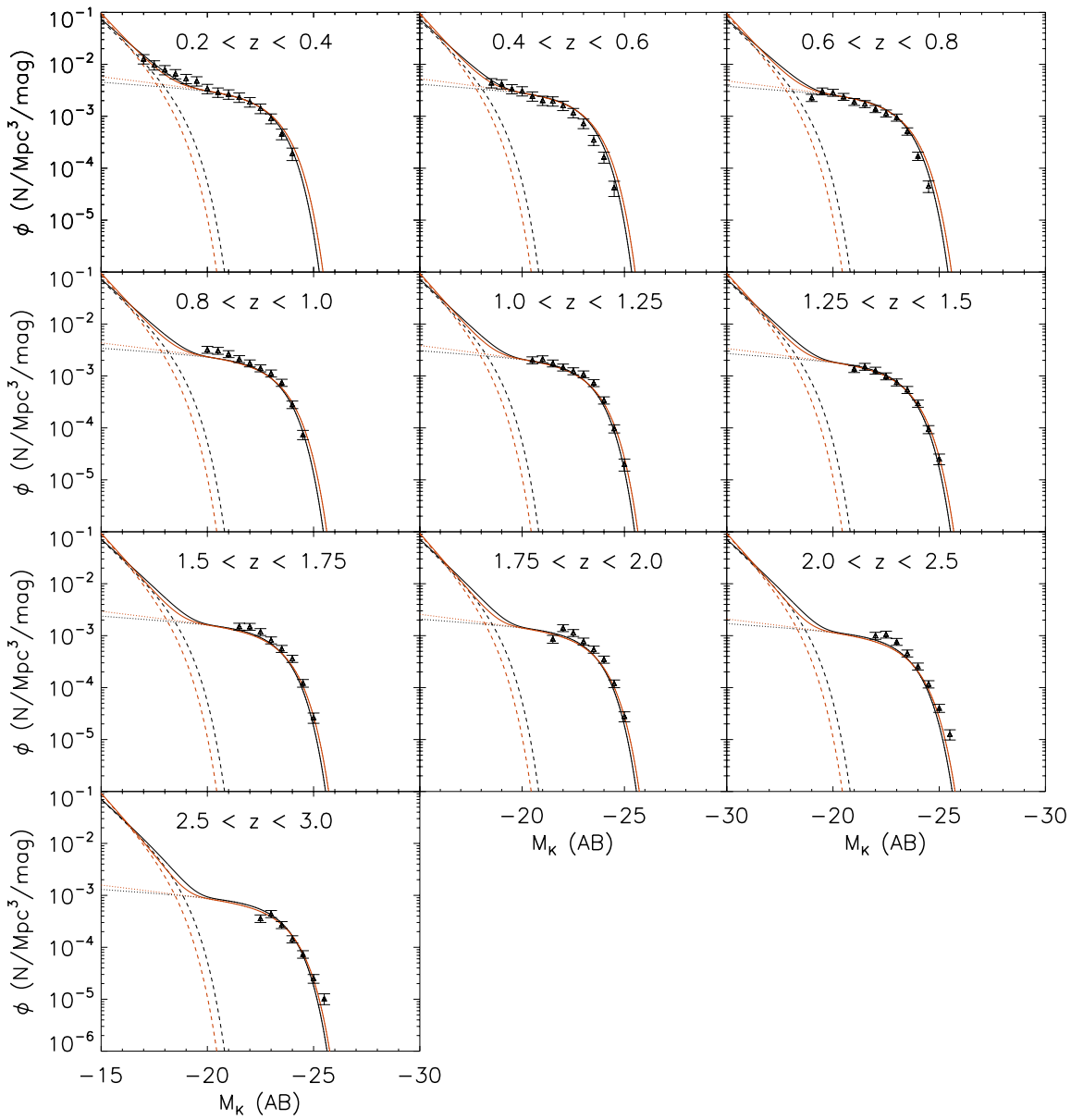

Figure 4.21: Median and best-fit double Schechter functions between $0.2 < z < 3$ in VIDEO-CFHTLS-D1 with luminosity dependent density evolution evolution following the Cirasuolo et al. (2010) parameterisation. The fit parameters are listed in the third column of Table 4.3. Black triangles are the VIDEO-CFHTLS-D1 $1/V_{max}$ points, the solid lines are the double Schechter functions and the dotted and dashed lines show the bright and faint parts of the double Schechter function respectively. The best-fit is shown in black and the median in red.

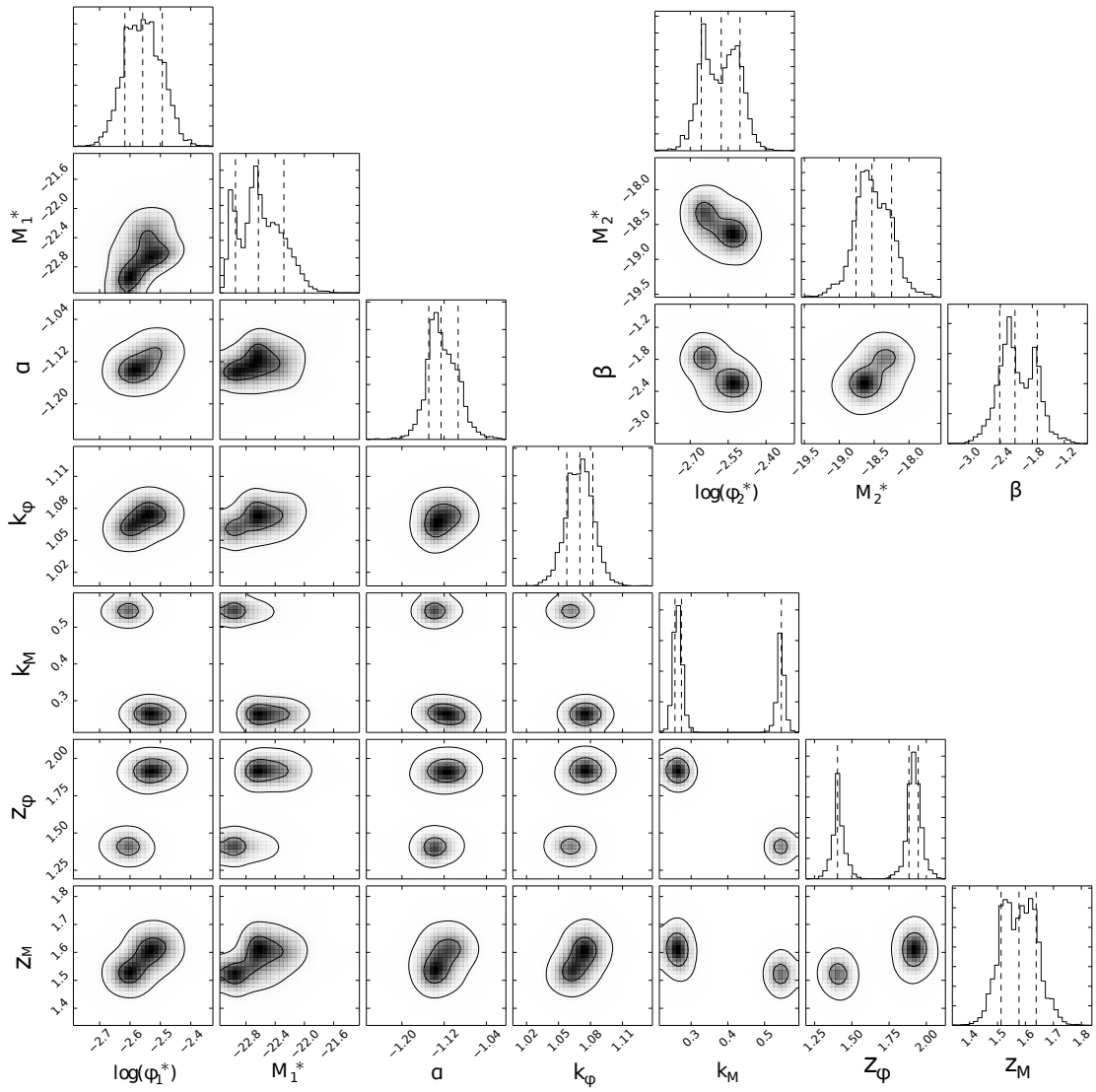

Figure 4.22: Estimation of the posterior PDF for a double Schechter function with luminosity dependent density evolution following the Cirasuolo et al. (2010) parameterisation. The 2-D plots show the marginalised PDF for each two parameters with contours plotted at the 95 and 68 per cent confidence levels, while the 1-D histograms show the marginalised PDF for each parameter individually.

Table 4.3: The median and best-fit double Schechter parameters and best reduced χ^2 from Equation 4.6 with luminosity evolution, density evolution or luminosity dependent density evolution taken from Cirasuolo et al. (2010), according to either Equation 4.11 or Equation 4.10, or both, along with the best-fit parameters single Schechter parameters from the UDS.

	Evolution type			
	M_1^* only	ϕ_1^* only	M_1^* & ϕ_1^* both	UDS
		Median values		
$\log_{10}(\phi_{1_0}^*/\mathrm{Mpc}^{-3})$	$-2.47^{+0.05}_{-0.06}$	$-2.55^{+0.08}_{-0.22}$	$-2.56^{+0.06}_{-0.06}$	-3.46 ± 0.05
$M_{1_0}^*$	$-22.48^{+0.28}_{-0.24}$	$-22.46^{+0.36}_{-0.40}$	$-22.63^{+0.35}_{-0.31}$	-22.26 (fixed)
α	$-1.11^{+0.02}_{-0.02}$	$-1.11^{+0.01}_{-0.05}$	$-1.13^{+0.03}_{-0.02}$	-1.07 ± 0.1
k_ϕ	0 (fixed)	$1.14^{+0.02}_{-0.13}$	$1.07^{+0.01}_{-0.01}$	1.47 ± 0.1
z_ϕ	-	$1.99^{+0.18}_{-0.40}$	$1.88^{+0.06}_{-0.48}$	1.70 ± 0.09
k_m	$0.25^{+0.02}_{-0.02}$	0 (fixed)	$0.27^{+0.27}_{-0.02}$	0.47 ± 0.2
z_m	$1.63^{+0.10}_{-0.07}$	-	$1.58^{+0.06}_{-0.06}$	1.78 ± 0.15
$\log_{10}(\phi_2^*/\mathrm{Mpc}^{-3})$	$-2.62^{+0.06}_{-0.06}$	$-2.46^{+0.20}_{-0.14}$	$-2.58^{+0.07}_{-0.08}$	-
M_2^*	$-18.58^{+0.31}_{-0.34}$	$-17.87^{+0.49}_{-0.61}$	$-18.53^{+0.28}_{-0.22}$	-
β	$-1.12^{+0.24}_{-0.26}$	$-1.41^{+0.59}_{-0.90}$	$-2.12^{+0.42}_{-0.29}$	-
		Best-fit values		
$\log_{10}(\phi_{1_0}^*/\mathrm{Mpc}^{-3})$	$-2.45^{+0.08}_{-0.05}$	$-2.71^{+0.19}_{-0.37}$	$-2.50^{+0.14}_{-0.06}$	
$M_{1_0}^*$	$-22.50^{+0.05}_{-0.06}$	$-22.61^{+0.19}_{-0.36}$	$-22.47^{+0.17}_{-0.06}$	
α	$-1.20^{+0.15}_{-0.07}$	$-1.25^{+0.19}_{-0.19}$	$-1.08^{+0.10}_{-0.08}$	
k_ϕ	0 (fixed)	$0.92^{+0.20}_{-0.21}$	$1.08^{+0.09}_{-0.06}$	
z_ϕ	-	$2.12^{+0.13}_{-0.20}$	$1.99^{+0.09}_{-0.09}$	
k_m	$0.21^{+0.10}_{-0.12}$	0 (fixed)	$0.30^{+0.09}_{-0.06}$	
z_m	$1.51^{+0.09}_{-0.13}$	-	$1.74^{+0.03}_{-0.14}$	
$\log_{10}(\phi_2^*/\mathrm{Mpc}^{-3})$	$-2.58^{+0.14}_{-0.05}$	$-2.27^{+0.15}_{-0.08}$	$-2.51^{+0.15}_{-0.06}$	
M_2^*	$-18.23^{+0.11}_{-0.06}$	$-16.73^{+0.05}_{-0.14}$	$-18.82^{+0.06}_{-0.15}$	
β	$-1.43^{+0.07}_{-0.17}$	$-1.09^{+0.09}_{-0.21}$	$-1.92^{+0.12}_{-0.06}$	
χ^2 (reduced)	6.33	5.27	2.58	-

used to check whether the chains have converged, telling the fitting algorithm that it could stop sampling (Dunkley et al., 2005). Finally, a different sampling algorithm than Metropolis-Hastings, such as affine-invariant MCMC may well provide a better option for fitting a posterior which is potentially multi-modal and degenerate, with more objectivity as there is less need to define a sensible trial distribution initially in order to obtain realistically practicable convergence times (Allison & Dunkley, 2014).

As previously mentioned, the high number of parameters involved make this evolutionary model difficult to fit. It is possible that fewer parameters would produce a clearer picture of the behaviour of the LF over this redshift range. This could either be achieved by assuming a simpler version of the Schechter function, either a single Schechter function, which would manage well in all but the lowest redshift bins, or a double Schechter function with less parameters. This may mean that there is less degeneracy and that the parameters could all be better constrained. Similarly, a simpler evolutionary model or one that uses local measured values of the characteristic luminosity and volume density at $z = 0$ rather than fitting them, as is done in Cirasuolo et al. (2010), would remove some of the complication.

4.5 Discussion

The various evolutionary forms tested in Section 4.4.1 show a combined evolution in luminosity and density over cosmic time. There is a substantial brightening of $\Delta M \gtrsim 1$ in luminosity from $z = 0$ to $z = 3$ at a reasonably constant rate, in agreement with previous studies (Caputi et al., 2006; Cirasuolo et al., 2007, 2010; Ilbert et al., 2005). Simultaneously, the number density of galaxies has evolved much more rapidly, although in two stages. Since $z \approx 1.75$, it has increased by only a factor of 2, whereas from $z = 3$ to $z = 1.75$ it increased by a factor of 4.

Rest-frame K_s-band accesses the bulk of the stellar mass of a galaxy, providing the

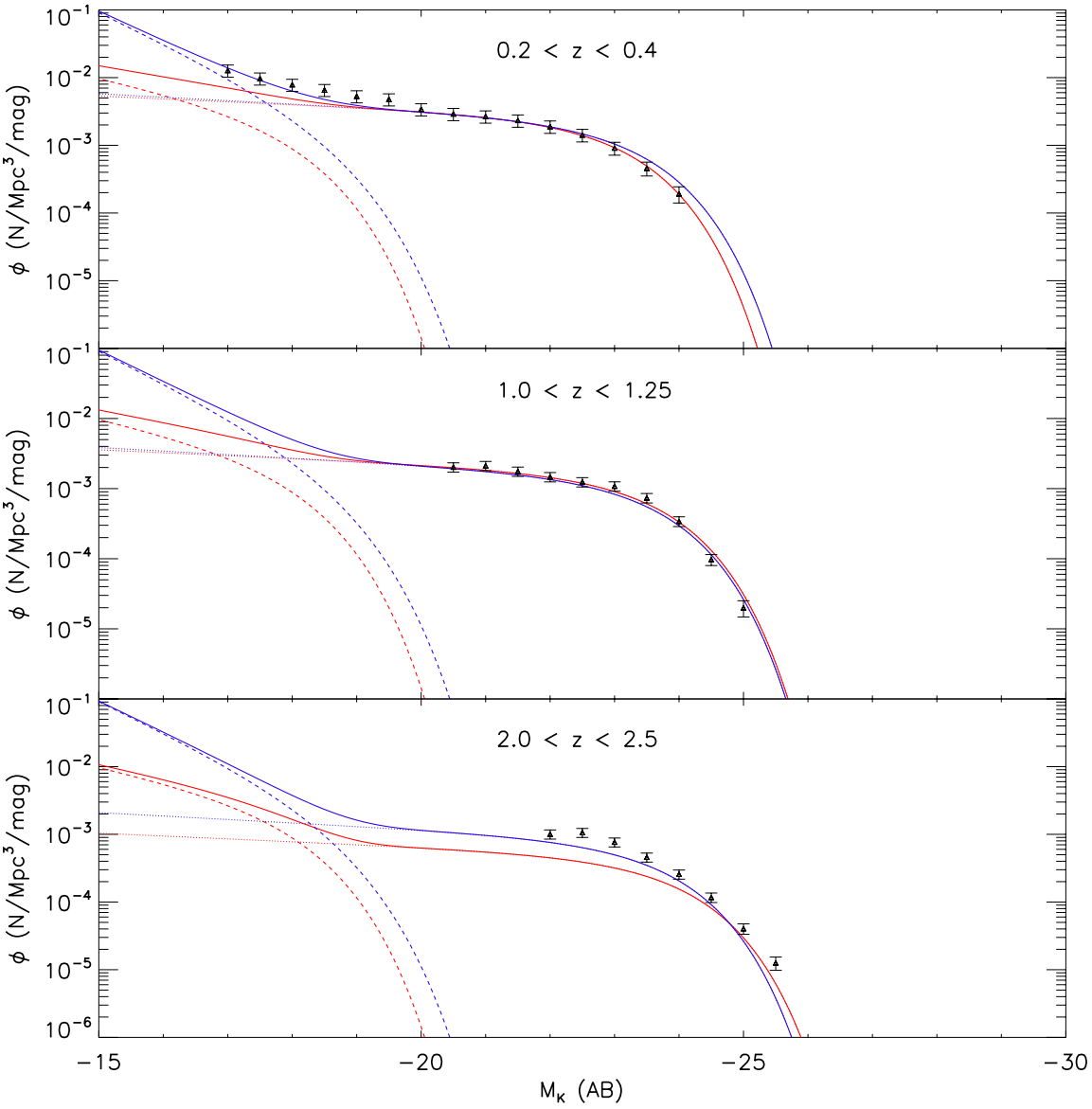

Figure 4.23: Comparison of the median LFs from Section 4.4.1 (red) and Section 4.4.2 (blue) at $z \approx 0$ (top panel), $z \approx 1$ (middle panel) and $z \approx 2$ (bottom panel). As before, the brighter Schechter function is shown in dotted lines, the fainter Schechter function is shown in dashed lines and the full double Schechter function is shown in solid lines.

perfect probe to try to quantify how the number and brightness of the vast majority stars in a galaxy are behaving. Overall, the K_s-band luminosity functions presented here imply a very rapid build up in the number of galaxies from $z \approx 3$ until $z \approx 1.75$.

The steep shape of the bright end of the LF means it is best described by luminosity evolution. Brighter galaxies contain the bulk of the stellar mass and the evolution of smaller galaxies has little effect on the characteristic brightness, and so the luminosity evolution of the LF follows the evolution of the brightest galaxies. The gentle single-strength decrease in luminosity measured in Section 4.4 hints at passive evolution for bright galaxies. These galaxies form the bulk of their mass at high redshift, before they are quenched, leaving a slowly dimming, ageing stellar population.

Density evolution has a much stronger effect on the faint end of the LF due to its flatter shape. The two-term density evolution in Section 4.4 shows an initial regime at higher redshift where the evolution is dominated by haloes collapsing to form increasing numbers of galaxies. Since $z \approx 1.75$, the slower rate of build up implies that instead of the number density mostly being driven by the formation of new, smaller galaxies, mergers are having a greater effect, working to decrease the density of galaxies and so slowing the overall density evolution.

The interpretation of passive evolution dominating the bright-end of the LF and a rapid build up of smaller galaxies at the faint end of the LF is in line with downsizing, where the combination of massive passive galaxies that have formed their stellar mass very early and active small galaxies which are still forming their stellar mass leads to larger galaxies having a smaller specific SFR. If massive galaxies form early and fast and subsequently stop forming stars, the brightest galaxies would not be growing in luminosity, as they have stopped forming new stars, but would be ageing passively following their stellar populations, becoming slowly redder and dimmer as they lose the all but the stars with very long lifetimes. Meanwhile, the small galaxies, which are young and actively forming stars, would be moving from the extremely large

population of very faint galaxies through the luminosity function to contribute to brighter populations, increasing the volume density towards the knee of the LF. This would produce the evolution in luminosity and density seen here.

At low redshift, the faint-end of the luminosity function is well constrained. The upturn visible in the two lowest redshift bins provides support for a double-Schechter parameterisation (see Figure 4.10, showing that, at least at low redshift, the number density of very low brightness galaxies is too high to be described by a single Schechter function with a steep faint-end slope. However, for the bulk of the redshift range discussed here, a double Schechter function is not well supported.

It is possible to convert a luminosity function to a stellar mass function with the use of synthetic spectra made with stellar population synthesis models, such as the model of Bruzual & Charlot (2003), fitting the models with a code such as Le Phare, used to fit the photometric redshifts used here, or CIGALE (Burgarella et al., 2005; Giovannoli et al., 2011; Noll et al., 2009), an SED fitting code optimised to produce physical properties (e.g. (Ilbert et al., 2013; Johnston et al., 2015). This provides each galaxy with a stellar mass, and a mass limit for detection dependent on the mass-to-light ratio of the particular model that was used. From this point, a mass function can be built in the same manner as a luminosity function. Mass functions can be useful as they provide a much more physical picture. It is possible to trace how different size, colours and types of galaxies assemble their mass by tracing the evolution of their respective mass functions (Ilbert et al., 2013). It is very straightforward to compare them to physical models, which deal in mass rather than light. However, there are many uncertainties involved in them; they are very derived properties based on several more steps with inbuilt assumptions than luminosity functions, which are more directly related to observations. For this reason, while it is important to measure mass functions and compare them directly to physical models, it is also important to produce luminosity functions from those models and compare them directly to

observed luminosity functions.

4.6 Conclusions

I have presented rest-frame K_s-band luminosity functions out to $z \approx 3$ from the VIDEO-CFHTLS-D1 field, which provides the best combination of area, depth and available photometric bands. The number of bands and the depth of the photometric data allowed for the production of a catalogue of objects with photometric redshifts, from which I used the $1/V_{max}$ method to derive luminosity functions in 10 redshift bins ranging from $z = 0.2$ to $z = 3$.

The large volume sampled by the VIDEO survey fills in the bright-end of the luminosity function with reliable points as far as $M = -24$ at $z \approx 0.2$ and $M = -26$ at $z \approx 3$. This has allowed for the full measurement of the bright-end and knee of the Schechter function out to $z = 3$, constraining M^* and its evolution. The deep IR imaging has allowed me to characterise the faint end of the luminosity function at lower redshifts, reaching down to absolute magnitudes of $M = -20$ at $z = 1$ and $M = -17$ at $z = 0.2$. I have fitted a variety of evolutionary forms over the redshift range, and see an evolution that is a combination of slow brightening of characteristic luminosity and a two-tone rapid evolution in characteristic number density until $z = 3$.

Chapter 5

Luminosity Functions in the VIDEO-CFHTLS-W1 Field

5.1 Introduction

The galaxy LF presents a measure by which to constrain theories of galaxy evolution. Tracing how populations of galaxies evolve in luminosity and density, as well as the relative distribution of faint to bright galaxies, gives insight into the processes that shape them. The importance of large surveys is ever more evident as we continue to advance our understanding of galaxy evolution both theoretically and observationally via this method.

The faint-end of the LF allows us to investigate the effect of feedback from star formation and supernovae on the evolution of galaxies. At low redshift, there is a visible upturn at the faint-end of the LF, measured at $z < 0.1$ (Loveday et al., 2012, 2015) and at extremely low redshift (Baldry et al., 2005; Blanton et al., 2005; Geller et al., 2012). This is an area that represents one of the biggest mismatches between theory and observations, with simulations of galaxy evolution in a ΛCDM universe over-predicting the number density of faint galaxies, and so is of critical

importance to study. Additionally, observational issues with observing the faint end of the galaxy LF exacerbate this problem, as low luminosity galaxies tend to have lower surface brightnesses (Cameron & Driver, 2007; Driver, 1999) which makes them harder to detect, leading to the underestimation of the faint, low surface brightness dwarf galaxies that make up the bulk of the number densities at this end of the LF.

The galaxy LF has been measured in many deep surveys at $z > 1$ such as the VIMOS VLT Deep Survey (VVDS; Ilbert et al., 2006; Le Fèvre et al., 2005), the UKIDSS Ultra Deep Survey (UDS; Cirasuolo et al., 2010; Lawrence et al., 2007, and the COSMOS survey (Scoville et al., 2007; Zucca et al., 2009) and very large surveys at low redshift such as the Two Degree Field Galaxy Redshift Survey (2dF; Cole et al., 2001; Colless et al., 2001, the Sloan Digital Sky Survey (SSDS; Adelman-McCarthy et al., 2008; Baldry et al., 2005; York et al., 2000), and the Galaxy And Mass Assembly survey (GAMA; Driver et al., 2009, 2011; Loveday et al., 2012), but the necessary combination of large area and high sensitivity makes it difficult to link up the evolution between $0 < z < 1$, as well the difficulty inherent in combining the vastly different techniques of the spectroscopic surveys at low redshift and the photometric surveys at higher redshift. The VIDEO survey's coverage of the XMM fields, overlapping with one of the CFHTLS-Wide fields, supplies an area of 4.5 degree^2 with deep optical and IR imaging. The area is wide enough to sample large comoving volumes even at low redshift, allowing for the characterisation of the bright end of the LF. The deep imaging, with a 5σ limit of $K_s = 23.8$ and i = 24.8 (see Table 4.1), allows for the measurement of the LF down to faint magnitudes consistently below M^* out to $z > 1$. This combination lets us examine both luminosity evolution, which will have a very strong effect on the bright end of the LF and density evolution, which will require LFs with good constraints beyond L^* to fit.

In this chapter I present $1/V_{max}$ luminosity functions from the 4.5 degree^2 VIDEO and CFHTLS-W1 overlap, VIDEO-CFHTLS-W1, out to $z = 1.5$ and down to an

absolute magnitude of $M_{K_s} \sim -20$ at $z = 1$ and $M_{K_s} \sim -17$ at $z = 0.3$. These are particularly useful for studying the bright end of the LF as the large area produces the necessary number counts to find rare, bright objects, and for studying the faint-end of the luminosity function at lower redshift where the small size of the comoving volume element makes it much harder to robustly characterise the LF.

The structure of this chapter is as follows: first, I describe the VIDEO-CFHTLS-W1 data, the catalogue creation and photometric redshift fitting in Section 5.2 and describe measuring the luminosity functions using the $1/V_{max}$ procedure in Section 5.3. I then present K_s-band luminosity functions for the VIDEO-CFHTLS-W1 field in Section 5.4, fitting them with a variety of evolving Schechter functions as in Chapter 4 in Section 5.4.1 and 5.4.2 before discussing the results in Section 5.5, and finally I present my conclusions in Section 5.6.

5.2 Data

In this Chapter, I use the whole 4.5 degree^2 of the VIDEO near-IR $ZYJHK_s$ coverage over the XMM-LSS field, with optical $ugriz$ data provided by the much larger (72 degree^2) CFHTLS-W1 field. A description of the VIDEO survey can be found in Section 4.2.1 and Jarvis et al. (2013). As can be seen from Table 4.1, the near-IR VIDEO imaging has the same depths over the whole field, whereas the optical data from CFHTLS-W1 are approximately a magnitude shallower than the optical data from CFHTLS-D1.

The data reduction and catalogue production were carried out in the same way as for the VIDEO-CFHTLS-D1 field, as described briefly in Section 4.2 and fully in Jarvis et al. (2013), leaving a catalogue of 281,299 objects identified in the K_s-band with $K_s < 23.5$ with photometric redshifts also calculated in an identical way as the VIDEO-CFHTLS-D1 field. The number counts are shown in Figure 5.2 and the

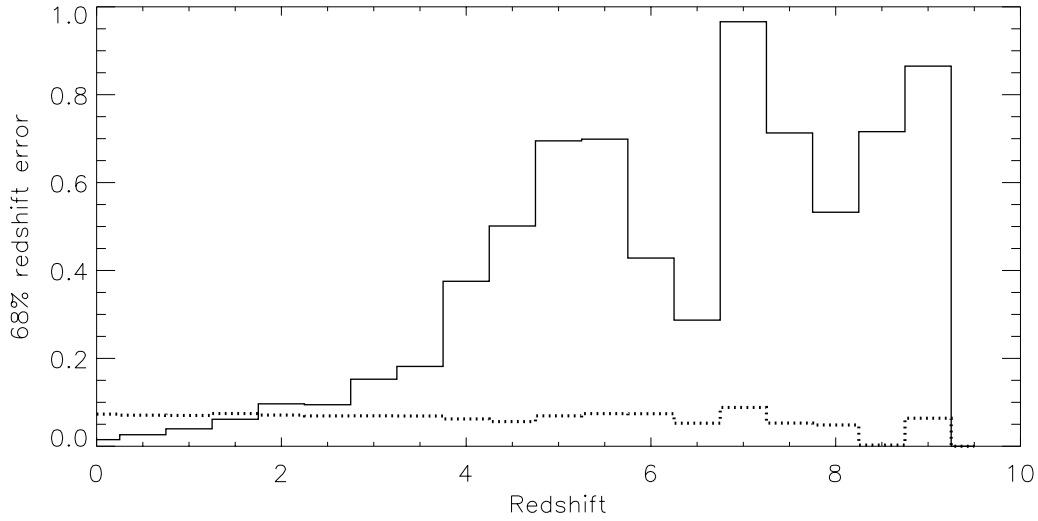

Figure 5.1: The average error on the photometric redshift at different redshifts for galaxies detected in the VIDEO-CFHTLS-D1 (dotted) and VIDEO-CFHTLS-W1 (solid) fields.

redshift distribution in Figure 5.3.

As the catalogue used has a detection criterion in the K_s-band, the reduced depth of the optical data from CFHTLS-W1 compared to CFHTLS-D1 will not directly effect the measurement of the $1/V_{max}$ LFs. However, because the optical bands are so key to photometric redshift fitting, it will affect the best-fit redshifts that are then used in the $1/V_{max}$ analysis. This will have the largest effect on objects that are close to the depth limits of the photometry, such as those at high redshift.

The shallower optical limits will increase the uncertainty on the best-fit redshifts. As can be seen from Figure 5.1, this will have a larger effect on high redshift objects as they are more likely to be faint, and so the average error will be larger. However, it will also have an effect of low redshift sources. The shallower optical limits will also increase the fraction of incorrectly assigned redshifts, visible as outliers in Figure 4.6, particularly for faint galaxies. This will have an effect at every redshift, but lower number counts and fainter galaxies at high redshift will mean that the effect has a larger impact there. For this reason, galaxies in VIDEO-CFHTLS-W1 field in the

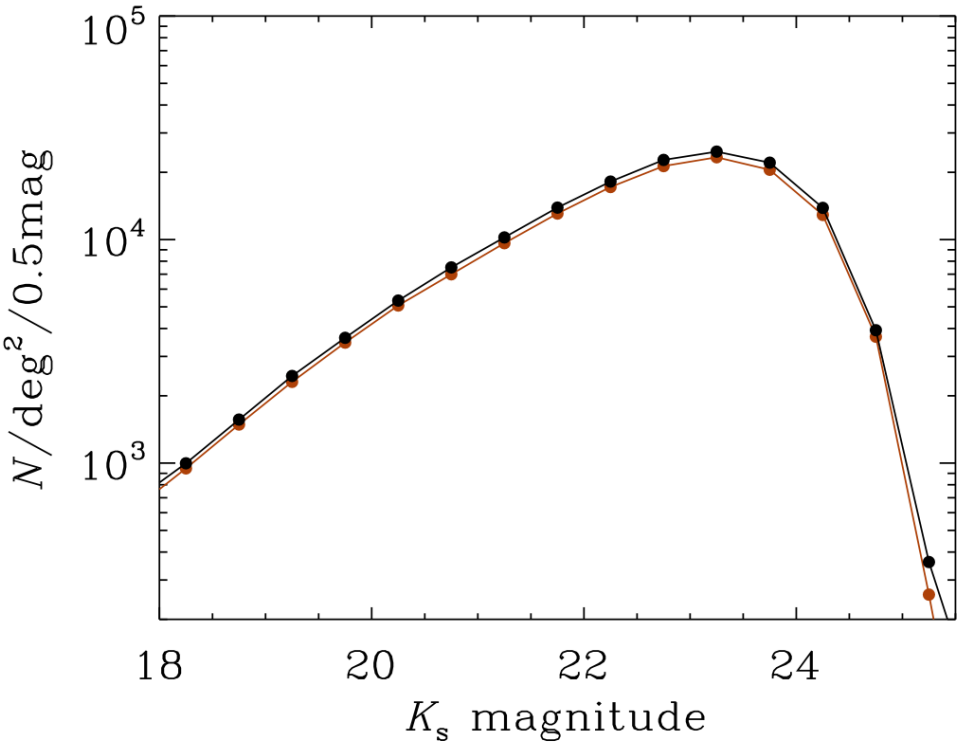

Figure 5.2: Total magnitude differential number counts for galaxies detected in the K_s-band in the VIDEO-CFHTLS-W1 and VIDEO-CFHTLS-D1 field. The number counts for the VIDEO-CFHTLS-D1 field are shown in red and the VIDEO-CFHTLS-W1 field in black. The Poisson uncertainties are smaller than the symbol size. For comparison with other fields, see Figure 4.4 in Chapter 4.

$1.5 < z < 3.0$ redshift range have not been analysed here.

5.3 Luminosity Functions

The VIDEO-CFHTLS-W1 luminosity functions were produced using the $1/V_{max}$ method in an identical way to the VIDEO-CFHTLS-D1 field, as described in Section 4.3.1. The uniform K_s-band depth over the whole of the XMM-LSS field allows the $K_s < 23.5$ magnitude cut used in the $1/V_{max}$ analysis in Chapter 4 to be applied here. The shallower optical data will mean that the photometric redshifts are not as reliable in

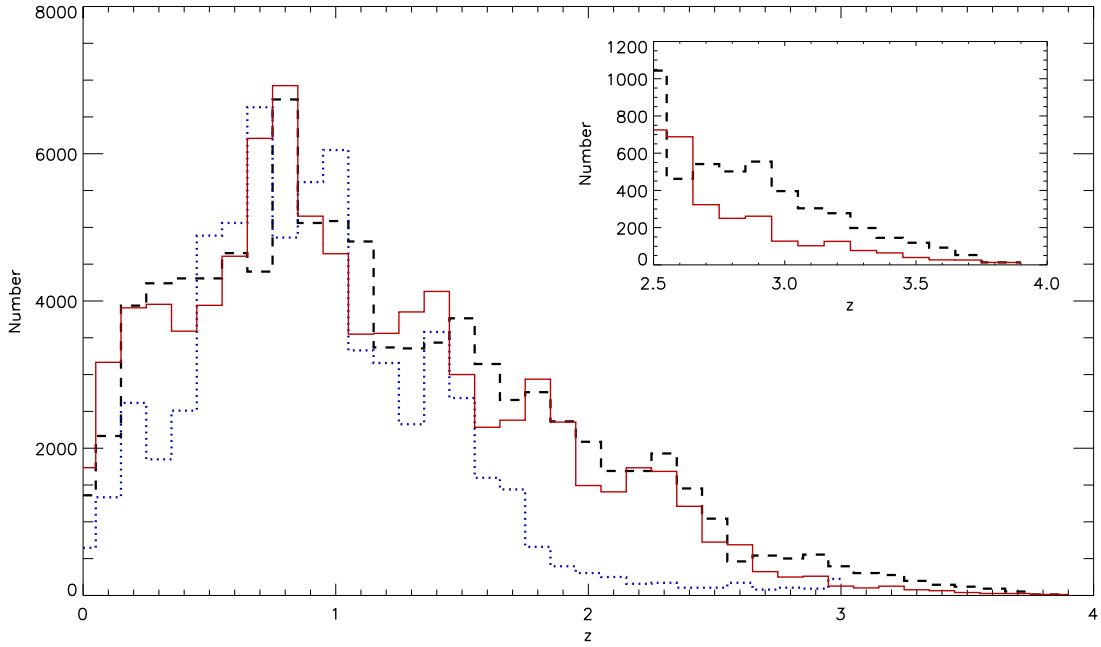

Figure 5.3: Redshift distribution of sources in the VIDEO-CFHTLS-W1 catalogue (red solid histogram), trimmed according to the criteria laid out in Section 4.2.1. The black dashed line shows the redshift distribution of the VIDEO-CFHTLS-D1 catalogue and the blue dotted line shows the UDS sample used in Cirasuolo et al. (2010) both scaled to the size of the VIDEO-CFHTLS-W1 catalogue. The inset shows a zoomed in region comparing the distributions in the VIDEO CFHTLS-W1 field (red solid histogram) and VIDEO-CFHTLS-D1 field (black dashed histogram) over the range $2.5 < z < 4$. The UDS catalogue has 25,564 sources, the VIDEO-CFHTLS-D1 catalogue has 90,519 and the VIDEO-CFHTLS-W1 catalogue has 281,299 sources.

the VIDEO-CFHTLS-W1 field as in the VIDEO-CFHTLS-D1 field, particularly at high redshift and for fainter sources as more galaxies will have faint apparent magnitudes closer to the sensitivity limit of the optical data, and as such the analysis in this Chapter has been limited to below $0.2 < z < 1.5$.

The VIDEO-CFHTLS-W1 LF is shown in Figure 5.4, along with the VIDEO-CFHTLS-D1 LF from Chapter 4 and the UKIDSS UDS LF from Cirasuolo et al. (2010). The three determinations agree relatively well, with most points within $1-2\sigma$ of each other up to $z \approx 1.5$. Both the VIDEO-CFHTLS-W1 and VIDEO-CFHTLS-D1 fields are slightly denser than the UDS LF in the $0.8 < z < 1.0$ redshift bin with most points consistently $\sim 1\sigma$ denser in the two VIDEO fields, which may be due to large scale structure at this redshift.

Both the VIDEO-CFHTLS-W1 and the VIDEO-CFHTLS-D1 LFs clearly show the upturn at the faint-end extending down to $M_{K_s} = -17$, most obvious in the $0.2 < z < 0.4$ bin but also visible in the $0.4 < z < 0.6$ bin. The VIDEO-CFHTLS-W1 LF extends brighter than both the VIDEO-CFHTLS-D1 and the UDS LFs, due to the increased area of 4.5 degree^2 instead of 1 and 0.7 degree^2 giving a higher chance of finding rare, incredibly bright objects.

5.4 Fitted Schechter Functions in the VIDEO-CFHTLS-W1 Field with CFHTLS-Wide

I used the same parameterisation as in Chapter 4, laid out in Equations 4.6 to 4.11. As before, I used MCMC to fit the different evolutions.

5.4.1 Results

I present the best-fit solutions for evolving double Schechter functions fitted to the VIDEO-CFHTLS-W1 LF. Luminosity dependent evolution, density dependent evo-

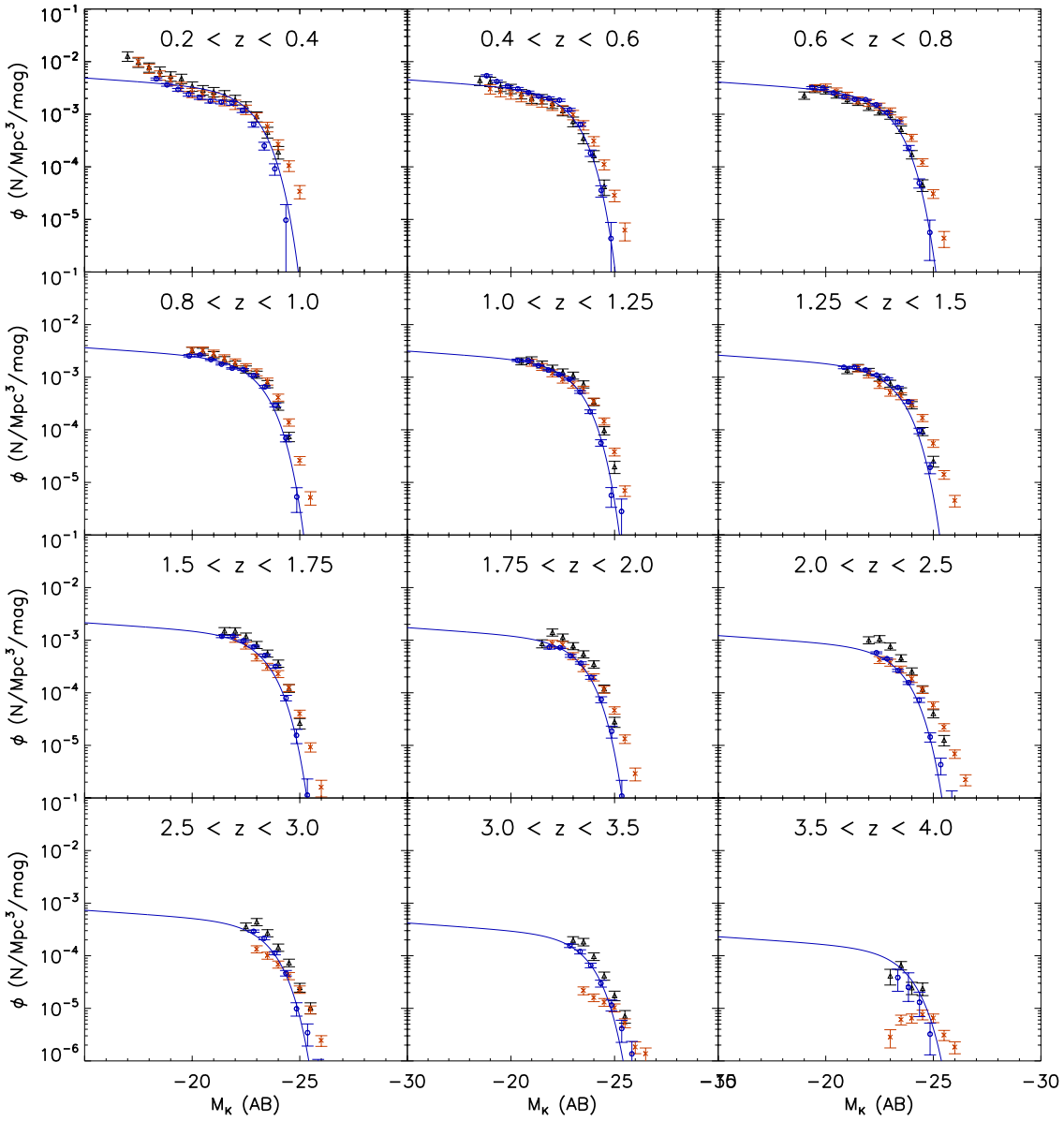

Figure 5.4: $1/V_{max}$ **LF in the VIDEO-CFHTLS-W1 field. The red triangles represent the** $1/V_{max}$ **LF from the VIDEO-CFHTLS-W1 catalogue presented here and the black triangles are the** $1/V_{max}$ **points from the VIDEO-CFHTLS-D1 LF presented in Section 4.3.2. The blue open circles and the solid blue line are the** $1/V_{max}$ **LF and the best-fit evolving Schechter function obtained by maximum likelihood analysis from the UKIDSS Ultra Deep Survey from Cirasuolo et al. (2010).**

lution and luminosity dependent density evolution are presented separately. Figures 5.5, 5.7 & 5.9 show the double schechter functions for the three types of evolution corresponding to the median and best-fit values of the fit parameters, with Figures 5.6, 5.8 & 5.10 showing the associated posterior PDFs for the different evolutions with contours at the 95 and 68 per cent confidence levels plotted. The median values for the parameters are listed in Table 5.1, along with the best-fit values and the best-fit reduced χ^2 values for each evolution.

As with the VIDEO-CFHTLS-D1 LF, pure luminosity evolution gives the worst fit to the VIDEO-CFHTLS-W1 LF. The two fits to the evolution are in very good agreement with each other, with the median parameters all agreeing to within 1σ. As before, there is no need for a two-term luminosity evolution; k_{M1} and k_{M2} agree to within 1σ and again, $z_c = 1.37$ is very near the top of the redshift range, limiting the effect k_{M2} has on the evolution. This is to be expected, given that the redshift range studied only goes up to $z = 1.5$, and is analogous to the case in VIDEO-CFHTLS-D1 LF, where $z_c = 2.75$ is also just inside the relevant redshift range. The evolution is very gentle, producing a dimming of 0.2 mag from $z \approx 1.5$ to $z \approx 0.3$.

Density dependent evolution is a slightly better fit for the VIDEO-CFHTLS-W1 LF, and is also in very good agreement with the VIDEO-CFHTLS-D1 density dependent evolution. As before, there is a very gentle evolution with $k_{\phi 1} = -0.62$ below $z_c = 1.18$ changing to a much faster one above it with $k_{\phi 2} = -2.48$. The best reduced χ^2 values for the luminosity and density dependent evolution are much more similar here, which can be explained by the fact that for the bulk of the data, both cases only need very weak evolution; the median value of k_{M1} agrees with no low-redshift luminosity evolution (i.e. $k_{M1} = 0$) to within 1σ and the median value of $k_{\phi 1}$ agrees with no low-redshift density evolution (i.e. $k_{\phi 1} = 0$) to within 2σ. Pure luminosity evolution has more trouble fitting the fainter end of the LF than pure density evolution, but both cases struggle with the bright end of the highest redshift bin.

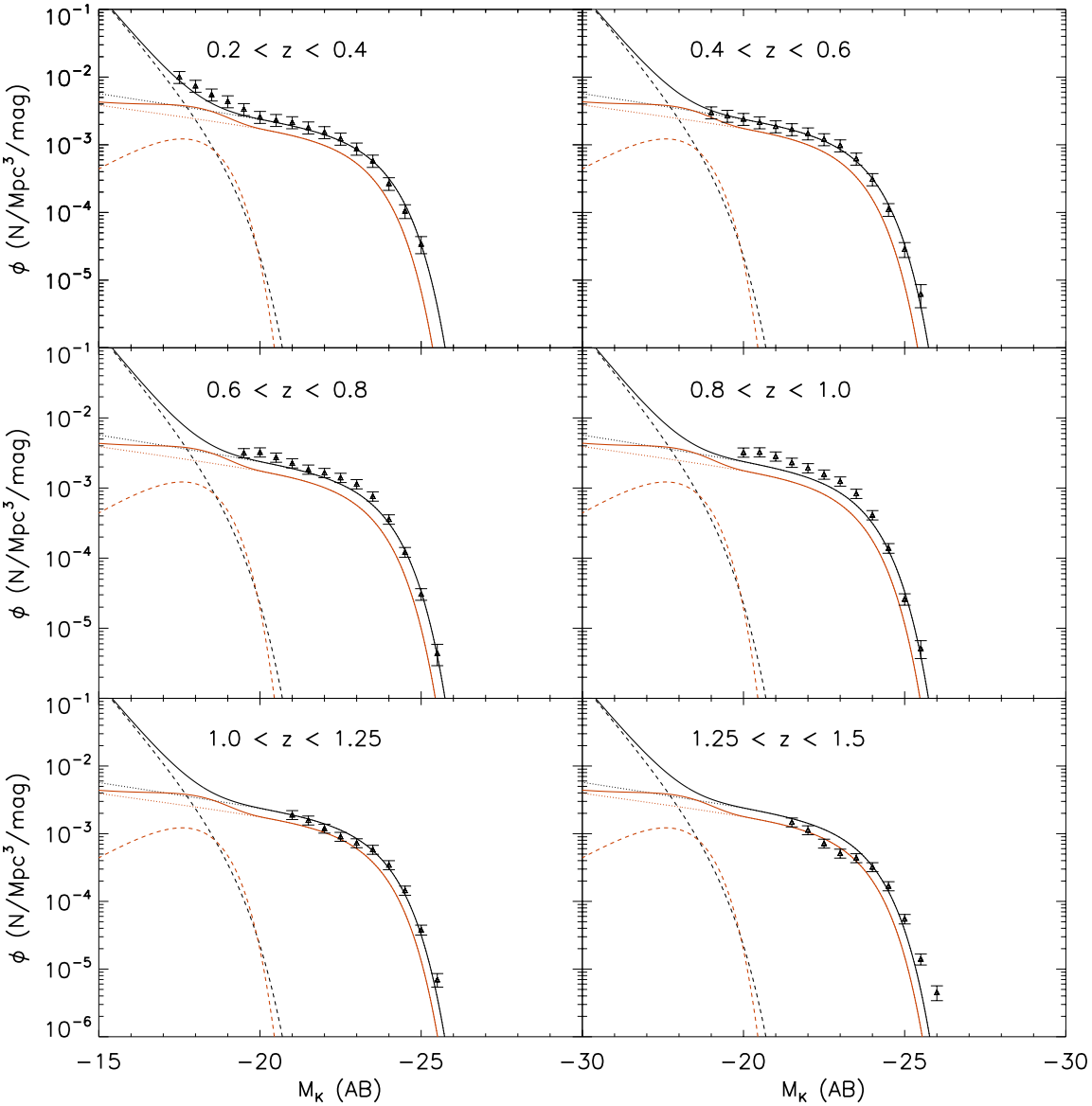

Figure 5.5: Median and best-fit double Schechter functions between $0.2 < z < 1.5$ in VIDEO-CFHTLS-W1 with pure luminosity dependent evolution. The fit parameters are listed in the first column of Table 5.1. Black triangles are the VIDEO-CFHTLS-W1 $1/V_{max}$ points, the solid lines are the double Schechter functions and the dotted and dashed lines show the bright and faint parts of the double Schechter function respectively. The best-fit evolution is shown in black and the median fit in red.

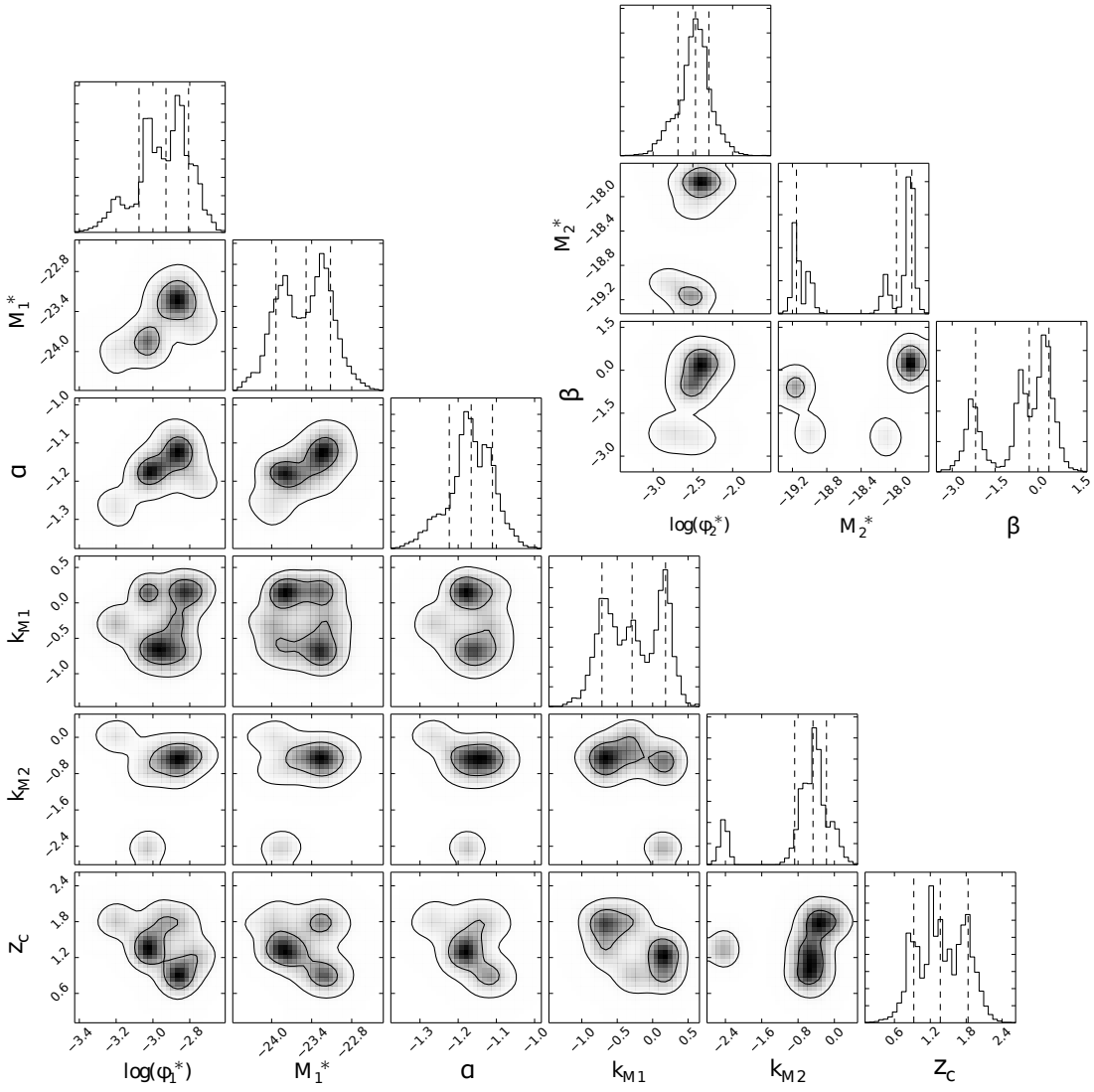

Figure 5.6: Estimation of the posterior PDF for a double Schechter function with pure luminosity dependent evolution. The 2-D plots show the marginalised PDF for each two parameters with contours plotted at the 95 and 68 per cent confidence levels, while the 1-D histograms show the marginalised PDF for each parameter individually, with dotted lines showing the 16th, 50th and 84th percentiles.

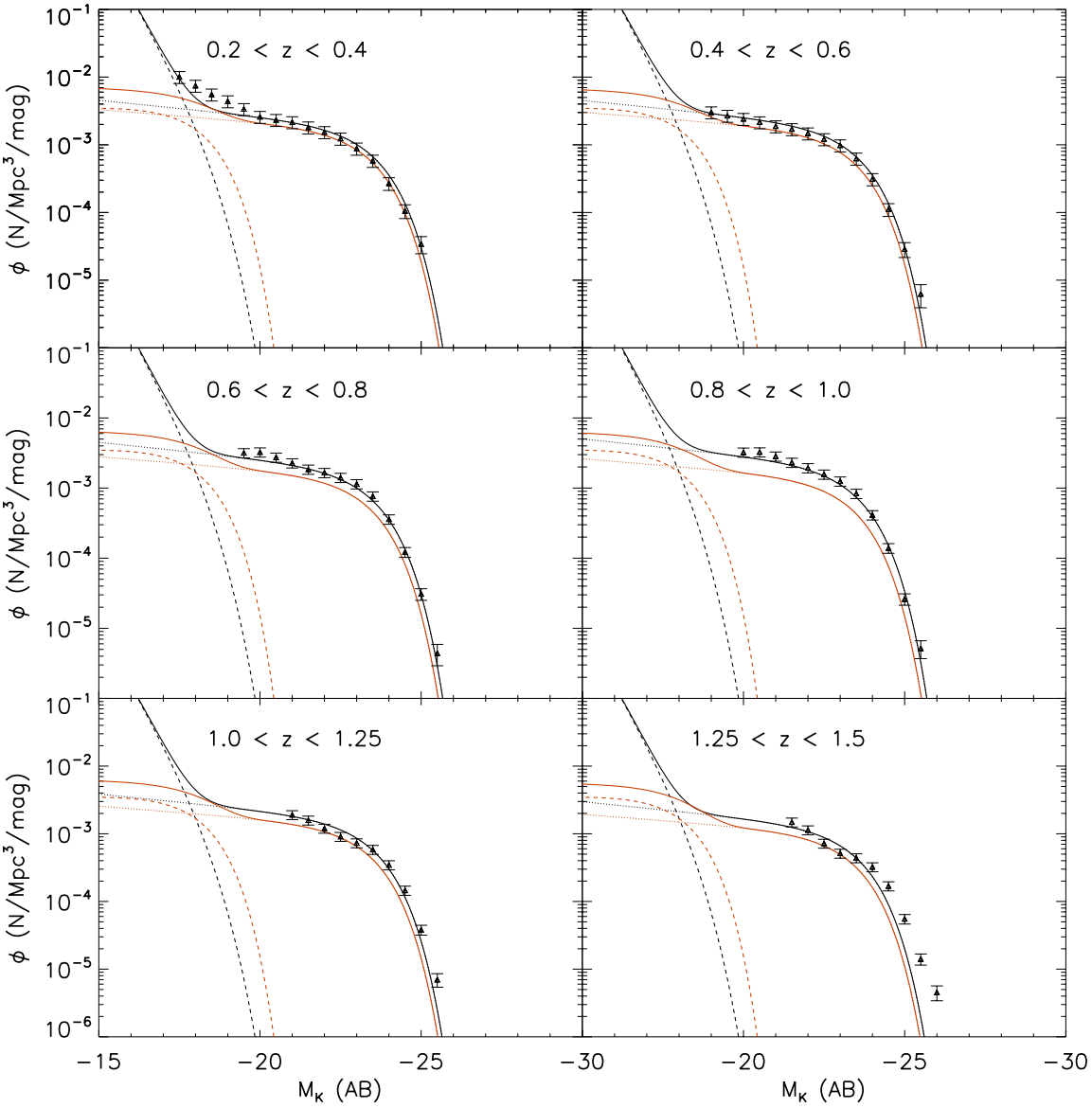

Figure 5.7: Median and best-fit double Schechter functions between $0.2 < z < 1.5$ in VIDEO-CFHTLS-W1 with pure density dependent evolution. The fit parameters are listed in the middle column of Table 5.1. Black triangles are the VIDEO-CFHTLS-W1 $1/V_{max}$ points, the solid lines are the double Schechter functions and the dotted and dashed lines show the bright and faint parts of the double Schechter function respectively. The best-fit evolution is shown in black and the median fit in red.

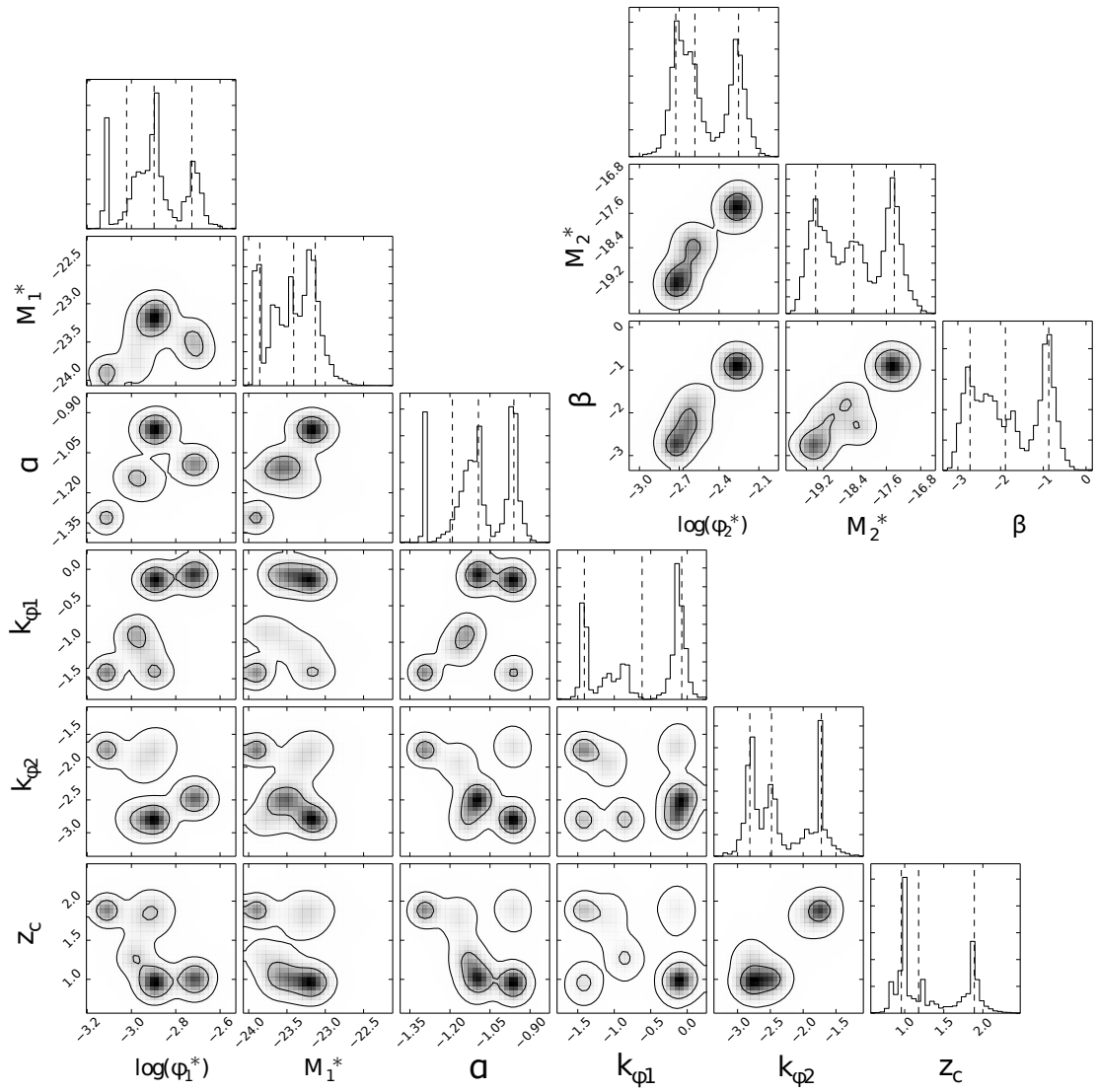

Figure 5.8: Estimation of the posterior PDF for a double Schechter function with pure density dependent evolution. The 2-D plots show the marginalised PDF for each two parameters with contours plotted at the 95 and 68 per cent confidence levels, while the 1-D histograms show the marginalised PDF for each parameter individually, with dotted lines showing the 16th, 50th and 84th percentiles.

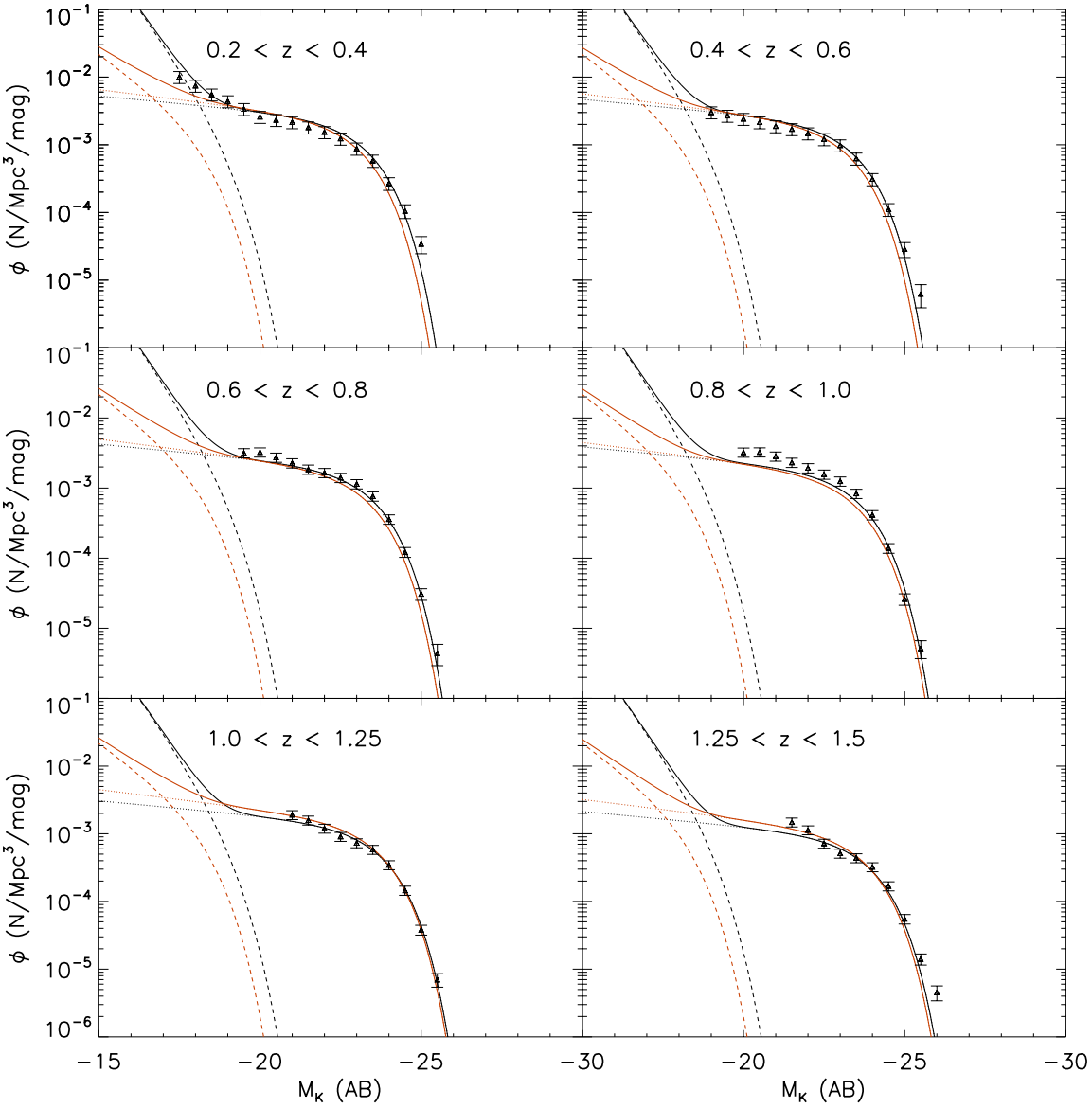

Figure 5.9: Median and best-fit double Schechter functions between $0.2 < z < 1.5$ in VIDEO-CFHTLS-W1 with luminosity dependent density evolution. The fit parameters are listed in the last column of Table 5.1. Black triangles are the VIDEO-CFHTLS-W1 $1/V_{max}$ points, the solid lines are the double Schechter functions and the dotted and dashed lines show the bright and faint parts of the double Schechter function respectively. The best-fit evolution is shown in black and the median fit in red.

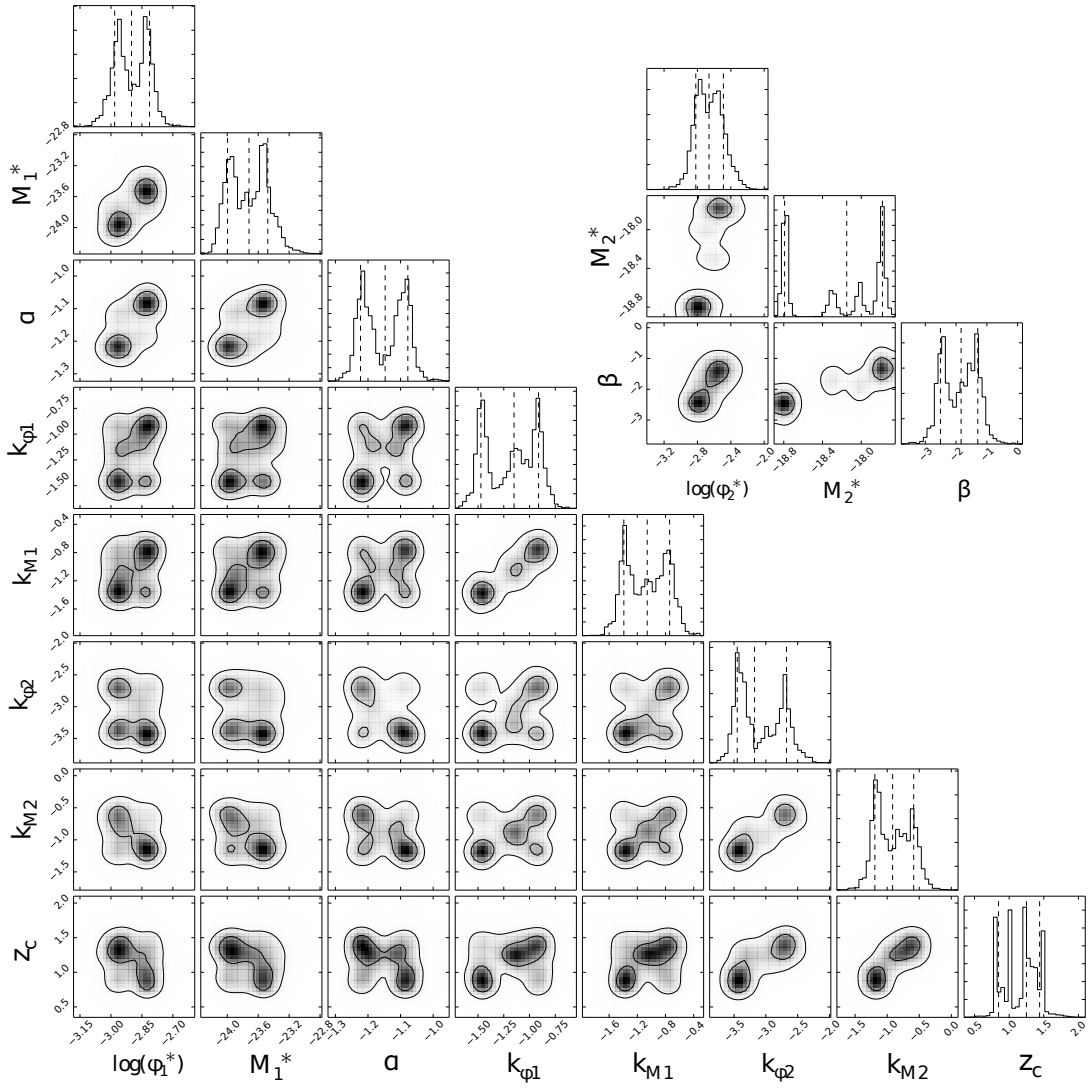

Figure 5.10: Estimation of the posterior PDF for a double Schechter function with luminosity dependent density evolution. The 2-D plots show the marginalised PDF for each two parameters with contours plotted at the 95 and 68 per cent confidence levels, while the 1-D histograms show the marginalised PDF for each parameter individually, with dotted lines showing the 16th, 50th and 84th percentiles.

Again, the best fit is given by luminosity dependent density evolution, which is also in very good agreement with the VIDEO-CFHTLS-D1. There is a gentle dimming of 0.8 mags from $z = 1.5$ to $z = 0.3$, while the volume density has slightly more than doubled. Most of the evolution is governed by the low redshift evolutionary term (k_{M1} and $k_{\phi 1}$) for both the luminosity and density dependent aspects, as can be expected from the reduced redshift range. Both the luminosity and density dependent parts of the evolution are stronger than they were individually, as before. As can be seen from Figure 5.10, $k_{\phi 1}$ and k_{M1}, and $k_{\phi 2}$ and k_{M2} are highly correlated, with most of the probability density split between either low k_ϕ and low k_M, or high k_ϕ and high k_M, meaning that the luminosity and density evolutionary parameters are always working to balance each other. The best reduced χ^2 values for all three fits are much closer than in the VIDEO-CFHTLS-D1 field, which is unsurprising given that the data is mostly in the weak evolutionary regime, with only one redshift bin constraining $k_{\phi 2}$ and k_{M2}.

5.4.2 Comparison with UDS

As in Chapter 4, I have also fitted double Schechter functions evolving according to the parameterisation in Cirasuolo et al. (2010) laid out in Equations 4.10 and 4.11. Here I present Schechter functions with pure luminosity evolution, pure density evolution and luminosity dependent density evolution.

Figure 5.11 shows the median and best fits for luminosity dependent evolution, with the associated posterior PDF shown in Figure 5.12 with 1 and 2σ contours plotted on it. Figure 5.13 shows the median and best fits for density dependent evolution with associated contour plots in Figure 5.14, and Figure 5.15 shows the median and best-fit Schechter functions with luminosity dependent density evolution with the associated contour plots in Figure 5.14. The median and best-fit values for each parameterisation are listed in Table 5.2, with the best available reduced

Table 5.1: The median double Schechter parameters and best-fit reduced χ^2 from Equation 4.6 with luminosity dependent evolution, density dependent evolution or luminosity dependent density evolution according to either Equation 4.8 or Equation 4.7, or both, fitted to the VIDEO-CFHTLS-W1 LF.

	Evolution type		
	M_1^* only	ϕ_1^* only	M_1^* & ϕ_1^* both
	Median values		
$\log_{10}(\phi^*_{1_z}/\mathrm{Mpc}^{-3})$	$-2.93^{+0.13}_{-0.15}$	$-2.90^{+0.17}_{-0.12}$	$-2.90^{+0.08}_{-0.08}$
$M^*_{1_z}$	$-23.48^{+0.37}_{-0.45}$	$-23.41^{+0.28}_{-0.44}$	$-23.72^{+0.24}_{-0.28}$
α	$-1.17^{+0.06}_{-0.06}$	$-1.09^{+0.13}_{-0.10}$	$-1.15^{+0.07}_{-0.08}$
$k_{\phi 1}$	0 (fixed)	$-0.62^{+0.54}_{-0.79}$	$-1.15^{+0.24}_{-0.32}$
$k_{\phi 2}$	0 (fixed)	$-2.48^{+0.76}_{-0.33}$	$-3.18^{+0.50}_{-0.27}$
k_{m1}	$-0.29^{+0.47}_{-0.43}$	0 (fixed)	$-1.06^{+0.32}_{-0.33}$
k_{m2}	$-0.47^{+0.30}_{-0.40}$	0 (fixed)	$-0.91^{+0.33}_{-0.28}$
z_c	$1.37^{+1.37}_{-0.46}$	$1.18^{+0.72}_{-0.22}$	$1.25^{+0.19}_{-0.40}$
$\log_{10}(\phi_2^*/\mathrm{Mpc}^{-3})$	$-2.47{+}0.17_{-0.22}$	$-2.35^{+0.33}_{-0.39}$	$-2.66^{+0.17}_{-0.16}$
M_2^*	$-17.98^{+0.18}_{-1.16}$	$-18.12^{+1.04}_{-1.01}$	$-18.15^{+0.37}_{-0.64}$
β	$-0.31^{+0.69}_{-1.87}$	$-0.96^{+1.21}_{-2.06}$	$-1.83^{+0.54}_{-0.75}$
	Best-fit values		
$\log_{10}(\phi^*_{1_z}/\mathrm{Mpc}^{-3})$	$-2.84^{+0.22}_{-0.13}$	$-2.72^{+0.13}_{-0.17}$	$-2.78^{+0.13}_{-0.07}$
$M^*_{1_z}$	$-23.65^{+0.13}_{-0.23}$	$-23.52^{+0.10}_{-0.19}$	$-23.65^{+0.07}_{-0.10}$
α	$-1.18^{+0.14}_{-0.28}$	$-1.12^{+0.09}_{-0.19}$	$-1.11^{+0.07}_{-0.11}$
$k_{\phi 1}$	0 (fixed)	$-0.04^{+0.12}_{-0.18}$	$-0.89^{+0.15}_{-0.08}$
$k_{\phi 2}$	0 (fixed)	$-2.34^{+0.19}_{-0.09}$	$-3.41^{+0.10}_{-0.22}$
k_{m1}	$-0.01^{+0.24}_{-0.14}$	0 (fixed)	$-0.79^{+0.17}_{-0.10}$
k_{m2}	$-0.40^{+0.14}_{-0.16}$	0 (fixed)	$-1.29^{+0.09}_{-0.15}$
z_c	$1.17^{+0.15}_{-0.41}$	$1.00^{+0.10}_{-0.21}$	$1.00^{+0.11}_{-0.09}$
$\log_{10}(\phi_2^*/\mathrm{Mpc}^{-3})$	$-3.00{+}0.29_{-0.14}$	$-2.46^{+0.08}_{-0.18}$	$-2.56^{+0.18}_{-0.11}$
M_2^*	$-19.03^{+0.15}_{-0.40}$	$-18.13^{+0.11}_{-0.20}$	$-18.77^{+0.11}_{-0.22}$
β	$-2.40^{+0.22}_{-0.24}$	$-3.04^{+0.16}_{-0.15}$	$-2.63^{+0.22}_{-0.24}$
χ^2 (reduced)	1.76	1.44	1.26

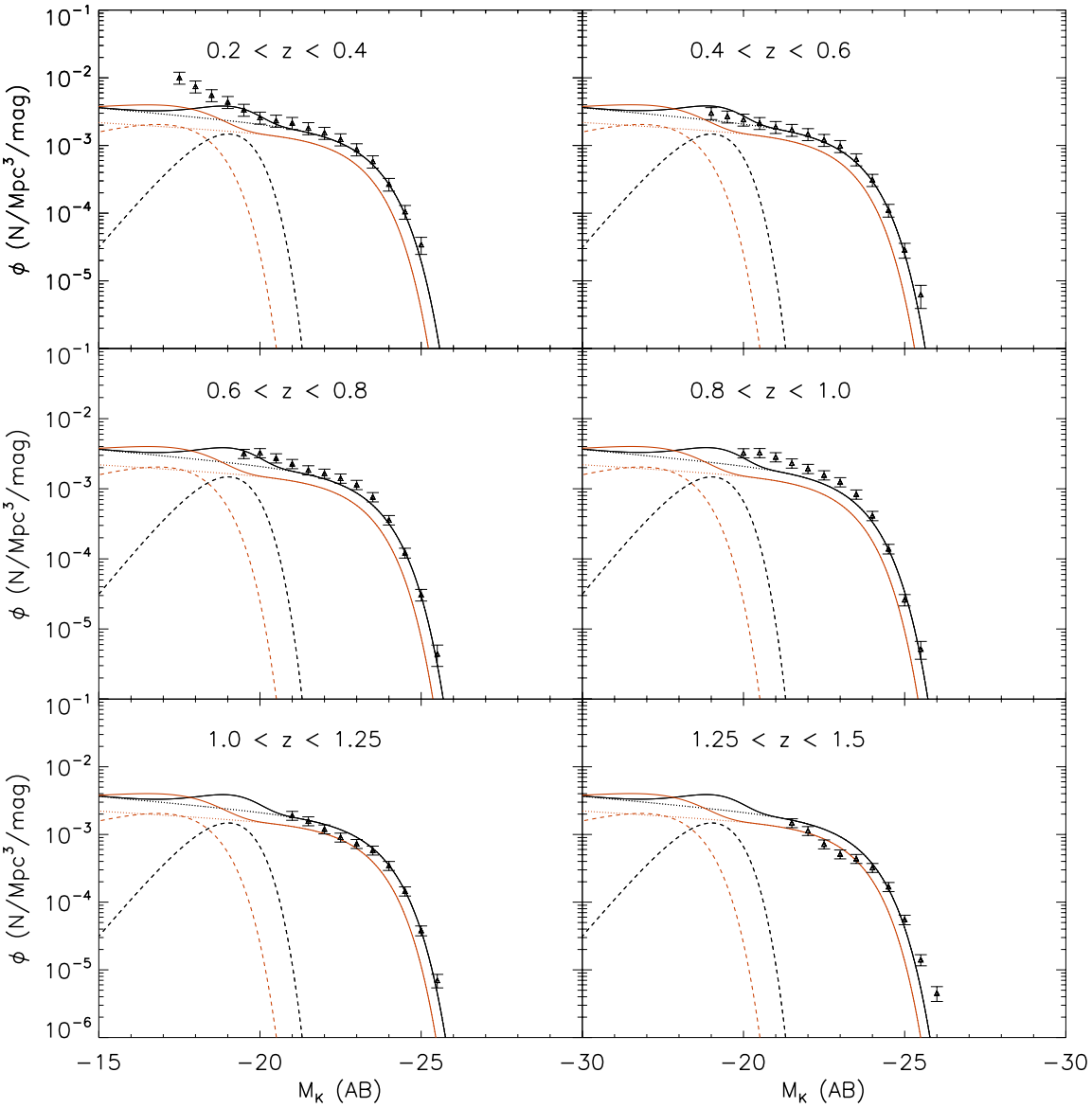

Figure 5.11: Median and best-fit double Schechter functions between $0.2 < z < 1.5$ in VIDEO-CFHTLS-W1 with pure luminosity dependent evolution following the Cirasuolo et al. (2010) parameterisation. The fit parameters are listed in the first column of Table 5.2. Black triangles are the VIDEO-CFHTLS-W1 $1/V_{max}$ points, the solid lines are the double Schechter functions and the dotted and dashed lines show the bright and faint parts of the double Schechter function respectively. The best-fit evolution is shown in black and the median fit in red.

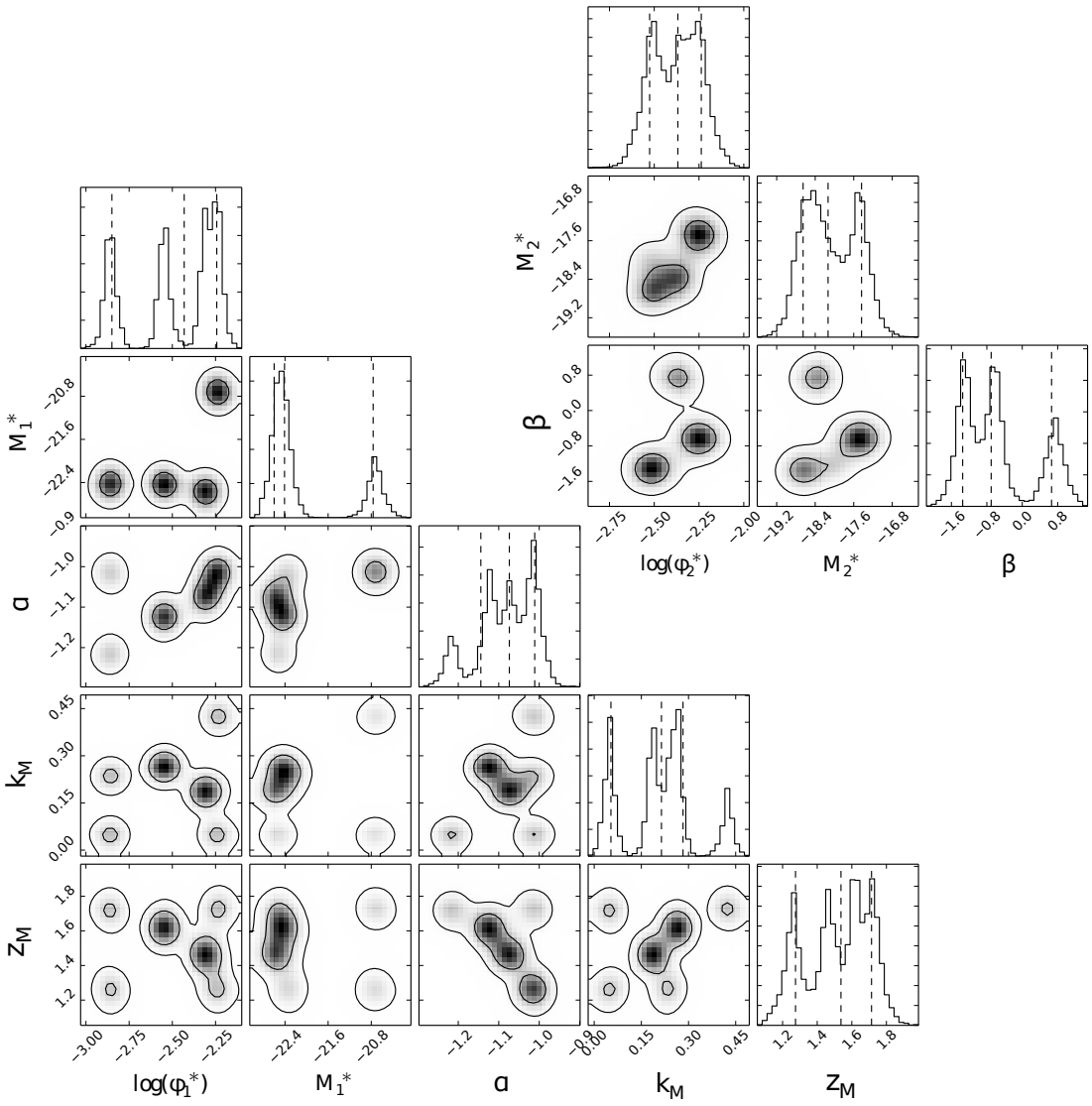

Figure 5.12: Estimation of the posterior PDF for a double Schechter function with pure luminosity dependent evolution following the Cirasuolo et al. (2010) parameterisation. The 2-D plots show the marginalised PDF for each two parameters with contours plotted at the 95 and 68 per cent confidence levels, while the 1-D histograms show the marginalised PDF for each parameter individually, with dotted lines showing the 16th, 50th and 84th percentiles.

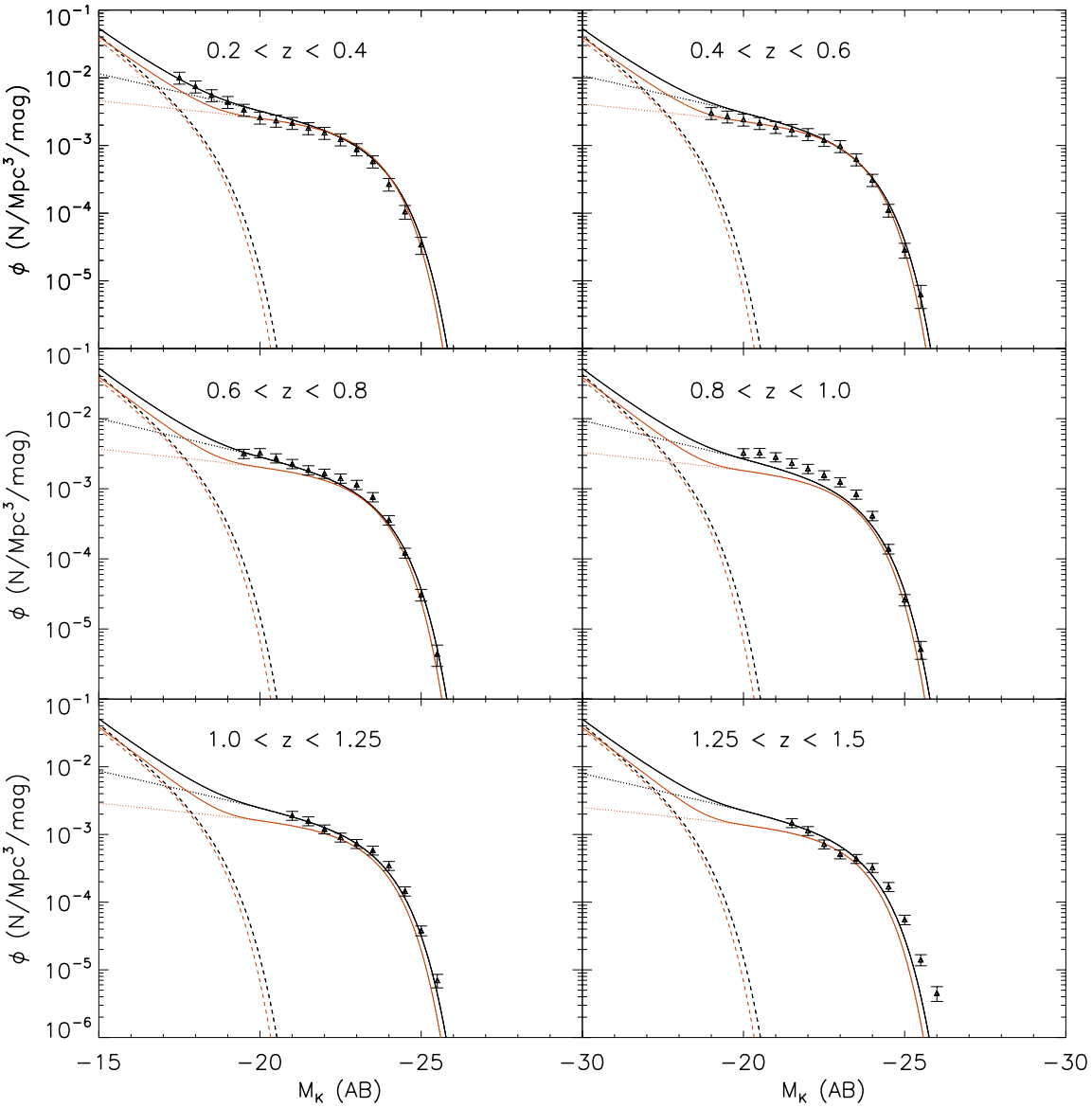

Figure 5.13: Median and best-fit double Schechter functions between $0.2 < z < 1.5$ in VIDEO-CFHTLS-W1 with pure density dependent evolution following the Cirasuolo et al. (2010) parameterisation. The fit parameters are listed in the second column of Table 5.2. Black triangles are the VIDEO-CFHTLS-W1 $1/V_{max}$ points, the solid lines are the double Schechter functions and the dotted and dashed lines show the bright and faint parts of the double Schechter function respectively. The best-fit evolution is shown in black and the median fit in red.

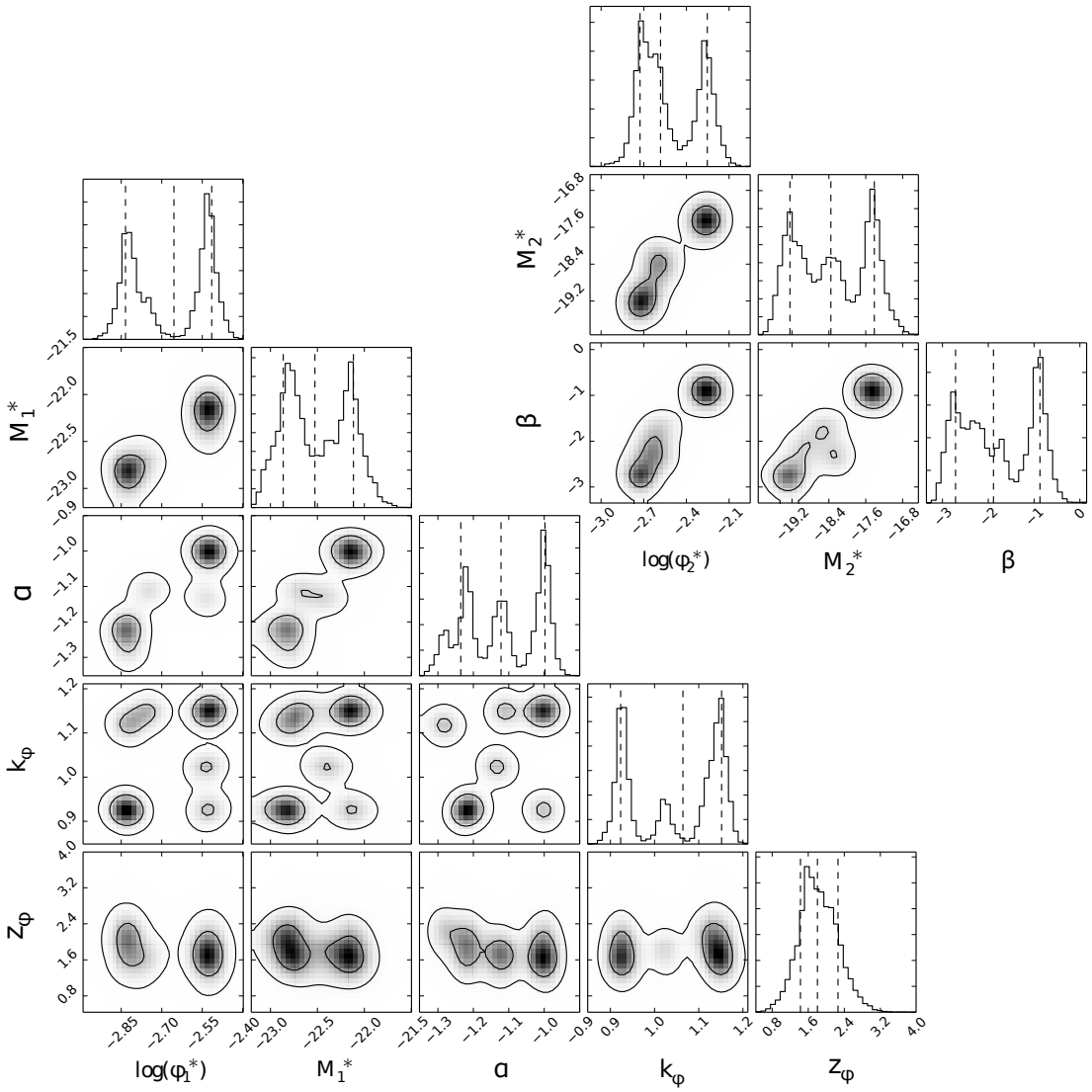

Figure 5.14: Estimation of the posterior PDF for a double Schechter function with pure density dependent evolution following the Cirasuolo et al. (2010) parameterisation. The 2-D plots show the marginalised PDF for each two parameters with contours plotted at the 95 and 68 per cent confidence levels, while the 1-D histograms show the marginalised PDF for each parameter individually, with dotted lines showing the 16th, 50th and 84th percentiles.

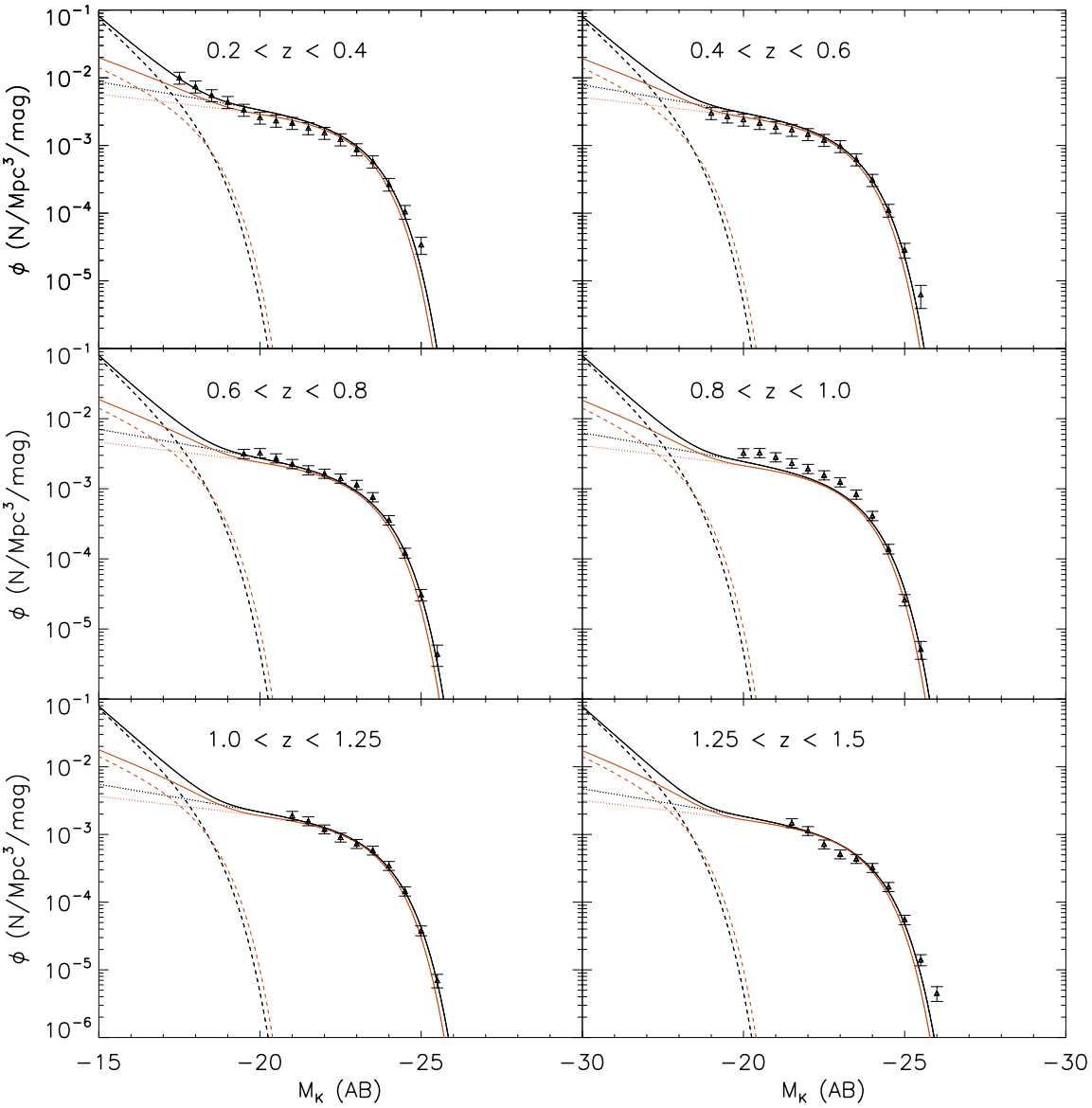

Figure 5.15: Median and best-fit double Schechter functions between $0.2 < z < 1.5$ in VIDEO-CFHTLS-W1 with luminosity dependent density evolution following the Cirasuolo et al. (2010) parameterisation. The fit parameters are listed in the third column of Table 5.2. Black triangles are the VIDEO-CFHTLS-W1 $1/V_{max}$ points, the solid lines are the double Schechter functions and the dotted and dashed lines show the bright and faint parts of the double Schechter function respectively. The best-fit evolution is shown in black and the median fit in red.

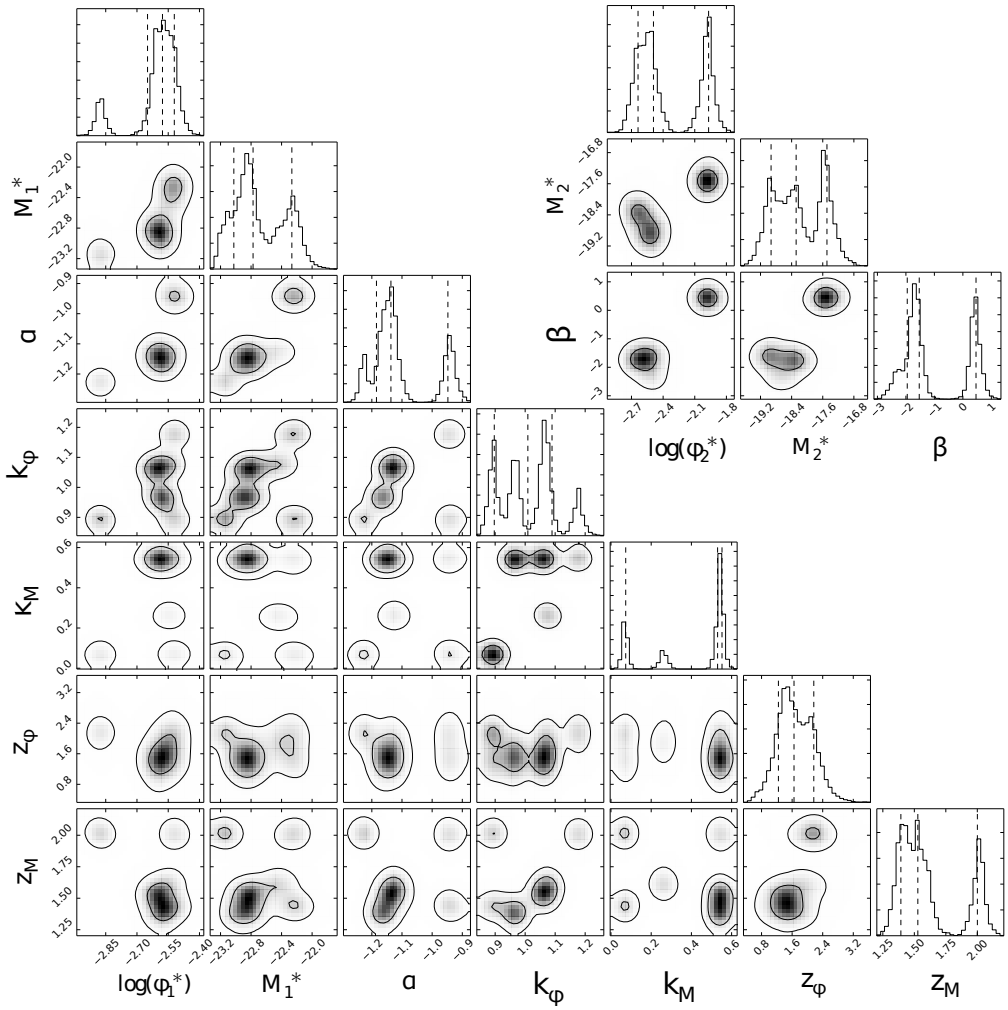

Figure 5.16: Estimation of the posterior PDF for a double Schechter function with luminosity dependent density evolution following the Cirasuolo et al. (2010) parameterisation. The 2-D plots show the marginalised PDF for each two parameters with contours plotted at the 95 and 68 per cent confidence levels, while the 1-D histograms show the marginalised PDF for each parameter individually, with dotted lines showing the 16th, 50th and 84th percentiles.

χ^2 quoted as well. As with the evolution presented for the VIDEO-CFHTLS-D1 feld in Chapter 4, pure luminosity dependent evolution produces the highest reduced χ^2, followed by pure density dependent evolution giving an intermediate fit, with luminosity dependent density evolution giving the best fit and lowest reduced χ^2. However, as with the results presented in Section 5.4.1, the difference between the three cases is much less extreme for this reduced redshift range. Pure luminosity evolution struggles more with the faint end (particularly at low redshift) and the knee (particularly at high redshift) of the LF and pure density dependent evolution has difficulty with the bright end of the LF, particularly in the highest redshift bin. This is still a small problem for the luminosity dependent density evolution in the highest redshift bin, but the fit is good elsewhere.

As in the VIDEO-CFHTLS-D1 field, the median parameters here mostly agree to within 1σ with the parameters measured in the UDS field, with the notable exceptions of ϕ_1^*, the volume density of the brighter Schechter function at $z = 0$, and k_ϕ. As before, this may be because of the noticeable upturn at faint magnitudes in the two lowest redshift bins, although this appears to be well described by the fainter Schechter function. It is also worth noting that M_1^* is fixed in Cirasuolo et al. (2010) at a value that is a slightly fainter than the value found here, which would require a slightly higher volume density, making the discrepancy slightly worse.

Unlike in Chapter 4, the different forms of evolution presented in Section 5.4.1 and Section 5.4.2 have much more similar reduced χ^2s, mostly due to the fact that the redshift range discussed here probes below the change in behaviour seen previously. The qualitative forms of the luminosity and density evolutions are much more similar up to $z = 1.5$, as can be seen from Figure 5.17, where the blue and red lines showing the two forms of evolution are very similar at all three redshifts, and they produce very similar dimming from $z = 1.5$ to $z = 0.3$ of 0.7 mags in Section 5.4.1 and 0.5 mags in Section 5.4.2, along with a comparable change in volume density, roughly

Table 5.2: The median double Schechter parameters and best reduced χ^2 from Equation 4.6 with luminosity dependent evolution, density dependent evolution or luminosity dependent density evolution taken from Cirasuolo et al. (2010), according to either Equation 4.11 or Equation 4.10, or both, fitted to the VIDEO-CFHTLS-W1 LF, along with the best-fit parameters single Schechter parameters from the UDS.

	Evolution type			
	M_1^* only	ϕ_1^* only	M_1^* & ϕ_1^* both	UDS
	Median values			
$\log_{10}(\phi_{1_0}^*/\mathrm{Mpc}^{-3})$	$-2.44^{+0.20}_{-0.41}$	$-2.66^{+0.15}_{-0.17}$	$-2.58^{+0.06}_{-0.07}$	-3.46 ± 0.05
$M_{1_0}^*$	$-22.41^{+1.64}_{-0.19}$	$-22.52^{+0.41}_{-0.33}$	$-22.77^{+0.51}_{-0.25}$	-22.26 (fixed)
α	$-1.07^{+0.06}_{-0.07}$	$-1.12^{+0.12}_{-0.12}$	$-1.14^{+0.19}_{-0.05}$	-1.07 ± 0.1
k_ϕ	0 (fixed)	$1.07^{+0.09}_{-0.14}$	$1.01^{+0.08}_{-0.11}$	1.47 ± 0.1
z_ϕ	-	$1.79^{+0.45}_{-0.38}$	$1.65^{+0.52}_{-0.41}$	1.70 ± 0.09
k_m	$0.22^{+0.07}_{-0.16}$	0 (fixed)	$0.53^{+0.22}_{-0.46}$	0.47 ± 0.2
z_m	$1.53^{+0.18}_{-0.26}$	-	$1.53^{+0.47}_{-0.13}$	1.78 ± 0.15
$\log_{10}(\phi_2^*/\mathrm{Mpc}^{-3})$	$-2.37^{+0.14}_{-0.15}$	$-2.57^{+0.32}_{-0.15}$	$-2.49^{+0.52}_{-0.15}$	-
M_2^*	$-18.14^{+0.69}_{-0.52}$	$-18.36^{+0.95}_{-0.89}$	$-18.28^{+0.79}_{-0.64}$	-
β	$-0.70^{+1.36}_{-0.63}$	$-1.86^{+1.00}_{-0.87}$	$-1.53^{2.00}_{-0.42}$	-
	Best-fit values			
$\log_{10}(\phi_{1_0}^*/\mathrm{Mpc}^{-3})$	$-2.37^{+0.12}_{-0.49}$	$-2.81^{+0.26}_{-0.18}$	$-2.61^{+0.05}_{-0.38}$	-3.46 ± 0.05
$M_{1_0}^*$	$-22.66^{+0.34}_{-0.16}$	$-22.76^{+0.26}_{-0.19}$	$-22.91^{+0.05}_{-0.38}$	-22.26 (fixed)
α	$-1.05^{+0.27}_{-0.47}$	$-1.27^{+0.10}_{-0.14}$	$-1.20^{+0.12}_{-0.29}$	-1.07 ± 0.1
k_ϕ	0 (fixed)	$1.08^{+0.07}_{-0.25}$	$1.06^{+0.07}_{-0.05}$	1.47 ± 0.1
z_ϕ	-	$2.85^{+0.04}_{-0.09}$	$1.54^{+0.05}_{-0.28}$	1.70 ± 0.09
k_m	$0.13^{+0.28}_{-0.43}$	0 (fixed)	$0.52^{+0.05}_{-0.28}$	0.47 ± 0.2
z_m	$1.45^{+0.27}_{-0.34}$	-	$1.43^{+0.05}_{-0.37}$	1.78 ± 0.15
$\log_{10}(\phi_2^*/\mathrm{Mpc}^{-3})$	$-2.53^{+0.27}_{-0.34}$	$-2.70^{+0.26}_{-0.17}$	$-2.46^{+0.06}_{-0.06}$	-
M_2^*	$-18.40^{+0.48}_{-0.18}$	$-18.62^{+0.24}_{-0.09}$	$-18.28^{+0.06}_{-0.07}$	-
β	$-1.06^{+0.13}_{-0.27}$	$-1.96^{+0.20}_{-0.12}$	$-2.05^{0.11}_{-0.30}$	-
χ^2 (reduced)	2.09	1.67	1.22	-

doubling the number of galaxies over the same redshift range. Combined, they give evidence for a gentle evolution since $z = 1.5$ of slowly increasing numbers of galaxies that are gradually dimming overall.

The upturn at the faint-end of the LF in the lowest redshift bins is more pronounced in the VIDEO-CFHTLS-W1 LF than the VIDEO-CFHTLS-D1 LF presented in Chapter 4, making a double Schechter function more necessary than in VIDEO-CFHTLS-D1 (a comparison of a single and double Schechter function is shown in Figure 4.10). All of the fits describe the upturn at the faint end of the LF at low redshift with the fainter of the two Schechter functions, either with a steep faint-end slope, β, which is favoured by almost all of the best-fit double Schechter functions, or with a high ϕ_2^* providing a bump over the necessary magnitude range. The contours in Figures 5.6, 5.8, 5.10, 5.12, 5.14 & 5.16 show a wide range in β, as is obvious from the errors in Tables 5.1 & Tables 5.2, though it tends to be correlated with ϕ_2^*, the volume density of the fainter Schechter function. Either a very negative β or a high ϕ_2^* will produce an upturn in the faint-end slope, although most of the fits prefer a steep β. In particular, the contours for the two parameterisations of luminosity dependent density evolution in Figures 5.10 & 5.16 will allow only either an extremely steep β or a high ϕ_2^*, with best-fits preferring and extreme β, while the fits corresponding to the median values are caught between the two peaks of the PDF.

As with Chapter 4, a similar multimodality affects many of the parameters, with several instances of degeneracy. The most obvious case is in the parameters describing the faint Schechter function for the luminosity dependent density evolution following the parameterisation of Cirasuolo et al. (2010) shown in Figure 5.16, as could be expected by the fact that in the region constrained by data, a very steep faint-end slope β or a high ϕ_2^* both look very similar, although they are extremely different elsewhere, where there are no constraints. The Cirasuolo et al. (2010) parameterisation also has a lot of degeneracy in the various redshift evolution parameters, as it is most sensitive

to change at higher redshift (at $z \sim z_\phi$ and $z \sim z_M$) where it is weakly constrained. Similarly, α, the faint end slope of the brighter Schechter function shows some degeneracy, as it describes a region also being described by three other parameters, namely the fainter Schechter function. As suggested before, this may show that, despite the low redshift upturn in the faint-end of the LF, a single Schechter function may provide a clearer picture, or a simpler form of evolution which uses local measurements for the values of the characteristic luminosity and density at $z = 0$.

5.5 Discussion

Before discussing the implications of the results presented in Section 5.4.1, I will first discuss the effect of photometric redshift uncertainties. Throughout my analysis I have assumed that the photometric redshifts in the VIDEO-CFHTLS-D1 and -W1 catalogues are correct. Errors on photometry, the width of the photometric bands and unconstrained sections of the SED will all add to the uncertainty on the photometric redshift for a galaxy; the fitting code provides a probability distribution giving the most likely redshift for each galaxy, used here, but also the probability that the galaxy is actually at a different redshift. This may be a small difference due to the width of probability peak at the best-fit redshift, or it may be large if there is a secondary peak elsewhere in the distribution. This will cause an uncertainty in the absolute magnitude of the galaxy, and so will mean that it contributes to the volume density of the wrong magnitude bin, or even the wrong redshift slice. In order to address this uncertainty, one would need to create mock catalogues where the redshifts are perturbed according to the redshift probability distribution and use these catalogues to create LFs, measuring the perturbing effect on the LF and so producing error bars accounting for photometric redshift uncertainties. This is a difficult process as the probability distributions only reflect how easy it is to fit the

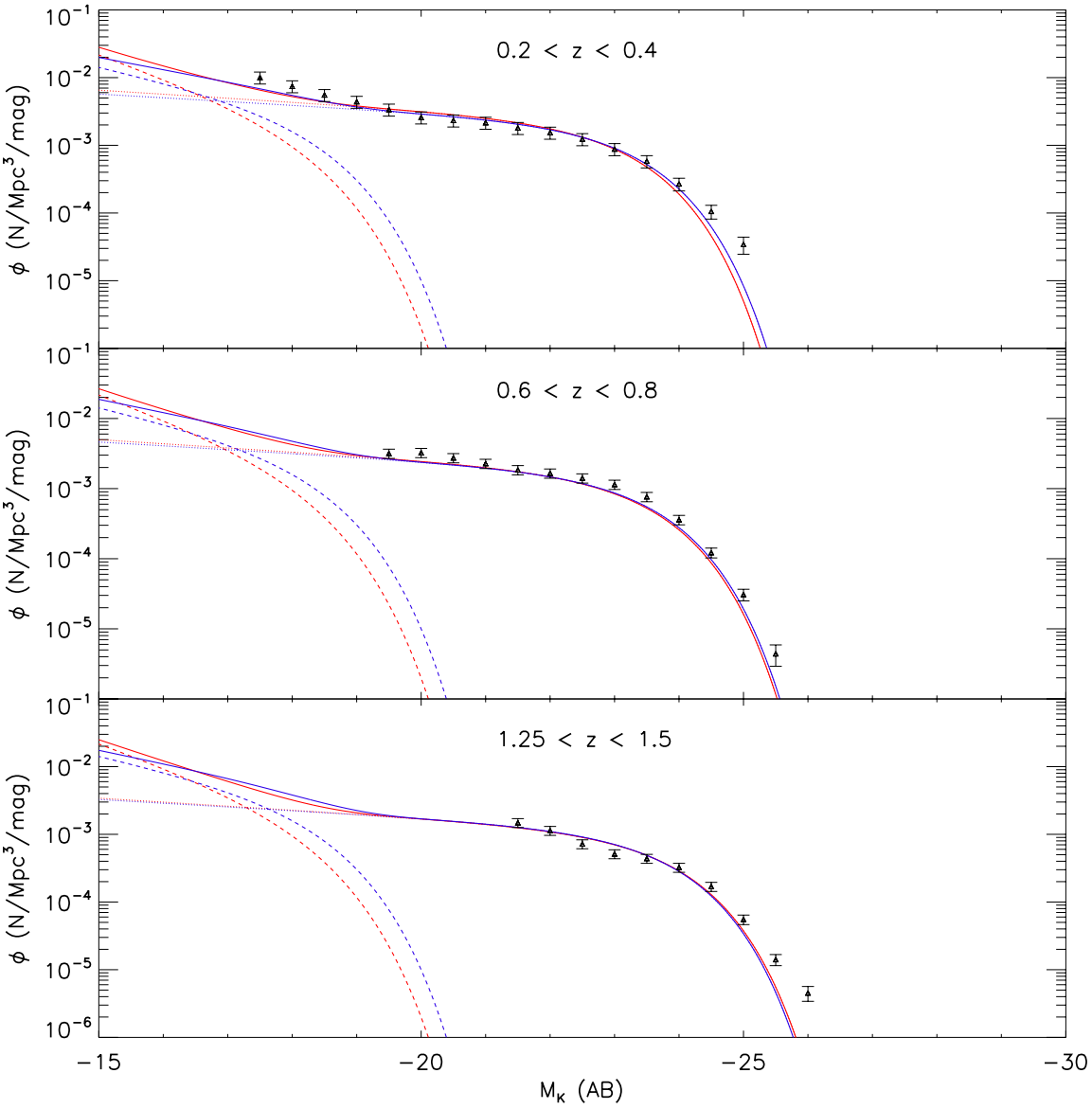

Figure 5.17: Comparison of the median LFs from Section 5.4.1 (red) and Section 5.4.2 (blue) at $z \approx 0.3$ (top panel), $z \approx 0.7$ (middle panel) and $z \approx 1.5$ (bottom panel). As before, the brighter Schechter function is shown in dotted lines, the fainter Schechter function is shown in dashed lines and the full double Schechter function is shown in solid lines.

data to a SED at a particular redshift, rather than the true probability that a galaxy is at a particular redshift, and so they can be misleading. Improved photometric redshift fitting with, for instance, some accounting for how likely different SEDs are, would produce more realistic redshift probability distributions, as well as more better photometric redshifts, leading to a better ability to account for this source of uncertainty.

As in Chapter 4, I find a combined evolution in density and luminosity to be the best fit to the VIDEO-CFHTLS-W1 LFs. Both forms of evolution presented in Section 5.4.1 and Section 5.4.2 represent a constant change in both luminosity and volume density that adds up to a decrease in M^* of $\Delta M = 0.6$ from $z = 1.5$ to $z = 0.3$ and while ϕ^* has increased two and a half times over the same redshift range. The VIDEO-CFHTLS-W1 K_s-band LF at $z < 1.5$ undergoes a mixture of slow luminosity evolution dominated by passive ageing of the stellar populations in the largest galaxies, and slow density evolution as mergers take a dominant role in evolving the number density of galaxies.

This evolution is consistent with what was measured in the VIDEO-CFHTLS-D1 field as well as with several previous studies such as Caputi et al. (2006), who measure the K_s-band LF of 2905 galaxies in the 131 arcmin^2 GOODS Chandra Deep Field South out to $z \approx 2.5$, Cirasuolo et al. (2010) who measure the K-band LF of 50,000 galaxies up to $z \approx 4$ in the 0.7 degree^2 UDS, and Cool et al. (2012), who measure the optical luminosity function of 12,500 spectroscopically selected galaxies from $0.05 < 0.75$ over the 7.6 degree^2 Boötes field. However, it is at odds with the decrease in the volume density since $z \approx 0.65$ measured in Loveday et al. (2015), who present the $ugriz'$ LFs of 170,000 galaxies in the 180 degree^2 GAMA-II survey, but they postulate this may be due to a local underdensity masquerading as evolution.

The obvious upturn in the faint-end of the low-redshift LF fainter than $M_K \sim -20$ necessitates the use of a double Schechter function, as found by Loveday et al. (2012)

at $z < 0.5$ (though they only see an upturn at $z < 0.1$, and do not reach faint enough at higher redshifts to see any upturn; their z'-band LF only goes down to $M_{z'} = -22$ at $z \approx 0.15$, compared to $M_K = -17.5$ at $z \approx 0.3$ reached here) and by Blanton et al. (2005) at extremely low redshift. The steepness of the faint-end slope is likely to be slightly underestimated due to the correlation between luminosity and surface brightness (Cameron & Driver, 2007; Driver, 1999) introducing an observational bias that tends to undercount dwarf galaxies. Blanton et al. (2005) and Geller et al. (2012) both find that a careful consideration of the completeness of low surface brightness galaxies causes the measured faint-end slope to steepen. It is worth emphasising that for this reason the steepening of the faint-end slope between the three lowest redshift LFs presented here and in Chapter 4 (particularly visible between the two lowest redshift LFs in this Chapter) is unlikely to be due to evolution and is more likely to be an effect of the incompleteness of low surface brightness galaxies, which is worse at fainter apparent magnitude and will increasingly flatten the faint-end of the LF in the higher redshift bins.

Baldry et al. (2008) suggest that the increase in number density at low luminosities and low stellar mass may be due to the efficiency of the feedback mechanisms in this luminosity range levelling off with luminosity, rather than continuing to increase in efficiency with decreasing luminosity. The correlation between luminosity and surface brightness will mean that the faint-end of the LF is increasingly dominated by low surface brightness galaxies at lower luminosities (as seen at low redshift by Blanton et al., 2005). Low surface brightness galaxies have been seen to have very low star formation rates compared to equivalent luminosity galaxies of higher surface brightness (O'Neil et al., 2007; van Zee, 2001). They appear to be less efficient at converting their gas into stars than higher surface brightness galaxies (Schombert et al., 2001), with star formation rate efficiencies an order of magnitude lower (Boissier et al., 2008), as well as having a history of very low star formation rates (Schombert et al., 2001)

and present day populations of very young stars. O'Neil et al. (1998) suggest that the star formation histories of low surface brightness galaxies may only be explainable by a fundamentally different form of star formation. Given this combination of reduced star formation rate efficiency and a low star formation history compared to higher surface brightness galaxies of equivalent mass and luminosity, it may be that star formation and supernovae have less of a feedback effect on these galaxies, and so on the very faint end of the LF where they come to dominate.

5.6 Conclusions

I have presented the rest-frame K_s-band luminosity functions out to $z = 1.5$ for the VIDEO-CFHTLS-W1 field, where the combination of large area and deep IR and optical imaging provides a vast number of objects with photometric redshifts. I have used the $1/V_{max}$ method to measure the luminosity functions of these objects over the range of $0.2 < z < 1.5$ in 6 redshift slices.

The fact that the VIDEO-CFHTLS-W1 field has such a large area has allowed me to probe very large volumes in every redshift slice, producing robust volume densities as bright as M = -26 at $z = 1.5$ and M = -25 at $z = 0.2$, allowing for the measurement of the bright end and the knee of the LF as well as constraining the luminosity and density evolution over this redshift range. I find an increase in characteristic magnitude and a decrease in density with redshift, with galaxies at $z = 1.5$ approximately 0.6 magnitudes brighter and 2.5 times less dense than at low redshift. The high sensitivity has allowed me to reach down to very faint apparent magnitudes and capture the beginning of the upturn of the faint-end of the LF at $z \sim 0.2-0.6$, providing constraints in this crucial luminosity regime that is so sensitive to feedback from supernovae and star formation.

Chapter 6

Comparison of the VIDEO Luminosity Functions with the Horizon-AGN Simulation

6.1 Introduction

Observational astronomy is unable to frame an experiment and instead can only observe what already exists. For this reason, it is crucial to compare observations to simulations as this is a key way of testing our assumptions about the physics that govern the evolution of our Universe. For galaxy evolution, this means modelling the formation of structure using large simulations set within the ΛCDM paradigm and accounting for gravity, hydrodynamics, black hole growth, star formation, feedback from AGN and supernovae, and the creation of different stellar populations and levels of chemical enrichment.

There are two main routes to modelling galaxy evolution; the most direct is a numerical hydrodynamic simulation which solves the equations of gravity, thermal physics and hydrodynamics for all of its particles, representing stars, gas and dark

matter and tracing the evolution of all three as well as heavy metals (e.g. Sijacki et al. 2015; Springel 2010; Vogelsberger et al. 2014). However, this method is extremely computationally expensive, making it difficult to cover the very large range in scale necessary to fully describe galaxy evolution, and normally resorts to sub-grid prescriptions of the smaller scale processes such as black hole growth, star formation and feedback mechanisms which are then difficult to test comprehensively. Alternatively, semi-analytical modelling (SAM; e.g Somerville et al. 2008; White & Frenk 1991; White & Rees 1978) can be used to simulate galaxies over very large ranges and volumes and to test a wide range of the sub-grid physics used to describe processes below the resolution of a simulation by comparison with observations. The combination of these two methods allows for a semi-direct way of modelling the formation of galaxies and extra-galactic structure that uses sub-grid physics that has been tested and tuned to agree with a restricted set of observations (e.g. Dubois et al. 2012; Schaye et al. 2015; Vogelsberger et al. 2013), usually at $z = 0$, such as the proportionality constant between gas density and star formation density (Kennicutt, 1998; Krumholz & Tan, 2007), the local supermassive black hole density (Shankar et al., 2004), the correlations between black hole mass and bulge mass (Häring & Rix, 2004) or black hole mass and velocity dispersion (Tremaine et al., 2002), the stellar mass-halo mass relation as measured with abundance matching (Guo et al., 2010; Moster et al., 2010, 2013), stellar mass functions (Baldry et al., 2008) or the cosmic SFRD (Behroozi et al., 2013; Hopkins & Beacom, 2006).

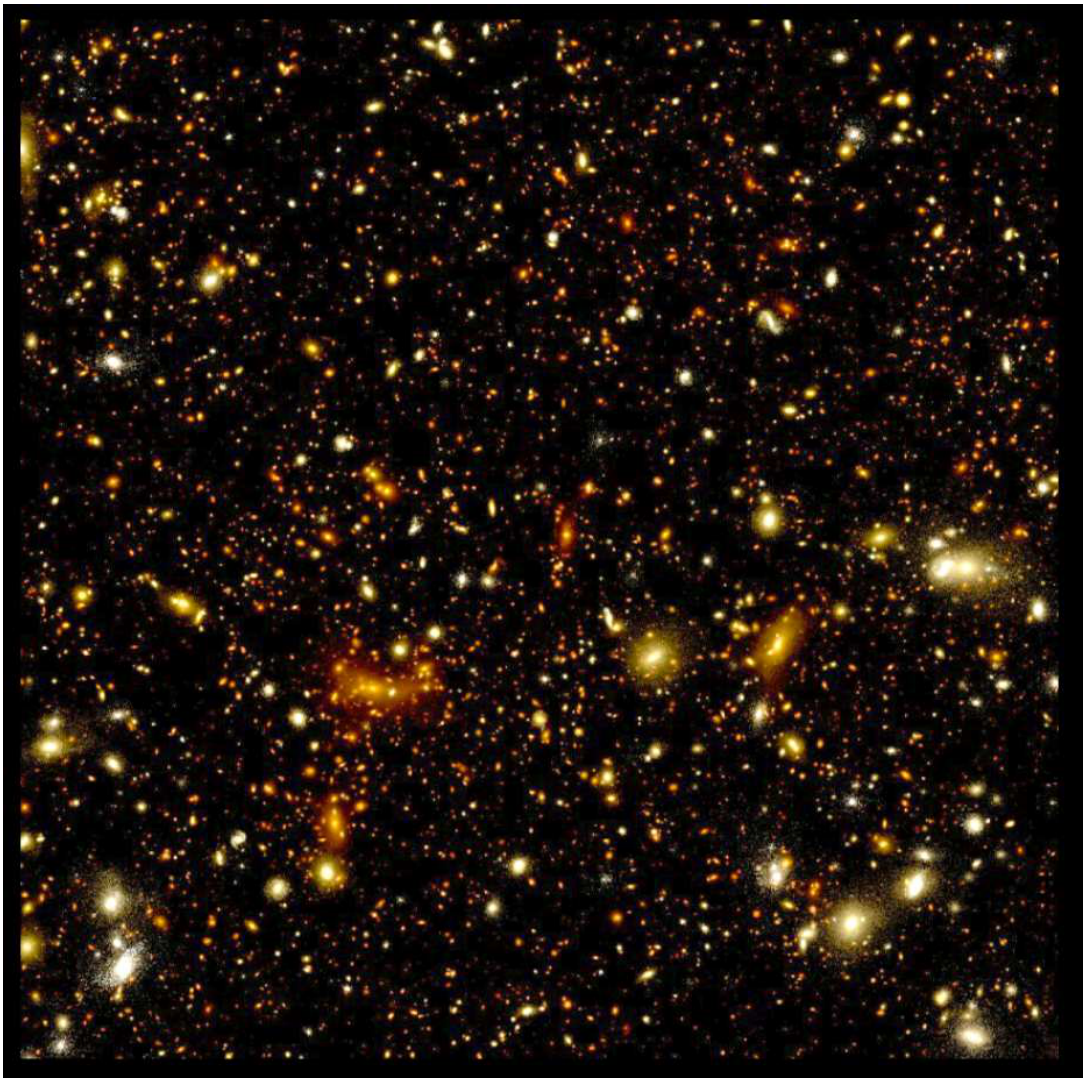

Figure 6.1: A 14 arcmin^2 simulated composite image from Horizon-AGN in the u, r and z filters. The resolution is 0.15"/pixel and the image is computed using star particles in the redshift range $0.1 < z < 5.8$. Dust extinction is not taken into account. Figure and caption taken from Kaviraj et al. (2016).

6.2 Comparing the K_s-band VIDEO Luminosity Functions with the Horizon-AGN simulation

6.2.1 Description of the Horizon-AGN simulation

Horizon-AGN is a large cosmological hydrodynamical simulation that uses the adaptive mesh refinement code RAMSES (Teyssier, 2002). It is described fully in Dubois et al. (2012) and Dubois et al. (2014), and briefly in Kaviraj et al. (2016). The simulation box is 100 h^{-1} Mpc on a side, corresponding to an angle of $\sim$ 6.7 degrees at $z = 0.3$ and $\sim$ 1.7 degrees at $z = 1.7$, with 1024^3 dark matter particles. The simulation uses cosmological values measured from the CMB in the WMAP 7 year release (Komatsu et al., 2011) and local measurements of the efficiency with which stars are formed for a given gas density (Kennicutt, 1998; Krumholz & Tan, 2007). It is tested against local supermassive black hole characteristics: the local number density (Shankar et al., 2004) and the correlations between black hole mass and velocity dispersion (Tremaine et al., 2002), and black hole mass and bulge mass locally (Häring & Rix, 2004), and galaxy colours are dust-calibrated using the ratio of dust to gas metal mass (Draine et al., 2007).

The observables compared to here are produced by first identifying galaxies using the structure finder AdaptaHOP (Aubert et al., 2004; Tweed et al., 2009), where local densities that are 178 times denser than the average and consist of more than 50 star particles are selected. Each star particle is treated as a simple stellar population, and fluxes and magnitudes are calculated using the mass and metallicity of the star particle combined with the stellar models from Bruzual & Charlot (2003) with a Chabrier (2003) initial mass function. These are then combined to produce the total SED for a particular galaxy. Dust attentuation is calculated using the SUNSET code, where gas density and metallicity are extracted from the simulation and used to find the dust mass, assuming a dust-to-metal ratio of 0.4. This is used to produce a column

density and line-of-sight optical depth with the $R = 3.1$ Milky Way dust grain model from Weingartner & Draine (2001). The spatial distribution of the dust is given by the spatial distribution of the metallicity, and the contribution from each star particle is summed to give a total dust-corrected SED. This is then used to produce fluxes and magnitudes by convolving with the required filter curves and extracting the magnitudes with a Petrosian aperture (Blanton et al., 2001; Petrosian, 1976). For the K_s-band, the dust is not expected to have a large effect and the dust-corrected and uncorrected LFs were found to be virtually identical (Kaviraj et al., 2016).

For the Horizon-AGN simulation, the feedback from star formation and supernovae necessary to flatten the faint end of the LF takes the form of enrichment and the injection of momentum and mechanical energy from Type Ia and Type II supernovae, as well as feedback from stellar winds in e.g. Wolf-Rayet stars and the asymptotic giant branch. Mass, momentum and kinetic energy are injected from supernovae and stellar winds into the ISM by temporarily switching off gas cooling while a blast wave propagates. The energy, mass and momentum are released locally into the surrounding gas by a spherical blast wave approximately 10 Myr after the birth of a star cluster particle. The feedback from Type Ia supernovae comes mainly in the form of enrichment, as they contribute ≈ 50 per cent of the iron from supernovae, but only ≈ 10 per cent of the total kinetic energy.

AGN feedback, the preferred mode of limiting the size and luminosities to which the biggest galaxies can grow, is input as either the radio or quasar mode, depending on the accretion rate of the black hole computed at each timestep. The quasar mode takes place when the central black hole has a high accretion rate (> 1 per cent of its Eddington rate) and releases energy radiatively. The rest-mass energy of the accreted gas is stored until it is sufficient to raise the temperature of the gas around the black hole above 10^7 K, at which point it is released as thermal energy in a bubble around the black hole with an efficiency of coupling between the radiated energy and the gas

of 1.5 per cent.

The radio mode describes the situation when the central black hole has a low accretion rate (< 1 per cent of its Eddington rate) and produces a kinetic jet. This is modelled in Horizon-AGN by spreading the mass, momentum and energy of a jet-like outflow over a cylinder around the black hole, in a way that describes the wind that carries most of the momentum arising from a larger region surrounding the black hole. Feedback via the radio mode has a much higher efficiency of ~ 10 per cent.

6.2.2 Comparison between the observed and predicted Luminosity Functions

In Figure 6.2, I compare the two K_s-band LFs measured in the 1 degree^2 VIDEO-CFHTLS-D1 field and the 4.5 degree^2 VIDEO-CFHTLS-W1 field with the predicted K-band LFs at $z = 0.3$, $z = 0.9$ and $z = 1.7$ from the Horizon-AGN simulation (Kaviraj et al., 2016). The best agreement occurs at the lowest redshift compared, $z \approx 0.3$, where the knee and the bright end of the LFs match well although the faint end is over-predicted, with the simulated number densities twice as high as the observed number densities. The over-prediction of faint galaxies gets worse with redshift, with the predicted LF more than three times higher than the observed LF below $M_K = -23$ at $z = 1.7$. While this is the main difference, I also find that at $z = 0.9$ and $z = 1.7$ the simulation under-predicts the number density of the very brightest galaxies, and is a factor of four less dense than the observed number density in the brightest bin at both $z = 0.9$ and $z = 1.7$.

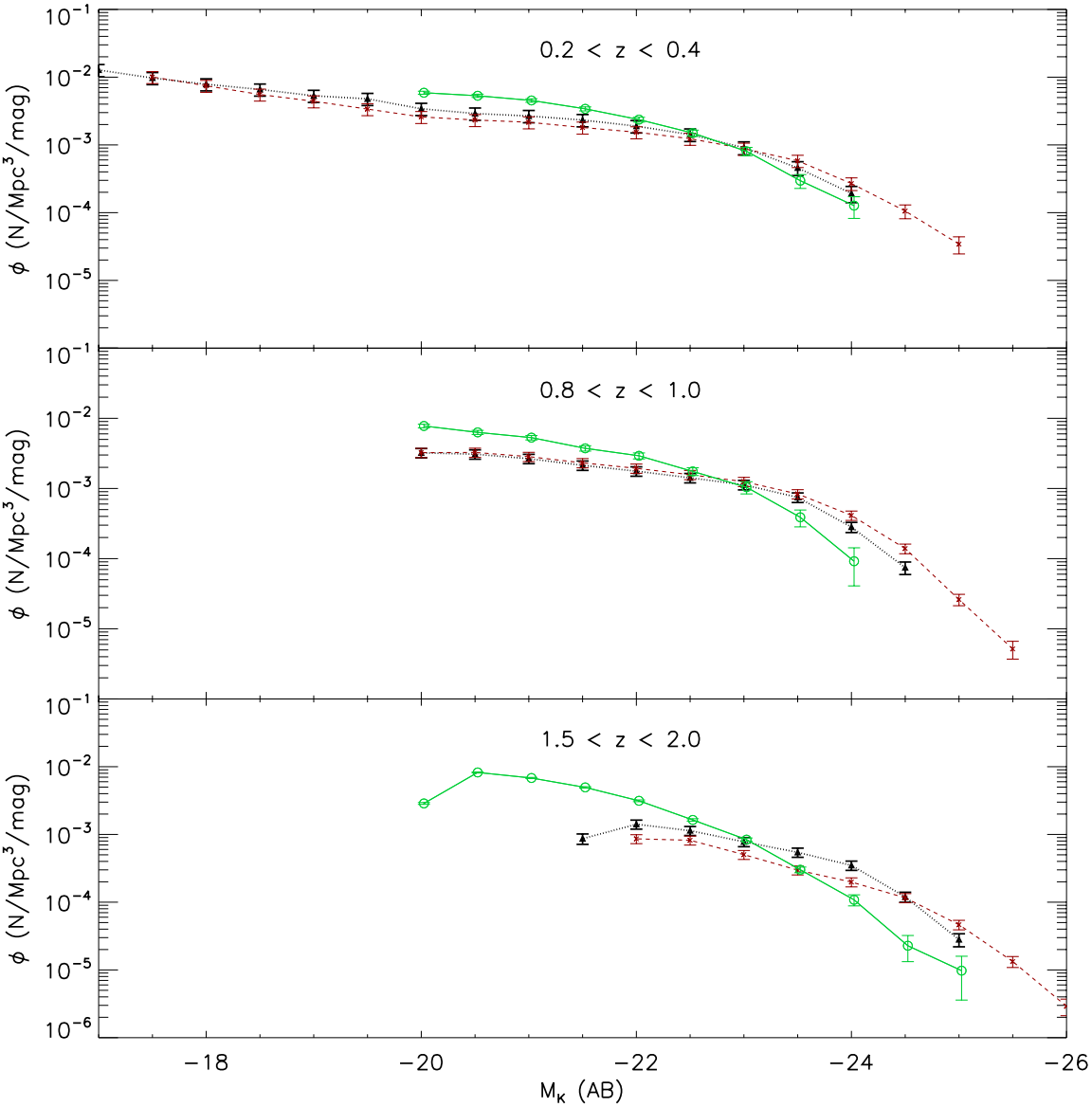

Figure 6.2: K_s**-band luminosity functions in the 4.5 degree^2 VIDEO-CFHTLS-W1 field presented in Chapter 5 (red crosses with red dotted line), the 1 degree^2 VIDEO-CFHTLS-D1 field presented in Chapter 4 (black triangles with black dashed line) along with the predicted K-band luminosity function from the Horizon-AGN simulation (Kaviraj et al., 2016) (green circles with solid green lines). The simulated LFs are at $z = 0.3$ (top panel), $z = 0.9$ (middle panel) and $z = 1.7$ (bottom panel).**

6.3 Discussion

6.3.1 The faint end of the luminosity function

The over-prediction of faint galaxies is a problem that affects many simulations and represents one of the areas where it is most difficult to fully describe the physics that determines the shape of the LF. The form of the luminosity function for the faintest galaxies is set by feedback from supernovae and star formation. The disagreement here may imply that there is missing physics that is not being accounted for by the simulation which would increase the efficiency of the feedback, or that the feedback that is included is not strong enough in small haloes to regulate star formation, which would boost the size of the galaxies within them.

There is evidence that describing behaviours on a smaller scale than is possible in the Horizon-AGN simulation may make SN feedback much more effective, such as increasing the strength of the star formation driven winds, either by adopting the enhanced star formation rates seen in clusters (Agertz & Kravtsov, 2015) or by including the clumpyness of the interstellar medium, which allows for enhanced wind speeds along low density channels (Kimm et al., 2015). There is also likely a resolution effect in the smallest galaxies as the size of the star particles becomes comparable to the size of the galaxy, allowing for no internal structure and thus no treatment of the variation in feedback efficiency with the location of any particular supernova or burst of star formation.

The method of implementing feedback from star formation and supernovae used here, that of a blast wave with delayed cooling, has been seen to overproduce star formation rates particularly at high redshift, but still noticeably at low redshift, which would match the disparity in faint number densities seen here. Stinson et al. (2013) found that adding a prescription for feedback from early star formation in the form of a photo-ionising background, to mimic the UV flux and stellar outflows from young

stars as soon as they formed, counteracted this for a single galaxy simulation, implying that something similar may be necessary here.

Gas in small galaxies can also be removed by external means that can be dependent on environment. Marasco et al. (2016) find that for satellite galaxies in groups, gas removal at $z = 0$ is mostly due to the ram pressure of the IGM, but that galaxies which have already lost their gas by $z = 0$ were mostly stripped of it by tidal disruption caused by interactions between satellite galaxies, both of which will be dependent on environment (they suggest this is due to the fact that tidal stripping has a very short timescale, stopping it from being dominant at any one redshift, but has the largest aggregate effect). As this is the larger effect over a range of redshift, it may be that the difficulty in resolving the large numbers of small satellites in massive haloes results in an underestimate of the effect this would have on star formation in small galaxies. McGee et al. (2014) find that satellite galaxies in clusters, where the intracluster medium is too hot for gas to easily condense, quench themselves by outflows from star formation and supernovae driving gas out of the galaxy, at which point it is unable to recondense. Both of these results will mean that environment can play a very large role in determining the star formation and survival rates of small galaxies, and so need to be considered in a more comprehensive way in the simulation.

Finally, it is worth mentioning that there is also an observational bias at work in the lowest redshift bin, as faint low surface brightness galaxies are much harder to identify than high surface brightness galaxies of the same apparent magnitude, which, combined with the correlation between low luminosity and low surface brightness (Cameron & Driver, 2007; Driver, 1999), will lead to the observed LF slightly underestimating the number densities of the dwarf galaxies that make up the faint end of the intrinsic LF. This can be seen by the steepening of the faint-end of the measured LF when accounting for surface brightness incompleteness (Blanton et al., 2005; Geller et al., 2012), showing intrinsically higher number densities of faint galax-

ies that will be closer to the high number densities found in simulations. However, the disagreement in the lowest redshift bin is far brighter than the limit of the data, and at high redshift, is bright enough that low surface galaxies would not be dominant, implying any correction to the observed LF would be very small.

6.3.2 The bright end of the luminosity function

Unlike the discrepancies at the faint end of the LF, the tension seen at the bright end of the LF is less common than tension at the faint end when comparing observed and simulation measurements. The form of the LF in the brightest regime is generally determined by feedback from AGN either in the radio mode or quasar mode. The radio mode is observationally seen to be predominantly at low redshift in the largest cluster galaxies, forming hot bubbles of gas visible in X-ray in the intra cluster medium. The quasar mode is mostly seen at high redshift when the AGN is young, and is thought to eventually lead to the shutting off of accretion to the black hole and self-termination. This mode peaks at $z \sim 1-3$ (e.g. Croom et al. 2001; Richards et al. 2009).

The redshift dependence of these modes in the Horizon-AGN simulation can be seen in Figure 6.3 taken from Dubois et al. (2012), which shows the relative contributions to the AGN LF by objects in the radio and quasar mode for two simulations of different resolution (the simulation shown in the left panels has twice the resolution of the one on the right, with a minimum resolution at $z = 0$ of 0.76 kpc $h^{-}1$ instead of 1.52 kpc h^{-1}). Most of the AGN activity is due to objects accreting in the quasar mode until $z \sim 2$, at which point they are overtaken by objects accreting in the radio mode. As the discrepancy in the bright end is worse at high redshift, this implies it may be to do with either the quasar mode or the changeover between the two. Comparing the redshift dependence for the two simulations shown in Figure 6.3, the higher resolution simulation has a sharper peak with redshift in the quasar mode

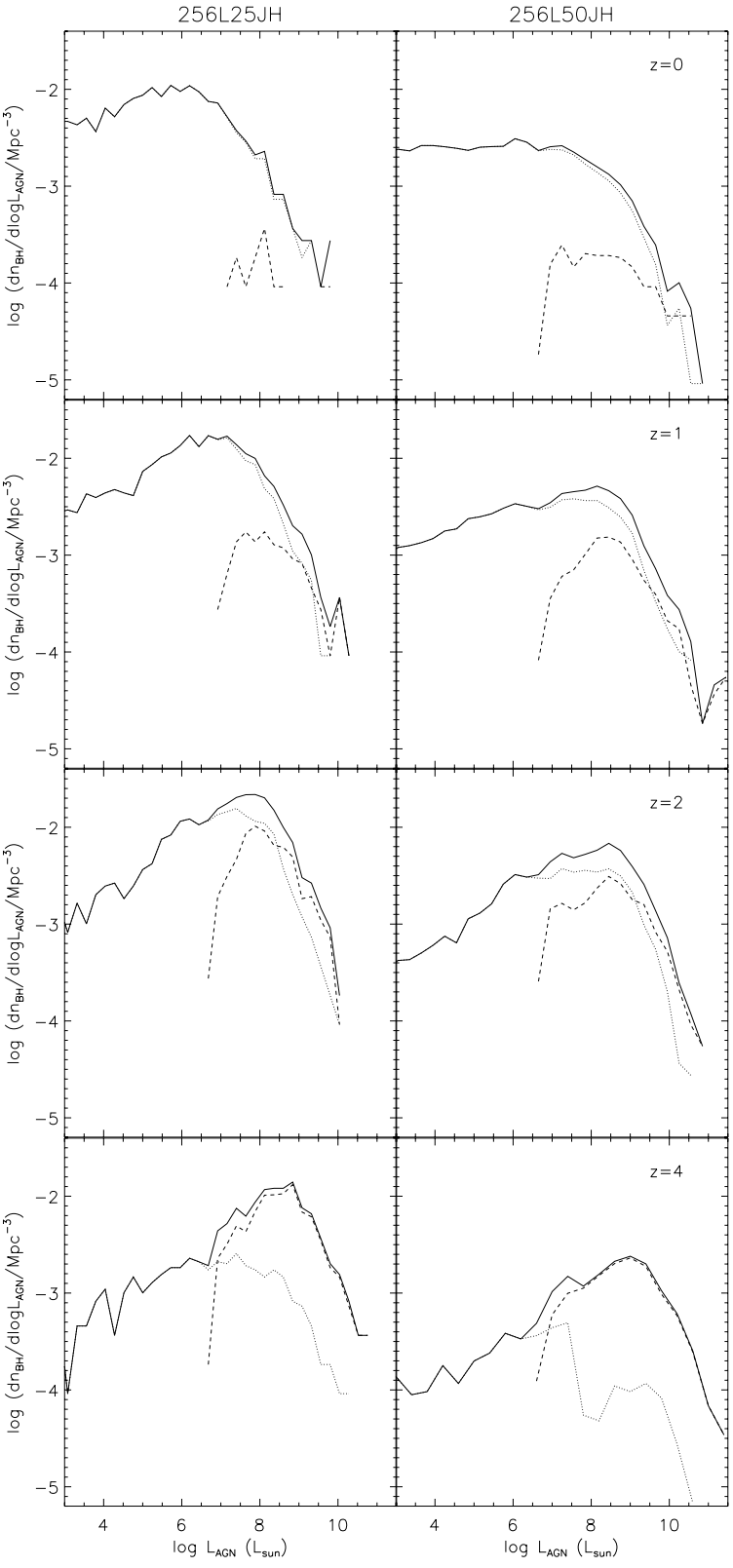

Figure 6.3: The contributions of objects in the radio and quasar mode to the total AGN LF at different redshifts in two Horizon-AGN runs with different resolutions. The simulation on the left has twice the resolution compared to the simulation on the right. The total LF is shown in a solid line, the contribution from the radio mode in a dotted line and from the quasar mode in a dashed line. Figure taken from Dubois et al. (2012).

which declines faster and earlier than the lower resolution simulation. This suggests that the issue may be resolution-based, as a faster decline at earlier times would lessen the effect of the quenching. Both modes are also modelled in ways that neglect physical aspects that will have an effect on them, such as the X-ray photons released by quasars which will have a non-negligible effect on radiative transfer, and the fact the jets in the radio mode would be affected by the presence of non-thermal cosmic rays and a strong magnetic field (Dubois et al., 2012). It is also possible that resolution is affecting the way the AGN LF has been calculated rather than the behaviour of the simulation itself; any such problem would also affect the galaxy LF and so may be adding to the discrepancy.

There is a population of quasar-mode objects that have powerful radio jets, such as radio-loud quasars and radio galaxies (Jarvis et al., 2001; Laor, 2000; Prestage & Peacock, 1988; Xu et al., 1999) where it is inevitable that both radiative and mechanical feedback will be occurring, showing that the treatment of AGN feedback as cleanly separated into two modes that dominate at separate redshifts is over-simplistic.

Volonteri et al. (2016) also show that the Horizon-AGN simulation over-predicts the AGN LF at high redshift, which might in turn over-damp the bright end of the galaxy LF at high redshift before normalising at lower redshift. It is also relevant that a significant amount of the growth of the largest galaxies in the Horizon-AGN simulation is due to minor mergers. The smaller accreted galaxies are not well resolved at higher redshift, potentially leading to an underestimation in the sizes of galaxies which would be most noticeable at the bright end of the LF. As this effect would correct with redshift, it could produce the difference seen here.

6.4 Conclusions

While the predicted K-band LF from Horizon-AGN matches the knee and the bright end of the observed K_s-band LFs from VIDEO-CFHTLS-D1 and VIDEO-CFHTLS-W1 reasonably well, there is significant disagreement at the faint end, and the numbers of low mass galaxies, especially at high redshift, are vastly over-predicted by the Horizon-AGN simulation. While some disagreement may be caused by errors in the photometric redshift and accounting for this would increase the observed error bars and reduce the disagreement, this highlights an obvious issue with the feedback processes dominant in shaping this end of the LF, namely feedback from star formation and supernovae.

An improved implementation of the feedback from supernovae and star formation could be aided by increasing resolution, more accurately modelling the clumpy nature of the IGM, applying the higher star formation rate efficiencies seen in star clusters or by applying a prescription for the feedback from very young stars before they become supernovae. Better accounting for the differences in environment such as the effects of ram pressure or tidal stripping in groups would also will also be important in reproducing the faint end of the LF.

The under-prediction at the bright end may also be improved by increasing the resolution of the simulation, which would allow for more accurate histories of galaxies at high redshift and potentially lead to an earlier decline in feedback from the quasar mode. A more realistic treatment of the transition from one feedback mode to the other that takes into account the fact that both modes have been observationally seen to coexist will also be critical for getting the feedback prescription correct. Furthermore, it is becoming clear from observations that the accretion rate in radio galaxies appears to be bimodal (e.g. Best & Heckman, 2012; Fernandes et al., 2015). The feedback prescriptions in the simulations should also be tested against this to ensure that they are at least similar to what is observed.

Chapter 7

Conclusions & Future Work

In this thesis I measure the luminosity function of galaxies first at high redshift ($z > 6$) in Chapters 2 & 3, and then at lower redshift in Chapters 4 & 5 before finally comparing some of these luminosity functions to those predicted by simulations. Measuring this key diagnostic across a broad range in redshift has allowed me to explore important questions about the formation and evolution of galaxies over time. At high redshift I use the Lyman break technique to select galaxies in deep *HST* imaging and measure the UV luminosity function to gain insight into the abundance of high redshift galaxies. I then follow this evolution to intermediate and low redshift using wider and shallower ground-based surveys. In this Chapter, I will first summarise the main conclusions from my investigation into the numbers of high redshift galaxies in GOODS-North, before following this to lower redshift by describing my conclusions from my measurement of the luminosity functions in the VIDEO-CFHTLS-D1 and VIDEO-CFHTLS-W1 fields, and from a comparison with a predicted luminosity function from the Horizon-AGN simulation. Finally, I will describe some possibilities for future work investigating the processes that have shaped the galaxy luminosity function over cosmic time.

7.1 The UV Luminosity Functions and Cosmic Variance of Galaxies at $z \approx 7-9$ in GOODS

In Chapter 2, I present a list of candidate high redshift galaxies estimated to be at $z \approx 7$ and $z \approx 8-9$ seen in the CANDELS/GOODS-North field. These candidates were found by analysing the *HST*/WFC 3 and ACS imaging of the CANDELS/GOODS-North field and applying the Lyman break technique to isolate galaxies potentially at high redshift. I also estimate both the contamination due to stars and intermediate redshift red galaxies, and the completeness of the final candidate list. From this, I present 22 possible $z \approx 7$ galaxies and 6 possible $z \approx 8-9$ galaxies, of which 13 have not been previously presented.

In Chapter 3, I compare these candidates to a sample found using an identical method in the GOODS-South field by Lorenzoni et al. (2013). I investigate the effect of cosmic variance between the two fields, finding that the difference in number counts is consistent with the expected Poisson noise, indicating that for a field of this depth and shape, cosmic variance is not the dominant source of variation.

As the two fields are consistent with each other to within the expected Poisson error on the number counts, I combine the candidates from GOODS-North from Chapter 2 with the candidates from GOODS-South in Lorenzoni et al. (2013). This gives me the number counts necessary to constrain the bright end of the UV luminosity function, using candidate galaxies from the XDF selected in an identical fashion (Lorenzoni et al. in prep) to also constrain the faint-end. I present best-fit Schechter parameters from this combined sample of high redshift galaxies at $z \approx 7$ and $z \approx 8-9$. Both the $z \approx 7$ and $z \approx 8-9$ Schechter functions agree with other determinations, although the $z \approx 8-9$ luminosity function is based on too few galaxies to add much constraint. I see more evolution in density (ϕ^*) than in the characteristic luminosity (M^*_{1600}) from $z \approx 7$ to $z \approx 8-9$, implying that the dominant change is due to the

formation of new galaxies, rather than the growth of individual galaxies, as one would expect a relatively short time after the Big Bang.

7.2 The K_s-band Luminosity Functions of Galaxies in the VIDEO-XMM Fields

In Chapters 4 & 5, I present the rest-frame K_s-band luminosity functions from the overlaps between the VIDEO imaging of the XMM-LSS field and the CFHTLS D1 and W1 fields. The VIDEO-CFHTLS-D1 field provided photometric redshifts for 90,519 galaxies, from which I measure the K_s-band LF with the $1/V_{max}$ method in 10 redshift bins from $z = 0.2$ to $z = 3$. The VIDEO-CFHTLS-W1 field provided 281,299 galaxies with photometric redshifts, allowing me to measure the K_s-band LF in 6 redshift bins from $z = 0.2$ to $z = 1.5$. The VIDEO-CFHTLS-W1 LFs were measured over a smaller redshift range as the photometric redshift fitting above this point was less reliable due to the shallower optical data from CFHTLS-W1 compared to CFHTLS-D1.

The VIDEO survey covers a large area, which has allowed me to measure the bright-end of the luminosity function with reliable points as far as $M = -25$ at $z \approx 0.2$ and $M = -26$ at $z = 1.5$ in VIDEO-CFHTLS-W1, and $M = -26$ at $z \approx 3$ in VIDEO-CFHTLS-D1, while the deep IR imaging has allowed me to characterise the faint end of the luminosity function, especially at lower redshifts, reaching down to absolute magnitudes of $M = -20$ at $z = 1$ and $M = -17$ at $z = 0.2$. This combination has provided constraints on the characteristic luminosity (M^*) and its evolution, as well as the abundance ϕ^* and the density evolution.

I find that the evolution of the K_s-band LFs is best described by luminosity dependent density evolution. The characteristic magnitude of the LFs is dimmer at higher redshift, evolving at a constant speed to produce a difference of just over

1 mag by $z = 3$ compared to $z = 0.2$. The number density of the LFs is higher now than at high redshift. From $z = 3$ to $z \approx 1.5$ the number density of galaxies increases rapidly as new galaxies form, before the effects of mergers act to slow this evolution from $z \approx 1.5$ to $z \approx 0.2$. The combination of galaxies having lower number densities but higher luminosities at higher redshift is in line with downsizing; massive galaxies, which form the bulk of their stellar mass early, will dominate the luminosity evolution of the LF, causing it to dim as they passively evolve through their ageing stellar populations. At the same time, the build up of smaller galaxies forming at later times will produce an increase in the number density at lower redshift.

The very deep photometry coupled with a reasonably sized area has also allowed me to measure the upturn in the faint-end of the LF at $z \sim 0.2 - 0.6$. From this, it can be seen that the efficiency of the feedback from star formation and supernovae does not continue to increase with decreasing luminosity at the same rate in the faintest galaxies, but instead levels off, resulting in higher number counts than can be described by a single Schechter function.

In Chapter 6, I compare the K_s-band LFs from VIDEO-CFHTLS-D1 and VIDEO-CFHTLS-W1 with the predicted K-band LF from the Horizon-AGN simulation. I find that the number counts at the faint end of the LF were significantly over-predicted, and the number counts at the bright end of the LF were slightly under-predicted, with both disagreements worse at higher redshift. This is most easily explained by an under-efficiency in the star formation feedback and a slight over-efficiency in the AGN feedback implemented by the Horizon-AGN simulation to shape the faint and the bright end of the LF. The efficiency of the feedback from star formation and supernovae may be improved by better modelling the clumpy nature of the ISM, accounting for the feedback from very young stars before they evolve off the main sequence, using the high star formation efficiencies seen in star clusters, or by increased resolution. The AGN feedback could be improved by a more realistic implementation

of the radio and quasar modes which better deals with the transitions between them, as well as accounting for the fact that they have been observationally found to coexist.

7.3 Future Work

At high redshift, the James Webb Space Telescope (JWST; Gardner et al., 2006) and the Atacama Large Millimetre Array (ALMA; Hills et al., 2010) will provide the ability to measure far more information about high redshift galaxies than is currently possible. The massive improvement in resolution and sensitivity in the millimetre and submillimetre range available with ALMA will enable the measurement of dust emission from high redshift galaxies, as well as emission lines from molecular gas and information on their metallicity. The extra sensitivity and larger field of view of JWST compared to *HST* will produce large samples of galaxies at $z > 7$ reaching down to fainter magnitudes, allowing for the measurement of the luminosity function of high redshift galaxies to be well measured, with a better characterisation of the faint end slope and enough sources at very high redshift to constrain its early evolution with more statistical significance. This will aid in answering whether there are sufficient small galaxies at high redshift to produce the required number of ionising photons needed for reionisation (e.g. Bouwens et al., 2012; Robertson et al., 2015). JWST will also provide information about these galaxies previously unobtainable in the form of observations of the rest-frame optical light unfeasible with telescopes such as *Spitzer*, due to the necessary resolution and sensitivity, as well as, possibly most importantly, spectroscopic information about these galaxies. In combination with measurements from ALMA, this will lead not only to spectroscopic redshifts, but will allow the measurement of, for instance, galaxy masses, metallicities and the ages of the stellar populations, unveiling what the star formation history of these early galaxies has been. Furthermore, JWST will be able to observe the high redshift AGN

population, extending our knowledge about the processes that shape galaxies to the earliest epochs of galaxy evolution.

Galaxy evolution in the VIDEO fields could be further studied by sub-dividing the LFs into separate populations of galaxies. Investigating bright and faint galaxies separately would allow the effects of downsizing to be better characterised as the two populatisons would be expected to have different strengths of evolution at different times. Similarly, examining galaxies of different colour or SFR separately would allow the measurement of the different shapes of the LFs and their different evolutions. This would give us information about which galaxies dominate different types of evolution at different times. Splitting galaxies both by colour and SFR will also help to investigate the observational effects of such selections on the measured evolution. This breakdown of the LFs by colour and SFR would show which populations contribute to the upturn at the faint end of the LF, giving us more of an insight into how the feedback from star formation varies between galaxies.

The next generation of surveys such as the Large Synoptic Survey Telescope (LSST; LSST Science Collaboration et al., 2009) and *Euclid* (Laureijs et al., 2011) will provide increasing coverage and depth. Coupled with the progress in photometric redshift fitting necessary for these large surveys, this will lead to catalogues of galaxies out to higher redshift that provide a comprehensive picture of the Universe between $1 < z < 3$ in the way that SDSS did at $z < 0.5$. This will allow for a much more complete characterisation of the LF and how it evolves for different populations of galaxies past the peak in SFRD at $z \sim 2 - 3$, providing an exquisite tool with which to study galaxy evolution.

From the comparison between the simulated and the measured luminosity functions in Chapter 6, it is clear that more work is necessary to understand the processes by which supernovae and AGN affect the star formation rates of different sizes of galaxies. Future radio surveys and facilities such as the MIGHTEE survey with

MeerKAT (Jarvis, 2012) and the Square Kilometre Array (SKA; SKA Organisation, 2015) will be able to observe HI gas in low mass galaxies at low redshift, and will provide important information about quite how the feedback from supernovae is affecting the cold gas reservoir from which molecular clouds and stars form. In particular, they will shed light upon the interplay between supernova feedback and environment, directly observing under what circumstances cold gas is stripped from galaxies in both dense and sparse environments, as well as detecting the smallest galaxies with incredibly low HI masses. Follow up from facilities such as ALMA will be able to trace the molecular gas, infrared and optical measurements will give information about the stellar populations, and the radio observations will provide star formation rates unpolluted by dust (Condon, 1992; Smith et al., 2014). This will make it possible to study all of the different stages between gas and star formation up to $z \sim 1$ in the future with MIGHTEE and the SKA in combination with surveys like VIDEO, *Euclid* and LSST.

A better understanding of the mechanisms behind AGN feedback is crucial to implementing this feedback in large scale simulations, with particular focus on the different accretion modes of AGN. Radio observations provide the cleanest method of selecting AGN, with a well understood selection function, but emission line studies, as well as supplying the redshift information that cannot be accessed by radio observations, are needed to separate AGN into objects in high or low accretion rate modes and to remove the contributions from star formation (Best & Heckman, 2012; Fernandes et al., 2015). For this reason, upcoming multi-object spectrographs such as WEAVE (Dalton et al., 2012), MOONS (Cirasuolo et al., 2014) and 4MOST (de Jong et al., 2014) will be incredibly useful in obtaining spectroscopic information on large samples of radio-selected AGN. For instance, the WEAVE-LOFAR survey will do exactly this, facilitating the investigation of different AGN accretion modes with enough sources to allow the study of how the AGN differ with, for example, redshift, mass

and environment (Smith, 2015).

Bibliography

Abel T., Anninos P., Zhang Y., Norman M. L., 1997, New Astronomy, 2, 181

Adelman-McCarthy J. K., et al., 2008, The Astrophysical Journal Supplement Series, 175, 297

Agertz O., Kravtsov A. V., 2015, The Astrophysical Journal, 804, 18

Alam S., et al., 2016, arXiv eprints, arXiv:1607.03155

Allison R., Dunkley J., 2014, Monthly Notices of the Royal Astronomical Society, 437, 3918

Almosallam I. A., Lindsay S. N., Jarvis M. J., Roberts S. J., 2016, Monthly Notices of the Royal Astronomical Society, 455, 2387

Arnouts S., Cristiani S., Moscardini L., Matarrese S., Lucchin F., Fontana A., Giallongo E., 1999, Monthly Notices of the Royal Astronomical Society, 310, 540

Arnouts S., et al., 2007, Astronomy & Astrophysics, 476, 137

Arons J., Wingert D. W., 1972, The Astrophysical Journal, 177, 1

Aubert D., Pichon C., Colombi S., 2004, Monthly Notices of the Royal Astronomical Society, 352, 376

Balbus S., 1986, The Astrophysical Journal Letters, 303, L79

Baldry I. K., Glazebrook K., Brinkmann J., Ivezić Ž., Lupton R. H., Nichol R. C., Szalay A. S., 2004, The Astrophysical Journal, 600, 681

Baldry I. K., et al., 2005, Monthly Notices of the Royal Astronomical Society, 358, 441

Baldry I. K., Balogh M. L., Bower R. G., Glazebrook K., Nichol R. C., Bamford S. P., Budavari T., 2006, Monthly Notices of the Royal Astronomical Society, 373, 469

Baldry I. K., Glazebrook K., Driver S. P., 2008, Monthly Notices of the Royal Astronomical Society, 388, 945

Baldry I. K., et al., 2010, Monthly Notices of the Royal Astronomical Society, 404, 86

Baldry I. K., et al., 2012, Monthly Notices of the Royal Astronomical Society, 421, 621

Ball N. M., Brunner R. J., Myers A. D., Strand N. E., Alberts S. L., Tcheng D., 2008, The Astrophysical Journal, 683, 12

Balogh M. L., Baldry I. K., Nichol R., Miller C., Bower R., Glazebrook K., 2004, The Astrophysical Journal Letters, 615, L101

Barro G., et al., 2013, The Astrophysical Journal, 765, 104

Batchelor G. K., 2000, An Introduction to Fluid Dynamics. Cambridge Mathematical Library, Cambridge University Press

Beckwith S. V. W., et al., 2006, The Astronomical Journal, 132, 1729

Behroozi P. S., Wechsler R. H., Conroy C., 2013, The Astrophysical Journal Letters, 762, L31

Bell E. F., et al., 2004, The Astrophysical Journal, 608, 752

Benson A. J., 2010, Physics Reports, 495, 33

Benson A., Bower R., Frenk C., Lacey C., Baugh C., Cole S., 2003, The Astrophysical Journal, 599, 38

Bertin E., Arnouts S., 1996, Astron. Astrophys. Suppl. Ser., 117, 393

Best P. N., Heckman T. M., 2012, Monthly Notices of the Royal Astronomical Society, 421, 1569

Best P. N., Ker L. M., Simpson C., Rigby E. E., Sabater J., 2014, Monthly Notices of the Royal Astronomical Society, 445, 955

Bielby R. M., et al., 2011, Monthly Notices of the Royal Astronomical Society, 414, 2

Binney J., 1977, The Astrophysical Journal, 215, 492

Binney J., Tremaine S., 1987, Galactic Dynamics, second edi edn. Princeton University Press

Blanton M. R., et al., 2001, The Astronomical Journal, 121, 2358

Blanton M. R., et al., 2003, The Astrophysical Journal, 592, 819

Blanton M. R., Lupton R. H., Schlegel D. J., Strauss M. A., Brinkmann J., Fukugita M., Loveday J., 2005, The Astrophysical Journal, 631, 208

Boissier S., et al., 2008, The Astrophysical Journal, 681, 244

Bolzonella M., Miralles J.-M., Pelló R., 2000, Astronomy & Astrophysics, 363, 476

Bondi H., 1952, Monthly Notices of the Royal Astronomical Society, 112, 195

Bondi H., Hoyle F., 1944, Monthly Notices of the Royal Astronomical Society, 104, 273

Bouwens R. J., et al., 2003, The Astrophysical Journal, 595, 589

Bouwens R. J., Illingworth G. D., Blakeslee J. P., Broadhurst T. J., Franx M., 2004a, The Astrophysical Journal Letters, 611, L1

Bouwens R. J., et al., 2004b, The Astrophysical Journal Letters, 616, L79

Bouwens R. J., Illingworth G. D., Blakeslee J. P., Franx M., 2006, The Astrophysical Journal, 653, 53

Bouwens R. J., Illingworth G. D., Franx M., Ford H., 2007, The Astrophysical Journal, 670, 928

Bouwens R. J., et al., 2009, The Astrophysical Journal, 705, 936

Bouwens R. J., et al., 2011, Nature, 469, 504

Bouwens R. J., et al., 2012, The Astrophysical Journal Letters, 752, L5

Bouwens R. J., et al., 2014, The Astrophysical Journal, 793, 115

Bouwens R. J., et al., 2015, The Astrophysical Journal, 803, 34

Bouwens R. J., Illingworth G. D., Oesch P. A., Atek H., Lam D., Stefanon M., 2016, arXiv eprints, arXiv:1608.00966

Bower R. G., 1991, Monthly Notices of the Royal Astronomical Society, 248, 332

Bower R. G., Benson A. J., Malbon R., Helly J. C., Frenk C. S., Baugh C. M., Cole S., Lacey C. G., 2006, Monthly Notices of the Royal Astronomical Society, 370, 645

Bowler R. A. A., et al., 2014, Monthly Notices of the Royal Astronomical Society, 440, 2810

Bowler R. A. A., et al., 2015, Monthly Notices of the Royal Astronomical Society, 452, 1817

Bowler R. A. A., Dunlop J. S., McLure R. J., McLeod D. J., 2016, arXiv eprints, arXiv:1605.05325

Boylan-Kolchin M., Ma C.-P., Quataert E., 2008, Monthly Notices of the Royal Astronomical Society, 383, 93

Bradley L. D., et al., 2012, The Astrophysical Journal, 760, 108

Bruzual G., Charlot S., 2003, Monthly Notices of the Royal Astronomical Society, 344, 1000

Bunker A. J., Stanway E. R., Ellis R. S., McMahon R. G., 2004, Monthly Notices of the Royal Astronomical Society, 355, 374

Bunker A. J., et al., 2010, Monthly Notices of the Royal Astronomical Society, 409, 855

Burgarella D., Buat V., Iglesias-Páramo J., 2005, Monthly Notices of the Royal Astronomical Society, 360, 1413

Burgarella D., et al., 2006, Astronomy & Astrophysics, 450, 69

Burgarella D., et al., 2013, Astronomy & Astrophysics, 554, A70

Calzetti D., Armus L., Bohlin R., Kinney A., Koornneef J., Storchi-Bergmann T., 2000, The Astrophysical Journal, 533, 682

Cameron E., Driver S. P., 2007, Monthly Notices of the Royal Astronomical Society, 377, 523

Caputi K. I., McLure R. J., Dunlop J. S., Cirasuolo M., Schael a. M., 2006, Monthly Notices of the Royal Astronomical Society, 366, 609

Caruana J., Bunker A. J., Wilkins S. M., Stanway E. R., Lorenzoni S., Jarvis M. J., Ebert H., 2014, Monthly Notices of the Royal Astronomical Society, 443, 2831

Castellano M., et al., 2012, Astronomy & Astrophysics, 540, A39

Castellano M., et al., 2016, The Astrophysical Journal Letters, 818, L3

Chabrier G., 2003, Publications of the Astronomical Society of the Pacific, 115, 763

Chandrasekhar S., 1943, Lecture Notes in Physics, 97, 255

Churazov E., Forman W., Jones C., 2000, Astronomy & Astrophysics, 356, 788

Cirasuolo M., et al., 2007, Monthly Notices of the Royal Astronomical Society, 380, 585

Cirasuolo M., McLure R. J., Dunlop J. S., Almaini O., Foucaud S., Simpson C., 2010, Monthly Notices of the Royal Astronomical Society, 401, 1166

Cirasuolo M., et al., 2014, Proc. SPIE, 9147, 91470N

Coe D., et al., 2013, The Astrophysical Journal, 762, 32

Cole S., et al., 2001, Monthly Notices of the Royal Astronomical Society, 326, 255

Coleman G. D., Wu C.-C., Weedman D. W., 1980, The Astrophysical Journal Supplement Series, 43, 393

Colless M., et al., 2001, Monthly Notices of the Royal Astronomical Society, 328, 1039

Condon J. J., 1992, Annual Review of Astronomy and Astrophysics, 30, 575

Conselice C. J., et al., 2011, Monthly Notices of the Royal Astronomical Society, 413, 80

Cool R. J., et al., 2012, The Astrophysical Journal, 748, 10

Cowie L. L., Hu E. M., 1998, The Astronomical Journal, 115, 1319

Cowie L. L., Songaila A., Hu E. M., Cohen J. G., 1996, The Astronomical Journal, 112, 839

Croom S. M., Smith R. J., Boyle B. J., Shanks T., Loaring N. S., Miller L., Lewis I. J., 2001, Monthly Notices of the Royal Astronomical Society, 322, L29

Croton D. J., et al., 2006, Monthly Notices of the Royal Astronomical Society, 365, 11

Cucciati O., et al., 2012, Astronomy & Astrophysics, 539, A31

Curtis-Lake E., et al., 2013, Monthly Notices of the Royal Astronomical Society, 429, 302

Curtis-Lake E., et al., 2016, Monthly Notices of the Royal Astronomical Society, 457, 440

Da Cunha E., Charlot S., Elbaz D., 2008, Monthly Notices of the Royal Astronomical Society, 388, 1595

Dalton G., et al., 2012, Proc. SPIE, 8446, 84460P

Darg D. W., et al., 2010a, Monthly Notices of the Royal Astronomical Society, 401, 1043

Darg D. W., et al., 2010b, Monthly Notices of the Royal Astronomical Society, 401, 1552

Di Matteo T., Springel V., Hernquist L., 2005, Nature, 433, 604

Dickinson M., Giavalisco M., GOODS Team 2003, The Great Observatories Origins Deep Survey. Springer Berlin Heidelberg, Berlin, Heidelberg, pp 324–331, doi:10.1007/10899892_78, http://dx.doi.org/10.1007/10899892{_}78

Dickinson M., et al., 2004, The Astrophysical Journal Letters, 600, L99

Draine B. T., et al., 2007, The Astrophysical Journal, 663, 866

Driver S. P., 1999, The Astrophysical Journal Letters, 526, L69

Driver S. P., et al., 2009, Astronomy & Geophysics, 50, 5.12

Driver S. P., et al., 2011, Monthly Notices of the Royal Astronomical Society, 413, 971

Dubois Y., Devriendt J., Slyz A., Teyssier R., 2012, Monthly Notices of the Royal Astronomical Society, 420, 2662

Dubois Y., et al., 2014, Monthly Notices of the Royal Astronomical Society, 444, 1453

Dunkley J., Bucher M., Ferreira P. G., Moodley K., Skordis C., 2005, Monthly Notices of the Royal Astronomical Society, 356, 925

Dunlop J. S., McLure R. J., Robertson B. E., Ellis R. S., Stark D. P., Cirasuolo M., de Ravel L., 2012, Monthly Notices of the Royal Astronomical Society, 420, 901

Dunlop J. S., et al., 2013, Monthly Notices of the Royal Astronomical Society, 432, 3520

Ellis R. S., et al., 2013, The Astrophysical Journal Letters, 763, L7

Faber S. M., et al., 2007, The Astrophysical Journal, 665, 265

Fan X., et al., 2006, The Astronomical Journal, 132, 117

Fernandes C. A. C., et al., 2015, Monthly Notices of the Royal Astronomical Society, 447, 1184

Field G. B., 1965, The Astrophysical Journal, 142, 531

Finkelstein S. L., Papovich C., Giavalisco M., Reddy N. A., Ferguson H. C., Koekemoer A. M., Dickinson M., 2010, The Astrophysical Journal, 719, 1250

Finkelstein S. L., et al., 2012, The Astrophysical Journal, 756, 164

Finkelstein S. L., et al., 2015, The Astrophysical Journal, 810, 71

Firth A. E., Lahav O., Somerville R. S., 2003, Monthly Notices of the Royal Astronomical Society, 339, 1195

Font A. S., et al., 2008, Monthly Notices of the Royal Astronomical Society, 389, 1619

Fontanot F., De Lucia G., Monaco P., Somerville R. S., Santini P., 2009, Monthly Notices of the Royal Astronomical Society, 397, 1776

Friedmann A., 1922, Zeitschrift f{ü}r Physik, 10, 377

Friedmann A., 1924, Zeitschrift f{ü}r Physik, 21, 326

Galametz A., et al., 2013, The Astrophysical Journal Supplement Series, 206, 10

Gardner J. P., et al., 2006, Space Science Reviews, 123, 485

Geller M. J., Diaferio A., Kurtz M. J., Dell'Antonio I. P., Fabricant D. G., 2012, The Astronomical Journal, 143, 102

Gelman A., Rubin D., 1992, Statistical Science, 7, 457

Gelman A., Roberts G., Wilks G., 1996, Bayesian Statistics, Vol 5. Oxford University Press, Oxford

Giallongo E., Salimbeni S., Menci N., Zamorani G., Fontana A., Dickinson M., Cristiani S., Pozzetti L., 2005, The Astrophysical Journal, 622, 116

Giavalisco M., et al., 2004, The Astrophysical Journal Letters, 600, L93

Gingold R., Monaghan J., 1977, Monthly Notices of the Royal Astronomical Society, 181, 375

Giovannoli E., Buat V., Noll S., Burgarella D., Magnelli B., 2011, Astronomy & Astrophysics, 525, A150

Grogin N. A., et al., 2011, The Astrophysical Journal Supplement Series, 197, 35

Gruppioni C., et al., 2013, Monthly Notices of the Royal Astronomical Society, 432, 23

Gunn J., Peterson B., 1965, The Astrophysical Journal, 142, 1633

Guo Q., White S., Li C., Boylan-Kolchin M., 2010, Monthly Notices of the Royal Astronomical Society, 404, 1111

Guo Q., et al., 2011, Monthly Notices of the Royal Astronomical Society, 413, 101

Gwyn S. D. J., 2012, The Astronomical Journal, 143, 38

Häring N., Rix H.-W., 2004, The Astrophysical Journal Letters, 604, L89

Hathi N. P., Mobasher B., Capak P., Wang W.-H., Ferguson H. C., 2012, The Astrophysical Journal, 757, 43

Henriques B. M. B., Thomas P. A., Oliver S., Roseboom I., 2009, Monthly Notices of the Royal Astronomical Society, 396, 535

Henriques B. M. B., White S. D. M., Thomas P. A., Angulo R. E., Guo Q., Lemson G., Springel V., 2013, Monthly Notices of the Royal Astronomical Society, 431, 3373

Hickey S., Bunker A., Jarvis M. J., Chiu K., Bonfield D., 2010, Monthly Notices of the Royal Astronomical Society, 404, 212

Hills R. E., Kurz R. J., Peck A. B., 2010, Proc. SPIE, 7733, 773317

Hinshaw G., et al., 2013, The Astrophysical Journal Supplement Series, 208, 19

Hogan R., Fairbairn M., Seeburn N., 2015, Monthly Notices of the Royal Astronomical Society, 449, 2040

Hopkins A. M., Beacom J. F., 2006, The Astrophysical Journal, 651, 142

Hoyle F., 1949, in Problems of Cosmical Aerodynamics; Proceedings of a Symposium on the Motion of Gaseous Masses of Cosmical Dimensions held at Paris, August 16-19, 1949. p. 195

Hu E. M., Cowie L. L., Barger A. J., Capak P., Kakazu Y., Trouille L., 2010, The Astrophysical Journal, 725, 394

Hubble E., 1925, Popular Astronomy, 33, 252

Hubble E., 1929, Proceedings of the National Academy of Science, 15, 168

Ilbert O., et al., 2005, Astronomy & Astrophysics, 439, 863

Ilbert O., et al., 2006, Astronomy & Astrophysics, 457, 841

Ilbert O., et al., 2013, Astronomy & Astrophysics, 556, A55

Illingworth G. D., et al., 2013, The Astrophysical Journal Supplement Series, 209, 6

Infante L., et al., 2015, The Astrophysical Journal, 815, 18

Jarvis M. J., 2012, African Skies, 16, 44

Jarvis M. J., Rawlings S., Eales S., Blundell K. M., Bunker A. J., Croft S., McLure R. J., Willott C. J., 2001, Monthly Notices of the Royal Astronomical Society, 326, 1585

Jarvis M. J., et al., 2013, Monthly Notices of the Royal Astronomical Society, 428, 1281

Jiang L., et al., 2008a, The Astronomical Journal, 135, 1057

Jiang C. Y., Jing Y. P., Faltenbacher A., Lin W. P., Li C., 2008b, The Astrophysical Journal, 675, 1095

Jiang L., et al., 2009, The Astronomical Journal, 138, 305

Johnston R., Vaccari M., Jarvis M., Smith M., Giovannoli E., Häußler B., Prescott M., 2015, Monthly Notices of the Royal Astronomical Society, 453, 2540

Katz N., 1992, The Astrophysical Journal, 391, 502

Katz N., White S. D. M., 1993, The Astrophysical Journal, 412, 455

Kaviraj S., Laigle C., Kimm T., Devriendt J., Dubois Y., Pichon C., Slyz A., 2016, arXiv eprints, arXiv:1605.09379

Kennicutt R. C., 1998, The Astrophysical Journal, 498, 541

Kim J.-h., Wise J. H., Abel T., 2009, The Astrophysical Journal Letters, 694, L123

Kim J.-W., Edge A. C., Wake D. A., Stott J. P., 2011, Monthly Notices of the Royal Astronomical Society, 410, 241

Kimm T., Cen R., Devriendt J., Dubois Y., Slyz A., 2015, Monthly Notices of the Royal Astronomical Society, 451, 2900

Kinney A. L., Calzetti D., Bohlin R. C., McQuade K., Storchi-Bergmann T., Schmitt H. R., 1996, The Astrophysical Journal, 467, 38

Kirkpatrick J. D., et al., 2012, The Astrophysical Journal, 753, 156

Knapp G. R., et al., 2004, The Astronomical Journal, 127, 3553

Knebe A., et al., 2011, Monthly Notices of the Royal Astronomical Society, 415, 2293

Kochanek C. S., et al., 2012, The Astrophysical Journal Supplement Series, 200, 8

Koekemoer A. M., Fruchter A. S., Hook R. N., Hack W., 2002, in The 2002 HST Calibration Workshop : Hubble after the Installation of the ACS and the NICMOS Cooling System. p. 337, http://adsabs.harvard.edu/abs/2003hstc.conf..337K

Koekemoer A. M., et al., 2011, The Astrophysical Journal Supplement Series, 197, 36

Koekemoer A. M., et al., 2014, in American Astronomical Society, AAS Meeting #223 id 254.02.

Komatsu E., et al., 2011, The Astrophysical Journal Supplement Series, 192, 18

Kravtsov A. V., Klypin A. A., Khokhlov A. M., 1997, The Astrophysical Journal Supplement Series, 111, 73

Krumholz M. R., Tan J. C., 2007, The Astrophysical Journal, 654, 304

LSST Science Collaboration et al., 2009, arXiv e-prints, arXiv:0912.0201

Lacey C., Cole S., 1993, Monthly Notices of the Royal Astronomical Society, 262, 627

Landau L. D., Lifshitz E. M., 1987, Fluid Mechanics: Volume 6 (Course of Theoretical Physics), 2nd edn. Course of Theoretical Physics, Butterworth-Heinemann

Laor A., 2000, The Astrophysical Journal Letters, 543, L111

Larson R. B., 2000, ESA Spec. Pub., 445, L13

Laureijs R., Amiaux J., Arduini S., Augueres J. L., Brinchmann J., Cole R., 2011, in ESA/SRE(2011)12. (arXiv:0912.0914)

Lawrence A., et al., 2007, Monthly Notices of the Royal Astronomical Society, 379, 1599

Le Fèvre O., et al., 2005, Astronomy & Astrophysics, 439, 845

Leitherer C., et al., 1999, The Astrophysical Journal Supplement Series, 123, 3

Lilly S. J., Tresse L., Hammer F., Crampton D., Le Fèvre O., 1995, Journal of Chemical Information and Modeling, 545, 108

Lilly S. J., Le F. O., Hammer F., Crampton D., 1996, The Astrophysical Journal, 460, L1

Lilly S. J., et al., 2007, The Astrophysical Journal Supplement Series, 172, 70

Lorenzoni S., Bunker A. J., Wilkins S. M., Stanway E. R., Jarvis M. J., Caruana J., 2011, Monthly Notices of the Royal Astronomical Society, 414, 1455

Lorenzoni S., Bunker A. J., Wilkins S. M., Caruana J., Stanway E. R., Jarvis M. J., 2013, Monthly Notices of the Royal Astronomical Society, 429, 150

Lotz J. M., et al., 2014, in American Astronomical Society, AAS Meeting #223 id 254.01.

Loveday J., et al., 2012, Monthly Notices of the Royal Astronomical Society, 420, 1239

Loveday J., et al., 2015, Monthly Notices of the Royal Astronomical Society, 451, 1540

Lu Y., Mo H. J., Weinberg M. D., Katz N., 2011, Monthly Notices of the Royal Astronomical Society, 416, 1949

Lynden-Bell D., Ostriker J. P., 1967, Monthly Notices of the Royal Astronomical Society, 136, 293

Madau P., 1995, The Astrophysical Journal, 441, 18

Madau P., Dickinson M., 2014, Annual Review of Astronomy and Astrophysics, 52, 415

Magnelli B., Elbaz D., Chary R. R., Dickinson M., Le Borgne D., Frayer D. T., Willmer C. N. A., 2009, Astronomy & Astrophysics, 496, 57

Magnelli B., et al., 2013, Astronomy & Astrophysics, 553, A132

Magorrian J., et al., 1998, The Astronomical Journal, 115, 2285

Maller A., Bullock J., 2004, Monthly Notices of the Royal Astronomical Society, 355, 694

Marasco A., Crain R. A., Schaye J., Bahé Y. M., van der Hulst T., Theuns T., Bower R. G., 2016, Monthly Notices of the Royal Astronomical Society, 461, 2630

Marchesini D., et al., 2007, The Astrophysical Journal, 656, 42

Mastropietro C., Moore B., Mayer L., Debattista V. P., Piffaretti R., Stadel J., 2005, Monthly Notices of the Royal Astronomical Society, 364, 607

McAlpine K., Smith D. J. B., Jarvis M. J., Bonfield D. G., Fleuren S., 2012, Monthly Notices of the Royal Astronomical Society, 423, 132

McCracken H. J., et al., 2012, Astronomy & Astrophysics, 544, A156

McGee S. L., Goto R., Balogh M. L., 2014, Monthly Notices of the Royal Astronomical Society, 438, 3188

McLeod D. J., McLure R. J., Dunlop J. S., 2016, Monthly Notices of the Royal Astronomical Society, 459, 3812

McLure R. J., Dunlop J. S., 2002, Monthly Notices of the Royal Astronomical Society, 331, 795

McLure R. J., Cirasuolo M., Dunlop J. S., Foucaud S., Almaini O., 2009, Monthly Notices of the Royal Astronomical Society, 395, 2196

McLure R. J., Dunlop J. S., Cirasuolo M., Koekemoer A. M., Sabbi E., Stark D. P., Targett T. A., Ellis R. S., 2010, Monthly Notices of the Royal Astronomical Society, 403, 960

McLure R. J., et al., 2011, Monthly Notices of the Royal Astronomical Society, 418, 2074

McLure R. J., et al., 2013, Monthly Notices of the Royal Astronomical Society, 432, 2696

McNamara B. R., et al., 2000, The Astrophysical Journal Letters, 534, L135

Meurer G. R., Heckman T. M., Calzetti D., 1999, The Astrophysical Journal, 521, 64

Mo H., van den Bosch F., White S. D. M., 2010, Galaxy Formation and Evolution.. Cambridge University Press (arXiv:1104.0012), doi:10.1017/CBO9780511807244, papers://e1f660dc-e86d-4910-82ad-4b2b33c2f9ed/Paper/p10838

Moore B., Katz N., Lake G., Dressler A., Oemler A., 1996, Nature, 379, 613

Mortlock D. J., Patel M., Warren S. J., Hewett P. C., Venemans B. P., McMahon R. G., Simpson C., 2012, Monthly Notices of the Royal Astronomical Society, 419, 390

Moster B. P., Somerville R. S., Maulbetsch C., van den Bosch F. C., Macciò A. V., Naab T., Oser L., 2010, The Astrophysical Journal, 710, 903

Moster B. P., Somerville R. S., Newman J. A., Rix H.-W., 2011, The Astrophysical Journal, 731, 113

Moster B. P., Naab T., White S. D. M., 2013, Monthly Notices of the Royal Astronomical Society, 428, 3121

Moustakas J., et al., 2013, The Astrophysical Journal, 767, 50

Muñoz J. A., Trac H., Loeb A., 2010, Monthly Notices of the Royal Astronomical Society, 405, 2001

Newman J. A., Davis M., 2002, The Astrophysical Journal, 564, 567

Noll S., Burgarella D., Giovannoli E., Buat V., Marcillac D., Muñoz-Mateos J., 2009, Astronomy & Astrophysics, 507, 1793

Norberg P., et al., 2002, Monthly Notices of the Royal Astronomical Society, 336, 907

O'Neil K., Bothun G. D., Schombert J., 1998, The Astronomical Journal, 116, 2776

O'Neil K., Oey M. S., Bothun G., 2007, The Astronomical Journal, 134, 547

Oesch P. A., et al., 2010, The Astrophysical Journal Letters, 709, L21

Oesch P. A., et al., 2012, The Astrophysical Journal, 759, 135

Oesch P. A., et al., 2013, The Astrophysical Journal, 773, 75

Oesch P. A., et al., 2016, The Astrophysical Journal, 819, 129

Ono Y., et al., 2012, The Astrophysical Journal, 744, 83

Ono Y., et al., 2013, The Astrophysical Journal, 777, 155

Ostriker J. P., Gnedin N. Y., 1996, The Astrophysical Journal Letters, 472, L63

Ouchi M., et al., 2013, The Astrophysical Journal, 778, 102

Oyarzún G. A., et al., 2016, The Astrophysical Journal Letters, 821, L14

Peebles P. J. E., 1969, The Astrophysical Journal, 155, 393

Peebles P., 1980, The Large-scale Structure of the Universe. Princeton series in physics, Princeton University Press

Peng Y.-j., et al., 2010, The Astrophysical Journal, 721, 193

Pentericci L., et al., 2014, The Astrophysical Journal, 793, 113

Pérez-González P. G., et al., 2008, The Astrophysical Journal, 675, 234

Perlmutter S., Turner M. S., White M., 1999, Phys. Rev. Lett., 83, 670

Petrosian V., 1976, The Astrophysical Journal Letters, 209, L1

Pirzkal N., et al., 2013, The Astrophysical Journal, 772, 48

Planck Collaboration 2014, Astronomy & Astrophysics, 571, A1

Planck Collaboration 2015, arXiv eprints, arXiv:1502.0158

Planck Collaboration 2016, arXiv eprints, arXiv:1605.03507

Powell L. C., Slyz A., Devriendt J., 2011, Monthly Notices of the Royal Astronomical Society, 414, 3671

Prescott M., et al., 2016, Monthly Notices of the Royal Astronomical Society, 457, 730

Press W. H., Schechter P., 1974, The Astrophysical Journal, 187, 425

Prestage R. M., Peacock J. A., 1988, Monthly Notices of the Royal Astronomical Society, 230, 131

Prevot M. L., Lequeux J., Maurice E., Prevot L., Rocca-Volmerange B., 1984, Astronomy & Astrophysics, 132, 389

Reddy N. A., Steidel C. C., 2009, The Astrophysical Journal, 692, 778

Reed D. S., Bower R., Frenk C. S., Jenkins A., Theuns T., 2007, Monthly Notices of the Royal Astronomical Society, 374, 2

Reed D. S., Bower R., Frenk C. S., Jenkins A., Theuns T., 2009, Monthly Notices of the Royal Astronomical Society, 394, 624

Rees M. J., Ostriker J. P., 1977, Monthly Notices of the Royal Astronomical Society, 179, 541

Rhoads J. E., et al., 2013, The Astrophysical Journal, 773, 32

Richards G. T., et al., 2009, The Astrophysical Journal Supplement Series, 180, 67

Riess A. G., et al., 1998, The Astronomical Journal, 116, 1009

Robertson B. E., Ellis R. S., Dunlop J. S., McLure R. J., Stark D. P., 2010, Nature, 468, 49

Robertson B. E., et al., 2013, The Astrophysical Journal, 768, 71

Robertson B. E., Ellis R. S., Furlanetto S. R., Dunlop J. S., 2015, The Astrophysical Journal Letters, 802, L19

Robotham A. S. G., Driver S. P., 2011, Monthly Notices of the Royal Astronomical Society, 413, 2570

Romeo A. B., Agertz O., Moore B., Stadel J., 2008, The Astrophysical Journal, 686, 1

Rowan-Robinson M., McCrea W. H., 1968, Monthly Notices of the Royal Astronomical Society, 138, 445

SKA Organisation 2015, Advancing Astrophysics with the Square Kilometre Array. http://pos.sissa.it/cgi-bin/reader/conf.cgi?confid=215

Sandage A., Tammann G. a., Yahil A., 1979, The Astrophysical Journal, 232, 352

Sanders D. B., Mazzarella J. M., Kim D.-C., Surace J. A., Soifer B. T., 2003, The Astronomical Journal, 126, 1607

Scannapieco C., et al., 2012, Monthly Notices of the Royal Astronomical Society, 423, 1726

Schawinski K., Thomas D., Sarzi M., Maraston C., Kaviraj S., Joo S.-J., Yi S. K., Silk J., 2007, Monthly Notices of the Royal Astronomical Society, 382, 1415

Schawinski K., et al., 2014, Monthly Notices of the Royal Astronomical Society, 440, 889

Schaye J., et al., 2015, Monthly Notices of the Royal Astronomical Society, 446, 521

Schechter P., 1976, The Astrophysical Journal, 203, 297

Schenker M. A., Stark D. P., Ellis R. S., Robertson B. E., Dunlop J. S., McLure R. J., Kneib J.-P., Richard J., 2012, The Astrophysical Journal, 744, 179

Schenker M. A., et al., 2013, The Astrophysical Journal, 768, 196

Schenker M. A., Ellis R. S., Konidaris N. P., Stark D. P., 2014, The Astrophysical Journal, 795, 20

Schlegel D. J., Finkbeiner D. P., Davis M., 1998, The Astrophysical Journal, 500, 525

Schmidt M., 1968, The Astrophysical Journal, 151, 393

Schmidt K. B., et al., 2016, The Astrophysical Journal, 818, 38

Schombert J. M., McGaugh S. S., Eder J. A., 2001, The Astronomical Journal, 121, 2420

Scoville N., et al., 2007, The Astrophysical Journal Supplement Series, 172, 1

Shankar F., Salucci P., Granato G. L., De Zotti G., Danese L., 2004, Monthly Notices of the Royal Astronomical Society, 354, 1020

Sheth R. K., Tormen G., 1999, Monthly Notices of the Royal Astronomical Society, 308, 119

Sijacki D., Vogelsberger M., Genel S., Springel V., Torrey P., Snyder G. F., Nelson D., Hernquist L., 2015, Monthly Notices of the Royal Astronomical Society, 452, 575

Silk J., Mamon G. A., 2012, Research in Astronomy and Astrophysics, 12, 917

Smethurst R. J., et al., 2015, Monthly Notices of the Royal Astronomical Society, 450, 435

Smith D. J. B., 2015, arXiv e-prints, arXiv:1506.05630

Smith D. J. B., Hayward C. C., 2015, Monthly Notices of the Royal Astronomical Society, 453, 1597

Smith R., Sánchez-Janssen R., Fellhauer M., Puzia T. H., Aguerri J. A. L., Farias J. P., 2013, Monthly Notices of the Royal Astronomical Society, 429, 1066

Smith D. J. B., et al., 2014, Monthly Notices of the Royal Astronomical Society, 445, 2232

Somerville R. S., Davé R., 2015, Annual Review of Astronomy and Astrophysics, 53, 51

Somerville R. S., Primack J. R., Faber S. M., 2001, Monthly Notices of the Royal Astronomical Society, 320, 504

Somerville R. S., Lee K., Ferguson H. C., Gardner J. P., Moustakas L. A., Giavalisco M., 2004, The Astrophysical Journal Letters, 600, L171

Somerville R. S., Hopkins P. F., Cox T. J., Robertson B. E., Hernquist L., 2008, Monthly Notices of the Royal Astronomical Society, 391, 481

Springel V., 2010, Monthly Notices of the Royal Astronomical Society, 401, 791

Springel V., Hernquist L., 2003, Monthly Notices of the Royal Astronomical Society, 339, 289

Springel V., et al., 2008, Monthly Notices of the Royal Astronomical Society, 391, 1685

Stanway E. R., Bunker A. J., McMahon R. G., 2003, Monthly Notices of the Royal Astronomical Society, 342, 439

Stanway E. R., McMahon R. G., Bunker A. J., 2005, Monthly Notices of the Royal Astronomical Society, 359, 1184

Stanway E. R., Bremer M. N., Squitieri V., Douglas L. S., Lehnert M. D., 2008, Monthly Notices of the Royal Astronomical Society, 386, 370

Stark D. P., Ellis R. S., Bunker A., Bundy K., Targett T., Benson A., Lacy M., 2009, The Astrophysical Journal, 697, 1493

Stark D. P., Ellis R. S., Chiu K., Ouchi M., Bunker A., 2010, Monthly Notices of the Royal Astronomical Society, 408, 1628

Stark D. P., Ellis R. S., Ouchi M., 2011, The Astrophysical Journal Letters, 728, L2

Stark D. P., et al., 2015, Monthly Notices of the Royal Astronomical Society, 450, 1846

Steidel C. C., Giavalisco M., Dickinson M., Adelberger K. L., 1996, The Astronomical Journal, 112, 352

Steidel C. C., Adelberger K. L., Giavalisco M., Dickinson M., Pettini M., 1999, The Astrophysical Journal, 519, 1

Stinson G. S., Brook C., Macciò A. V., Wadsley J., Quinn T. R., Couchman H. M. P., 2013, Monthly Notices of the Royal Astronomical Society, 428, 129

Strateva I., et al., 2001, The Astronomical Journal, 122, 1861

Straughn A. N., et al., 2009, The Astronomical Journal, 138, 1022

Summers F., Davis M., 1995, The Astrophysical Journal, 454, 1

Takeuchi T. T., Yoshikawa K., Ishii T. T., 2003, The Astrophysical Journal Letters, 587, L89

Teyssier R., 2002, Astronomy & Astrophysics, 385, 337

Thomas D., Maraston C., Schawinski K., Sarzi M., Silk J., 2010, Monthly Notices of the Royal Astronomical Society, 404, 1775

Thompson R. I., 2003, The Astrophysical Journal, 596, 748

Tormen G., Diaferio A., Syer D., 1998, Monthly Notices of the Royal Astronomical Society, 299, 728

Tremaine S., et al., 2002, The Astrophysical Journal, 574, 740

Trenti M., Stiavelli M., 2008, The Astrophysical Journal, 676, 767

Tweed D., Devriendt J., Blaizot J., Colombi S., Slyz A., 2009, Astronomy & Astrophysics, 506, 647

Vogelsberger M., Genel S., Sijacki D., Torrey P., Springel V., Hernquist L., 2013, Monthly Notices of the Royal Astronomical Society, 436, 3031

Vogelsberger M., et al., 2014, Nature, 509, 177

Volonteri M., Dubois Y., Pichon C., Devriendt J., 2016, arXiv eprints, arXiv:1602.01941

Weingartner J., Draine B., 2001, The Astrophysical Journal, 548, 296

White S. D. M., Frenk C. S., 1991, The Astrophysical Journal, 379, 52

White S. D. M., Rees M. J., 1978, Monthly Notices of the Royal Astronomical Society, 183, 341

White M., Tinker J. L., McBride C. K., 2014, Monthly Notices of the Royal Astronomical Society, 437, 2594

White S. V., Jarvis M. J., Haussler B., Maddox N., 2015, Monthly Notices of the Royal Astronomical Society, 448, 2665

Wilkins S. M., Bunker A. J., Lorenzoni S., Caruana J., 2011a, Monthly Notices of the Royal Astronomical Society, 411, 23

Wilkins S. M., Bunker A. J., Stanway E., Lorenzoni S., Caruana J., 2011b, Monthly Notices of the Royal Astronomical Society, 417, 717

Wilkins S. M., Stanway E. R., Bremer M. N., 2014, Monthly Notices of the Royal Astronomical Society, 439, 1038

Williams R., et al., 1996, The Astronomical Journal, 112, 1335

Willott C. J., et al., 2013, The Astronomical Journal, 145, 4

Wolf C., Enheimer K. M., Rix H.-W., Borch A., Dye S., Kleinheinrich M., 2003, Astronomy & Astrophysics, 401, 73

Wyder T. K., et al., 2005, The Astrophysical Journal Letters, 619, L15

Wyder T. K., et al., 2007, The Astrophysical Journal Supplement Series, 173, 293

Xu C., Livio M., Baum S., 1999, The Astronomical Journal, 118, 1169

Yang X., Mo H. J., van den Bosch F. C., 2009, The Astrophysical Journal, 695, 900

York D. G., et al., 2000, The Astronomical Journal, 120, 1579

Zucca E., et al., 2006, Astronomy & Astrophysics, 455, 879

Zucca E., et al., 2009, Astronomy & Astrophysics, 508, 1217

de Jong R. S., et al., 2014, Proc. SPIE, 9147, 91470M

van Zee L., 2001, The Astronomical Journal, 121, 2003